Karlsruhe Institute of Technology

Combined Rheo-Dielectric: Insights into Polymer Dynamics and Charge Transport

Zur Erlangung des akademischen Grades eines

DOKTORS DER NATURWISSENSCHAFTEN

(Dr. rer. nat.)

von der KIT-Fakultät für Chemie und Biowissenschaften
des Karlsruher Instituts für Technologie (KIT)

genehmigte

DISSERTATION

von

M.Sc. Maxi Hoffmann

aus Dresden

1. Referent:	Prof. Dr. Manfred Wilhelm
2. Referent:	Prof. Dr. Michael Meier
Tag der mündlichen Prüfung:	27. April 2023

Die vorliegende Arbeit wurde von Oktober 2019 bis März 2023 unter der Betreuung von Herrn Prof. Dr. Manfred Wilhelm am Institut für Technische Chemie und Polymerchemie (ITCP) des Karlsruher Institut für Technologie (KIT) - Universitätsbereich angefertigt.

Ich versichere hiermit wahrheitsgemäß, die Arbeit selbstständig verfasst, alle benutzten Hilfsmittel vollständig und genau angegeben, und alles kenntlich gemacht zu haben, was aus Arbeiten anderer unverändert oder mit Abänderungen entnommen wurde, sowie die Satzung des KIT zur Sicherung guter wissenschaftlicher Praxis in der jeweils gültigen Fassung beachtet zu haben.

Maxi Hoffmann

Karlsruhe, den 17.02.2024

Zusammenfassung

Der Ausbau umweltfreundlicher Energiealternativen und -speichersysteme ist ein wichtiger Baustein zur Linderung des menschengemachten Klimawandels. Dabei sind Batteriespeichersysteme ein wichtiger Faktor um, zum Beispiel, die volatile erneuerbare Energieerzeugung auszugleichen. Hierbei stellen organische Flüssigelektrolyte, ein zentraler Bestandteil von Energiespeichersystemen, unter anderem aufgrund ihrer Toxizität und leichten Entflammbarkeit, ein Sicherheitsrisiko dar. Eine risikoärmere Alternative sind Polymerelektrolyte, welche aber oftmals eine noch nicht ausreichende ionische Leitfähigkeit aufweisen und daher Gegenstand aktueller Forschung sind. Eingebettet in diesen Rahmen, ist die vorliegende Arbeit in drei Themengebiete gegliedert.

Teil eins beschäftigt sich mit der Untersuchung von ionischen Flüssigkeiten (ILs) und deren (vernetzten) Polymeren. Hierfür werden zuerst der Ladungstransport und die Diffusionseigenschaften von Mischungen einer auf Imidazolium basierenden ionischen Flüssigkeit und dem dazugehörigen Polymer mittels Feldgradienten Kernspinresonanzspektroskopie (PFG-NMR) und einer Kopplung von Rheologie und dielektrischer Spektroskopie (Rheo-Dielektrik) untersucht. Anschließend werden die über PFG-NMR und dielektrische Spektroskopie erhaltenen Diffusionskoeffizienten der Ionen mittels des Haven Verhältnisses (H_R, Quotient des Diffusionskoeffizienten bestimmt mittels PFG-NMR und bestimmt mittels dielektrischer Spektroskopie) verglichen, um zu untersuchen, wie die Zugabe einer ionischen Flüssigkeit zum dazugehörigen Polymer sich auf die Anzahl der Aggregate und somit Effizienz des Ladungstransports auswirkt. Hierbei stellt sich heraus, dass das Haven Verhältnis der Mischungen im Vergleich zum reinen Polymer deutlich kleiner wird und somit weniger Aggregate vorhanden sind, zumal diese für einen größeren Bereich an Mischungsverhältnissen (30 gew% bis 70 gew% IL) konstant bleiben. Da eine hohe ionische Leitfähigkeit der Proben (z.B. 0.1 $\mathrm{mS\,cm^{-1}}$) zum Nachteil der mechanischen Eigenschaften erreicht wird, wird anschließend ein Vernetzer, basierend auf der zuvor untersuchten ionischen Flüssigkeit, synthetisiert, um so mechanisch stabile und ionisch leitfähige Gele herzustellen. Der Ladungstransport, die rheologischen Eigenschaften und das elektrochemische Verhalten der mit einer ionischen Flüssigkeit und einem Lithium-Salz geschwollenen Gele werden untersucht und die Ergebnisse werden mit Gelen, hergestellt mit einem kommerziell erhältlichem Vernetzer, verglichen. Es zeigt sich, dass die ionisch leitfähigen Gele eine deutlich höhere Lithium-Ionen Transportzahl und damit einen besseren Lithium-Ionen Transport, sowie in symmetrischen Lithium-Zellen eine bessere Leistung und Kompatibilität aufweisen.
Im zweiten Teil der Arbeit werden Polystyrol (S) und Polyisopren (I) Triblockcopoly-

mere (ISI und SIIS) anionisch synthetisiert und mittels nichtlinearer Rheologie werden verschiedene makroskopische Orientierungen (senkrecht, parallel und biaxial) herbeigeführt. Der Orientierungsprozess der phasenseparierten Blockcopolymere wird *in-situ* mittels Rheo-Dielektrik beobachtet um auch Zwischenzustände, sowie die Kinetik des Prozesses zu untersuchen. Ein besonderes Augenmerk wird auf den Einfluss der Block-Reihenfolge auf die erreichten makroskopischen Orientierungen, sowie die Zwischenzustände und Kinetik gelegt. Es zeigt sich, dass die Blockreihenfolge (ISI vs. SIIS), und somit -dynamik, einen großen Einfluss auf die erhaltenen makroskopischen Orientierungen hat und dadurch verschiedene makroskopische Orientierungen unter Anwendung der gleichen Parameter erhalten werden können.

Anschließend verknüpft der dritte Teil den ersten und zweiten und untersucht, wie sich die makroskopische Orientierung von ionisch leitfähigen Blockcopolymeren auf deren ionische Leitfähigkeit auswirkt. Die Ladung wird auf zwei verschiedene Möglichkeiten eingebracht: (I) ein Polystyrol-*b*-Poly-2-vinylpyridin Blockcopolymer wird mit einer ionischen Flüssigkeit gemischt und (II) mittels kontrollierter radikalischer Polymerisation von Polystyrol und einem Polystyrolderivat und anschließender Funktionalisierung des Derivats wird Ladung in einen Block eingebracht. Beide Proben werden anschließend mittels nichtlinearer Rheologie orientiert und die erhaltene makroskopische Orientierung wird mit der Änderung der ionischen Leitfähigkeit korreliert. Insbesondere für das ionische Blockcopolymer wird eine Korrelation zwischen einer parallelen Ausrichtung der Lamellen und einer Abnahme der ionischen Leitfähigkeit von max. 52 % beobachtet.

Abstract

The expansion of environmentally friendly energy alternatives and storage systems is an important component in mitigating human-made climate change. In this context, battery storage systems are an important factor to, e.g., balance volatile renewable energy generation. Organic liquid electrolytes, currently a key component of battery storage systems, pose a safety risk due to their toxicity and flammability, among other factors. A lower risk alternative are polymer electrolytes, but these often lack sufficient ionic conductivity and are therefore the subject of current research. In this context, the present thesis is divided into three parts.

The first part deals with the investigation of ionic liquids (ILs) and their (crosslinked) polymers. For this purpose, the charge transport and diffusion properties of mixtures of an imidazolium-based ionic liquid and the corresponding polymer are first investigated by field gradient nuclear magnetic resonance spectroscopy (PFG-NMR) and a coupling of rheology and dielectric spectroscopy (rheo-dielectric). Subsequently, the diffusion coefficients of the ions obtained via PFG-NMR and dielectric spectroscopy are compared by means of the Haven ratio (H_R, ratio of the diffusion coefficient determined via PFG-NMR and determined via dielectric spectroscopy) to investigate how the addition of an IL affects the number of aggregates and thus the efficiency of charge transport. Here, it is found that H_R of the blends is significantly smaller compared to the pure polymer and thus fewer aggregates are present, which remain constant for a wider range of mixing ratios (30 wt% to 70 wt% IL). Since a high ionic conductivity (e.g., $0.1\,\mathrm{mS\,cm^{-1}}$) of the samples is achieved at the expense of mechanical properties, a crosslinker based on the previously studied ionic liquid is then synthesized to prepare mechanically stable and ion-conductive gels. The charge transport, the rheological properties and the electrochemical behavior of the gels swollen with an ionic liquid and a lithium salt are studied and the results are compared with gels prepared with a commercially available crosslinker. It is found that the ion-conductive polymer gels have a significantly higher lithium ion transport number and thus better lithium ion transport, as well as a better performance and compatibility in symmetrical lithium cells.
In the second part of this thesis, polystyrene (S) and polyisoprene (I) triblock copolymers (ISI and SIIS) are anionically synthesized and different macroscopic orientations (perpendicular, parallel and biaxial) are induced by means of nonlinear rheology. The orientation process of the phase-separated block copolymers is observed *in-situ* by rheo-dielectric to investigate also intermediate states, as well as the kinetics of the process. Special attention

is paid to the influence of the block order on the obtained macroscopic orientations, as well as the intermediate states and kinetics. It is shown that the block order (ISI vs. SIIS), and thus dynamics, has a large influence on the macroscopic orientations and hence different macroscopic orientations can be obtained using the same parameters.
Subsequently, the third part links the first and second and investigates how the macroscopic orientation of ion-conductive block copolymers affects their ionic conductivity. Charge is introduced in two different ways: (I) a polystyrene-*b*-poly-2-vinylpyridine block copolymer is mixed with an IL and (II) charge is introduced into a block by means of controlled free radical polymerization of polystyrene and a polystyrene derivative and subsequent functionalization of the derivative. Both samples are then oriented by nonlinear rheology and the macroscopic orientation obtained is correlated with the change in ionic conductivity. In particular, for the charged block copolymer, a correlation is observed between a parallel orientation of the lamellae and a decrease in ionic conductivity of max. 52 %.

Contents

1 Introduction

Mitigating climate change requires environmentally friendly energy solutions and the challenges often lie in battery storage technology. A major problem with batteries is the organic liquid electrolyte, which is a key component, as it is highly flammable, volatile and toxic. The following section provides a brief overview of the topic and solid polymer electrolytes as an alternative, as well as the challenges they pose including an outline of the thesis.

Climate change and its consequences pose a serious threat to the world's population. Global warming will continue to increase in the coming years and extreme weather phenomena such as heat waves and flooding are becoming more likely.[1,2] Therefore, the demand and search for environmentally friendly energy solutions is increasing significantly, especially in the area of electric mobility and energy storage for renewable energies. In recent years, research has increasingly focused on rechargeable lithium-ion batteries (LIBs) because of their many advantages, such as high energy density, low self-discharge and long life.[3] However, most current LIBs still use organic liquid electrolytes, which pose a safety hazard because of their high flammability, toxicity and potential leakage due to their low viscosity at room temperature. Alternatives include solid polymer electrolytes (SPEs), which are leak-proof due to their solid aggregate state. While SPEs have the advantage of mechanical, electrochemical and chemical stability and low toxicity, they often suffer from low ionic conductivity.[4–6] One possibility to improve the ionic conductivity is the addition of a plasticizer, which enhances the segmental motion of the polymer electrolyte and thus the ion transport (e.g., addition of an IL to a polymerized ionic liquid (PolyIL)), as already demonstrated in the literature.[7–10] However, most of the studies in this field are focused on application and there is still a lack of understanding of the effect of a plasticizer on the polymer electrolyte, especially in terms of charge transport, dynamics and aggregation. In addition, if the ionic conductivity is sufficient, the mechanical stability of the electrolyte may no longer be given, making it prone to leakage or lithium dendrite growth. Two ways to overcome this problem are: (I) crosslinking of the polymer electrolyte, which results in mechanically stable ionogels or (II) design of ion-conductive block copolymers (BCPs), which have the advantage that the non-conductive block can provide mechanical stability, while the ion-conductive block can be plasticized.

To obtain the highest possible ionic conductivity in BCPs, they should have few defects and a good long-range order.[11,12] Structurally well organized BCPs can be obtained by annealing the samples (e.g., thermal or solvent vapor annealing) or by alignment through external forces (e.g., mechanical or magnetic fields).[12–14] The alignment of BCP model systems in the melt by mechanical fields, i.e., large amplitude oscillatory shear (LAOS), has already been studied in detail for diblock copolymer model systems based on polystyrene (PS) and polyisoprene (PI), which represent the mechanically stable and conductive phase, respectively.[15–17] The most commonly observed orientations were a perpendicular and a parallel orientation of the lamellae, depending on the applied parameters.[15] To increase ionic conductivity, a perpendicular orientation is preferred because the ions can then move within the lamellae along a direct path from one electrode to the other.[12,18] Riise *et al.* studied PS and PI diblock and triblock copolymers and while they found parallel and perpendicular alignment for the diblock, the poly(styrene)-*b*-poly(isoprene)-*b*-poly(styrene) (SIS) triblock showed only perpendicular alignment.[19] In addition, they found a high degree of perpendicular orientation in SIS that was never achieved in diblocks.[19] While the alignment mechanism of diblock copolymers has been studied *in-situ*, this is not the case for triblock copolymers, where the effect of block order on the alignment mechanism and intermediate alignment states has yet to be studied.[20,21] After investigating the model systems, it can be tested whether the results can be transferred to ion-conductive BCPs. First steps have already been taken in the field of orientation of ion-conductive diblock copolymers, but often the focus was not on the mechanism itself, but on the application.[11,12] Publications in this field reported an increased ionic conductivity upon perpendicular orientation of the lamellae.[12,13,18] However, there is no detailed study of the orientation of ion-conductive BCPs and the mechanism involved yet.

Based on the aforementioned challenges, this thesis addresses various aspects of the ion transport in polymer electrolytes as well as the orientation of (ion-conductive) BCPs and is composed of three different parts.
The first part deals with the synthesis and characterization of an IL, a PolyIL and their blends. After investigating their viscoelastic and dielectric properties by coupled rheology and dielectric spectroscopy (rheo-dielectric), the charge transport was analyzed by pulsed-field gradient nuclear magnetic resonance spectroscopy (PFG-NMR). The diffusion coefficients obtained in this way were compared with those obtained by broadband dielectric spectroscopy (BDS) using the Haven ratio (H_R). The blends with a sufficiently high ionic conductivity did not have sufficient mechanical properties. To overcome this issue, an ionic crosslinker was synthesized to prepare ionogels which were swollen with an IL. Their rheological and electrochemical properties were evaluated and compared with those of ionogels prepared with a commercially available crosslinker.
The second part of this thesis deals very fundamentally with the orientation of anionically synthesized PI and PS triblock copolymers with different block order and thus block dynamics (i.e., of ISI and SIS with an electric dipole inverted middle block). Their *in-situ* alignment behavior under LAOS has been investigated using a coupled rheo-dielectric

combination. The use of dielectric spectroscopy, small angle X-ray scattering (SAXS) and rheology allowed us to study the orientation on three different length scales, from a nanoscopic to a macroscopic length scale.
The third and final part combines the content of the first and second parts and deals with the orientation of ion-conductive BCPs. Ions are introduced either by incorporating an IL into an uncharged BCP or by introducing charges into one of the blocks. The synthesized BCPs are then oriented by LAOS and the change in ionic conductivity is correlated to the macroscopic orientation of the sample.

2 Synthesis of Polymers

This chapter provides an overview of the polymerization techniques used in this thesis. First, anionic polymerization is introduced and the mechanism is discussed in detail. Furthermore, its kinetics and molecular weight distribution are considered and its advantages and disadvantages are highlighted. Then a brief introduction to free radical polymerization is given, followed by controlled radical polymerization.

2.1 Anionic Polymerization

In 1956, the concept of anionic polymerization was first introduced by Szwarc *et al.*[22] They demonstrated the first polymerization with 'living' anions as active centers without termination or chain transfer reactions during the polymerization. The termination of active centers was prevented by repulsive Coulombic interactions between the chain ends and the exclusion of air (in particular O_2 and CO_2) during the chain-growth polymerization. Because of the absence of termination and chain transfer reactions, a precise molecular weight and small dispersity (Đ, typically 1.01 to 1.10) can be obtained.[23] Furthermore, anionic polymerization bears the advantage of the 'living' anion and thus complex architectures, e.g., stars, pom-poms or BCPs, can be easily built.[24,25] Despite its versatility, the use of anionic polymerization in industry is limited by its high technical level and thus high cost compared to other polymerizations. As a result, for example, only over 700 kt multiblock copolymers were produced by anionic polymerization in 2017, while a total of 348 Mt polymers were produced.[26,27]

Monomers and Solvents

Anionic polymerization is limited in the use of monomers and solvents due to possible side reactions of the anionic species. Therefore, only aprotic and non-electrophilic solvents can be used which must be dried and purified before the synthesis. Frequently used monomers are vinyl monomers, whose reactivity is determined by the stabilization of the carbanion formed, i.e., by electron-withdrawing functional groups, e.g., cyano-, or ester-groups, see Figure 2.1.[28] However, other monomers can also be used such as heterocyclic structures in anionic ring-opening polymerizations, e.g., epoxides or lactones, where either a nucleophilic substitution or addition takes place.[29]

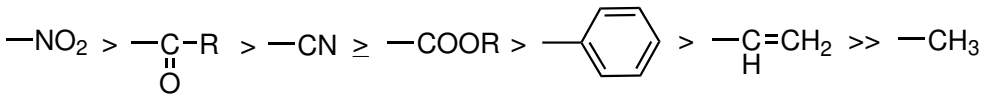

Figure 2.1: Effect of the electron withdrawing group (X) on the reactivity of vinyl monomers CH_2=CHX from highest to lowest.

Initiation

The anionic polymerization can be initiated using organometallic compounds like alkali organyls (e.g., butyllithium), alkali amides (e.g., sodium amide) and Grignard reagents (e.g., ethylmagnesium bromide). Sodium naphthalene can also be used to initiate polymerization by electron transfer. In the case of alkali organyls, for example, polymerization is initiated by the attack of a nucleophile Nu^- on the carbon-carbon double bond

$$M^+Nu^- + CH_2{=}CHX \longrightarrow Nu{-}CH_2{-}CHX^-M^+,$$

where M^+ is the counter ion. It is important that the initiation is significantly faster than the growth reaction to ensure a narrow molecular weight distribution and thus low Đ.[29] Therefore, the initiator has to be chosen carefully and depends on the monomer, i.e., less electrophilic monomers need strong nucleophilic initiators. Usually strong nucleophilic Lewis bases such as butyllithium are used for polymerization of monomers with weak electron withdrawing groups (e.g., styrene). Figure 2.2 shows the initiation of styrene with *s*-butyllithium (*s*-BuLi).

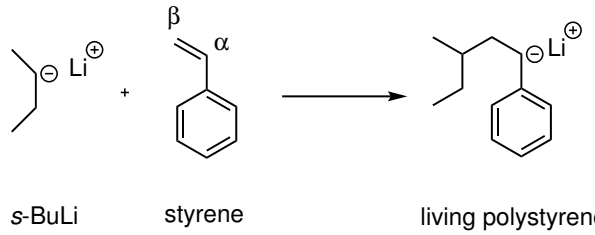

Figure 2.2: Initiation of styrene with *s*-butyllithium (*s*-BuLi). The resulting anion is stabilized by the aromatic ring, favoring an attack at the β position of styrene.

Propagation

After the initiation, monomers are constantly added and the chain grows as

$$P_i^- + M \longrightarrow P_i{-}M^-,$$

where P_i is the propagating chain, i the number of monomers added and M the monomer. Propagation continues until complete conversion of the monomer is achieved. After all the monomer is consumed, the carbanion remains active and propagation continues if more monomer units are added. If the added monomer is chemically different from the previous one, a BCP is formed. It should be noted, however, that not all carbanions are reactive enough to initiate chemically different monomers. While a BCP of isoprene and styrene can be polymerized from either monomer, methyl methacrylate does not allow initiation of styrene.[29] Figure 2.3 shows the chain growth using styrene as an example.

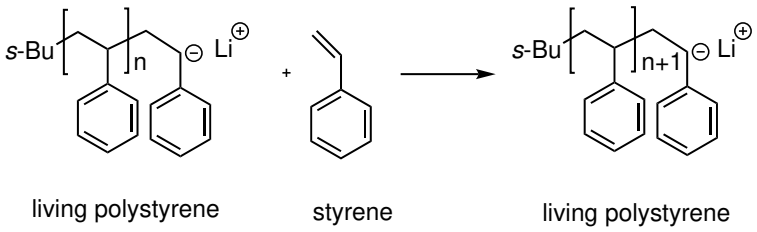

Figure 2.3: Propagation of styrene in anionic polymerization. The monomer is attacked by the electron pair of the carbanion.

In the ideal case, without side reactions or termination, the concentration of active carbanions is equal to the initiator concentration ($[I_0]$) and therefore the degree of polymerization (P_n) at each time (t) can be calculated by

$$P_\mathrm{n}\,(t) = \frac{[M_0]\,[M_\mathrm{t}]}{[I_0]} \tag{2.1}$$

where $[M_0]$ is the initial monomer concentration and $[M_\mathrm{t}]$ the monomer concentration at time t. Thus, the final P_n is predicted by the inital concentration of the monomer as

$$P_\mathrm{n} = \frac{[M_0]}{[I_0]} \tag{2.2}$$

and polymers with a defined molecular weight can be synthesized.

Termination

The active carbanions can be terminated with protic or electrophilic compounds. A commonly used termination method is the addition of a protic alcohol (e.g., degassed methanol, MeOH)

$$\mathrm{RM_n^-Li^+ + MeOH \longrightarrow RM_nH + MeOLi}$$

as shown on the example of styrene in Figure 2.4.

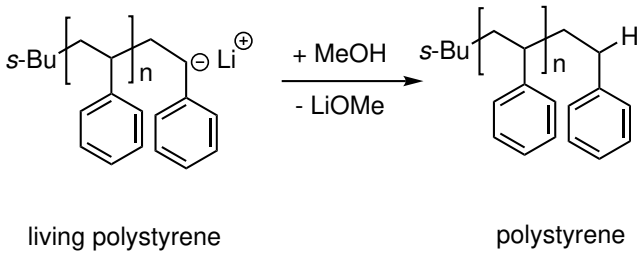

Figure 2.4: Termination of living polystyrene with methanol.

The possible termination by impurities such as O_2, H_2O or CO_2 emphasizes the importance of dried and purified reagents, clean glassware and an inert atmosphere. While a proton is transferred when the carbanion is terminated with water, a carboxylate is formed when carbon dioxide is added. Neither the remaining hydroxyl group, nor the carboxylate is nucleophilic enough to reinitiate the polymerization. If the carbanions are terminated with oxygen, radicals can be coupled, resulting in a bimodal molecular weight distribution when

the coupled product has double the molecular weight. The terminations described are depicted in Figure 2.5.

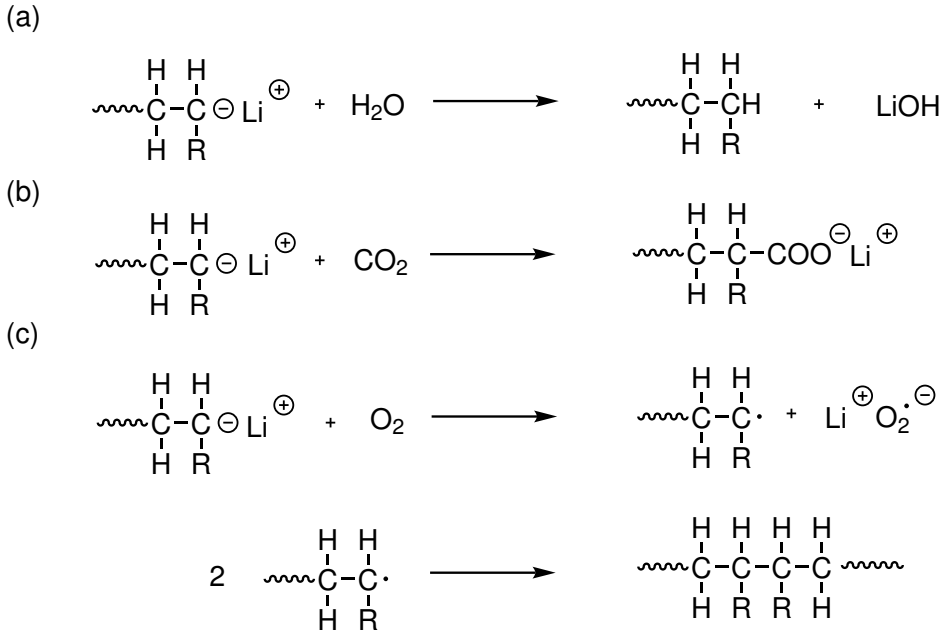

Figure 2.5: Termination by impurities such as **(a)** water, **(b)** carbon dioxide and **(c)** oxygen.

The choice of solvent influences the initiation and propagation rates. The organic lithium compounds used as initiators, e.g. *s*-BuLi, exist in solution as clusters, especially in nonpolar organic solvents. The use of polar solvents (e.g., THF) or the addition of certain reagents (e.g., crown ethers, see Figure 2.6) leads to the breakup of the aggregates and the initiation and propagation speed increase significantly.

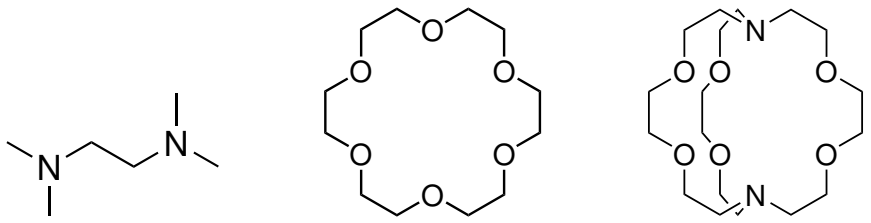

(a) (b) (c)

Figure 2.6: Examples for Lewis bases that are used in anionic polymerization to increase the initiation rate: **(a)** N,N,N',N'-tetramethylethane-1,2-diamine (TEMED), **(b)** 18-Crown-6 and **(c)** 2.2.2 Cryptand.

In addition, the choice of solvent can also affect the stereochemistry of the polymer, for example, in the case of 1,3-dienes, as shown in Figure 2.7 for PI. In unpolar solvents 1,4-*cis* PI is preferred, while in polar solvents a higher share of the 3,4-isomer is found. In order to obtain the generally intended 1,4-*cis* microstructure the reaction anion, counterion and monomer must be highly coordinated.[30,31] As the polarity of the solvent increases, the coordination decreases, as does the amount of 1,4-*cis*-PI. In THF, for example, the reaction anion is free and the 3,4-isomer is preferred to the 1,4-*cis*-isomer. However, not only the

1,4-*cis*-polyisoprene 1,4-*trans*-polyisoprene 3,4-polyisoprene 1,2-polyisoprene

Figure 2.7: The four possible microstructures of polyisoprene (PI). Their ratios depend on the solvent and counterion during the synthesis.

solvent but also the counterion and the substituents in the 1,3-diene play an important role and the polymerization of butadiene in polar solvents, for example, favors the 1,2-product.

Kinetics and Molecular Weight Distribution

The kinetics of an ideal anionic polymerization are based on the following assumptions:[32]

- The initiation is significantly faster than the propagation step and consequently all chains start at the same time.
- All chains grow under the same conditions and have an identical growth rate.
- The number of growing chains remains constant.
- The growth continues until all monomer is fully consumed or the polymerization is terminated.

Under these assumptions and since the kinetic chain length $v = P_\mathrm{n} - 1 \approx P_\mathrm{n}$ for high P_n, it can be shown that the molecular weight distribution corresponds to a Poisson distribution, see Equation 2.3.[33]

$$P\left(n\right) = \frac{\left(P_\mathrm{n} - 1\right)^{n-1} e^{(1-P_\mathrm{n})}}{(n-1)!} \tag{2.3}$$

The Poisson distribution is extraordinarily narrow and it can be shown that Đ calculates as[29]

$$Đ := \frac{M_\mathrm{w}}{M_\mathrm{n}} = 1 + \frac{P_\mathrm{n}}{\left(P_\mathrm{n}+1\right)^2} \approx 1 + \frac{1}{P_\mathrm{n}} \quad \text{for high } P_\mathrm{n}, \tag{2.4}$$

where M_n and M_w are the number and weight average molecular weight, respectively. Therefore, the theoretical dispersity of a polymer with $P_\mathrm{n} \geq 100$ is $Đ \leq 1.01$. Experimental values, however, are usually in the range of 1.01 to 1.10 due to impurities, polymerization conditions or inaccuracies in the analytical method.[22]

2.2 Radical Polymerization

Compared to anionic polymerization, radical polymerization takes one of the leading positions in industry because of its accessibility to many monomers and ease of practical implementation. Like the anionic polymerization, the free radical polymerization is divided

into three steps: initiation, propagation and termination.

Initiation

In most cases, the initiating free radicals are formed slowly *in-situ* by thermal or light induced cleavage of atomic bonds. Commonly used initiators are peroxides or azo compounds. The free radical then reacts with the first monomer unit.

$$\mathrm{I} \longrightarrow 2\,\mathrm{R}\cdot$$
$$\mathrm{R}\cdot + \mathrm{M} \longrightarrow \mathrm{RM}\cdot$$

Propagation

The chain continues to grow and monomer is added with a rather high rate. The stereochemistry of the polymer often depends on the stability of the propagating radical and styrene, for example, favors a head-tail polymerization.[29]

$$\mathrm{RM}\cdot + \mathrm{M} \longrightarrow \mathrm{RMM}\cdot$$

Termination

Termination in radical polymerization can occur by either recombination or disproportionation of two growing chains.

$$2\,\mathrm{RM}\cdot \longrightarrow \mathrm{RM{-}MR}$$
$$2\,\mathrm{RM}\cdot \longrightarrow \mathrm{R{=}M} + \mathrm{MR}$$

While recombination leads to a doubling of the molecular weight, disproportionation does not change the molecular weight. Both termination mechanisms occur simultaneously, but usually recombination is favored due to the higher activation energy of the disproportionation mechanism. At high temperatures, disproportionation is more favored for entropic reasons. However, steric effects and the presence or absence of a hydrogen atom in the β position can have an influence. Polystyrene, for example, terminates predominantly by recombination until 160 °C.[29] Chain termination can also be intentionally induced by the addition of inhibitors or retarders (e.g., benzophenone). This leads to the formation of mesomerically stabilized compounds that, in the case of inhibitors, cannot initiate further chain growth.

Chain Transfer Reactions

Furthermore, chain transfer reactions are likely to occur during the radical polymerization. In a chain transfer reaction, the radical is substituted by another atom such as hydrogen or halogens (X).[29]

$$\mathrm{RM}\cdot + \mathrm{HX} \longrightarrow \mathrm{RMH} + \mathrm{X}\cdot$$

Since the radical is still present after the chain transfer, a new chain continues to grow. Therefore, P_n is limited and also higher dispersities ($Đ \geq 2$) are reached.

Controlled Radical Polymerization

Controlled radical polymerization was developed in the late 20th century.[24,34–36] In this method, the radicals are reversibly deactivated and a dormant species is formed during the reaction to reduce the concentration of active chain ends. On average, all chains grow at the same rate and therefore a Poisson distribution of the molecular weight is found, resulting in a low dispersity. Moreover, chemically different monomers can be added to synthesize BCPs. Typical controlled radical polymerizations are atom transfer radical polymerization (ATRP), nitroxide-mediated radical polymerization (NMP) and reversible-addition-fragmentation chain-transfer polymerization (RAFT). In ATRP a carbon-carbon bond is formed with a transition metal complex,[37] while NMP uses alkoxyamines to form a stable radical species.[38] RAFT instead uses thiocarbonylthio compounds as a chain transfer agents to mediate the polymerization process.[39] The RAFT polymerization was first published in 1998 and, compared to other controlled radical polymerizations, has the advantage that it can be applied to a wide range of monomers and conditions, and polymers with a narrow distribution ($Đ < 1.2$) are obtained.[34]

3 Characterization Techniques

This chapter first describes the fundamentals of rheology. Starting from the basic principles, viscoelastic models and small amplitude oscillatory shear (SAOS) are introduced. Furthermore, the response of the material to nonlinear oscillatory shear is discussed and the concept of Fourier- transform rheology is explained. In addition, an overview of broadband dielectric spectroscopy (BDS) is given and both methods are discussed in terms of polymer characterization. Then the basic theory of small angle X-ray scattering (SAXS) is introduced and the properties and characterization of BCPs are discussed.

3.1 Rheology

Rheology is defined as the study of the flow and deformation of matter.[40,41] Materials are classified from ideal viscous to ideal elastic according to their behavior on deformation. Ideally viscous materials, so called Newtonian liquids, are ideal liquids whose viscosity remains constant during deformation, e.g., water. In a phenomenological model, their behavior can be described by a dash pot filled with an ideal liquid. Ideal solids have elastic properties, e.g., an iron spring. They follow Hooke's law and can be modeled by an ideal spring. However, most materials possess both characteristics and are so called viscoelastic materials, e.g., polymers. Rheology is the study of the response of these materials to deformation so that conclusions on their molecular structure can be drawn. Especially for polymeric materials, a variety of properties such as molecular weight, glass transition temperature, relaxation times and topology are accessible.

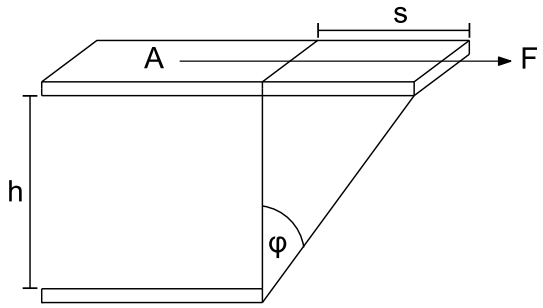

Figure 3.1: The shear experiment. The upper plate with a certain area (A) is moved by a force (F) by a certain displacement (s). The lower plate is fixed and h is the distance between the two plates.

The simplest rheological experiment is the shear experiment, displayed in Figure 3.1 on the example of the two plate model, which explains the basics of rheology. In the two-plate model, a material is placed in between two plates with the distance h and the area A of each plate. In the shear experiment, a force (F), respective stress, is applied to the upper plate and displaces it a certain distance (s), while the lower plate is fixed. The shear stress (σ) is given by

$$\sigma = \frac{F}{A} \tag{3.1}$$

where F is the applied force and A is the area of the plate. The shear strain (γ) is defined as the absolute deflection normalized to the plate distance.

$$\gamma = \frac{s}{h} \tag{3.2}$$

The velocity (v) of the shear motion is not uniform along the height of the material. Therefore the shear rate ($\dot{\gamma}$) defined by the following equation is used instead.

$$\dot{\gamma} = \frac{\mathrm{d}\gamma}{\mathrm{d}t} = \frac{v}{h} = \frac{1}{h}\left(\frac{\mathrm{d}s}{\mathrm{d}t}\right) \tag{3.3}$$

Phenomenological Models

The different material properties can be described by phenomenological models. Ideal elastic materials can be modeled by an ideal spring and obey Hooke's law (see Figure 3.2a and Equation 3.4). When a force is applied, the deformation of the spring occurs immediately and after the applied force is removed, the system immediately restores the initial state. Here, the stress is directly proportional to the deformation with the shear modulus (G) as constant of proportionality.

$$\sigma = G\gamma \tag{3.4}$$

The shear modulus is a characteristic material constant that provides information about the rigidity of a material. In Table 3.1 typical moduli of different materials are shown.

Material	G [Pa]
Glass, Metal	$> 10^{10}$
Ice, $-4\,^{\circ}\mathrm{C}$	10^{9}
Polymers	$0.1-10^{9}$
Hydrogels	10^{3}

Table 3.1: Typical shear moduli of different materials.[41,42]

Ideal liquids, so called Newtonian liquids, can be modeled by a Newtonian dashpot as displayed in Figure 3.2b. Unlike the Hooke model, the system does not return to its initial state after the applied force is removed. Here, the shear stress is proportional to the shear rate and the system follows

$$\sigma = \eta\dot{\gamma} \tag{3.5}$$

where the dynamic viscosity η is the proportionality constant.

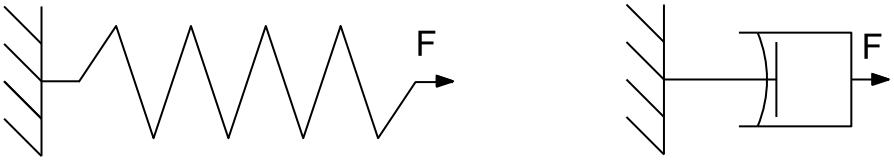

(a) Hooke model (b) Newton model

Figure 3.2: Both simple linear 1-dimensional rheological models, **(a)** the Hooke model (spring) for modeling ideal solids and **(b)** the Newton model (dashpot) for modeling ideal liquids.

In the case of oscillatory shear, a sinusoidal deformation is applied to the system over a time (t) with

$$\gamma(t) = \gamma_0 \sin(\omega_1 t) \tag{3.6}$$

where γ_0 is the strain amplitude and ω_1 is the excitation frequency. In the Hooke model for ideal solids, the time-dependent stress ($\sigma(t)$) is in phase with the oscillatory deformation as obtained by combining Equation 3.4 and 3.6.

$$\sigma(t) = G\gamma_0 \sin(\omega_1 t) \tag{3.7}$$

For the Newton model, the combination of Equation 3.5 and the time derivative of Equation 3.6 yields the following Equation.

$$\sigma(t) = \eta\gamma_0\omega_1 \cos(\omega_1 t) \tag{3.8}$$

Figure 3.3 graphically illustrates the response of the Hooke and Newton model to oscillatory excitation. While shear strain and stress are in phase for the Hooke model, a phase shift of $\delta = 90°$ is observed for the Newton model.

Viscoelastic materials, which have both elastic and viscous properties, can be described by a combination of the Hooke and Newton model.[42] The combination in series is the so-called Maxwell model, while the parallel combination is referred to as Kelvin-Voigt model, see Figure 3.4.

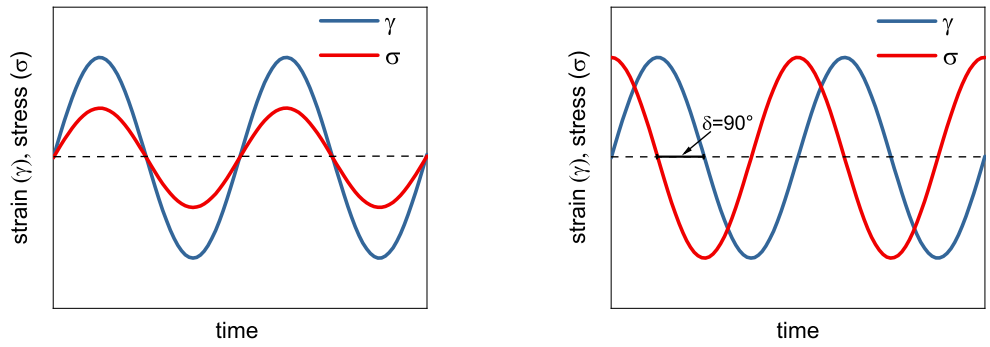

(a) Hooke model (b) Newton model

Figure 3.3: Oscillatory deformation and response of the material for **(a)** an ideal solid and **(b)** and ideal liquid.

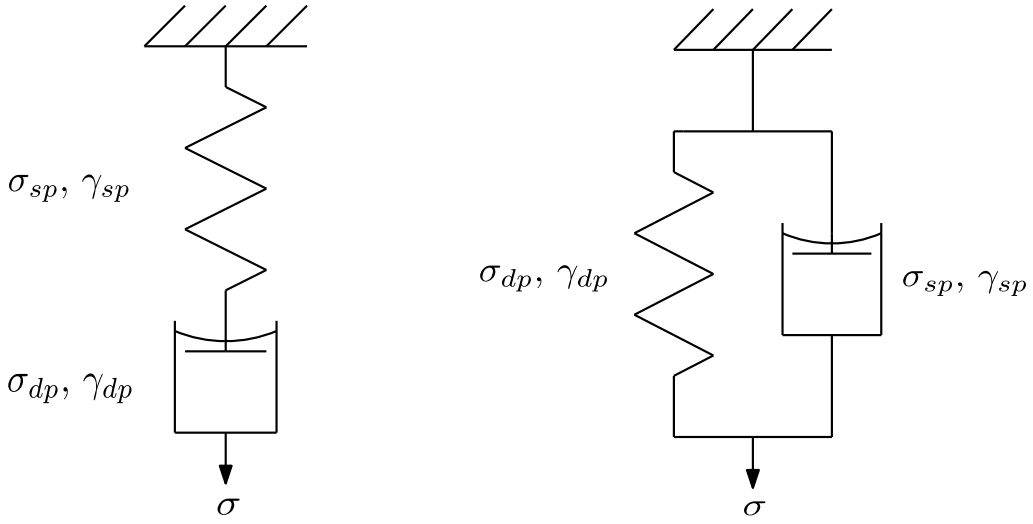

(a) Maxwell model (b) Kelvin-Voigt model

Figure 3.4: Combination of the linear models **(a)** in series as Maxwell model and **(b)** parallel combination as Kelvin-Voigt model where 'sp' refers to the spring and 'dp' to the dashpot.

The Maxwell model is used to describe viscoelastic liquids, which exhibit the same behavior as a Newtonian liquid with a small elastic component. The system does not return to its initial state after an applied force is removed due to the viscous component. For the Maxwell model, the total strain is the sum of the individual strains, while the total stress is equal to the individual stresses and is given by

$$\sigma = \sigma_{\mathrm{sp}} = \sigma_{\mathrm{dp}} \tag{3.9}$$

$$\gamma = \gamma_{\mathrm{sp}} + \gamma_{\mathrm{dp}} \tag{3.10}$$

where 'sp' refers to the spring and 'dp' to the dashpot. The ordinary differential equation for the Maxwell model is obtained by substituting Equation 3.5 and the time derivative of

the Equation 3.4 into the time derivative of Equation 3.10.

$$\dot{\gamma} = \frac{\dot{\sigma}}{G} + \frac{\sigma}{\eta} \tag{3.11}$$

Assuming an oscillatory shear with $\dot{\gamma}(t) = \gamma_0 \omega_1 \cos(\omega_1 t)$ and the relaxation time $\tau = \frac{\eta}{G}$ yields[42,43]

$$\sigma(t) = \gamma_0 \left(G \frac{(\omega_1 \tau)^2}{1 + (\omega_1 \tau)^2} \sin(\omega_1 t) + G \frac{\omega_1 \tau}{1 + (\omega_1 \tau)^2} \cos(\omega_1 t) \right) \tag{3.12}$$

$$= \gamma_0 \left(G' \sin(\omega_1 t) + G'' \cos(\omega_1 t) \right) \tag{3.13}$$

where G' is the storage modulus and G'' is the loss modulus.

$$G'(\omega) = G \frac{(\omega \tau)^2}{1 + (\omega \tau)^2}, \tag{3.14}$$

$$G''(\omega) = G \frac{\omega \tau}{1 + (\omega \tau)^2} \tag{3.15}$$

The storage modulus reflects the energy stored by the elastic part of the system, while the loss modulus characterizes the viscous part and the dissipated energy. At small frequencies, $G' \propto \omega^2$ and $G'' \propto \omega$, see Equation 3.12. Furthermore, the loss tangent ($\tan \delta_{\mathrm{Rheo}}$) is given by

$$\tan \delta_{\mathrm{rheo}} = \frac{G''}{G'} \tag{3.16}$$

resulting in an ideal elastic behavior for $\tan \delta \to 0$ and an ideal viscous behavior for $\tan \delta \to \infty$.

The behavior of a viscoelastic solid is described by the Kelvin-Voigt model, see Figure 3.4b. Here, the system returns to its initial state after the applied force is removed. The total deformation corresponds to that of the individual models, whereas the total stress is given by their sum.

$$\gamma = \gamma_{\mathrm{sp}} = \gamma_{\mathrm{dp}} \tag{3.17}$$

$$\sigma = \sigma_{\mathrm{sp}} + \sigma_{\mathrm{dp}} \tag{3.18}$$

Both models represent the simplest viscoelastic models in the linear regime and it should be noted that they are often insufficient to describe the rheological behavior of complex systems such as polymer melts. Therefore, multimode models have been developed to account for their complexity, e.g., the Burger model (combination of a Maxwell and a Kelvin-Voigt model in series).[41]

Small Amplitude Oscillatory Shear

In small amplitude oscillatory shear (SAOS), small amplitudes are used during the oscillatory excitation to obtain a linear response of the material. It is one of the most widely used methods for characterizing the linear viscoelastic properties of polymer melts.[41] In the linear region, the deformation is small enough that G' and G'' are independent of the applied strain.[43] When a polymer melt is studied using SAOS, G' and G'' as a function of frequency are obtained and different relaxation times, such as the longest or segmental relaxation time, are accessible. The frequency range is limited by mechanical or time constraints, but can be extended by the time-temperature superposition (TTS) principle.

Time-Temperature Superposition

The TTS principle allows G' and G'' to be studied over a wide dynamic range.[44] For this, frequency sweeps are performed at different temperatures in the linear regime. The frequency sweeps are then shifted horizontally along the frequency scale with respect to a reference temperature (T_{ref}), resulting in a master curve $G'(\omega)$, $G''(\omega)$.[43] The method is based on the fact that in viscoelastic materials all relaxation modes have the same temperature dependence. The mathematical relationship between the horizontal shift factor ($a_{\mathrm{T}} = \omega_{\mathrm{ref}}/\omega$), T_{ref} and the measurement temperature T is given by the Williams-Landell-Ferry (WLF) equation as[45]

$$\log a_T = \frac{C_1 (T - T_{\mathrm{ref}})}{C_2 + (T - T_{\mathrm{ref}})} \tag{3.19}$$

where C_1 and C_2 are empirical parameters and T_{g} is the glass transition temperature. If T_{g} is chosen as T_{ref}, C_1= 17.44 and C_2= 51.6 K are found for a wide range of linear, monodisperse polymer melts. At high temperatures, the product of C_1 and C_2 is related to an activation energy and consequently C_1C_2 is not a function of T_{ref}. However, it should be noted that the TTS principle is only valid as long as there are no phase transitions or structural changes in the investigated regime.

The obtained master curve contains crucial information about the material under investigation and is characterized by four different regimes, see Figure 3.5.

1. Viscous/flow regime: The relaxation of the polymer chain is faster than the excitation, resulting in a dominant viscous behavior.

2. Rubber plateau: The excitation is faster than the chain relaxation, so that a quasi-network is formed by the entanglements of the polymer chains and the elastic response dominates. The maximum elastic response is reached for the minimum of $\tan\delta_{\mathrm{Rheo}}$ and the crossover at low frequencies corresponds to the longest relaxation time (τ_{relax}).

3. Transition zone to the glass regime.

4. Glass regime: Below T_{g}, the polymer resembles a glass and exhibits high moduli in the range of 10^9 Pa to 10^{10} Pa.

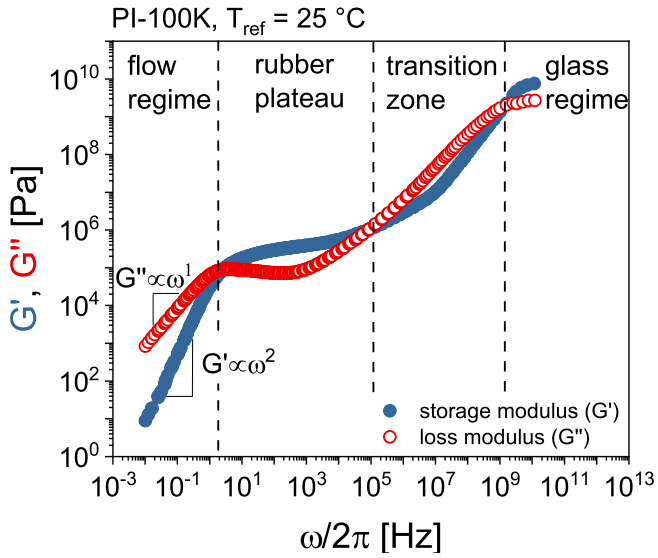

Figure 3.5: Example of a master curve of polyisoprene ($M_n = 100\,\mathrm{kg\,mol^{-1}}$) over 13 decades. The different regimes of the master curve are indicated by the dotted lines.

Large Amplitude Oscillatory Shear - The Nonlinear Regime

Up to now the linear regime has been discussed where the shear moduli are independent of the applied strain amplitude. However, this is not the case for large strain amplitudes where the moduli start to decrease with increasing strain amplitude upon entering the nonlinear regime (shear thinning behavior), see Figure 3.6a. This is due to the alignment of the chains, which facilitates sliding past each other at high strain amplitudes. Other effects include strain hardening (increase in shear moduli), as in polyvinyl alcohol-borax solutions or an initial weak or strong strain overshoot followed by shear thinning, as shown by emulsions or suspensions.[46–48] In LAOS, the nonlinear response of a material to shear is no longer purely sinusoidal, see Figure 3.6b.

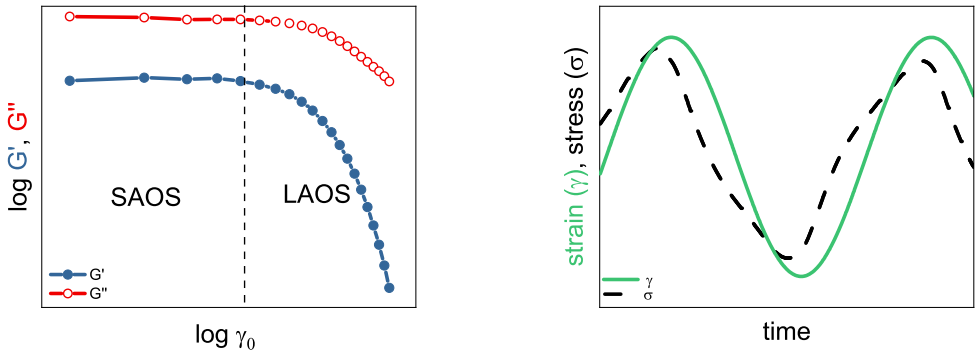

(a) (b)

Figure 3.6: Exemplary **(a)** strain sweep showing the linear (SAOS) and nonlinear (LAOS) regime including shear thinning and **(b)** sinusoidal excitation and nonlinear (not purely sinusoidal) response of the material.

It is not always easy to distinguish between linear and nonlinear behavior by considering only the direct response of the material. Furthermore, quantification of the nonlinearity without further data treatment is not possible. Therefore, the following section introduces Fourier-transform (FT) rheology to determine and quantify nonlinear viscoelastic behavior. In the following, a short introduction on FT rheology is given and further information on this topic can be found in the literature.[49–52]
Fourier-transform is used to transform a given dimension into its reciprocal dimension (e.g., time into frequency within spectroscopy or space into inverse space within scattering). In rheology, FT is used to decompose a time signal $s(t)$ into its component frequencies, and thus into a frequency spectrum $S(\omega)$ using Equation 3.20.[53] This transformation can also be reversed, whereby the original function is recovered from the frequency spectrum by Equation 3.21.

$$S(\omega) = \int_{-\infty}^{\infty} s(t)\, e^{-i\omega t} \mathrm{d}t \tag{3.20}$$

$$s(t) = \frac{1}{2\pi} \int_{-\infty}^{\infty} S(\omega)\, e^{i\omega t} \mathrm{d}\omega \tag{3.21}$$

An important property of FT is its linearity, i.e., a superposition in the time domain is transformed into a superposition in the frequency domain.[50]

$$s(t) + g(t) \overset{\mathrm{FT}}{\longleftrightarrow} S(\omega) + G(\omega) \tag{3.22}$$

Since FT is inherently complex (see Equation 3.20 and 3.21), even a real data set, e.g., torque vs. time , $s(t)$ will result in a complex spectrum $S(\omega)$ with a real (Re) and an imaginary (Im) part or magnitude (m) and phase (ϕ), see Equation 3.23 and 3.24. Figure 3.7 visualizes the connection between the different representations in a Gauss plane.

$$m(\omega) = \sqrt{Re\left(F(\omega)\right)^2 + Im\left(F(\omega)\right)^2} \tag{3.23}$$

$$\tan\left(\phi(\omega)\right) = \frac{Im\left(F(\omega)\right)}{Re\left(F(\omega)\right)} \tag{3.24}$$

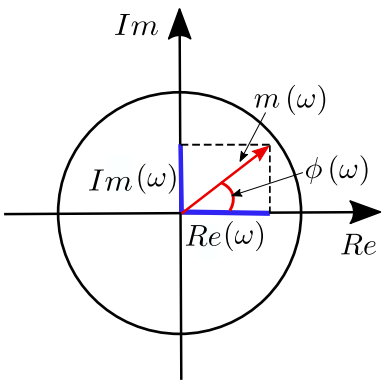

Figure 3.7: Visualization of a complex number (Gauss plane) with the real (Re) and imaginary part (Im) or the magnitude (m) and phase (ϕ).

In FT rheology, the raw stress signal is converted into a frequency dependent complex spectrum. In a LAOS measurement, oscillatory deformation is applied at a certain frequency. Therefore, higher frequencies, which are observed in the stress response, result from nonlinear behavior of the sample. The behavior of ideal Newtonian fluids is described by Newton's law (Equation 3.5) and the viscosity is independent of the applied shear rate. For a non-Newtonian fluid, the viscosity is a function of the shear rate that is independent of the direction of shear, so that $\eta(\dot{\gamma}) = \eta(-\dot{\gamma})$. The viscosity can consequently be approximated by a Taylor expansion having only even terms with respect to the shear rate.

$$\eta = \eta_0 + a\dot{\gamma}^2 + b\dot{\gamma}^4 + \dots \tag{3.25}$$

Using the simplified complex notation for the time-dependent strain in oscillatory shear, the strain and shear rate are given by the following equations.

$$\gamma(t) = \gamma_0 e^{i\omega_1 t} \tag{3.26}$$

$$\dot{\gamma}(t) = i\omega_1\gamma_0 e^{i\omega_1 t} \tag{3.27}$$

The shear stress is obtained by substituting Equation 3.25 and 3.27 into Newton's law (Equation 3.5), which gives the following expression

$$\sigma(\gamma, t) = \left(\eta_0 + a\dot{\gamma}^2 + b\dot{\gamma}^4 + \dots\right)\dot{\gamma} \tag{3.28}$$

$$= \left(\eta_0 + a\gamma_0^2 i^2\omega_1^2\gamma_0^2 e^{i2\omega_1 t} + b\gamma_0^4 i^4\omega_1^4\gamma_0^4 e^{i4\omega_1 t} + \dots\right) i\omega_1\gamma_0 e^{i\omega_1 t} \tag{3.29}$$

$$= \underbrace{\eta_0 i\omega_1\gamma_0}_{I_1} e^{i\omega_1 t} + \underbrace{a i^3\omega_1^3\gamma_0^3}_{I_3} e^{i3\omega_1 t} + \underbrace{b i^5\omega_1^5\gamma_0^5}_{I_5} e^{i5\omega_1 t} + \dots \tag{3.30}$$

where I_n are the intensities of the higher harmonics. By normalizing the higher harmonics to their fundamental, intensive values are obtained that can be used to quantify nonlinear behavior.

$$I_{n/1} = \frac{I_n}{I_1} \tag{3.31}$$

The intensity value of the higher harmonics, in particular $I_{3/1}$, is hypothesized to correlate with the number of grain boundaries in a BCP and thus allows conclusions about the evolution of grain boundaries, e.g., during orientation processes.[20,54]

3.2 Broadband Dielectric Spectroscopy

Broadband dielectric spectroscopy (BDS) investigates the effect of an electric field on a sample. The electric field ($\overrightarrow{E}$) leads to a polarization ($\overrightarrow{P}$) in the sample that is shifted by the phase angle δ_{BDS} to the applied electric field. From Maxwell's equations, the relation between $\overrightarrow{E}$ and the dielectric displacement ($\overrightarrow{D}$) is given by[55,56]

$$\overrightarrow{D} = \epsilon^* \epsilon_0 \overrightarrow{E} \tag{3.32}$$

where ϵ^* is the complex permittivity and ϵ_0 is the vacuum permittivity. For an oscillating electric field which is described by

$$\overrightarrow{E}(t, \omega_1) = \overrightarrow{E_0} e^{(-i\omega_1 t)}, \tag{3.33}$$

the complex permittivity reads as

$$\epsilon^*(\omega) = \epsilon'(\omega) - i\epsilon''(\omega) \tag{3.34}$$

where $\overrightarrow{E_0}$ is complex the amplitude, ω_1 is the angular frequency, t is the time, ϵ' is the real part and ϵ'' is the imaginary part of the permittivity. The complex permittivity formally is a second rank tensor as $\overrightarrow{D}$ and $\overrightarrow{E}$ are vectors. As in rheology, the real part of the trace of the tensor represents the energy stored, whereas the imaginary part of the trace of the tensor describes the energy lost through dissipation. Similar to rheology, the loss tangent of BDS is defined as

$$\tan(\delta_{BDS}) = \frac{\epsilon''}{\epsilon'}. \tag{3.35}$$

The polarization of the samples induced by $\overrightarrow{E}$ is defined as

$$\overrightarrow{P} = \overrightarrow{D} - \overrightarrow{D_0} = (\epsilon^* - 1)\,\epsilon_0 \overrightarrow{E} = \chi^* \epsilon_0 \overrightarrow{E} \tag{3.36}$$

where χ^* is the complex dielectric susceptibility of the sample and $\chi^* = (\epsilon^* - 1)$.
The macroscopic polarization $\overrightarrow{P}$ of the sample is the sum of induced and permanent microscopic dipole moments ($\overrightarrow{p}_n$) of the sample within a certain volume (V) and reads as

$$\overrightarrow{P} = \frac{1}{V} \sum \overrightarrow{p}_n \tag{3.37}$$

where n is the number of dipole moments. The different dipole moments result from

1. electronic polarization: induced shift of electronic orbits (very fast),
2. atomic polarization: induced relative displacement of the nucleus studied (fast) and
3. dipole polarization: orientation of permanent dipoles, measured with BDS.

The relaxation phenomena observed in BDS can be described by the linear response theory, which states that the time dependent response of a system to a perturbation obeys a linear equation under the assumption of an isotropic system and small field strengths.[55,56] For BDS, where the perturbation is the electric field and the response is the polarization, the linear response theory yields

$$\overrightarrow{P}(t) = \overrightarrow{P}_\infty + \epsilon_0 \int_{-\infty}^{t} \epsilon(t - t') \frac{\mathrm{d}\overrightarrow{E}(t')}{\mathrm{d}t'} \mathrm{d}t' \tag{3.38}$$

where $\epsilon(t)$ is the time dependent dielectric function and $\overrightarrow{P}_{\infty}$ is the total polarization. A detailed discussion of the linear response theory can be found in the literature.[55] When an oscillating electric field $\left(\overrightarrow{E}(t,\omega_1)\right)$ is applied, Equation 3.38 gives

$$\overrightarrow{P}(t) = \epsilon_0 \left(\epsilon^*(\omega_1) - 1\right) \overrightarrow{E}(t,\omega_1) \tag{3.39}$$

where $\epsilon^*(\omega)$ and $\epsilon(t)$ are related by a one-sided FT as

$$\epsilon^*(\omega) = \epsilon'(\omega) - i\epsilon''(\omega) = \epsilon_\infty - \int_0^\infty \frac{\mathrm{d}\epsilon(t)}{\mathrm{d}t} e^{-i\omega t} \mathrm{d}t \tag{3.40}$$

with $\epsilon_\infty = \lim_{\omega\to\infty} \epsilon'(\omega)$.
The macroscopic dielectric polarization $\overrightarrow{P}(t)$, which fluctuates around a mean value $\overline{\overrightarrow{P}(t)}$ because of thermal motion, is expressed by an auto correlation function ($f(t)$) as

$$f(t) = \frac{\langle \Delta P(t)\, \Delta P(0) \rangle}{\langle \Delta P^2 \rangle} \tag{3.41}$$

with $\Delta\overrightarrow{P} = \overrightarrow{P} - \overline{\overrightarrow{P}}$. The spectral density ($(\Delta P^2)_\omega$) is the inverse Fourier transform of $f(t)$ and describes the frequency distribution of the dipole fluctuations. It reads as

$$\left(\Delta P^2\right)_\omega = \frac{\langle \Delta P^2 \rangle}{2\pi} \int_{-\infty}^{\infty} f(t)\, e^{i\omega t} \mathrm{d}t. \tag{3.42}$$

For a classical system, the Fluctuation Dissipation Theorem connects the macroscopic response to the microscopic fluctuations as[55]

$$\left(\Delta P^2\right)_\omega = \frac{1}{k_B T} \frac{\epsilon''(\omega) - 1}{\pi\omega} \tag{3.43}$$

where k_B is the Boltzmann constant and T is the absolute temperature.

In general, relaxation processes describe the return of a system to a steady state after a perturbation, which in dielectric spectroscopy is the applied electric field. A relaxation in dielectric spectroscopy is represented as a step in $\epsilon'(\omega)$ and a peak in $\epsilon''(\omega)$ and different models can be used to describe the relaxation behavior. The Debye model uses the most simple ansatz and assumes that

$$\frac{\mathrm{d}\overrightarrow{P}(t)}{\mathrm{d}t} = -\frac{1}{\tau_D} \overrightarrow{P}(t) \tag{3.44}$$

where τ_D is the characteristic relaxation time from the Debye model. From Equation 3.44 an exponential decay follows for $f(t)$ as

$$f(t) = e^{\left(-\frac{t}{\tau_D}\right)} \tag{3.45}$$

which then leads to

$$\epsilon^*(\omega) = \epsilon_\infty + \frac{\Delta\epsilon}{1 + i\omega\tau_D} \tag{3.46}$$

where $\Delta\epsilon = \epsilon_s - \epsilon_\infty$ is the relaxation strength with $\epsilon_s = \lim_{\omega\to 0}\epsilon'(\omega)$. However, most relaxation processes are not correctly described by the Debye model because the dielectric functions are broader and sometimes show asymmetric behavior.The Cole/Cole model (CC) includes a broadening of the dielectric function by

$$\epsilon^*{}_{\mathrm{CC}}(\omega) = \epsilon_\infty + \frac{\Delta\epsilon}{1 + (i\omega\tau_{\mathrm{CC}})^{\beta_{\mathrm{CC}}}} \tag{3.47}$$

where $0 < \beta_{\mathrm{CC}} \leq 1$ describes a symmetric broadening and τ_{CC} the position of the peak maximum. An asymmetric broadening is taken into account by the Cole/Davidson model (CD)

$$\epsilon^*{}_{\mathrm{CD}}(\omega) = \epsilon_\infty + \frac{\Delta\epsilon}{(1 + i\omega\tau_{\mathrm{CD}})^{\gamma_{\mathrm{CD}}}} \tag{3.48}$$

where $0 < \gamma_{\mathrm{CD}} \leq 1$. Unlike τ_{CC}, τ_{CD} does not give the position of the peak maximum. A combination of both models was proposed by Havriliak and Negami (HN) which reads as[57]

$$\epsilon^*{}_{\mathrm{HN}}(\omega) = \epsilon_\infty + \frac{\Delta\epsilon}{\left(1 + (i\omega\tau_{\mathrm{HN}})^{\beta_{\mathrm{HN}}}\right)^{\gamma_{\mathrm{HN}}}} \tag{3.49}$$

where β_{HN} represents the symmetric and γ_{HN} the asymmetric broadening with $0 < \beta_{\mathrm{HN}}$ and $\beta_{\mathrm{HN}} \cdot \gamma_{\mathrm{HN}} \leq 1$. As β becomes smaller, the peak becomes broader and for $\beta_{\mathrm{HN}} = 1$, a symmetrical peak results.

Broadband Dielectric Spectroscopy of Polymers

Broadband dielectric spectroscopy is used to study the molecular dynamics of polymers in a broad dynamical range from 10^{-3} Hz to 10^6 Hz. Polymers can be classified into three different types according to the position of their molecular dipoles, as illustrated in Figure 3.8 (Stockmayer classification).[58]

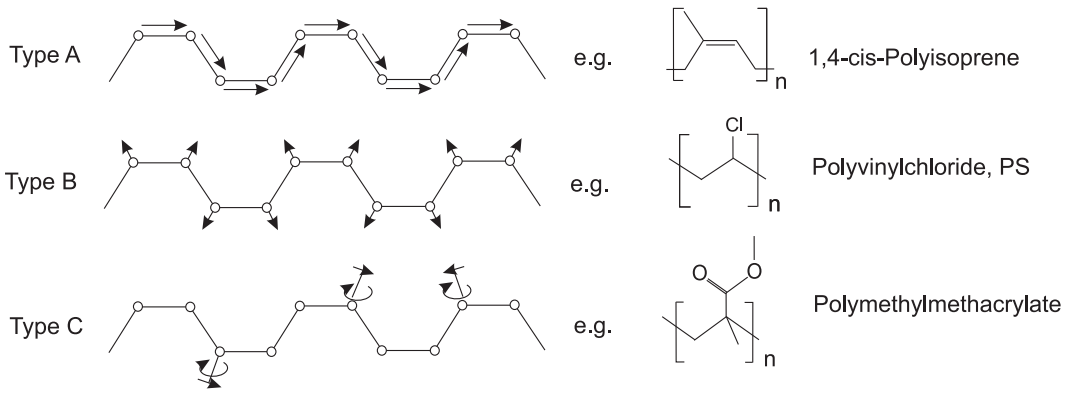

Figure 3.8: Classification of macromolecules according to Stockmayer.[58]

Type A polymers have a dipole moment parallel to their backbone, e.g., 1,4-*cis*-polyisoprene (1,4-*cis*-PI), while type B polymers have it perpendicular to their backbone, e.g., polyvinyl chloride. Type C polymers carry the dipoles in a flexible side chain such as polymethylmethacrylate. It should be noted that only type A polymers offer the possibility to study the relaxation of the whole chain ('normal mode'), while in the other cases only the

dynamics of the side groups can be observed. For example, in 1,4-*cis*-PI, the total dipole moment corresponds to the end-to-end vector, whose relaxation can be observed through the so-called normal mode in the dielectric spectrum. Figure 3.9 shows the normal mode and segmental relaxation (α-relaxation), describing the motion of chain segments, of PI and the influence of molecular weight. The data are normalized to the segmental relaxation peak.

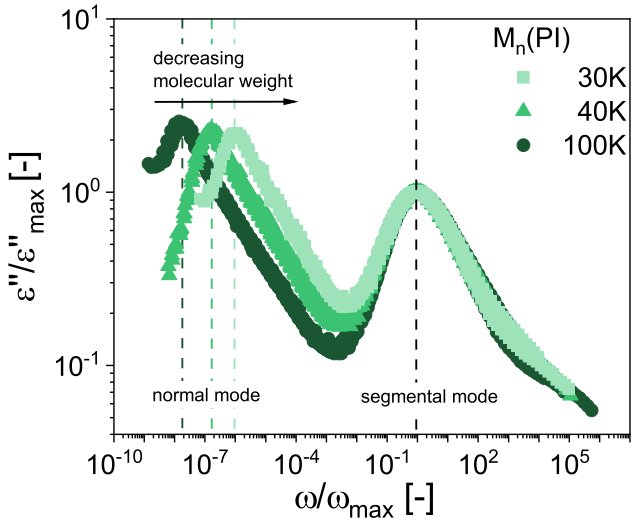

Figure 3.9: Dielectric spectra of three anionically synthesized polyisoprenes with different molecular weights. The data are double normalized to the segmental relaxation (α-relaxation) peak.

The normal mode relaxation, corresponding to τ_{relax}, is strongly dependent on the molecular weight of the sample and shifts to higher frequencies with decreasing molecular weight. In the literature, it is shown that $\tau_{relax} \propto M^{3.4}$.[43] Furthermore, an increase in temperature also leads to shorter relaxation times due to thermal activation and a Vogel-Fulcher-Tammann (VFT) temperature dependence is observed as[55]

$$\omega(T) = \omega_\infty e^{\left(-\frac{B}{T-T_0}\right)} \tag{3.50}$$

where ω_∞ is the frequency at infinite temperature, B is a fitting parameter related to the activation energy at high temperatures and T_0 is the Vogel temperature ($T_0 \approx T_g - 50\,\text{K}$). The VFT equation can be mathematically transformed into the Williams-Landell-Ferry (WLF) equation, since T_0 is related to C_2 at $T_\text{g} = T_\text{ref}$, when $T_0 = T_\text{g} - C_2$.
Both relaxations can also be detected by mechanical methods such as rheology. Figure 3.10a shows the dielectric and rheological master curves of a PI with $M_n = 40\,000\,\text{g mol}^{-1}$. The electric loss modulus (M'') is the imaginary part of the electric modulus (M^*) and is related to ϵ^* by the following equation.

$$M^*(\omega) = \frac{1}{\epsilon^*(\omega)} \tag{3.51}$$

Both methods show very good agreement for τ_{relax}. However, the segmental relaxation time is slightly longer in the mechanical method (see Figure 3.10b), which may be due to

the detection of different units by the different methods.[55] It is also possible to determine the T_g from BDS by extrapolating the VFT fit to $\tau = 100\,s$. The $T_{g,BDS}$ thus obtained was only 5 °C to 6 °C higher than that measured by dynamic scanning calorimetry (DSC, $T_g = -60\,°C$ vs. $T_{g,BDS} = -66\,°C$ for PI-30K). This T_g determination is not limited to BDS, but T_g can also be predicted in the same way using rheology. It should be noted that PI is very special in the sense that both the normal mode and the segmental relaxation can be detected by BDS, which is not possible for many other polymers.

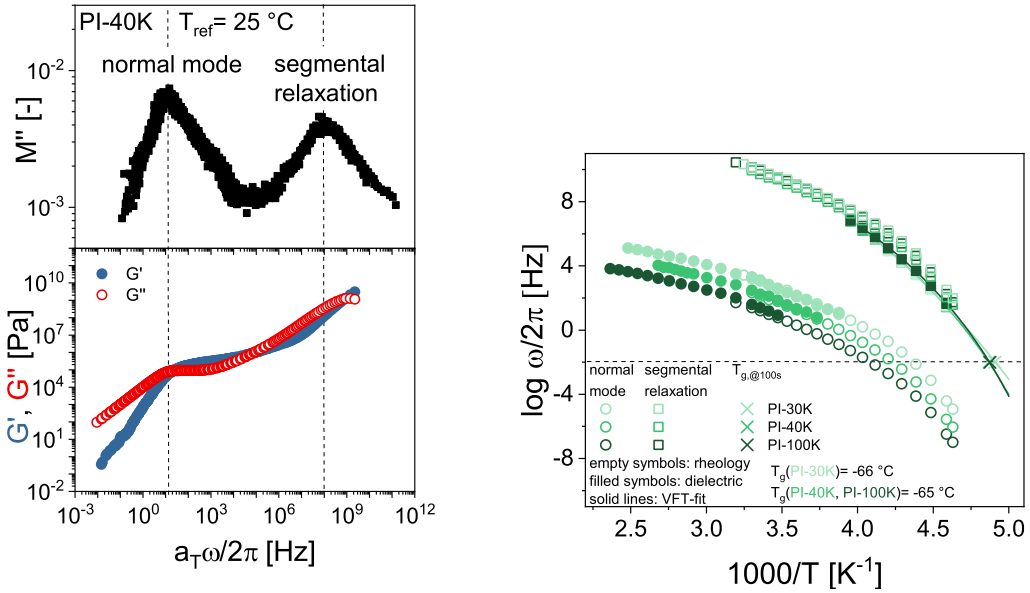

(a) (b)

Figure 3.10: **(a)** Dielectric and rheological master curves for PI-40K at $T_{ref} = 25\,°C$. **(b)** Longest relaxation times and segmental relaxation times determined by both methods, including a VFT fit (Equation 3.50) to determine the T_g by BDS.

3.3 Small Angle X-Ray Scattering

Small angle X-ray scattering (SAXS) can be used to characterize density differences in materials on nanometer length scale so that nanoparticle size distributions, pore sizes or morphology of phase separated materials can be studied.[59,60] It is based on the elastic scattering of X-rays in the material and the scattering is detected at small angles (about 0.1° to 10°). The smaller the angle of detection, the larger the dimensions that can be resolved.[61]

Irradiation of a material with electromagnetic waves leads to either adsorption or scattering of the applied radiation. In the case of SAXS, an elastic scattering process is observed, meaning that the scattered electromagnetic waves have the same frequency as the initial radiation. When the radiation hits the sample, it interacts with the electrons and induces dipoles, which in turn emit electromagnetic radiation. The spatial distribution of the induced dipoles causes interference of the electromagnetic waves and a diffraction pattern

is recorded by the detector. The Bragg equation describes when constructive interference is observed:[62]

$$n\lambda = 2d \sin \Theta \tag{3.52}$$

where n is an integer and λ is the wavelength, i.e., constructive interference occurs only at integers of the applied wavelength. Furthermore, d is the spatial periodicity of the scattering domains and Θ is the scattering angle for constructive interference. The schematic of a basic scattering experiment is shown in Figure 3.11.

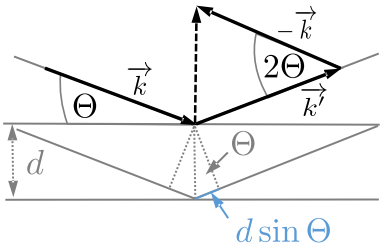

Figure 3.11: Scheme of a scattering experiment.

The initial electromagnetic wave described by the wave vector $\vec{k}$ is scattered. The resulting scattered electromagnetic radiation is now described by the wave vector $\vec{k'}$, which has the same wavelength (λ) as the initial radiation due to the elastic scattering process.

$$\left|\vec{k}\right| = \left|\vec{k'}\right| = \frac{2\pi}{\lambda} \tag{3.53}$$

The scattering vector $\vec{q}$ is the difference between the scattered wave vector and the initial wave vector.

$$\vec{q} = \vec{k'} - \vec{k} \tag{3.54}$$

Therefore, the magnitude of $|\vec{q}|$ is given by the following equation.

$$|\vec{q}| = \frac{4\pi \sin(\Theta)}{\lambda} \tag{3.55}$$

Combining Equation 3.52 and Equation 3.55 gives the relationship between q and d as $|\vec{q}| = \frac{2\pi}{d}$. The scattering intensity $I_s(\vec{q})$ is proportional to the square of the amplitude $A_s(\vec{q})$. Furthermore, both are proportional to the form and structure factor, $P(\vec{q})$ and $S(\vec{q})$, respectively.[60]

$$I_s(\vec{q}) \propto \left|A_s(\vec{q})^2\right| \propto P(\vec{q})\, S(\vec{q}) \tag{3.56}$$

The form factor contains information about the shape of the individual scattering objects while the structure factor gives insights into the spatial distribution or arrangement of the scattering objects.

3.4 Characterization of Block Copolymers in Melt and Solid State

Block copolymers are composed of blocks of at least two chemically different polymers and therefore combine the respective homopolymeric material properties.[63] Their high tunability and self-assembly makes them attractive as functional materials for a wide range of topics.[64]

One characteristic is their self-assembly to minimize the Gibbs free energy (ΔG_m).[65] The phase behavior of BCPs is controlled by three different parameters: (I) P_n, (II) the volume fraction of the blocks (f), and (III) Flory-Huggins parameter (χ_FH), where the latter describes the interactions of the monomers and is assumed to be independent of the number of blocks.[66–68] In the Flory-Huggins theory, the change in G_m for a diblock copolymer is derived as[69]

$$\frac{\Delta G_\mathrm{m}}{k_\mathrm{B}T} = \frac{f_\mathrm{i}}{P_\mathrm{n,i}} \ln f_\mathrm{j} + \frac{f_\mathrm{j}}{P_\mathrm{n,j}} \ln f_\mathrm{i} + f_\mathrm{i} f_\mathrm{j} \chi_\mathrm{FH} \tag{3.57}$$

where ΔG_m is the change in the Gibbs free energy, k_B is the Boltzmann constant, f_i is the volume fraction of block i, $P_\mathrm{n,i}$ is the degree of polymerization of block i, f_i is the volume fraction of block j and $P_\mathrm{n,j}$ is the degree of polymerization of block j. The first two terms in Equation 3.57 correspond to the mixing entropy, while the third term corresponds to the mixing enthalpy. The temperature dependence of the Flory-Huggins parameter can be described by[70]

$$\chi_\mathrm{FH} = \alpha_\mathrm{FH} T^{-1} + \beta_\mathrm{FH} \tag{3.58}$$

where α_FH and β_FH are experimentally determined parameters. Therefore, χ_FH decreases with increasing temperature and a transition from the microphase separated to a completely disordered state occurs at the so-called order-disorder temperature (T_ODT), see Figure 3.12.

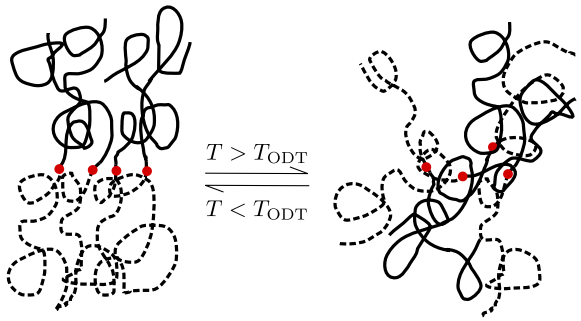

Figure 3.12: Temperature induced order-disorder transition in a diblock copolymer. The red dots indicate the covalent junctions between two polymer blocks.

This transition and the parameter T_ODT can for example be determined by rheology, SAXS or DSC.[64,71,72] Phase separation does not occur with every BCP. Whether phase separation occurs and how well the blocks are separated can be determined by the product of χ_FH and P_n. For phase separation to occur in a symmetric diblock copolymer (AB, $f_\mathrm{A} = f_\mathrm{B} = 0.5$), $\chi_\mathrm{FH} P_\mathrm{n} > 10.5$ whereas $\chi_\mathrm{FH} P_\mathrm{n} > 18$ for a symmetric triblock (ABA,

$f_A = f_B = 0.5$) copolymer because it is more difficult to confine two end blocks in their respective domains.[73] Three regions are defined that distinguish the degree of segregation: (I) weak ($\chi_{FH}P_n \approx 10$), (II) intermediate ($\chi_{FH}P_n \approx 10 - 100$) and (III) strong ($\chi_{FH}P_n \geq 100$) segregation.[64,74] At the same $\chi_{FH}P_n$, the BCPs can develop different structures depending on the volume fraction of each block. The calculated phase diagram for a poly(styrene-*b*-isoprene) BCP as a function of f is displayed in Figure 3.13 while Figure 3.14 gives a schematic representation of the different morphologies which can be determined from SAXS measurements.

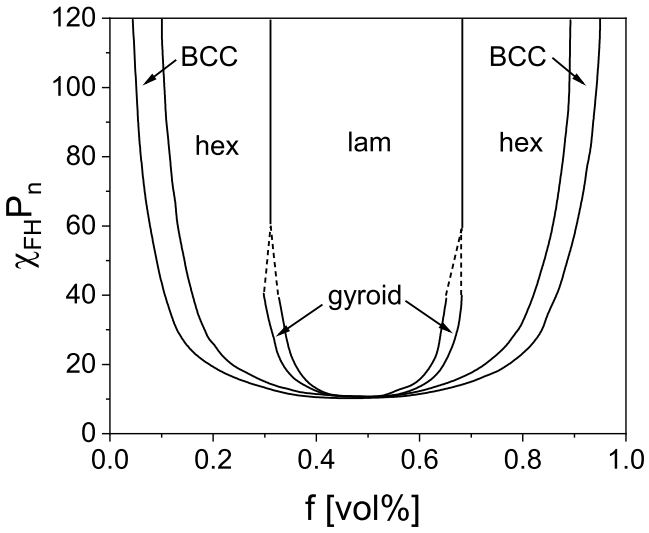

Figure 3.13: Calculated phase diagram of a symmetric PS-*b*-PI diblock copolymer with a BCC: body centered cubic, hex: hexagonal, gyroid: gyroidal and lam: lamellar morphology.[75,76]

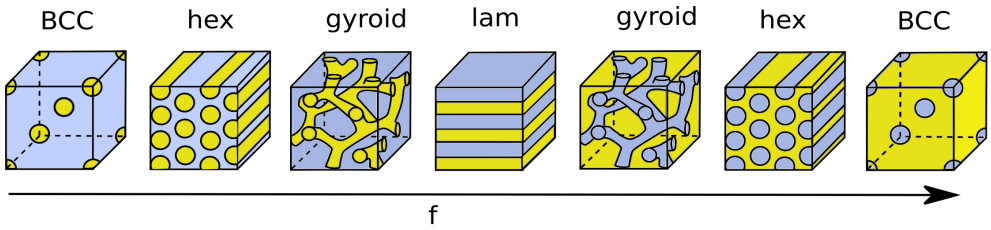

Figure 3.14: Scheme of the different morphologies at $\chi_{FH}P_n \approx 30$ and different volume fractions f with a BCC: body centered cubic, hex: hexagonal, gyroid: gyroidal and lam: lamellar morphologies.[75,76]

The exemplary SAXS pattern of a lamellar BCP including the higher maxima is displayed in Figure 3.15. Furthermore, two ways of averaging the SAXS patterns are indicated. The azimuthal average along the azimuthal angle (χ_{SAXS}) gives information about the degree of orientation in the sample. For this purpose, $I(\chi_{SAXS})$ can be fitted with a Gaussian function and the full width at half maximum (FWHM) quantifies the degree of orientation. The radial average along $\overrightarrow{q}$ gives information about the domain size and characteristic higher maxima allow conclusions about the morphology, see Table 3.2.[64]

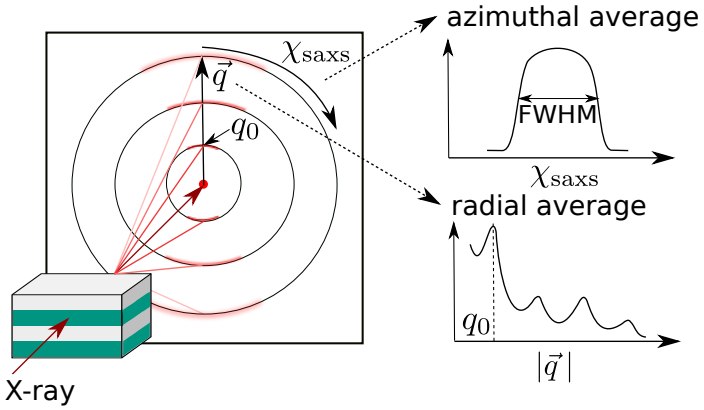

Figure 3.15: Analysis of the SAXS pattern of an oriented lamellar sample. The azimuthally averaged data provides information about the degree of macroscopic orientation, while the radial average provides information about the repeating length of the ordered structure and, if higher maxima are present, details on the morphology of the sample. The position of the first maximum is indicated by q_0.

Morphology	Characteristic Reflections					
Lamellar	q_0	$2q_0$	$3q_0$	$4q_0$	$5q_0$	$6q_0$ ...
Gyroidal	q_0	$3q_0$	$5q_0$	$7q_0$	$9q_0$	$11q_0$ ...
Hexagonal	q_0	$\sqrt{3}q_0$	$\sqrt{4}q_0$	$\sqrt{7}q_0$	$\sqrt{9}q_0$	$\sqrt{11}q_0$ ...
BCC	q_0	$\sqrt{2}q_0$	$\sqrt{3}q_0$	$\sqrt{4}q_0$	$\sqrt{5}q_0$	$\sqrt{6}q_0$ ...

Table 3.2: Characteristic reflections (higher maxima) for different morphologies with BCC: body centered cubic.[64]

Shear Alignment of Block Copolymers

Self-assembly of BCPs results in microscopically ordered structures on the nanometer length scale. While the grains are anisotropically ordered, their random orientation in the sample results in an isotropic material, see Figure 3.16. When an external field is applied, such as a mechanical, electric or magnetic field, macroscopic long-range order can be introduced so that the material exhibits an overall anisotropic order.[11,15,77] The mechanical alignment can take place by LAOS and three different orientations were observed in the literature: (I) a parallel, (II) a perpendicular and (III) a transverse orientation of the lammellae with respect to the shear field, see Figure 3.16. It should be noted that the transverse orientation does not reflect the complete reality, because the chains in the center would be frustrated due to their narrow spacing. In the literature, the transverse orientation is rarely observed and usually appears as a transition state to a macroscopic parallel or perpendicular orientation or at the cessation of flow.[15,78,79]

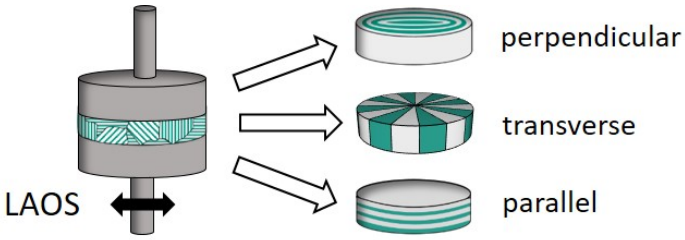

Figure 3.16: Schematic display of the final mechanical orientation of a lamellar block copolymer in a macroscopic parallel, transverse or perpendicular orientation.

4 Polymerized Ionic Liquids

In this Chapter the viscoelastic and dielectric properties of ionic liquids (ILs), polymerized ionic liquids (PolyILs) and their blends are investigated by coupled rheology and broadband dielectric spectroscopy (BDS). Their charge transport was furthermore examined by pulsed-field gradient nuclear magnetic resonance spectroscopy (PFG-NMR). The diffusion coefficients of the ions determined by pulsed-field gradient nuclear magnetic resonance spectroscopy (PFG-NMR) and BDS were evaluated using the Haven ratio (H_R). In addition, ionogels with an ionic liquid crosslinker similar in chemical structure to the IL used are synthesized and their ionic conductivity and performance in a symmetric Li-Li cell are compared to ionogels with a commercially available crosslinker.
The contents of this Chapter and the corresponding sections in the Appendix have been published in the journals Polymers from the Multidisciplinary Digital Publishing Institute (MDPI)[80] and Applied Materials and Interfaces from the American Chemical Society (ACS)[81] and have been adapted with permission. Maxi Hoffmann is the first author of these articles. The electrochemical experiments in[81] were performed in close collaboration with Dr. Andreas Butzelaar.

Polymerized ionic liquids are the polymers of ILs which are salts that are liquid below 100 °C due to of ions with delocalized charge and bulky structures that inhibit crystallization. ILs have many attractive properties such as low vapor pressure, high ionic conductivity, low flammability and a wide electrochemical stability window.[82,83] The unique properties of PolyILs combine those of ILs with the higher mechanical moduli of polymers and have therefore made them very attractive materials for electrochemical devices such as batteries, fuel cells and solar cells, among others.[6,84–86] Compared to classical liquid-electrolytes, solid-polymer electrolytes used in lithium ion batteries provide excellent mechanical properties and thermal stability without leakage, flammability or volatility.[4,5,87,88] However, their lower ionic conductivity compared to liquid electrolytes at room temperature has prevented their widespread commercialization in solid-state batteries.[6]
In the classical theory of ion conduction, segmental relaxation and charge transport in a polymer are related as follows:[89]

$$\sigma_0 \tau_\alpha T = constant \tag{4.1}$$

where σ_0 is the ionic conductivity, τ_α the segmental relaxation time and T the absolute

temperature. The Equation 4.1 implies that ion transport is only possible via segmental motion, which leads to a tremendous decrease of σ_0 below T_g due to a drastic increase of τ_α below T_g. Several studies have shown that a decoupling of the two processes can be achieved using rigid polymers, which would increase the ionic conductivity below T_g.[90,91] To gain deeper knowledge, several authors have focused on the study of the decoupling of charge transport from ion motion.[90,92–95] The influence of the degree of decoupling on the ionic conductivity below T_g was studied by Wang *et al.*[95] and Fan *et al.*[96] They found that the conductivity increases with the fragility (m_f) and an increasing m_f was achieved by incorporating particularly rigid structures into existing solid polymer electrolytes thus generating packing frustration.[95] Fan *et al.* found m_f in the range of 84 to 134 for their polyILs with varying pendant chains.[96]

$$m_f = \left.\frac{\mathrm{d}\log\tau_\alpha}{\mathrm{d}\left(\frac{T_g}{T}\right)}\right|_{T=T_g} \tag{4.2}$$

Nevertheless, the conductivity of pure PolyILs is still insufficient for practical applications at ambient temperatures, where a typical goal would be to achieve an ionic conductivity of $1 \times 10^{-3}\,\mathrm{S\,cm^{-1}}$ or higher. There are two ways to solve this problem: one is to increase the carrier density and the other is to increase the mobility of the ions in the material. In the following chapter, the two strategies mentioned above were combined and the corresponding monomer was added as a plasticizer to the PolyIL to increase the number of ions and accelerate the dynamics, thus improving the ionic conductivity.

4.1 Blends of Polymerized Ionic Liquids and Ionic Liquids

Recent publications already demonstrated the combination of highly conductive ILs with a host polymer. For example, Põhago-Esko *et al.* investigated blends of photopolymerized 1-[n-(methacryloyloxy)alkyl]-3-methylimidazolium bromides (n = 2, 6, 7 or 10) with 1-ethyl-3-methylimidazolium tetrafluoroborate ([EMIM]BF_4) as IL additive. The blends maintained solidity up to 40 %v/v of IL content, with ionic conductivities of approximately $1 \times 10^{-4}\,\mathrm{S\,cm^{-1}}$ (a typical goal would be to reach an ionic conductivity of $1 \times 10^{-4}\,\mathrm{S\,cm^{-1}}$ or higher). In addition, Marcilla *et al.* blended poly-(1-vinyl-ethyl-imidazolium) with different counter anions ($TFSI^-$, BF_4^- and Br^-) with 1-butyl-3-methylimidazolium bis(trifluoromethanesulfonimide) ([BMIM]TFSI), 1-butyl-3-methylimidazolium tetrafluoroborate ([BMIM]BF_4) and 1-butyl-3-methylimidazolium bromide ([BMIM]Br) as ILs.[8] They also observed ionic conductivities in the range of $1 \times 10^{-5}\,\mathrm{S\,cm^{-1}}$ to $1 \times 10^{-2}\,\mathrm{S\,cm^{-1}}$ at room temperature, which increased with the IL content. Furthermore, molecular simulations were performed by Mogurampelly *et al.* to study the ion transport in blends of ILs and their polymers. They studied mixtures of 1-butyl-3-methyl-imidazolium hexafluorophosphate and poly(1-butyl-3-vinylimidazolium) hexafluorophosphate and suggested the existence of a similar charge transport mechanism, controlled by intra- and intermolecular hopping of ions, as observed in their previous reports on PolyILs.[9,10] Additionally, they found stronger interactions between the anions

and the polymer cations than with the IL-cations. They observed that the non-monotonic behavior of the ionic conductivities in the blends of PolyILs and ILs was controlled by the interplay between ion mobility, decoupling of ion transport from the segmental motion of the polymer and the number of free ions, which reveals the rich properties in these materials.

Another way to investigate the mobility of the ions is PFG-NMR.[97] It allows for the determination of the translational dynamics and diffusion coefficients of the moieties.[98–100] To relate the diffusion coefficients to the ionic conductivities measured by BDS, the diffusion coefficient of the conduction process (D_σ) can be calculated according to the Nernst-Einstein equation, as follows:

$$D_\sigma = \frac{n_0 q_e^2}{k_B T} \sigma_0 \tag{4.3}$$

where n_0 is the number density of the ions, q_e the elementary charge and k_B the Boltzmann constant. The ionic conductivity σ_0 is determined from the frequency-independent plateau in the real part of the conductivity ($\sigma'(\omega)$) via BDS. The diffusion coefficient obtained by PFG-NMR is often reported to be larger than that obtained by BDS.[101]. This difference, or rather the related ratio, is considered to originate from the presence of ion pairs and aggregates, which do not contribute to the process of charge transport. The ratio of the two diffusion coefficients can be described quantitatively by the Haven ratio (H_R) as follows:

$$H_R = \frac{D_{mean}}{D_\sigma} = \frac{k_B T}{n_0 q_e^2 \sigma_0} D_{mean} \tag{4.4}$$

where D_{mean} corresponds to the mean diffusion coefficient $D_{mean} = (D_{anion} + D_{cation})/2$. If H_R exceeds 1, it indicates that ion pairs have formed; these ion pairs do not contribute to the charge transport and are therefore neglected in BDS measurements. Typical values of H_R are around 1.4 for ILs, indicating a low aggregate concentration, but higher values (e.g., $H_R = 5$), resulting in correlated ion motion in the material, have been found for PolyILs.[101–104]

Despite the numerous contributions, most of the studies focus mainly on the application of PolyIL/IL blends in energy storage. There is still a lack of understanding of the mechanism of charge transport and dynamics in these blends. Therefore, this chapter presents a systematic investigation of different blends of poly(1-butyl-3-(4-vinylbenzyl)imidazolium bis(trifluoromethane sulfonyl)imide) (poly[VBBI]TFSI) and the respective monomer to create thermally stable polymer electrolytes, avoid phase separation and improve the ionic conductivity of the final materials. The objective is to better understand the effect of an IL on the polymer host in terms of charge transport and segmental relaxation. The blends of the self-synthesized PolyIL and the related IL are characterized by a unique combination of rheology and BDS (rheo-dielectric) to study the influence of the IL on mechanical stability and ionic conductivity. Furthermore, the diffusion process in the IL as well as in two blends is studied to better understand the mechanism and efficiency of charge transport.

4.1.1 Sample Preparation and Characterization

1-Butyl-3-(4-vinylbenzyl)imidazolium bis(trifluoromethane sulfonyl)imide ([VBBI]TFSI) and poly[VBBI]TFSI were synthesized according to Section A.1.2. The structures of the synthesized IL monomer and its polymer are displayed in Figure 4.1 and their ^{1}H-nuclear magnetic resonance (NMR) spectra are shown in Figure A.2.1 and A.2.2 in the Appendix. Size exclusion chromatography (SEC) measurements were performed with 10 mM 1-butylimidazole and 10 mM lithium bis(trifluoromethane sulfonyl)imide (LiTFSI) in tetrahdrofuran (THF) as eluent.[24] The molecular weight was determined using the multi angle laser light scattering (MALLS) detector and the number average molecular weight of the PolyIL was M_n= 57 000 g mol^{-1} and Đ= 2.25. The detailed measurement procedure and additional information can be found in the Appendix A.1.3.2.

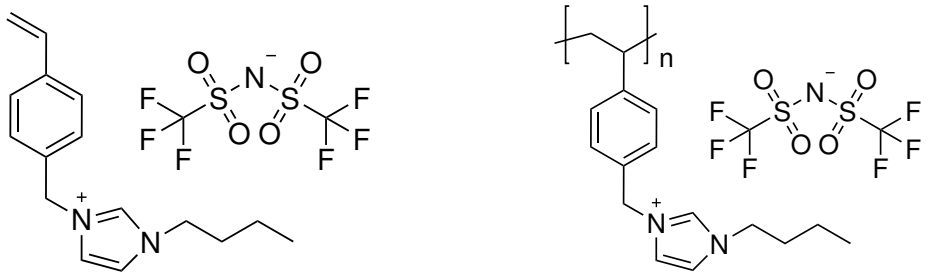

(a) Ionic liquid (b) Polymerized ionic liquid

Figure 4.1: Chemical structure of **(a)** 1-butyl-3-(4-vinylbenzyl)imidazolium bis(trifluoromethane sulfonyl)imide ([VBBI]TFSI) and **(b)** the corresponding polymer poly[VBBI]TFSI.

Table 4.1 gives an overview of the investigated samples, starting with the PolyIL, its blends with the corresponding IL and the pure IL. The table displays the corresponding T_g from DSC measurements, σ_0 and G' at room temperature.

Table 4.1: Overview of the samples: The names correspond to the mixing ratios of the pure polymerized ionic liquid (PolyIL) and ionic liquid (IL) in each weight percent. The glass transition temperature (T_g) from DSC measurements, the ionic conductivity (σ_0) and the storage modulus (G') at 25 °C and $\omega = 100\,\mathrm{rad\,s^{-1}}$ are displayed.

Sample Name	PolyIL [wt%]	IL [wt%]	$T_{g,DSC}$[a] [°C]	$\sigma_{0,25\,°C}$[b] [S cm^{-1}]	$G'_{25\,°C}$[b,c] [Pa]
Poly[VBBI]TFSI	100	0	8	3.4×10^{-7}	1.4×10^{7}
90/10	90	10	9	1.3×10^{-6}	7.2×10^{5}
70/30	70	30	−35	7.7×10^{-6}	3.3×10^{4}
50/50	50	50	−44	2.9×10^{-5}	5.8×10^{3}
30/70	30	70	−50	1.1×10^{-4}	1.8×10^{2}
20/80	20	80	−53	1.4×10^{-4}	7.5×10^{2}
10/90	10	90	−53	2.2×10^{-4}	1.8×10^{2}
[VBBI]TFSI	0	100	−54	3.4×10^{-4}	-

[a] T_g was measured by DSC with a heating rate of 10 °C min. [b] A graphical summary of σ_0 and G' as a function of IL content is displayed in A.2.3.[85] [c] The storage modulus was determined at 25 °C and $\omega = 100\,\mathrm{rad\,s^{-1}}$.

The DSC curves of the second heating cycle with a heating rate of 10 °C min are displayed in Figure 4.2. The T_g of the samples was determined from the inflection point of the second heating cycle.

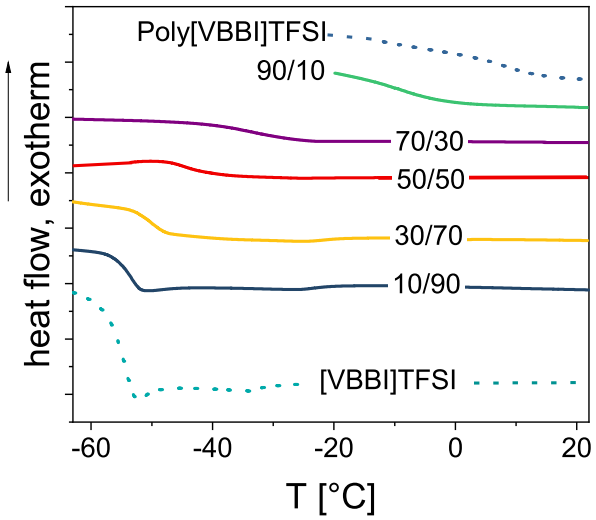

Figure 4.2: Dynamic scanning calorimetry (DSC) curves of all samples.

Additionally, wide angle X-ray scattering (WAXS) measurements were performed to investigate the change in the morphology with the addition of IL. The WAXS profile of the PolyIL shows three unique peaks corresponding to the key correlation lengths that characterize the morphology of the PolyILs. These lengths are related to the scattering wave vector q according to Bragg's law ($d = 2\pi/q$). The samples exhibit scattering peaks at $q_1 = 0.48\,\text{Å}^{-1}$, $q_2 = 0.82\,\text{Å}^{-1}$ and $q_3 = 1.33\,\text{Å}^{-1}$ ($d_1 = 13.09\,\text{Å}$, $d_2 = 7.66\,\text{Å}$ and $d_3 = 4.72\,\text{Å}$), see Figure 4.3. The higher angle peak q_1 corresponds to the main chain correlation length (backbone-to-backbone), whereas q_2 corresponds to the anion-anion correlations and q_3 to the spatial distance between ionic aggregates.[105,106] The intensity of q_1 and q_2 decreases with the addition of IL proving weaker ionic interactions.

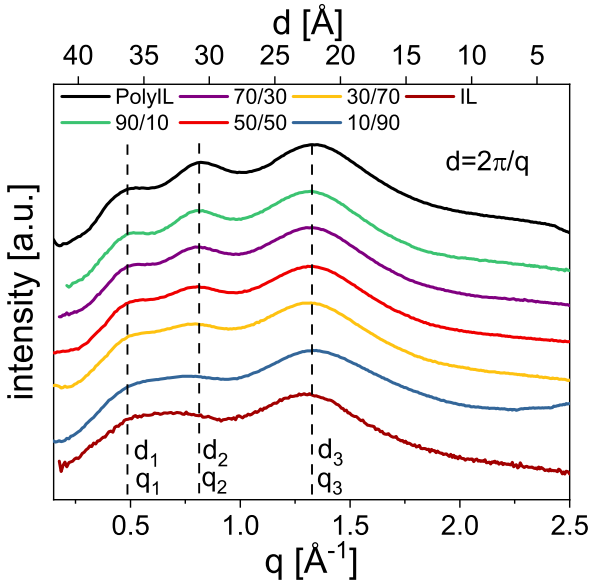

Figure 4.3: Wide angle X-ray scattering (WAXS) data of the neat PolyIL, blends and neat IL. The different peaks are indicated by the dotted lines where q_1 corresponds to the chain correlation length (backbone-to-backbone), q_2 to the anion-anion correlations and q_3 to the spatial distance between ionic aggregates.

4.1.2 Rheological Measurements

Small amplitude oscillatory shear measurements were performed to determine the influence of the amount of IL on the mechanical properties. Figure 4.4 presents the master curves of the shear storage $G'(\omega)$ and loss modulus $G''(\omega)$ of five selected samples obtained by the TTS principle at a reference temperature of $T_{\mathrm{ref}} = 0\,^{\circ}\mathrm{C}$. The graph also includes the corresponding shift factors a_{T} in the inset, while the master curves of the remaining samples are displayed in the appendix, see Figure A.2.4, p. 135. The TTS was found to work well for all samples as confirmed by the a_{T} shift factors. In the terminal regime, $G'' \propto \omega$ was observed, while $G' \propto \omega^{1.3-1.5}$. Each sample exhibited a crossover at high frequencies corresponding to the segmental relaxation (α- relaxation) at T_{g}. Furthermore, the samples displayed neither a crossover of the moduli at low frequencies nor a rubber plateau, which led to the assumption that no effective polymer chain entanglements are present for $M_{\mathrm{n}} = 57\,000\,\mathrm{g\,mol^{-1}}$. As the wt% of IL increased, G' is observed to decrease by 10^5 from 10 wt% IL to 90 wt% IL at 25 °C and $1\,\mathrm{rad\,s^{-1}}$, resulting in flowing samples with a G' of ca. 10 Pa for 90 wt% IL. This drastic decrease is caused by the IL acting as a plasticizer in the PolyIL.

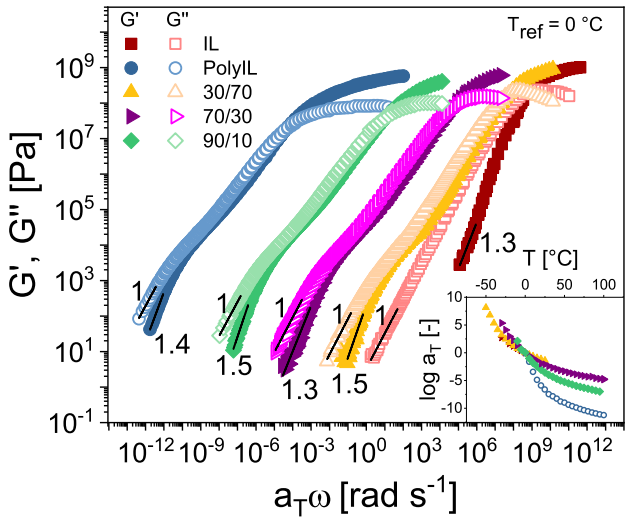

Figure 4.4: Rheological master curves of three different blends at a reference temperature of $T_{\mathrm{ref}} = 0\,^{\circ}\mathrm{C}$.

4.1.3 Dielectric Properties

The dielectric raw data for the IL and PolyIL as a function of the angular frequency at three different temperatures is displayed in Figure 4.5, where ϵ^* and the complex conductivity (σ^*) are related as follows:

$$\sigma^*(\omega, T) = i\epsilon_0\omega\epsilon^*(\omega, T) \tag{4.5}$$

with ϵ_0 being the vacuum permittivity and ω the angular frequency.

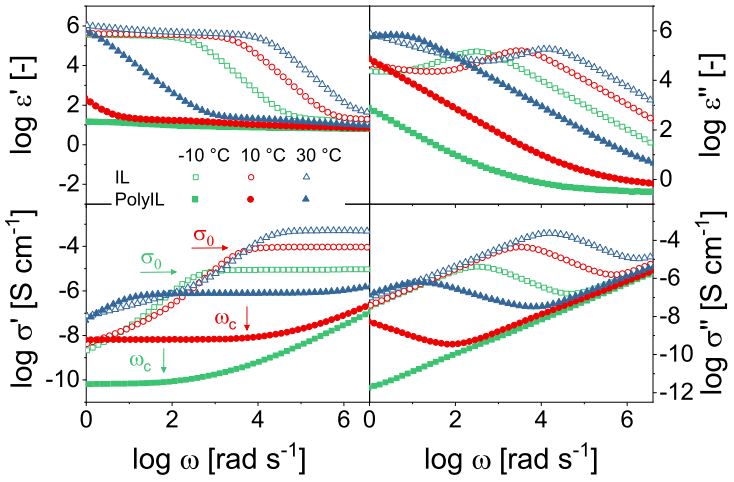

Figure 4.5: Dielectric raw data of the the PolyIL (closed symbols) and IL (open symbols). The graph displays the real and imaginary part of the dielectric permittivity (ϵ' and ϵ'') and conductivity (σ' and σ'') at three different temperatures. The ionic conductivity (σ_0) and rate of charge transport (ω_c) are indicated in σ'.

The decrease in the low-frequency regime of the real part of the conductivity (σ') is assigned to electrode polarization, where ions accumulate at the electrodes leading to the blocking of the electrodes.[107,108] Furthermore, σ_0 and ω_c, which are the two components of charge transport, are obtained from σ_0 as the independent frequency-plateau value and frequency at which σ_0 turns into a power law, respectively.[106] As the onset of the power law in σ' and therefore ω_c is hard to determine, the frequency of the maximum of the imaginary part of the electric modulus M'', which is known to be almost the same as ω_c (see Figure 4.6), is used.[55,109] The electric modulus M^* is related to ϵ^* and σ^* as follows:

$$M^*(\omega, T) = \frac{1}{\epsilon^*(\omega, T)} = \frac{i\epsilon_0\omega}{\sigma^*(\omega, T)}. \tag{4.6}$$

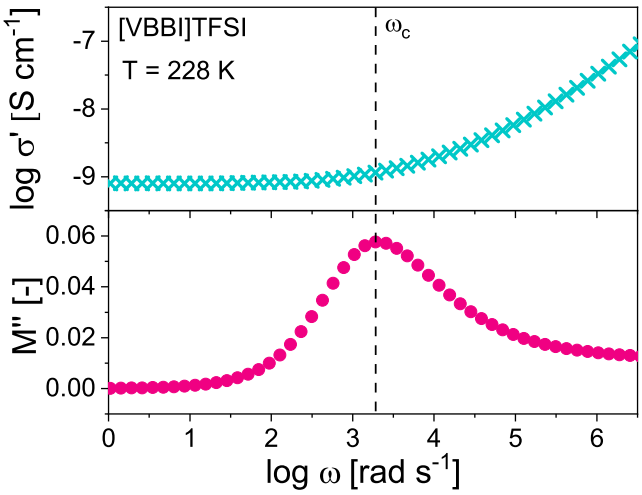

Figure 4.6: Determination of the rate of charge transport (ω_c) from the real part of the conductivity (σ') and the imaginary part of the electric loss modulus (M'').

Figure 4.5 shows that the ionic conductivity of the IL at 10 °C is about 4 decades higher than that of the corresponding PolyIL, which is due to the increased T_g and reduced mobility of the polymeric form. Additionally, only the anions participate in the charge transport in the PolyIL, resulting in a lower number of moving ions.[103] As a consequence, the addition of IL to the PolyIL should result in increased ionic conductivities due to (I) an enhanced mobility of the polymer and monomer and (II) a higher number of available charges because of the more mobile cations in the IL. This assumption is confirmed in Figure 4.7a, where the ionic conductivity increases with the amount of IL. Moreover, Figure 4.7 shows that an increase in temperature further increases the mobility of the ions and thus σ_0. The mobility of the ions is coupled to the segmental motion of the polymers as shown by the VFT behavior observed in $\sigma_0(1000/T)$ for $T > T_g$[110]

$$\sigma_0(T) = \sigma_\infty e^{\left(-\frac{B}{T-T_0}\right)} \tag{4.7}$$

where σ_∞ is the conductivity at an infinitely high temperature, B is a fitting parameter related to the activation energy and T_0 the Vogel temperature ($T_0 \approx T_g - 50\,\mathrm{K}$). While most of the samples display a VFT behavior over the entire temperature range studied, an

Arrhenius behavior is observed for the PolyIL and 90 wt% PolyIL at $T < T_g$ as[111]

$$\sigma_0(T) = \sigma_\infty^A \exp\left(-\frac{E_\mathrm{a}}{k_\mathrm{B}T}\right) \tag{4.8}$$

where σ_∞^A is the conductivity at an infinitely high temperature for the Arrhenius behavior and E_a is the activation energy. Since the polymer is frozen below T_g, it is assumed that only the mobile anions, see Figure 4.1, contribute to the charge transport in the PolyIL. In case of the blends, on the other hand, the cation of the IL also participates in the charge transport. The corresponding activation energy for the diffusion process below T_g is at 149 and 119 kJ mol^{-1} for 90 wt% PolyIL and the pure PolyIL, respectively (see Table 4.2), and is in the same order of magnitude as the values found in the literature.[102,112–114] The crossover between the VFT and Arrhenius behavior is found close to the T_g of both samples as predicted in the literature.[103,113] All the corresponding fit parameters for the samples are summarized in Table 4.2. Furthermore, the same behavior is found for ω_c as displayed in the inset in the lower left of Figure 4.7a.

Table 4.2: Fit parameters of VFT and Arrhenius fits applied to describe the temperature dependence of the ionic conductivity in Figure 4.7a.

	Volger-Fulcher-Tammann (VFT)				Arrhenius	
PolyIL/IL	σ_∞ [S cm^{-1}]	$B \times 10^{-3}$ [K]	T_0 [K]	T_g [K]	σ_∞^A [S cm^{-1}]	E_a [kJ mol^{-1}]
100/0	43.8	22.3	219	281	8.1×10^{13}	119
90/10	187.8	27.5	208	282	1.3×10^{-6}	149
70/30	239.5	30.3	196	238	–	–
50/50	282.5	31.1	190	229	–	–
30/70	82.6	26.4	189	223	–	–
20/80	97.3	27.3	186	220	–	–
10/90	91.0	26.0	187	220	–	–
0/100	70.0	24.6	187	219	–	–

Correlating σ_0 with G' as displayed on a log-log scale in Figure 4.7c, a linear dependence with a slope of -1.8 to -1.9 was observed for three temperatures (25 °C, 10 °C and 0 °C). With increasing temperature, fewer data points were available for $G'(\omega)$ at 1 rad s^{-1} because the sensitivity limit of the rheometer was reached. The inset in Figure 4.7c shows the temperature dependence of the y-axis intercept of the linear fits from Figure 4.7c with a slope of -1.8 and a linear dependence with a slope of 0.05 was observed. To the author's knowledge, the observed dependencies and scaling laws have not been investigated for other blends of PolyILs and ILs and it remains unclear whether the observed slopes apply more generally to other systems.

The charge transport mechanism can be described by the Barton–Nakajima–Namikawa relationship (BNN), σ_0 versus ω_c, which is displayed in the inset in the upper right of Figure 4.7a. Here, the BNN plot illustrates that the mechanism of charge transport is the same for all materials and blends and takes place by hopping of the charge carriers as described by the random barrier model.[115–117] Mogurampelly *et al.* observed the same

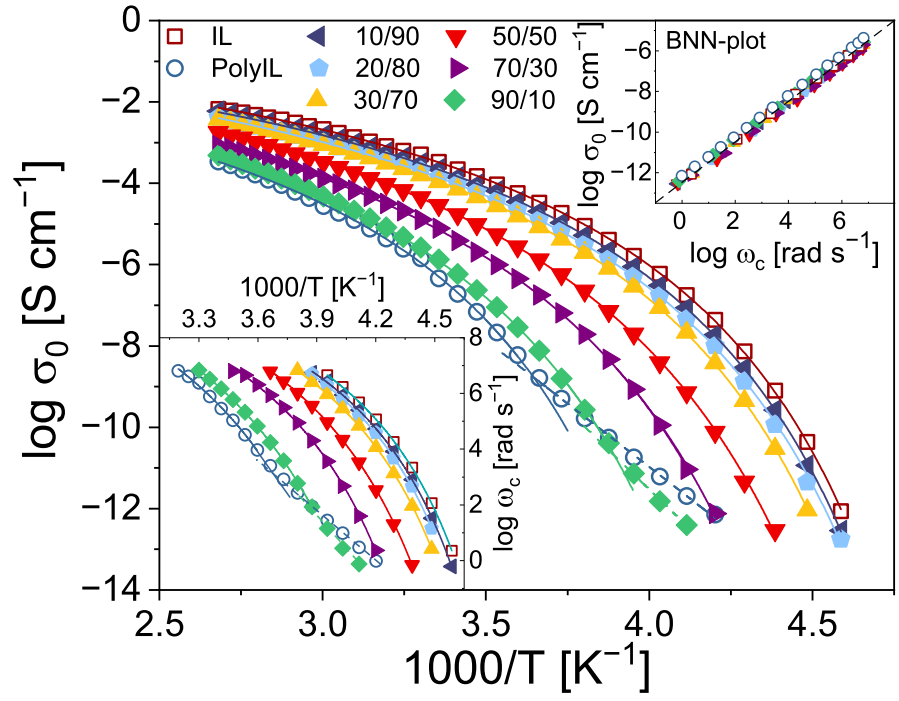

(a)

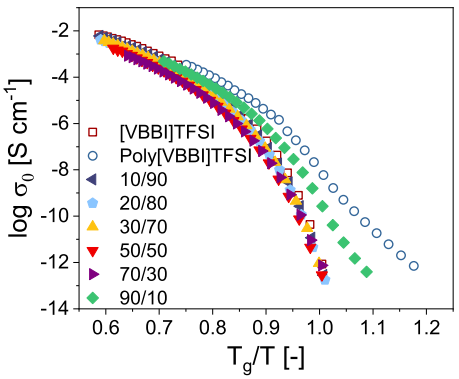

(b)

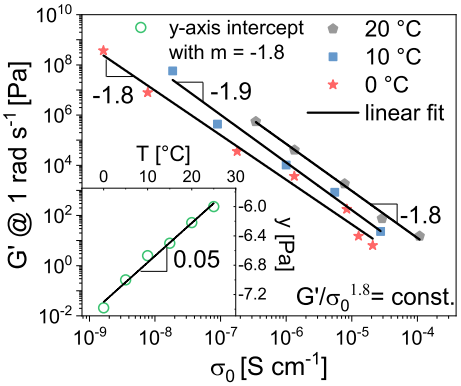

(c)

Figure 4.7: **(a)** Ionic conductivity (σ_0) as a function of inverse temperature including VFT and Arrhenius fits (solid and dashed lines, respectively). The upper right inset shows σ_0 versus the rate of charge transport (ω_c). The Barton–Nakajima–Namikawa relationship (BNN) indicates that charge transport mechanism is the same for all samples. The inset on the lower left displays the temperature dependence of ω_c, which is the same as for σ_0. **(b)** Ionic conductivity as a function of T_g/T to suppress the influence of the different T_gs of the samples. **(c)** The correlation between the storage modulus (G') at 1 rad s^{-1} and σ_0 at three temperatures is found to be linear to a good approximation. The inset in **(c)** shows the temperature dependence of the y-axis intercept of the linear fits from **(b)** using a slope of 1.8, which also shows a linear dependence on T.

mechanism using atomistic molecular dynamics simulations.[10] Their results showed that more than 90% of the hopping events take place along the polymer backbone through the formation and breaking of ion pairs. Furthermore, the inset shows that the ionic conductivity of the PolyIL is slightly higher (by a factor of 2) than that of the IL at the same rate of charge transport, suggesting small differences in the efficiency of charge transport. To evaluate these, the different mobilities and thus the influence of the different glass transition temperatures of the samples are suppressed by scaling T to T_g in Figure 4.7b. It stands out that the ionic conductivities of the 90 wt% PolyIL and the neat PolyIL are consistently higher compared to the other blends with coinciding σ_0-profiles. These two samples displayed a 6×10^2 (90 wt%) and 1.7×10^4 (pure PolyIL) times higher σ_0 at T_g suggesting more effective ion transport when scaled to T_g most likely due to the decoupling of charge transport from segmental motion.[118] A closer look at the decoupling is taken by analyzing the relaxation time of the segmental relaxation τ_α, the relaxation of charge transport τ_c and the ionic conductivity σ_0 of the PolyIL and 90 wt%, see Figure 4.8.

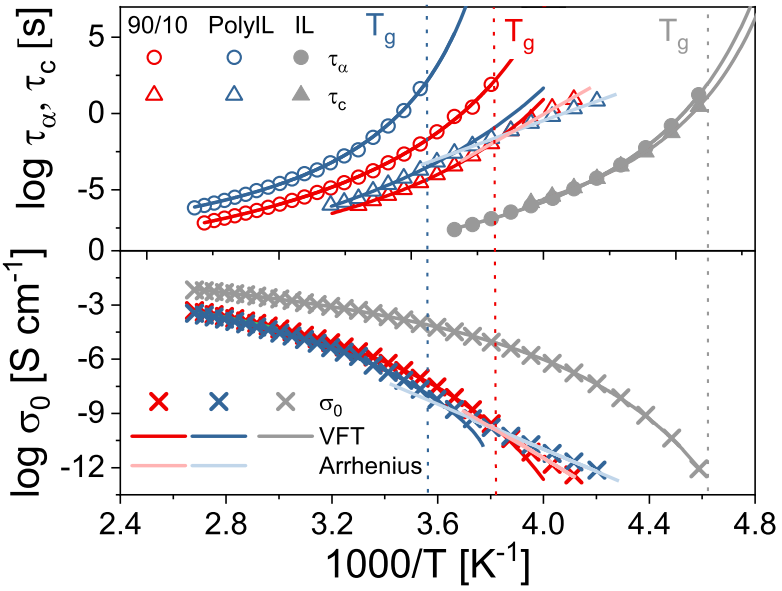

Figure 4.8: Temperature dependence of the segmental relaxation (τ_α), the relaxation of charge transport (τ_c) and the ionic conductivity (σ_0) of the IL, PolyIL and 90 wt% PolyIL. Dark solid lines represent a VFT fit, whereas light solid lines describe an Arrhenius fit to the data. The dotted lines represent the respective T_g, see Table 4.1.

While τ_α and τ_c show VFT behavior above T_g indicating the coupling of the two processes, the behavior at T_g is different: τ_α increases towards infinity and transitions to an Arrhenius behavior (light fit in Figure 4.8), as also observed for the ionic conductivity. Instead, both relaxation times overlap for the pure IL and show a drastic increase at T_g, confirming their strong coupling over the whole temperature range. The advantage of decoupling is only observed for one blend, which means that IL at 30 wt% already suppresses this phenomenon. For these samples, the coinciding curves in Figure 4.8 reflect the strong dependence of σ_0 on T_g, which is further emphasized by the functional dependence of T_g and σ_0 on IL concentration shown in Figure 4.9.

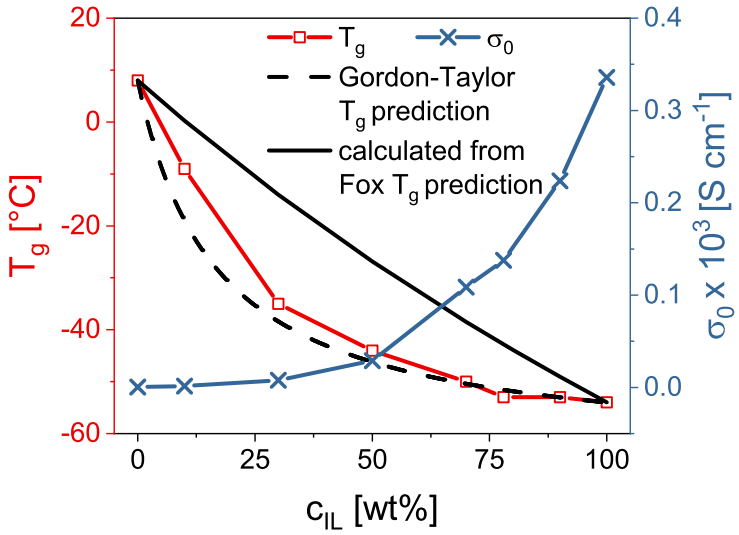

Figure 4.9: Influence of the ionic liquid concentration (c_{IL}) on the glass transition temperature (T_{g}, left y-axis, red) and ionic conductivity (σ_0) at 25 °C (right y-axis, blue). The black dashed line represents the Gordon-Taylor prediction for T_{g} with $k_{\mathrm{GT}} = 0.144$, whereas the black line indicates calculated T_{g}-values from the Fox prediction.

While σ_0 increases with the addition of IL, the T_{g} is found to decrease. Both effects result from an enhanced mobility due to the increasing amount of IL. In general, the T_{g} of a mixture of two components can be described by the Gordon-Taylor equation as follows:[119]

$$T_{\mathrm{g}} = \frac{w_1 T_{\mathrm{g},1} + k_{\mathrm{GT}} w_2 T_{\mathrm{g},2}}{w_1 + k_{\mathrm{GT}} w_2} \tag{4.9}$$

where w_1 and w_2 are the weight fractions of the two components, $T_{\mathrm{g},1}$ and $T_{\mathrm{g},2}$ the respective glass transition temperatures and k_{GT} is the Gordon-Taylor constant. The Gordon-Taylor equation is an extension of the well-known Fox equation.[120]

$$\frac{1}{T_{\mathrm{g}}} = \frac{w_1}{T_{\mathrm{g},1} + \frac{w_2}{T_{\mathrm{g},1}}} = \frac{w_1}{T_{\mathrm{g},1}} + \frac{w_2}{T_{\mathrm{g},2}} \tag{4.10}$$

For the fit, the measured T_{g} of the IL and PolyIL at −54 °C and 8 °C, respectively, were used and a unitless Gordon-Taylor constant of $k_{\mathrm{GT}} = 0.144$ was obtained. Similar values for k_{GT} were found in the literature.[121,122] Comparing the dependence of T_{g} on the concentration of ionic liquid (c_{IL}) with that of the ionic conductivities, the highest conductivity of $3.4 \times 10^{-4}\,\mathrm{S\,cm^{-1}}$ is obtained for the pure IL with the lowest T_{g}. Consequently, it reflects the importance of T_{g} in the design of highly conductive materials as it limits σ_0. However, σ_0 is not only influenced by the (de)coupling of the chain dynamics from the charge transport but also by the polarity of the medium, which provides insight into the accumulation of ions.[123,124] The polarity of a material is described by the static dielectric constant (ϵ_{s}) as the low-frequency plateau before the electrode polarization appears in $\epsilon'(\omega)$.[101,124] Figure 4.10 displays $\epsilon'(\omega)$ at 25 °C for all samples, where the value of ϵ_{s} is found as a plateau before electrode polarization and is indicated as a solid line.

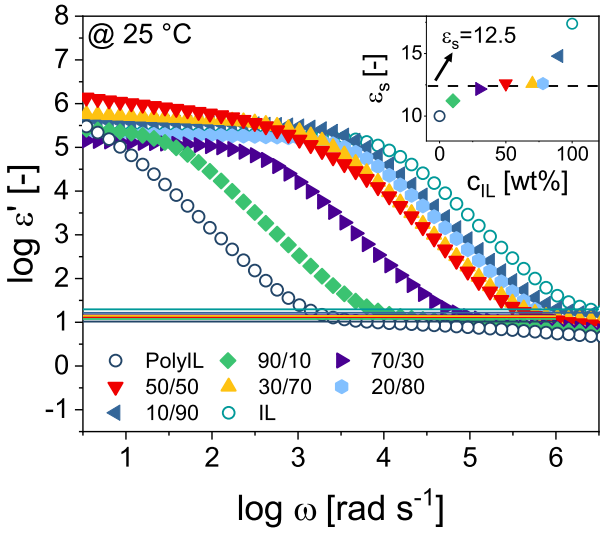

Figure 4.10: Real part of the permittivity (ϵ') and determination of the static dielectric constant (ϵ_s), plotted as solid line at the frequency plateau before electrode polarization sets in, at 25 °C. The inset in the upper right displays ϵ_s as a function of the IL concentration (c_{IL}) where a plateau is observed at ϵ_s= 12.5.

At room temperature, $\epsilon_s = 10$ was observed for the PolyIL and $\epsilon_s = 17$ for the IL, which is in the commonly observed range.[125] The addition of IL to the PolyIL led to an increase in ϵ_s until a plateau was observed at 70 wt% IL with $\epsilon_s = 12.5$, which is indicated by the dotted line in the inset in Figure 4.10. The inset shows the dependence of ϵ_s on c_{IL}. Since the behavior of ϵ_s is not linear, it reflects contributions from 'other effects' (e.g., interactions of PolyIL and IL) beyond just the respective polarities of the samples. For low polarity samples, ($\epsilon_s < 9$) clusters of aggregates and associated ions were observed by molecular simulation, leading to correlated ion motion.[124,126] These effects were shown to decrease with increasing polarity of the samples. Furthermore, polymerization can restrict ion motion and stronger anion and cation interactions are also observed for polymerized samples compared to the IL.[10] Thus, these results suggest that even the addition of a small amount of IL leads to weaker ionic interactions, resulting in increased ion mobility and less correlated ion motion.

4.1.4 Diffusion Measurements

To further characterize the motion of the ions, ^{1}H- and ^{19}F-PFG-NMR were measured on three different samples (IL, 30 wt% and 70 wt% PolyIL) at different temperatures and the translational diffusion coefficients of the anions and cations were obtained. Temperature ranges were adjusted for each sample as severe peak broadening was observed. The peak broadening occurs because of restricted molecular mobility near and below T_g and is reflected in the decreased transverse relaxation time (T_2). Diffusion coefficients of samples with higher contents of PolyIL and the pure PolyIL could not be measured in the investigated temperature range.

The diffusion coefficients of the cation were slightly higher than the ones of the anion (e.g., 1.8 vs. $2.2 \times 10^{-12}\,m^2\,s^{-1}$ for 70/30 at 40 °C) as presented in the inset in Figure

4.11a. Moreover, the mean diffusion coefficients ($D_{\mathrm{mean}} = (D_{\mathrm{anion}} + D_{\mathrm{cation}})/2$) of the samples are displayed and decrease with an increasing amount of PolyIL and therefore decreasing translational mobility, impeding ion transport. To compare D_{mean} with the ionic conductivities observed by BDS, the diffusion coefficient of the conduction process (D_σ) was calculated according to the Nernst-Einstein equation (Equation 4.3). Figure 4.11a displays the different diffusion coefficients over a wide temperature range of over 100 °C.

The temperature dependence of D_σ follows a VFT form, whereas a clear VFT dependence is not observed for the NMR detected D_{mean} because the temperature range was limited for experimental reasons. At the same temperature, D_{mean} is greater than D_σ, which has already been observed for other ILs and their composites.[101,103,104] For ILs, this difference is considered to result from ion pairs and aggregates, which do not contribute to the process of charge transport and can be quantitatively described by the Haven ratio, see Equation 4.4, p. 35. A Haven ration of 1 implies that all ions take part in the charge transport, whereas $H_{\mathrm{R}} > 1$ indicates the formation of ion pairs or aggregates.[101] Here, a H_{R} of approx. 1.4 (IL) and 1.45 (blends) was found, indicating that the formation of ion pairs in all three samples is almost temperature independent, see Figure 4.11b. While the H_{R} for ILs was previously observed to be in a similar range, the H_{R} of the blends is almost the same, despite the at least four times higher H_{R} of PolyILs.[101,103,104] The high H_{R} in PolyILs is assumed to result from strong ion-ion correlation that hinders ions to take part in the charge transport.[102,103] Thus, these results indicate that the interactions are reduced by the addition of the mobile IL, leading to an enhanced number of ions taking part in the charge transport. This finding might be related to the association of anions to a larger number of polycation chains (e.g., two to four) with the addition of IL resulting in an enhanced number of mobile ions.[10] The deviation at elevated temperatures (around 57 °C) is considered to result from charge transport's domination by thermal energy ($k_{\mathrm{B}}T$) at higher temperatures, therefore indicating less ion-ion correlation.[103] Moreover, as the H_{R} is found to be similar for both measured blends, it is suspected that the ion-ion correlation in the samples is independent of the amount of IL for 30 wt% and 70 wt% PolyIL, respectively. This assumption is also corroborated by the plateau of ϵ_{s} from 70 wt% to 30 wt% PolyIL. Additionally, these findings coincide with molecular simulations performed by Mogurampelly *et al.*, who obtained values in the same range and concluded that the dynamical ion correlations of an IL are not influenced by a PolyIL.[9] Consequently, an increased σ_0 for the blends of PolyIL and IL might be caused by the presence of more mobile anions with an increased mobility as a result of decreased ion-ion interactions compared to the pure PolyIL. Thus, blending ILs with their corresponding PolyIL is a method to obtain homogeneous, highly conductive polymeric electrolytes.

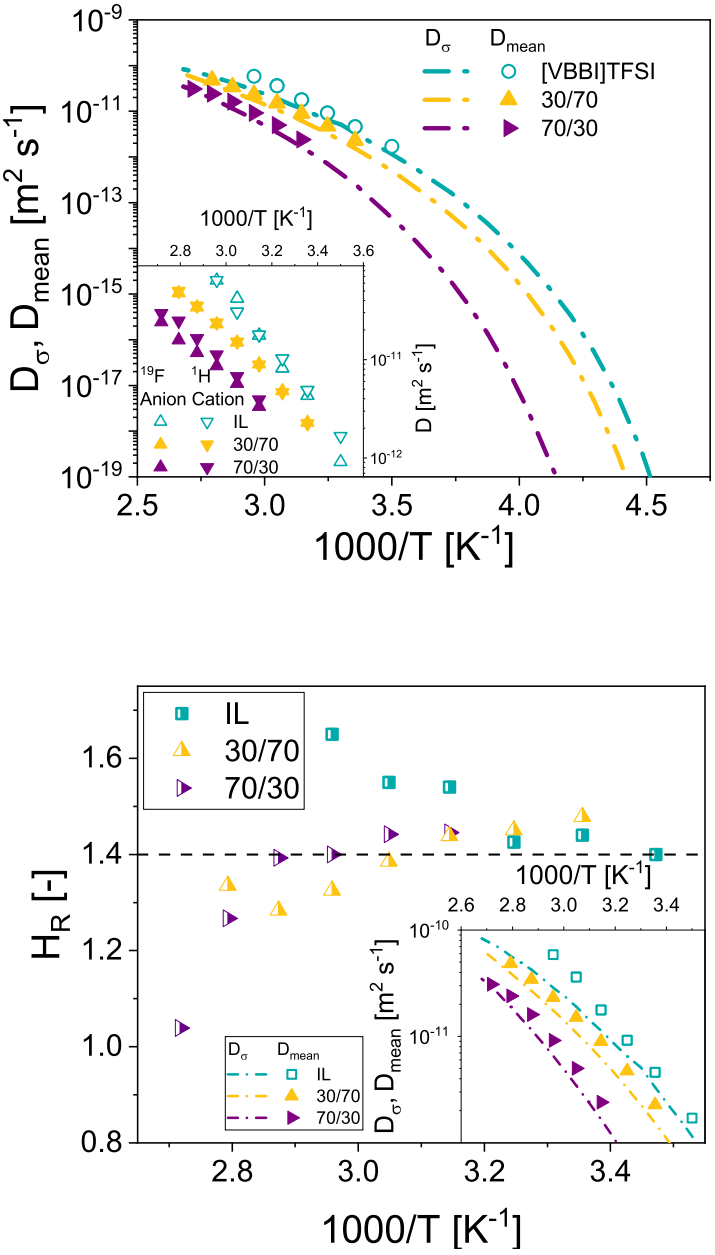

Figure 4.11: **(a)** Temperature dependence of the mean diffusion coefficients (D_{mean}) of the IL, 30 wt% PolyIL (30/70) and 70 wt% PolyIL (70/30) measured by PFG-NMR. The dashed lines represent the diffusion coefficient calculated from BDS (D_σ) according to Equation 4.4. The inset in **(a)** displays the diffusion coefficients of the polycation and anion measured by ^{1}H and ^{19}F-PFG-NMR, respectively. **(b)** Haven ratio (H_{R}) as a function of the temperature for [VBBI]TFSI, 30 wt% PolyIL (30/70) and 70 wt% PolyIL (70/30). The inset in **(b)** furthermore depicts D_{mean} over D_σ.

4.1.5 Summary

In this Section, the influence of different blending ratios of poly[VBBI]TFSI as PolyIL and the corresponding monomer [VBBI]TFSI on their ionic conductivity, diffusion and glass transition temperatures was investigated. The IL and PolyIL were synthesized and characterized by SEC and NMR. Blends with varying ratios of PolyIL to IL were prepared and further investigated via DSC, combined rheo-dielectric and PFG-NMR. The glass transition temperatures of the blends were found to obey the Gordon-Taylor equation (Equation 4.9, p. 44, $k = 0.144$) being in between the ones of the pure materials. To understand the influence of the increasing amount of IL on the mechanical properties, rheological measurements were performed. The storage modulus at a certain frequency was found to increase with an increasing amount of PolyIL and with a factor 10^4 for the highest (90 wt%) and lowest (10 wt%) amounts of IL at room temperature. Furthermore, BDS measurements revealed that the ionic conductivity of the PolyIL increased by a factor of 10^4 compared to its monomer at room temperature. Consequently, the ionic conductivities of the blends were also observed to increase, with increasing IL content due to accelerated dynamics and higher content of mobile anions. The temperature dependence of σ_0 followed a VFT behavior, which transitions into an Arrhenius behavior for 90 wt% PolyIL and the PolyIL at the respective T_g ($E_{a,90\,wt\%} = 149\,kJ\,mol^{-1}$ and $E_{a,PolyIL} = 119\,kJ\,mol^{-1}$). This decoupling of charge transport from segmental motion is only observed for the blend of 90 wt%, as already 30 wt% of IL led to its suppression. Furthermore, the static dielectric constant was determined to be 10 and 17 for the PolyIL and IL, respectively, and the blends showed a plateau at 12.5 from 70 wt% to 30 wt% PolyIL. The diffusion coefficients of the cation and anion for the IL, 30 wt% PolyIL and 70 wt% PolyIL were measured by ^{1}H- and ^{19}F-PFG NMR, respectively, and a slightly higher diffusion coefficient of the cations than of the anions (e.g., 1.8 vs. $2.2 \times 10^{-12}\,m^2\,s^{-1}$ for 70/30 at 40 °C) was observed. When the mean diffusion coefficients from PFG-NMR were compared to the calculated diffusion coefficients from BDS, the Haven ratio, see Equation 4.4, p. 35, was obtained and quantified. The H_R was found to be around 1.4 for the IL and 1.45 for 30 wt% and 70 wt% PolyIL at room temperature and only a slight decrease for the blends up to 1.25 was observed when the temperature increased. The value of H_R of 1.4 for the IL was expected to increase with the addition of PolyIL, as $H_R > 5$ was observed for PolyILs by Gainaru *et al.*[103] These results show that the blending of the components does not have a strong impact on the charge transport mechanism itself compared to the pure IL. Furthermore, it is highlighted that the increase in the ionic conductivity compared to the pure PolyIL might be attributed to the addition of a more mobile phase but also to its ability to reduce the ion-ion correlations in the PolyIL. However, the increase in ionic conductivity is achieved to the detriment of the mechanical properties, leading to flowing samples with $G'' > G'$, which are not mechanically strong enough to be applied in actual LIBs. Therefore, the next step should cope with the enhancement of the mechanical stability while preserving the high conductivity of the samples with a low wt% of PolyIL.

4.2 Crosslinking of Polymerized Ionic Liquids

One method to enhance the mechanical and dimensional stability of the matrix is chemical crosslinking of the polymer which is then doped with an IL (and a lithium salt for application as SPE). These so-called 'ternary ionogels' ((I)IL, (II) polymer and (III) lithium salt) possess a highly tunable composition with respect to the targeted material properties such as mechanical stability, ionic conductivity and electrochemical stability.[82,127] As chemical crosslinker, often commercially available bifunctional crosslinkers such as poly(ethylene glycol)diacrylate (PEGDA) are employed. The following paragraph gives an overview of the literature in the context of ionogels (IGs) focusing on the use of different ILs and matrices and their impact on σ_0.

4.2.1 Ionogels

The influence of the IL on the ionic conductivity of IGs was highlighted by Visentin *et al.*[128] They investigated PEGDA-based IGs in combination with three different ILs: (I) (1 ethyl-3-methylimidazolium tris(pentafluoroethyl)trifluorophosphate ([EMI]FAP), (II) 1-ethyl-3-methylimidazolium bis(trifluoromethane sulfonyl)imide ([EMI]TFSI) and (III) 1-ethyl-3-methylimidazolium tetra-cyanoborate ([EMI]TCB). They found the ionic conductivity after the gelation point ($G'(\omega,t) = G''(\omega,t)$) to be highly dependent on the incorporated IL, with the highest obtained value of $13\,\mathrm{mS\,cm^{-1}}$ for [EMI]TCB at room temperature for 7.2 wt% PEGDA. Furthermore, D'Angelo *et al.* investigated the impact of the polymer matrix and prepared PEGDA- and poly(methyl methacrylate)-based IGs.[129] They found an enhanced Li^+-ion diffusion for the PEGDA based gels due to the ethylene oxide chains serving as ion conductive pathways. More recently, PolyILs have also been used as matrices and the chemical analogy and ionic interactions between ILs and PolyILs, furthermore, prevent microscopic phase separation, ensure better miscibility and avoid leakage of the liquid phase.[6,130] Among these, poly(diallyldimethylammonium) bis(trifluoromethane sulfonyl)imide ([PDADMA]TFSI) is one of the most used PolyILs in IGs, because the corresponding chloride polyelectrolyte is commercially available. Brinkkötter *et al.* focused on the synthesis and characterization of these matrices and the improvement of mechanical stability and ionic conductivity.[131,132] They evaluated the influence of different anions specifically $TFSI^-$, bis(fluoro sulfonyl)imide (FSI^-), trifluoromethane sulfonate (TfO^-), 2,2,2-trifluoromethane sulfonyl-N-cyanoamide (TFSAM) and dicyanamide (DCA^-), where $TFSI^-$ and $TFSAM^-$ were found to be the most promising candidates for the use in lithium-metal batteries, with ionic conductivities of $0.48\,\mathrm{mS\,cm^{-1}}$ and $0.82\,\mathrm{mS\,cm^{-1}}$ at 20 °C, respectively.[131] Furthermore, the different parameters of the PolyIL with $TFSA^-$ anions such as the position of the ionic group, length of the spacer and rigidity were varied, increasing the ionic conductivities at 20 °C from $0.29\,\mathrm{mS\,cm^{-1}}$ to $0.49\,\mathrm{mS\,cm^{-1}}$.[132] They highlighted the importance of the specific chemical design of polymers depending on the chosen application and stated that optimized ion transport is obtained by the use of a rigid backbone without any spacer with respect to the side arm. Moreover, other PolyILs, e.g., poly[VBBI]TFSI were investigated because poly[VBBI]TFSI possesses an increased

thermal stability caused by the incorporated aromatic group and the $TFSI^-$ ion.[133] Sen *et al.* presented the polymerization of [VBBI]TFSI and incorporation of different ILs.[133] Furthermore, they explored the difference between poly[VBBI]TFSI as charged matrix and a chemically similar but neutral polymer matrix and found up to six times higher ionic conductivities for the PolyIL/IL samples. In a recent publication, Zhang *et al.* presented a BCP consisting of PEGDA and a PolyIL (poly(1-vinyl-3-butylimidazolium bis(trifluoromethylsulfonyl)imide), poly[VBIm]TFSI) as matrix and reported an improved σ_0 of the polymer matrix with LiTFSI of $0.14\,\mathrm{mS\,cm^{-1}}$ at $30\,^{\circ}\mathrm{C}$.[134]
Despite the high number of publications in this area, no study on the direct comparison of PEGDA- and PolyIL-based matrices has been conducted to the best of the author's knowledge. Furthermore, the performance of these ionogels as SPEs in lithium metal batteries is often solely predicted using the ionic conductivity of the whole sample. However, for samples containing a mix of ions participating in the charge transport, the ionic conductivity alone does not allow a direct conclusions to be drawn about the Li^+-ion conductivity, which is the only effective ion movement for the actual battery application.[135] Thus, it is necessary to gain more information about the actual Li^+-ion conductivity, e.g., by measurements of the Li^+-ion transference number (t_{Li^+}) via symmetric lithium cells or Li^+-ion diffusion via PFG-NMR.[136–138] However, those measurements are rarely conducted for PolyIL/IL samples, complicating the comparison of IGs. To the best of the author's knowledge, only Brinkkötter *et al.* reported t_{Li^+} of their SPEs to be in the range of 0.021 to 0.04.[131,132]
Therefore, the following Sections present a comprehensive study on the investigation of PEGDA- and PolyIL-based IGs to evaluate the difference between charged and non-charged matrices with a special focus on the Li^+-ion conductivity. For this, IGs with different ratios of PEGDA, [VBBI]TFSI as ionic liquid monomer (IL-M), 1-(p-vinylbenzyl)-3-vinyl imidazolium bis(trifluoromethane sulfonyl)imide ([VBVI]TFSI) as ionic liquid crosslinker (IL-CL), 1-butyl-3-methylimidazolium bis-(trifluoromethane sulfonyl)imide ([BMIM]TFSI) as IL and LiTFSI as lithium conducting salt were prepared by radical photopolymerization, see Figure 4.12. Self-standing films (see Figure 4.12) were obtained with different amounts of IL and LiTFSI and were characterized by infrared (IR) spectroscopy and thermal gravimetric analysis (TGA). Furthermore, the mechanical stability and ionic conductivity was measured by rheo-dielectric and the impact of different amounts of polymer, IL and LiTFSI, as well as the influence of charged (PolyIL-based) and non-charged (PEGDA-based) matrices, was thoroughly evaluated. Due to the potential application, the t_{Li^+} of all derived IGs was determined and the different as-obtained parameters were discussed in great detail. Consequently, the compatibility of the polymer electrolytes and lithium metal was evaluated by long-term lithium plating/stripping experiments.

4.2.2 Synthesis and Thermal Characterization

Ionogels with varying amounts of PEGDA or IL-CL, IL-M, ionic liquid electrolyte (IL-E) and LiTFSI were prepared by photopolymerization according to Section A.1.2, see Figure 4.12.

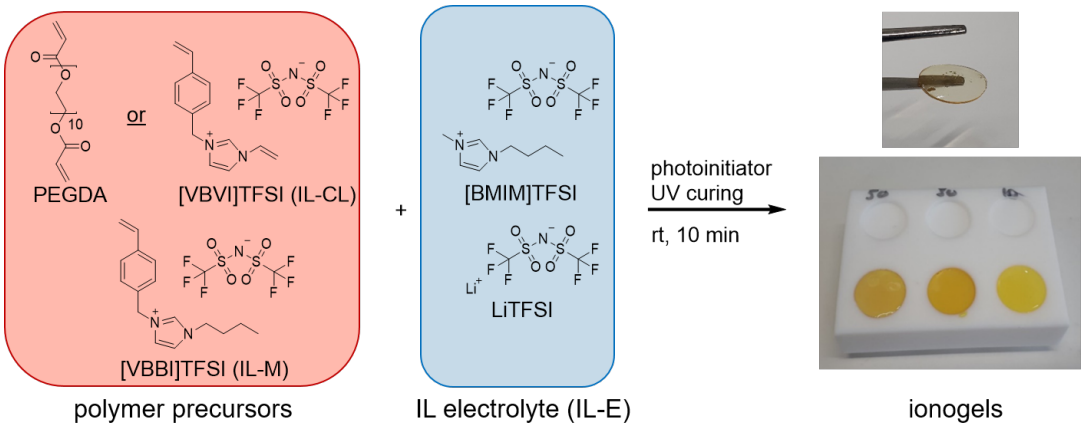

Figure 4.12: Synthesis of the IGs composed of PEGDA as a noncharged crosslinker or 1-(p-vinylbenzyl)-3-vinyl imidazolium bis(trifluoromethane sulfonyl)imide ([VBVI]TFSI) as the IL-CL, [VBBI]TFSI as the IL and [BMIM]TFSI with LiTFSI as the IL-E. Adapted with permission from[81]. Copyright 2022 American Chemical Society.

It has to be noted that the structures of the IL-M and IL-CL are almost identical except that the IL-CL possesses two polymerizable double bonds (one more than the IL-M, see Figure 4.12) thus introducing the possibility to form crosslinks. An overview of the sample composition is displayed in Figure 4.13.

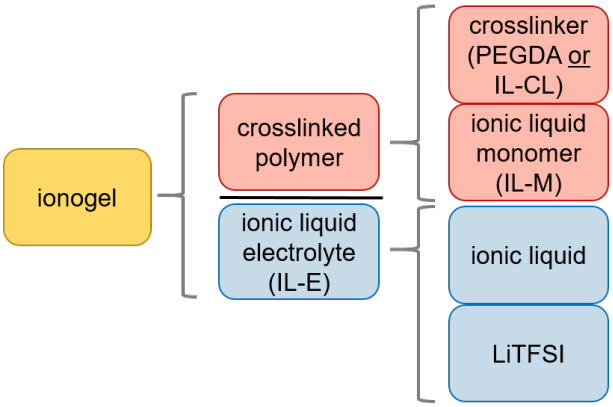

Figure 4.13: Overview of the different components of the ionogels. Adapted with permission from[81]. Copyright 2022 American Chemical Society.

The ratio of polymer (IL-CL or PEGDA and IL-M) to IL-E was 10/90, 30/70 or 50/50. Further, the amount of PEGDA inside the polymer fraction was 30 mol %, 50 mol % or 100 mol % in PEGDA-based films while the amount of IL-CL was 50 mol %, 70 mol % or 100 mol % in IL-CL-based films. Samples with 100 mol % crosslinker (PEGDA or IL-CL) did not contain any IL-M. Moreover, the amount of LiTFSI inside the IL-E was 0 mol %, 20 mol % or 40 mol %. Table 4.3 displays an overview of all synthesized samples and their compositions.

Table 4.3: Synthesized ionogels with different compositions of PEGDA, IL-CL, IL-M, IL-E and LiTFSI.[a]

Abbreviation	Crosslinker	Polymer/IL-E [wt%/wt%]	IL-CL or PEGDA within polymer [mol%]	LiTFSI within IL-E [mol%]
10/90-P30-0	PEGDA	10/90	30	0
10/90-P50-0	PEGDA	10/90	50	0
10/90-P100-0	PEGDA	10/90	100	0
30/70-P30-0	PEGDA	30/70	30	0
30/70-P50-0	PEGDA	30/70	50	0
30/70-P100-0	PEGDA	30/70	100	0
50/50-P30-0	PEGDA	50/50	30	0
50/50-P30-0	PEGDA	50/50	50	0
50/50-P30-0	PEGDA	50/50	100	0
30/70-P30-20	PEGDA	30/70	500	20
30/70-P30-20	PEGDA	30/70	100	20
30/70-P30-40	PEGDA	30/70	50	40
30/70-P30-40	PEGDA	30/70	100	40
30/70-V50-0	[VBVI]TFSI	30/70	30	0
30/70-V70-0	[VBVI]TFSI	30/70	50	0
30/70-V100-0	[VBVI]TFSI	30/70	100	0
30/70-V50-20	[VBVI]TFSI	50/50	30	20
30/70-V70-20	[VBVI]TFSI	50/50	50	20
30/70-V100-20	[VBVI]TFSI	50/50	100	20
30/70-V50-40	[VBVI]TFSI	30/70	500	40
30/70-V70-40	[VBVI]TFSI	30/70	100	40
30/70-V100-40	[VBVI]TFSI	30/70	50	40

[a]The abbreviations of all samples comprise (1) ratio of polymer to IL-E, (2) crosslinker (P: PEGDA, V: [VBVI]TFSI) and its amount within the polymer fraction in mol% and (3) LiTFSI concentration within IL-E.

Comparison of FT-IR spectra of the IL, IL-CL and the corresponding PEGDA- and VBVI-based IGs, as displayed in Figure 4.14, reveals the disappearance of the vibrational band at 1634 cm^{-1} and 1655 cm^{-1} for PEGDA- and VBVI-based IGs, respectively.
These vibrational bands are associated with the C=C double bond vibration[139] of the monomer so that their disappearance indicates a high degree of conversion to polymer. Furthermore, a blue shift was found for the carbonyl band of different PEGDA-based IGs, which is connected to the loss of conjugation after the polymerization,[139] see Figure 4.14b. On the contrary, the polymerization of VBVI-based samples and the addition of LiTFSI did not lead to any significant shift in the spectra compared to the single component spectra, see Figure 4.14c and 4.14d.

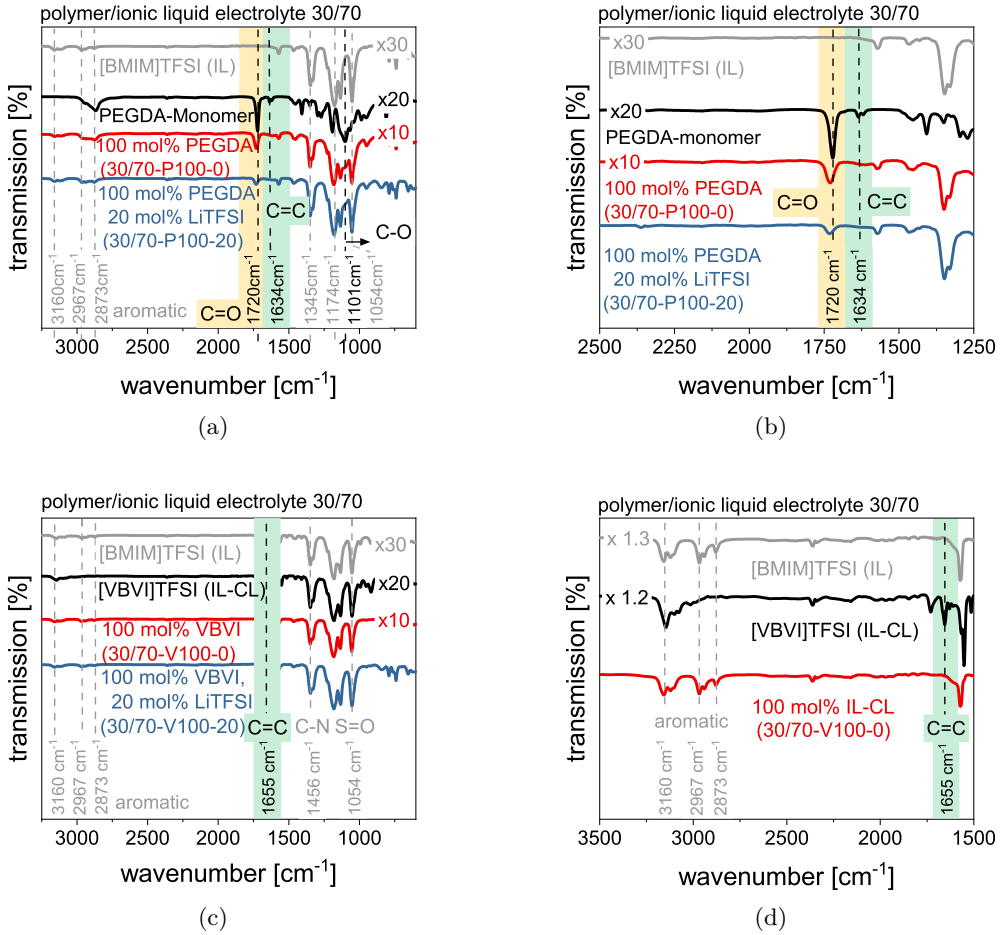

Figure 4.14: FT-IR spectra of the IL (gray) and crosslinker (black) as well as their corresponding IG with polymer/IL-E 30/70 and **(a)** 100 mol% PEGDA with 0 or 20 mol % LiTFSI at 20 °C and the enhancement in **(b)** to clearly indicate the disappearance of the band at 1634 cm^{-1} and blue shift of the C=O band upon polymerization. **(c)** 100 mol% [VBVI]TFSI with 0 or 20 mol % LiTFSI at 20 °C and the enhancement in **(d)** to clearly indicate the disappearance of the band at 1655 cm^{-1}. Adapted with permission from[81]. Copyright 2022 American Chemical Society.

TGA measurements of comparable PEGDA- and VBVI-based IGs revealed a 31 °C higher thermal stability of samples based on the IL-CL at a weight loss of 50 % ($T_{50\%}$) as displayed in Figure 4.15. The lower thermal stability of PEGDA-based IGs is most likely caused by the more sensitive carbon-oxygen bonds which are not present in the IL-CL. The thermograms display two distinct degradation temperatures, most likely corresponding to the degradation of the matrix (first process) and IL (second process), respectively. The influence of the addition of LiTFSI is displayed in Figure 4.15a and 4.15b. The degradation temperature at a weight loss of 50 % for PEGDA-based IGs increased by about 15 °C with the addition of LiTFSI. In contrast to that, $T_{50\%}$ was found to be decreased by maximum 4 °C with the addition of LiTFSI for VBVI-based IGs. Nonetheless, all VBVI-based IGs generally possessed higher degradation temperatures than the PEGDA-based IGs, thus showing a thermally more stable structure.

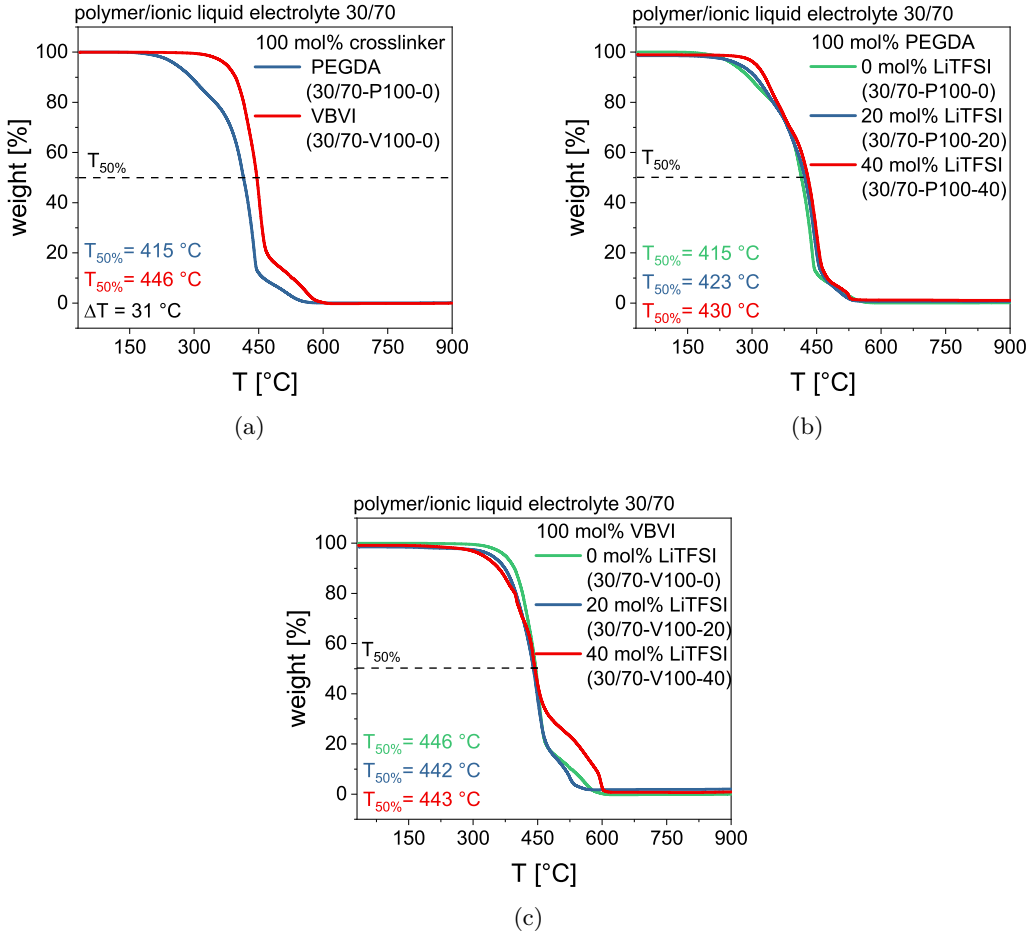

Figure 4.15: TGA thermogram of samples with 30/70 polymer/IL-E and 0 mol%, 20 mol% and 40 mol% LiTFSI based on **(a)** a PEGDA matrix and **(b)** a VBVI matrix. In **(c)** the higher thermal stability of VBVI-based IGs is emphasized as they featured a 31 °C higher degradation temperature (at a weight loss of 50 % ($T_{50\%}$)). Adapted with permission from[81]. Copyright 2022 American Chemical Society.

4.2.3 Coupled Rheo-Dielectric

To investigate the suitability of the synthesized IGs for application in LIBs, their rheological properties and ionic conductivities were determined by combined rheo-dielectric measurements, which simultaneously provided a comprehensive insight into the highly important frequency dependent mechanical and dielectric properties for polymer electrolytes as quantified simultaneously via $G'(\omega), G''(\omega), \epsilon'(\omega)$, $\epsilon''(\omega)$ and their related values.[5] Figure 4.16a and 4.16b display $G'(\omega)$ and $\sigma_0(1000/T)$ of the different PEGDA-based IGs.

Here, at each fixed ratio of polymer to IL-E (i.e., 10/90, 30/70 and 50/50), the PEGDA content was further changed to 30 mol %, 50 mol % and 100 mol %. This means an increasing overall amount of polymer as well as an increasing density of crosslinks within the polymer fraction is obtained by these variations. Consequently, a significant increase by a factor 2000 of the storage modulus from around 50 Pa representing the lowest polymer ratio and crosslinking density up to 1×10^5 Pa corresponding to the highest polymer ratio and

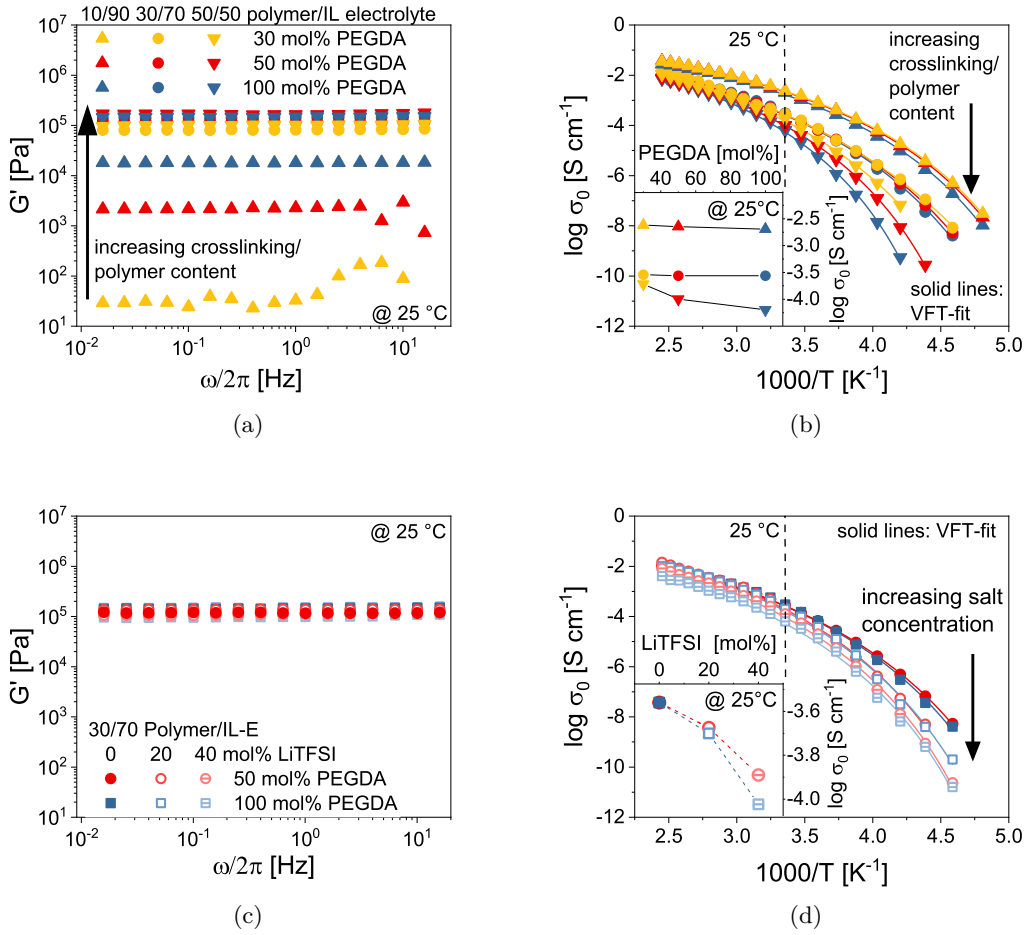

Figure 4.16: Simultaneously determined **(a)** storage moduli (G') of PEGDA-based IGs with different contents of crosslinker and polymer to IL-E ratio and **(b)** ionic conductivities (σ_0) at different temperatures. The solid lines correspond to a VFT fit; see Equation 4.7. The inset shows σ_0 as a function of the PEGDA content at 25 °C, emphasizing the decreasing ionic conductivity as the PEGDA content is increased. **(c)** Storage moduli and **(d)** ionic conductivities of PEGDA-based IGs with 30/70 polymer to IL-E ratio and 0 mol%, 20 mol% and 40 mol% LiTFSI within IL-E. The inset on the lower left emphasizes the influence of the concentration of LiTFSI in the IL-E on the ionic conductivities at 25 °C. The ionic conductivity decreases as the salt content is increased. Adapted with permission from[81]. Copyright 2022 American Chemical Society.

crosslinking density was found, as shown in Figure 4.16a. The loss moduli of all samples were ca. $9-10$x lower, resulting in $\tan\delta_{\text{Rheo}}$ of approx. 0.1. The storage moduli generally display a weak frequency dependence as a result of the approximately Hookean response. Similar values of G' of around 1×10^5 Pa were detected for a polymer/IL-E ratio of 30/70 and 50/50. Samples with lower polymer content, as in 10/90, exhibited decreased G', which dropped even further with a lower density of crosslinks. Thus, the influence of the mechanical stability provided by the polymer and chemical crosslinks was evaluated in great detail and at least 30 wt% polymer was found to be required to obtain stable gels with a G' value of around 1×10^5 Pa. This value opens up the possibility to hinder lithium dendrite growth, which is dependent on several parameters such as the mobility (diffusion), solubility of ions and the mechanical strength of the sample.[140–142]

In addition, σ_0 was determined from the frequency-independent plateau in the real part

of the conductivity. The corresponding ionic conductivities at given temperatures are displayed in Figure 4.16b. Generally, for polymer electrolytes the ionic conductivity is strongly coupled to the segmental motion of the polymer chains and therefore high ionic conductivities are obtained at high temperatures where thermal energy dominates.[143] With decreasing temperature, the polymer matrix becomes more rigid, thus also impeding ion movement through slowed-down segmental motion, resulting in a decreased ionic conductivity. As already introduced in Chapter 4.1.3, the temperature dependence of the ionic conductivity can be represented by the VFT equation.[110] The respective three fit parameters can be found in Table 4.4.

Table 4.4: Vogel-Fulcher-Tamman (VFT, see Equation 4.7, p. 40) fit parameters for the PEGDA-based IGs to describe the temperature dependence of the ionic conductivity in Figure 4.16b and 4.16d.[a]

Sample	σ_∞ [S cm^{-1}]	B [K]	T_0 [K]
10/90-P30-0	2.7	1.6	156
10/90-P50-0	2.8	1.6	156
10/90-P100-0	2.8	1.6	158
30/70-P30-0	3.4	1.7	156
30/70-P50-0	3.5	1.7	156
30/70-P100-0	3.5	1.7	156
50/50-P30-0	3.5	1.7	164
50/50-P50-0	2.9	1.6	175
50/50-P100-0	2.8	1.6	185
30/70-P50-20	3.8	1.7	166
30/70-P100-20	4.3	1.7	161
30/70-P50-40	3.9	1.7	166
30/70-P100-40	3.5	1.7	166

[a]The abbreviations of all samples comprise (1) ratio of polymer to IL-E, (2) crosslinker (P: PEGDA, V: [VBVI]TFSI) and its amount within the polymer fraction in mol% and (3) LiTFSI concentration within IL-E.

When examining the ionic conductivities of the different PEGDA-based IGs, the ionic conductivity was generally decreasing with an increasing amount of polymer and chemical crosslinks in contrast to the increasing G'. This is in line with expectations since a higher polymer content results in a lower relative amount of highly mobile IL molecules and therefore fewer charge carriers as well as a lower overall polymer segmental motion. Consequently, the highest ionic conductivity at 25 °C was obtained for 10/90 containing 30 mol % PEGDA with 2.41 mS cm^{-1} (lowest amount of crosslinker and highest amount of IL) whereas the lowest ionic conductivity was found to be 0.06 mS cm^{-1} for 50/50 and 100 mol % PEGDA (highest amount of crosslinker and lowest amount of IL). Therefore, the predicted behavior that a more rigid structure with increasing amounts of polymer and crosslinker would impede ion transport could be confirmed. For further clarity, the inset in Figure 4.16b highlights the dependence of the ionic conductivity on the amount of crosslinker: At lower overall polymer contents of polymer/IL-E of 10/90 and 30/70, the influence of a higher crosslinking density was found to be negligible, thus it seems

that the overall ionic conductivity here is strongly dominated by the IL. However, when examining a polymer/IL-E ratio of 50/50 drastic changes were observed when increasing the PEGDA amount from 30 mol % (0.19 mS cm^{-1}) up to 100 mol % (0.06 mS cm^{-1}). It can be concluded that once a certain threshold is reached, the overall ionic conductivity is then strongly dependent on the polymer, so that a higher crosslinking density and thus lower chain mobility needs to be taken into account. When comparing these findings with the mechanical stability, as seen in Figure 4.16a, it is obvious that G' and σ_0 behave inversely, such as a higher amount of crosslinker provides higher mechanical stability but lower ionic conductivity and vice versa. Thus, a well-balanced amount of polymer and crosslinker needs to be employed to reach the needed mechanical properties and maximum ionic conductivity since both are essential properties for the IGs. As a result of these considerations, the samples with a 30/70 ratio of polymer/IL-E and different amounts of crosslinker were chosen for further experiments, since they provided the best trade-off between both required properties, mechanical stability and ionic conductivity.

In a next step, the samples were doped with LiTFSI as Li^+-ions are crucial for the actual application of SPEs in lithium metal batteries and subsequently the change in mechanical stability as well as ionic conductivity was studied. As shown in Figure 4.16c, the addition of salt did not notably affect the mechanical properties of the samples and G' was still around 1×10^5 Pa. However, Figure 4.16d reveals that the addition of LiTFSI led to an overall decrease of the ionic conductivity with increasing salt concentration by a factor of 0.88 and 0.91 for 100 mol % PEGDA and 20 mol% and 40 mol % LiTFSI, respectively. In the literature, this is explained by anion aggregation around the Li^+-ions upon the addition of a Li-salt to ILs, which results in an increased viscosity of the IL and therefore an overall decreasing ionic conductivity, as also shown by molecular simulations and Raman spectroscopy.[144,145] Here, an increase in G' or the viscosity is not observed, as the mechanical behavior of the samples is dominated by the network and not the IL. The $\sigma_0(T)$-profiles again follow a VFT behavior (the three fit parameters are presented in Table 4.4). Moreover, it must be noted that the ionic conductivity of, e.g., 0.2 mS cm^{-1} at 25 °C for 100% PEGDA and 20 mol% LiTFSI is still sufficient for battery applications.

Subsequently, the storage moduli and ionic conductivities of the IGs with the charged VBVI matrix (50 mol%, 70 mol% and 100 mol % VBVI), 30/70 ratio of polymer to IL-E, and 0 mol%, 20 mol% and 40 mol% LiTFSI in the IL-E were measured and compared to the previously obtained results (Figure 4.17a and 4.17b).

Generally, both properties $G'(\omega)$ and $\sigma_0(1000/T)$ showed the same trends as in the PEGDA-based IGs such as: increasing G' with an increasing amount of crosslinker and decreasing ionic conductivity with an increasing crosslinker and LiTFSI content, thus being in line with the expectations regarding the interplay of the different parameters. The temperature dependence of the ionic conductivities could still be described by a VFT function and the fit parameters are displayed in Table 4.5.

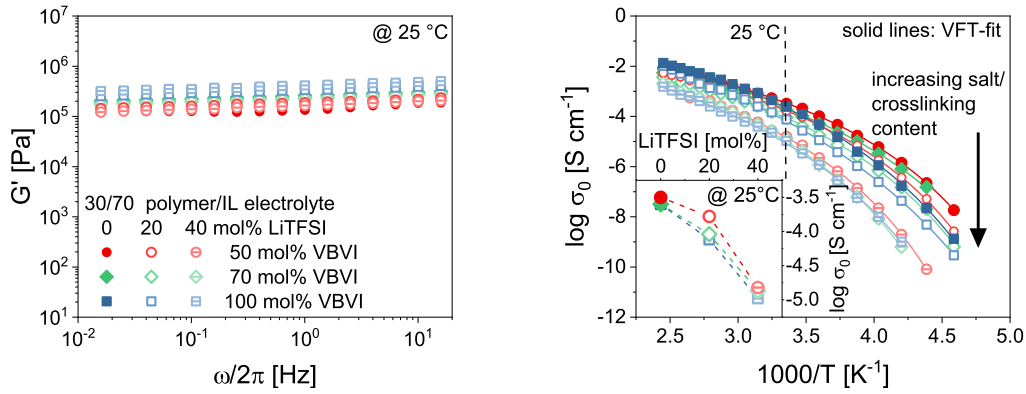

Figure 4.17: Simultaneously determined **(a)** storage moduli (G') and **(b)** ionic conductivities (σ_0) of samples with a charged matrix based on [VBVI]TFSI (IL-CL). The samples comprise a 30/70 polymer/IL-E ratio and contain different amounts of IL-CL (50 mol%, 70 mol% and 100 mol%), represented by closed symbols. Furthermore, the addition of 20 mol% and 40 mol% LiTFSI to the IL-E is presented by the lighter, open symbols. Adapted with permission from[81]. Copyright 2022 American Chemical Society.

Table 4.5: Vogel-Fulcher-Tamman (VFT) fit parameters for the VBVI-based IGs to describe the temperature dependence of the ionic conductivity in Figure 4.17.[a]

Sample	σ_∞ [S cm^{-1}]	B [K]	T_0 [K]
30/70-V50-0	2.4	1.6	158
30/70-V70-0	2.5	1.6	156
30/70-V100-0	3.9	1.7	156
30/70-V50-20	2.4	1.6	161
30/70-V70-20	2.7	1.7	158
30/70-V100-20	3.9	1.7	158
30/70-V50-40	2.9	1.7	169
30/70-V70-40	3.6	1.7	169
30/70-V100-40	4.0	1.8	164

[a]The abbreviations of all samples comprise (1) ratio of polymer to IL-E, (2) crosslinker (P: PEGDA, V: [VBVI]TFSI) and its amount within the polymer fraction in mol% and (3) LiTFSI concentration within IL-E.

However, the direct comparison of the PEGDA- and VBVI-based samples in Figure 4.18 revealed slightly higher G' values for the samples with the charged matrix.

The VBVI-based samples featured a larger, more rigid molecular structure in comparison to the flexible oligo(ethylene oxide) chain of PEGDA and thus form a stiffer network, as also further supported by the repulsive charge interactions of the monomers.[146] The samples without salt showed the same ionic conductivity values of around 0.3 mS cm^{-1} at 25 °C, which indicated that the ion transport is not strongly dependent on the polymer matrix in this case. However, upon the addition of LiTFSI, the ionic conductivity of the VBVI-based samples decreased by about one decade for the samples with 40 mol % LiTFSI and VBVI compared to the neutral PEGDA-based matrix. As a hypothesis, the larger number of ions present in the VBVI-based IGs results in a larger number of ionic

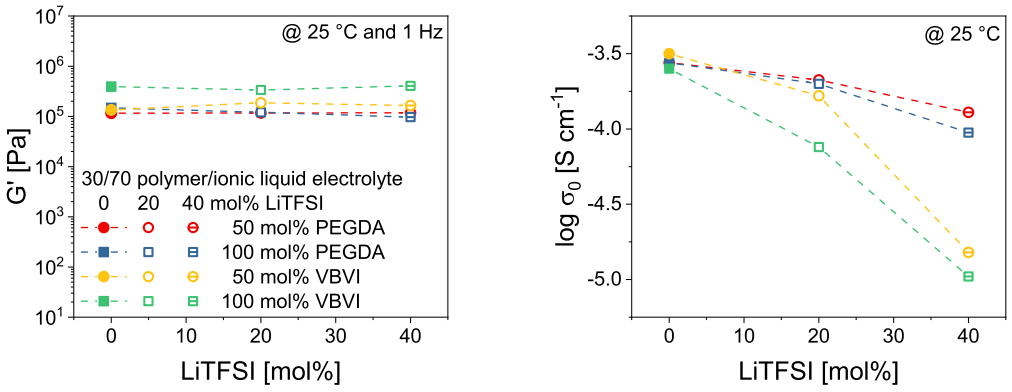

(a) (b)

Figure 4.18: Comparison of the **(a)** storage moduli (G') at $\omega/2\pi = 1\,\text{Hz}$ and **(b)** ionic conductivities (σ_0) at 25 °C of PEGDA- and VBVI-based IGs with a ratio of 30/70 polymer to IL-E and 0 mol%, 20 mol% and 40 mol% LiTFSI within the IL-E. Adapted with permission from[81]. Copyright 2022 American Chemical Society.

aggregates and interactions so that the effective overall ion movement is reduced. However, these results reflect the overall ionic conductivity comprising all ionic species. Thus, it needs to be noted that these observations are not sufficient to judge the performance of these ionogels as SPEs in lithium metal batteries because the transport of the Li^+-ions is the determining property. Therefore, the Li^+-ion transference number was investigated in detail, as discussed in the following section.

4.2.4 Li^+-Ion Transport

To gain insight into the actual Li^+-ion transport and not solely into the overall ionic conductivity, measurements and calculations of the t_{Li^+} as suggested by Evans *et al.*[137] (Equation 4.11) and Watanabe *et al.*[136] (Equation 4.12) were conducted as follows

$$t_{Li^+} = \frac{I_{ss}\,(\Delta V - I_0 R_0)}{I_0\,(\Delta V - I_{ss} R_s)} \tag{4.11}$$

$$t_{Li^+} = \frac{R_b}{\left(\frac{\Delta V}{I_{ss}} - R_0\right)} \tag{4.12}$$

$$I_{0,calc} = \frac{\Delta V}{R_b + R_0} \tag{4.13}$$

where R_b is the bulk resistance of the PE, I_{ss} is the steady state current, I_0 is the initial current, ΔV is the polarization voltage, and R_0 and R_s are the initial and steady-state PE|Li interfacial resistances (combination of the charge-transfer resistance R_{CT} and the SEI resistance R_{SEI}), respectively. In line with other reports[147] more consistent values were obtained with the latter calculation method (for more details, see the corresponding Section in the Appendix A.2.2, p. 136). Although these approaches were developed for diluted systems containing only two ionic species and thus are not perfectly suited for multi-ionic polyelectrolytes, they can be still used to compare the obtained values among

the systems to elaborate the differences. In addition to the calculation of t_{Li^+}, a closer look was taken at the different parameters obtained during the measurements, such as the area-specific resistance ($ASR_{\mathrm{CT+SEI}}$), I_0, I_{ss} and the ratio I_{ss}/I_0, Figure 4.19.

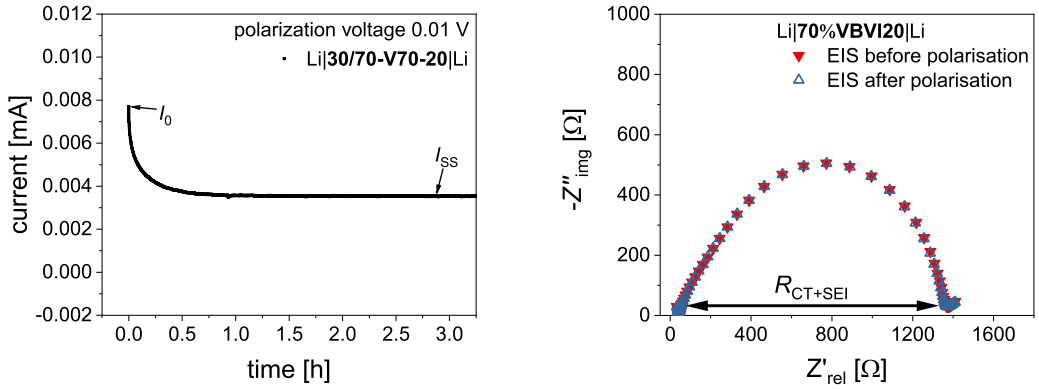

(a) (b)

Figure 4.19: Determination of the Li^+-ion transference number (t_{Li^+}, see Equation 4.12 and 4.11) by **(a)** combined chronoamperometry **(b)** and impedance spectroscopy, deriving the interfacial resistance ($R_{\mathrm{CT+SEI}}$), initial current (I_0) and steady-state current (I_{ss}). Adapted with permission from[81]. Copyright 2022 American Chemical Society.

When comparing IGs to other SPEs, it was observed that the Li^+-ion transference number (t_{Li^+}) shows relatively low values (below 0.05), see Table 4.6.[148–150] However, this behavior is expected because t_{Li^+} describes the Li^+-ion mobility and number in comparison to all other ions. Since IL-based PEs feature more than two ionic species, the t_{Li^+} of the Li^+-ions is decreased compared to a system with only one ionic species, even if the absolute Li^+-ion mobility stays unchanged. Nevertheless, high variations were found when comparing the t_{Li^+} of PEGDA-based IGs (0.006) and VBVI-based ones ($0.022 - 0.043$) with the latter ones being $4 - 7$ times higher. Additionally, the variation of the LiTFSI content led to a higher t_{Li^+} (0.043) when comparing 30/70-V100-40 to its counterpart with only 20 mol % of LITFSI ($t_{Li^+} = 0.028$), while there was no prominent difference observed in PEGDA-based samples (both $t_{Li^+} = 0.006$). It seems that a higher LiTFSI content leads to a higher t_{Li^+} at least for VBVI-based IGs. Generally, high t_{Li^+} values can be obtained by tethering the anions to the polymer backbone to immobilize their movement, creating so-called 'single-ion conducting polymer electrolytes'.[150] Nevertheless, immobilized cations, as used in this approach, have also shown their potential to increase t_{Li^+} through intermolecular interactions with the free anions, thus also immobilizing them to some degree.[151,152]
Taking a further look at the parameters that were derived from the t_{Li^+} measurements, see Table 4.6, the reasons for the difference between PEGDA-based and VBVI-based IGs can be elaborated in detail.

Table 4.6: Area-specific resistance ($ASR_{\mathrm{CT+SEI}}$), initial current (I_0), steady-state current (I_{ss}), the ratio of I_{ss}/I_0 and the Li^+-ion transference number (t_{Li^+}) derived from chronoamperometry (10 mV) and dielectric impedance spectroscopy of Li|PE|Li cells at 40 °C.[a]

Ionogel	$ASR_{\mathrm{CT+SEI}}$ $[\Omega\,\mathrm{cm}^2]$	$I_0{}^a$ [µA]	$I_{\mathrm{ss}}{}^a$ [µA]	$I_{\mathrm{ss}}/I_0{}^b$ [%]	$t_{Li^+}{}^c$	σ_0 $[\mathrm{mS\,cm}^{-1}]$
30/70-P100-40	379	6.18	0.43	7.0	0.006	0.14
30/70-P100-20	432	5.42	1.17	21.7	0.006	0.51
30/70-V100-40	198	11.1	2.94	26.4	0.043	0.03
30/70-V100-20	318	7.74	3.33	43.0	0.028	0.19
30/70-V70-20	332	6.90	3.57	51.8	0.022	0.21
30/70-V50-20[d]	320	7.93	3.18	40.1	0.023	0.37

[a] Additionally σ_0 at 40 °C is displayed for comparison. [b] Constant area of approx. 0.5 cm^2. [c] $t_{Li^+} = 0.039$ determined by Brinkkötter *et al.* for similar IGs.[131] [d] Best performing sample in a Li|SPE|Li cell.

The area specific resistance of charge transfer and the solid electrolyte interface ($ASR_{\mathrm{CT+SEI}}$) was calculated as

$$ASR_{\mathrm{CT+SEI}} = \frac{R_0 \cdot A}{2} \tag{4.14}$$

where A is the surface of the lithium electrodes. The $ASR_{\mathrm{CT+SEI}}$ was the lowest for the film comprising 100 mol % VBVI and 40 mol % LiTFSI (198 $\Omega\,\mathrm{cm}^2$), followed by the films with 100 mol % VBVI and 20 mol % LiTFSI (≈320 $\Omega\,\mathrm{cm}^2$), 30/70-P100-40 (379 $\Omega\,\mathrm{cm}^2$) and 30/70-P100-20 (432 $\Omega\,\mathrm{cm}^2$), all being in the range of comparable PEs.[153] Thus, the following can be concluded: (I) VBVI-based films show the formation of an improved solid electrolyte interface (SEI) in comparison to PEGDA-based films and (II) a higher amount of LiTFSI facilitates the formation of an SEI with a lower resistance independent of the employed polymer matrix. Furthermore, I_0, I_{ss} and the ratio of I_{ss}/I_0 upon applying a voltage of 10 mV were evaluated (constant interfacial area of 0.5 cm^2 among all measurements). Herein, 30/70-V100-40 showed the highest I_0 of 11.1 µA, followed by around 7.0 µA for 30/70-V100-20, 6.0 µA for 30/70-P100-40 and 5.5 µA for 30/70-P100-20, being a direct result of the interfacial resistance. However, the evaluation of I_{ss} and I_{ss}/I_0 reveals the crucial property for the intended application: the current that can be provided by the ionogel upon long-term application of a specific voltage (i.e., 10 mV). Herein, PEGDA-based films showed a reduction to 0.43 µA or 1.17 µA corresponding to an I_{ss}/I_0 ratio of only 7 % and 22 % for 30/70-P100-40 and 30/70-P100-20, respectively. This means that only a small amount of the initially provided current, which was already lower than for their VBVI counterparts, can be maintained. Thus, VBVI-based films featured not only higher initial currents but also significantly higher steady-state currents. They were able to maintain an I_{ss} of around 3 µA to 3.5 µA, being a factor $3-8$ higher than PEGDA-based IGs despite the previously shown lower overall ionic conductivity. Moreover, 30/70-V70-20 delivered the highest steady-state current with 3.57 µA which was 51 % of the initial current and 30/70-V100-40 delivered the lowest I_{ss} among the VBVI-based films with only 2.94 µA, which is 26 % of the initial value. Overall, it can be stated that VBVI-based IGs not only had a significantly higher calculated t_{Li^+} in comparison to their PEGDA-based counterparts,

but also displayed lower SEI resistances as well as higher initial and significantly higher steady-state currents. Therefore, it seems that the PEGDA-based films possessed higher overall ionic conductivities, as previously shown (see also Table 4.6), but significantly lower effective Li^+-ion conductivities. Most probably, these findings are a result of the known strong interaction between Li^+-ions and the ethylene oxide units[154–156] that are present in PEGDA. Therefore, the stochastic movement of the Li^+-ions is restricted and the mobility of the $TFSI^-$-anions is increased which leads to high overall ionic conductivities as a result of anion mobility. These findings show that the best performing IG cannot be predicted based on the ionic conductivity. Furthermore, this reveals that the evaluation of not only the calculated t_{Li^+}, but also the other derived parameters from these measurements provide information to predict the performance of IGs.

4.2.5 Lithium Plating and Stripping

Lithium plating and stripping experiments in symmetrical lithium-metal cells were carried out to further corroborate the findings from the t_{Li^+} measurements regarding the influence of the different matrices. Herein, lithium was constantly plated and stripped, while the current density (CD) was increased after each completed plating and stripping step. This approach enables a fast and efficient comparison of different solid polymer electrolytes regarding their critical current density.[135,157] Thus, a CD of 0.05 mA cm^{-2} was chosen as the starting point and subsequently, the CD was raised to 0.1, 0.2, 0.3 mA cm^{-2} and so forth until a short-circuit was observed or the safety limits (±5 V) were reached. Doing so, the trend which was already observed during the measurements of the transference number was confirmed. As observed in Figure 4.20a, the PEGDA-based IGs (I) show a high overvoltage even at low CDs (e.g., 110 mV and 270 mV at 0.1 mA cm^{-2}), (II) did not reach a stable voltage plateau even at low CDs and (III) eventually showed extreme polarization or a short circuit at 0.2 mA cm^{-2}.

Furthermore, 30/70-P100-40 showed a significantly higher overvoltage (e.g., 260 mV vs. 110 mV at a CD of 0.1 mA cm^{-2}) and stronger polarization at the same CD compared to 30/70-P100-20, which is in line with the lower I_{ss} observed in the t_{Li^+} measurements. In contrast to this, VBVI-based IGs generally showed lower overvoltage, less polarization and significantly higher achieved CDs. However, significant differences were observed among the series of VBVI-based IGs: as demonstrated in Figure 4.20b, the strongest polarization as well as the earliest short-circuit at a CD of 0.5 mA cm^{-2} was observed for 30/70-V100-40, which was again in line with the lowest I_{ss} among the VBVBI-based IGs as observed in the t_{Li^+} measurements. Subsequently, 30/70-V50-20 and 30/70-V100-20 showed a short-circuit at 0.7 mA cm^{-2} and 30/70-V70-20 at 0.8 mA cm^{-2}. However, among these three IGs, 30/70-V50-20 possessed the highest overvoltage already from the beginning, while in addition the voltage did not reach a plateau even at low CDs of 0.05 mA cm^{-2}, see Figure 4.20c. In comparison, 30/70-V70-20 and 30/70-V100-20 showed lower overvoltages and stable voltage plateaus at low CDs, implying a constant lithium deposition.[158] Consequently, for 30/70-V50-20 a substantially higher polarization of 1 V at 0.6 mA cm^{-2} was detected in comparison to around 280 mV for both other discussed IGs. Finally, the highest short-circuit

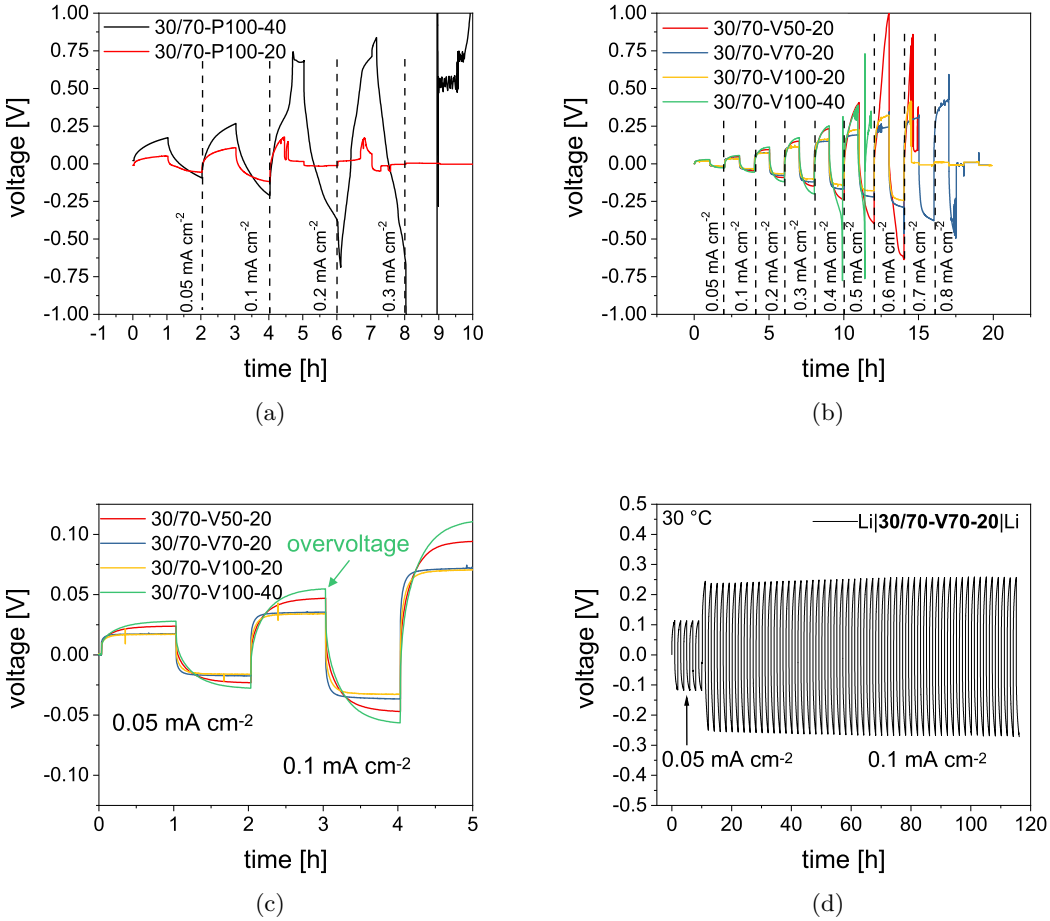

Figure 4.20: Lithium plating and stripping experiments with alternating current densities (CDs) at 60 °C of **(a)** PEGDA- and **(b)** VBVI-based IGs. **(c)** Low CD region of **(b)** showing the stable voltage plateau of 30/70-V100-20 and 30/70-V70-20. **(d)** Long-term plating and stripping of Li|30/70-V70-20|Li cells with 0.1 mA cm^{-2} over 53 full cycles 106 h at 30 °C. Adapted with permission from[81]. Copyright 2022 American Chemical Society.

CD of 0.8 mA cm^{-2} was found for 30/70-V70-20, implying the best interplay of Li^+-ion transport and mechanical properties. Overall, the findings from the t_{Li^+} measurements were confirmed by a straightforward approach employing lithium plating/stripping with alternating CDs. Here, significantly higher CDs for VBVI-based IGs in comparison to PEGDA-based ones were detected, again despite the lower overall ionic conductivity of the former. Therefore, the advantages of using VBVI as a matrix for IGs over the commonly employed PEGDA were verified.

Finally, 30/70-V70-20 was employed in long-term lithium plating stripping experiments to provide an outlook on the applicability of those IGs in lithium metal batteries. A constant lithium deposition could be reached at a CD of 0.1 mA cm^{-2} slightly above room temperature (30 °C). As visible in Figure 4.20d, after applying 53 full cycles (106 h), only a marginal increase ($\approx$ 5 %) in overvoltage was found implying a compatibility of 30/70-V70-20 and lithium metal. The same observation was made for 60 full cycles (120 h) at 60 °C, confirming the findings (see Figure A.2.7).

4.2.6 Summary

In this Section, IGs consisting of an IL-M, IL, LiTFSI and two different crosslinkers, namely PEGDA (neutral matrix) and [VBVI]TFSI (IL-CL, charged matrix) were prepared and compared concerning their use in lithium metal batteries (summary given in Table 4.7) was presented.

Table 4.7: Findings of the presented study comparing PEGDA (neutral) and [VBVI]TFSI (charged) as crosslinkers for IGs.

Parameter	PEGDA	[VBVI]TFSI	explanation
Storage moduli	−	+	Rigid structure of [VBVI]TFSI
Thermal stability	−	+	Prone C-O bonds
Ionic conductivity	+	−	Higher anion mobility of PEGDA-based IGs
t_{Li^+}	−	+	Interaction of Li^+-ions with ether oxygens
Interfacial resistance	−	+	Beneficial SEI composition of [VBVI]TFSI-based IGs
Critical CD	−	+	Higher Li^+-ion conductivity and lower interfacial resistance of [VBVI]TFSI-based IGs

Samples with varying amounts of components were synthesized by photopolymerization and characterized by IR spectroscopy and TGA measurements. The latter revealed a 31 °C higher thermal stability for VBVI-based films. Furthermore, combined rheo-dielectric measurements were conducted to determine the mechanical properties and ionic conductivities of the samples simultaneously. In general, samples with increasing content of crosslinker,that is, an increasing density of crosslinks within the polymer matrix, and overall increasing content of polymer led to higher storage moduli $G'(\omega)$ as both parameters result in increased mechanical rigidity. The highest mechanical moduli of around 4×10^5 Pa were found for VBVI-based IGs, displaying higher mechanical moduli than the PEGDA-based ones (1×10^5 Pa). The opposite trend was found for the ionic conductivities. Here, a higher content of crosslinker and polymer reduced the ionic conductivities, an effect attributed here to the more rigid structure that impedes ion transport. Further, the ionic conductivities of comparable PEGDA- and VBVI-based IGs without LiTFSI displayed the same value of around 0.3 mS cm^{-1} at 25 °C, indicating that the ion transport is not strongly dependent on the polymer matrix. However, the addition of LiTFSI led to an overall decrease of the ionic conductivities, with a maximum reduction of about one decade for the VBVI-based samples with 40 mol % LiTFSI, most likely due to the formation of aggregates. Therefore, it was assumed that the larger number of ions in the VBVI-based samples favors the formation of even more aggregates, reducing ion movement and thus decreasing the ionic conductivity. However, these results only revealed the overall ionic conductivity of the samples including all ions, whereas the movement of Li^+-ions is responsible for the performance of the IGs as polymer electrolytes in LIBs. Significant differences were found for the t_{Li^+} in the PEGDA- (0.006) and VBVI-based ($0.02 - 0.043$) samples, with

an enhanced Li^+-ion transport in VBVI-based IGs by factor $4-7$. Moreover, further parameters were extracted from the t_{Li^+} measurements such as the area specific resistance of charge transfer and the solid electrolyte interphase, initial current, steady state current and the ratio I_{ss}/I_0 and subsequently compared. Here, VBVI-based samples featured not only lower ASR_{CT+SEI} and higher I_0, but also significantly higher (factor $3-8$) I_{ss} in comparison to PEGDA-based IGs despite their lower ionic conductivity. This beneficial Li^+-ion transport was further corroborated by lithium plating and stripping experiments with alternating CDs. In accordance with the previous results, significantly higher CDs, lower overvoltage and more stable lithium deposition were found for VBVI-based IGs. Thus, these results highlight the importance of the study of the actual Li^+-ion transport and clearly demonstrate that the investigation of solely the ionic conductivity is not sufficient to evaluate the performance of IGs. Finally, long-term plating stripping experiments at 30 °C revealed the applicability of those VBVI-based IGs in lithium metal batteries, which shows the compatibility of the former with lithium metal and therefore provides an outlook for the actual LIB application.

5 Orientation of Block Copolymers

In this Chapter in-situ alignment behavior under LAOS of anionically polymerized isoprene and styrene triblock copolymers is investigated using coupled rheo-dielectric. The use of BDS, SAXS and rheology allows to investigate the orientation on three different length scales, from nanoscopic to macroscopic. The objective is to investigate the effect of block order on the orientation kinetics and final macroscopic orientation.
The content of this Chapter and the corresponding Sections in the Appendix are published in the journal Macromolecules[159] from the American Chemical Society (ACS). Maxi Hoffmann is the first author of this article.

Block copolymers attain big interest as functional materials as they combine the properties of at least to different polymers and are thus highly tunable.[64] Several industrial applications such as conductivity, energy harvesting or optical applications require macroscopically ordered materials.[63,160] In general, macroscopic orientation can be induced by external forces such as mechanical, magnetic or electric fields.[12,15] In the literature, the focus is often set on the mechanical alignment of diblock copolymers to fully understand its mechanism and influencing parameters.[19,161,162] One of the most commonly used methods for mechanical alignment of BCPs to date is large amplitude oscillatory shear (LAOS), which leads to different alignments depending on sample morphology and experimental parameters such as strain amplitude γ_0, temperature T and excitation frequency ω_{Rheo}.[15,163] For a lamellar diblock copolymer either a parallel, perpendicular, transverse or biaxial orientation of the lamellae to the shear direction can be achieved, see Figure 3.16, p. 31.[15,78,161] However, the morphological structure before and after orientation was mostly determined via *ex-situ* SAXS while the underlying mechanism and its kinetics were neglected, in particular, when it comes to BCPs with more than two blocks. To close this gap, many techniques have been developed to investigate the alignment mechanism and its dependence on different parameters in BCPs. Rheo-birefringence was used by Gupta *et al.* to investigate the orientation process of lamellar polystyrene-*b*-polyisoprene (SI) diblock copolymers *in-situ*.[164,165] The birefringence measurements offered insights into the kinetics of the alignment by showing the existence of a fast and slow process, which emphasizes that multiple mechanisms are responsible for flow-induced alignment.[164,165] However, birefringence measurements only provided information about the time-dependence of the process but did not offer enough spatial resolution for information on a nanometer length scale, such as structural changes. The development of online rheo-SAXS enabled researchers to simultaneously

enforce reorientation while monitoring the orientation kinetics with a time resolution of several seconds.[21,166–168] Finally, the coupling of rheology and BDS offered the possibility not only to control the orientation by rheological means, but also to continuously study the local chain dynamics of the PI segment during orientation. 1,4-*cis*-PI is a Stockmayer A polymer, i.e., its electrical dipole moment is parallel to the polymer chain (see Figure 3.8) and therefore dielectric spectroscopy can monitor the end-to-end vector of PI with respect to its dynamic and orientation. Both rheology and dielectric spectroscopy can be easily accessed and do not need high maintenance. Rheo-dielectric, for example, has been used to investigate the influence of processing conditions on percolated poly(ethylene butyl acrylate) nanocomposite hybrid polymers[169] and the influence of shear on nematic liquid crystals and polymer melts.[170–172] Meins *et al.* studied the orientation dynamics of SI-diblock copolymers having different molecular weights using a highly sensitive rheo-dielectric setup in combination with *ex-situ* SAXS measurements and found a perpendicular, parallel and biaxial orientation.[21,173] Furthermore, they found that the timescale of the evolution of $\epsilon''(t)$ correlated with the timescale of $I_{3/1}(t)$ as obtained from FT rheology. The nonlinear parameter is suspected to provide information on the number of grain boundaries, an internal area of the interphase in the sample.[20,174,175] Overall, they showed that both methods rheo-SAXS and rheo-dielectric enabled the observation of a deordering process under continuously applied oscillatory shear.[20,21]

After the orientation behavior of diblock copolymers had been investigated extensively, the interest of research expanded towards multiblock copolymers, e.g., tri- and pentablock copolymers.[163,176] Their alignment behavior was compared to diblock copolymers and the influence of loops and bridges between the phases in the multiblock copolymers was investigated thoroughly.[19,163,176,177] Riise *et al.* compared the orientation of di- and triblock copolymers and found that only a perpendicular orientation was obtained for SIS.[19] Moreover, SIS possessed a high degree of macroscopic order as has never been obtained for diblocks.[19] Other researchers showed that the conformation of the triblock copolymers in either a middle block loop, i.e., end blocks within the same microdomain, or a middle block bridge, i.e., end blocks in different microdomains, had an impact on the final alignment of the sample, as well as solid mechanical properties.[178] Wu *et al.* investigated the mechanical orientation of lamellar tri- to undecablock copolymers consisting of PS and PI ($M_{\mathrm{n,total}} = 21\,000 - 195\,000\,\mathrm{g\,mol^{-1}}$) by *ex-situ* SAXS measurements.[177] They found that all samples (except the undecablock) formed either a parallel or a perpendicular orientation, depending on the applied parameters. However, with increasing block number, a parallel orientation could only be formed at large strain amplitudes γ_0 and low frequencies ω_{Rheo}, e.g., $\gamma_0 = 600\,\%$, $\omega_{\mathrm{Rheo}}/2\pi = 1\,\mathrm{Hz}$ for SISISIS at $T = 170\,^{\circ}\mathrm{C}$. They assumed that the parallel orientation was caused by a predominantly loop conformation, which allows for layer sliding of the PI layer. In comparison, the undecablock copolymers showed only a perpendicular macroscopic orientation. So far, however, research has focused mainly on the effects of bridges and loops on the final alignment, while the kinetics of the alignment process itself has been neglected.[163,176,179] This might be especially important in the context of macroscopically ordered ion-conductive BCPs, where a perpendicular orientation

and high degree of order results in an increased ion transport due to fewer defects and lower tortuosity.[11,12,18] The objective of this Chapter is to investigate the orientation process of the lamellar microstructure under LAOS for PS and PI triblock copolymer systems with different block order, thus block dynamics, and local dipole orientation. In the following, the *in-situ* orientation process of ISI and SIIS is studied using coupled rheo-dielectric measurements. Since 1,4-*cis*-PI is a Stockmayer A polymer,[58,180] this unique method offers insight into the orientation process by monitoring the fluctuations of the end-to-end vector of PI. In general, by observing the PI normal mode, the anisotropic movement of the PI chains during the alignment process is followed, which already indicates the type of orientation, see Figure 5.1, where an increase in $\epsilon''(t)$ indicates a perpendicular and a decrease a parallel orientation. While in ISI the normal mode of the endblocks can be detected by BDS, the motion within the isoprene segment is dielectrically inert in SIS because the PI ends are fixed to the PS endblocks.[181] To circumvent this issue, dipole inverted SIS (SIIS), has been anionically synthesized, where the dipole inverted middle block enables the detection of the local, constrained PI normal mode.[182] In addition, rheology is assumed to provide information about the amount of grain boundaries during the alignment process while the final macroscopic orientation was determined via SAXS.

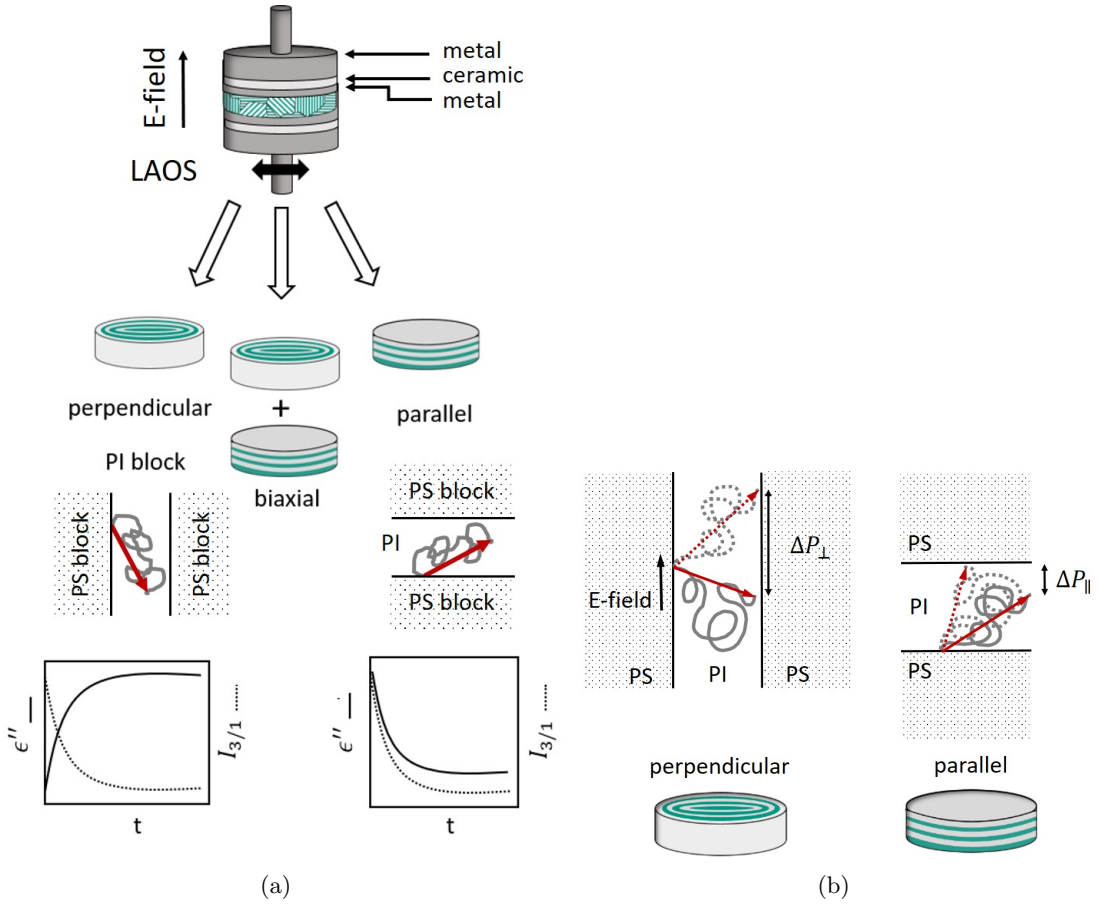

Figure 5.1: **(a)** Scheme of the observed orientations obtained by large amplitude oscillatory shear (LAOS) and the alignment of the electric dipole moment of PI in ISI. While dielectric spectroscopy observes the type of orientation, as the direction of change depends on the type, $I_{3/1}$ observes only the change in the total grain surface, which is similar for both orientations. **(b)** Schematic representation of the change in the dipole moment due to the applied E-field. The red arrows indicate the total dipole moment of PI before (solid lines) and after (dotted lines) polarization by an E-field. In the case of parallel alignment, the maximum possible change in polarity ($\Delta P_\parallel$) is smaller than in the case of perpendicular alignment ($\Delta P_\perp$), because the movement of the chains is restricted by the neighboring PS phase. The observable ΔP is limited by the available time (frequency of the E-field). The comparison with the possible ΔP in a non-oriented sample ($\left[\Delta P_\parallel + \Delta P_\perp\right]/2$) results in a decrease of $\epsilon''(t)$ for a perpendicular orientation and an increase for a parallel orientation. It needs to be noted that the used parallel plate geometry results in a radially dependent strain amplitude, respective shear rate, and thus morphology of the oriented sample with the highest degree of orientation at the edge. Furthermore, for simplicity, it is ignored that the interface between the domains is not just a line but an interface consisting of both polymers; also, the possibility of curved or undulating borders is ignored in the scheme. Adapted with permission from[159]. Copyright 2023 American Chemical Society.

5.1 Sample Preparation and Characterization

All samples were synthesized via anionic polymerization using high vacuum technique at room temperature using cyclohexane as solvent and *s*-BuLi as initiator. Figure 5.2 depicts the sequential polymerization of ISI with a reaction time of at least 24 h per step and the termination with degassed methanol. The red arrows indicate the direction of the dipole moment of PI. In the case of ISI, the dipole moments of both PI endblocks point in the same direction.

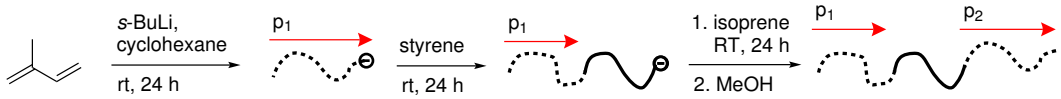

Figure 5.2: Sequential anionic polymerization of an ISI triblock copolymer. The red arrows indicate the direction of the dipole moment of PI, related to the normal mode. Adapted with permission from[159]. Copyright 2023 American Chemical Society.

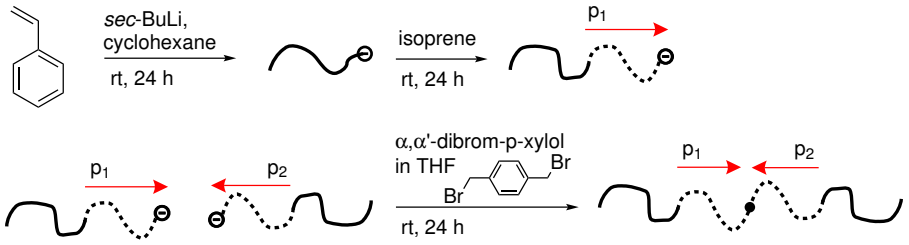

Figure 5.3: Sequential anionic polymerization of an SI^- diblock copolymer followed by coupling with α,α'-dibrom-p-xylol. The polymer was then purified by several fractionation cycles. The red arrows indicate the direction of the dipole moment of PI and the inversion of the dipoles in SIIS. Reprinted with permission from[159]. Copyright 2023 American Chemical Society.

The polymerization of SIIS was adapted from Watanabe *et al.*[181] and is depicted in Figure 5.3. First, SI^- was synthesized which was then coupled using α,α'-dibrom-p-xylol dissolved in dry THF. Subsequently, the uncoupled diblock was removed by several fractionation cycles in cyclohexane and isopropanol to obtain monodisperse SIIS, see Figure A.2.8. A detailed description of the synthetic procedures can be found in the literature.[181,183] After the synthesis, the samples were precipitated in methanol, redissolved in cyclohexane and 0.1 wt% butylated hydroxytoluene (BHT) was added as a stabilizer. Then, the samples were freeze-dried for 48 h. The synthesized samples and their properties are presented in Table 5.1.

Table 5.1: Anionically synthesized polymers and their molecular characteristics. Reprinted with permission from[159]. Copyright 2023 American Chemical Society.

Sample	$M_{n,PI}$ $\left[\mathrm{g\,mol^{-1}}\right]$	$M_{n,PS}$ $\left[\mathrm{g\,mol^{-1}}\right]^{a}$	$M_{n,total}$ $\left[\mathrm{g\,mol^{-1}}\right]^{a}$	Đ	f_{PI} [vol%]	$\chi_{PSPI}N^{b}$ (25 °C)	T_{ODT} [°C]^{c}	$T_{g,PI}$ [°C]	$T_{g,PS}$ [°C]
ISI-40K	11 000^{d}	16 000	39 000	1.07	55	≥26	184	−60	83
	12 000^{e}								
SIIS-40K	10 000	10 000^{c}	40 000	1.02	56	≥25	158	−60	74
	10 000	10 000^{d}							
PI-15K	–	–	15 000	1.04	–	–	–	−70	–
PS-30K	–	–	30 000	1.04	–	–	–	–	110

[a]The molecular weight of the blocks was calculated using SEC and ^{1}H-NMR data. [b]Determined using the total degree of polymerization, which was calculated using M_n of each block and $\chi_{PSPI} > 0.051$[184] at 25 °C, a temperature-dependent equation resulting in 0.0592[185] and an overview over different simulation and theories ranging from 0.05 to 0.18.[186] [c]As determined from rheology ($\omega_{Rheo}/2\pi = 1$ Hz) at the inflection point of $G'(T)$. [d]1st block and [e]3rd block of the total BCP.

Phase Separation

The phase separation of the synthesized samples was analyzed by DSC and SAXS measurements as displayed in Figure 5.4.

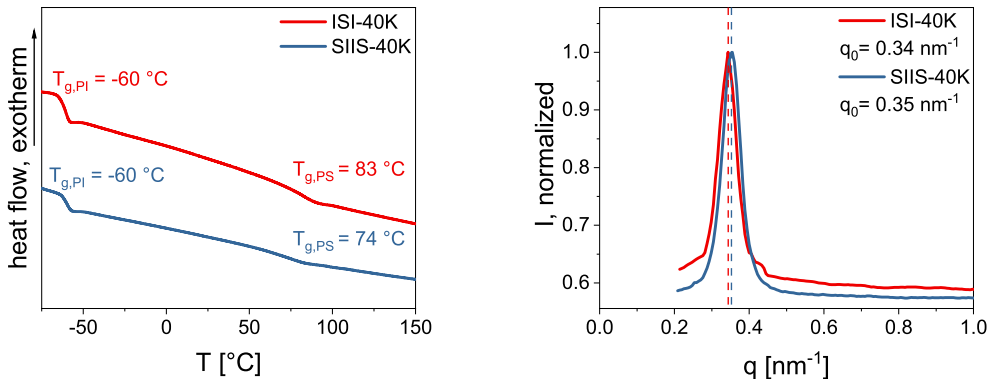

Figure 5.4: (a) DSC curves revealing the phase separation of ISI-40K and SIIS-40K by displaying the T_g of the PI and PS domains. **(b)** Radial averaged 2D-SAXS spectrum of the two samples prior to rheological treatment, indicating phase separation with $q_0 = 0.34\,\mathrm{nm}^{-1}$ and $q_0 = 0.35\,\mathrm{nm}^{-1}$ for ISI-40K and SIIS-40K, respectively. Reprinted with permission from[159]. Copyright 2023 American Chemical Society.

The DSC curves show two distinct T_gs at $-60\,°\mathrm{C}$ (PI) and $83\,°\mathrm{C}$ (PS) for ISI-40K and $-60\,°\mathrm{C}$ (PI) and $74\,°\mathrm{C}$ (PS) for SIIS-40K and thus indicate local phase separation. The phase separation was also confirmed by SAXS measurements where the primary scattering peak was observed at $q_0 = 0.34\,\mathrm{nm}^{-1}$ for ISI-40K and $q_0 = 0.35\,\mathrm{nm}^{-1}$ for SIIS-40K, see Table A2, p. 140. For a triblock copolymer with a volume block ratio of around 45/55 PS/PI a lamellar structure is expected.[64,187] The average lamellar thickness was calculated as

$$d_0 = \frac{2\pi}{q_0} \tag{5.1}$$

and $d_{\mathrm{ISI}} = 18.5\,\mathrm{mm}$ and $d_{\mathrm{SIIS}} = 18.0\,\mathrm{mm}$ was obtained, which is in agreement with comparable PS and PI BCPs.[163] The assumed lamellar structure was confirmed by investigating higher maxima of the primary scattering peak q_0 obtained by further SAXS measurements after the orientation procedure, Figure A.2.9, p. 140. The primary scattering maximum after rheological shear alignment was found at $q_0 = 0.35\,\mathrm{nm}^{-1}$ and higher maxima at $2q_0 = 0.71\,\mathrm{nm}^{-1}$ and $3q_0 = 1.07\,\mathrm{nm}^{-1}$ for ISI-40K and $q_0 = 0.36\,\mathrm{nm}^{-1}$, $2q_0 = 0.74\,\mathrm{nm}^{-1}$ and $3q_0 = 1.11\,\mathrm{nm}^{-1}$ for SIIS-40K indicating a lamellar structure as expected for a triblock copolymer with a block ratio of around 45/55 PS/PI.[64,187] For both polymers, slightly higher q-values ($\Delta q_0 = 0.01\,\mathrm{nm}^{-1}$) were found for the oriented samples independent of the macroscopic orientation, see Table A2, p. 140. Possible reasons for this might be (I) an asymmetric peak after orientation or (II) change in density due to, for example, an increased fraction of loops in the sample. The lamellar thickness of the oriented samples was $d_{\mathrm{ISI}} = 18.0\,\mathrm{mm}$ and $d_{\mathrm{SIIS}} = 17.5\,\mathrm{mm}$.

The phase separation of a sample is only preserved below the order-to-disorder-transition temperature, above which the sample transitions into a mixed phase. This transition was observed by a rheological temperature sweep where a sudden decrease in the moduli indicated T_{ODT}. The inflection point in the storage modulus $G'(T)$ was used to determine T_{ODT} as 184.4 °C for ISI-40K and 158.3 °C for SIIS-40K, see Figure 5.5.

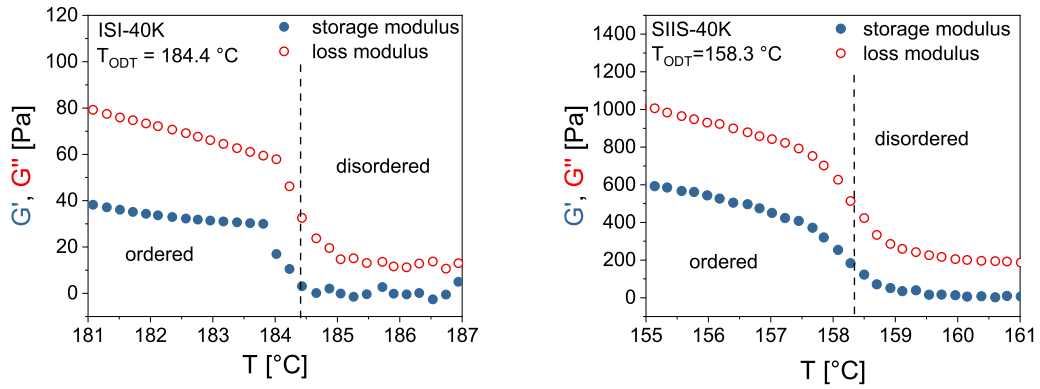

(a) (b)

Figure 5.5: Determination of the order-disorder temperature (T_{ODT}) for **(a)** ISI-40K and **(b)** SIIS-40K by a temperature sweep with a heating rate of $1\,^{\circ}\mathrm{C\,min^{-1}}$ and a strain amplitude of $\gamma_0 = 3\,\%$ at $\omega_{\mathrm{Rheo}}/2\pi = 1\,\mathrm{Hz}$. The inflection point in $G'(T)$ was used to determine T_{ODT}. Adapted with permission from[159]. Copyright 2023 American Chemical Society.

Broadband Dielectric Spectroscopy and Linear Rheology of ISI-40K

Frequency-dependent dielectric spectroscopy measurements have been conducted at different temperatures. The double logarithmic plot of $\epsilon''(\omega_{\mathrm{BDS}})$ of ISI-40K at different temperatures all below T_{ODT} is displayed in Figure 5.6a.

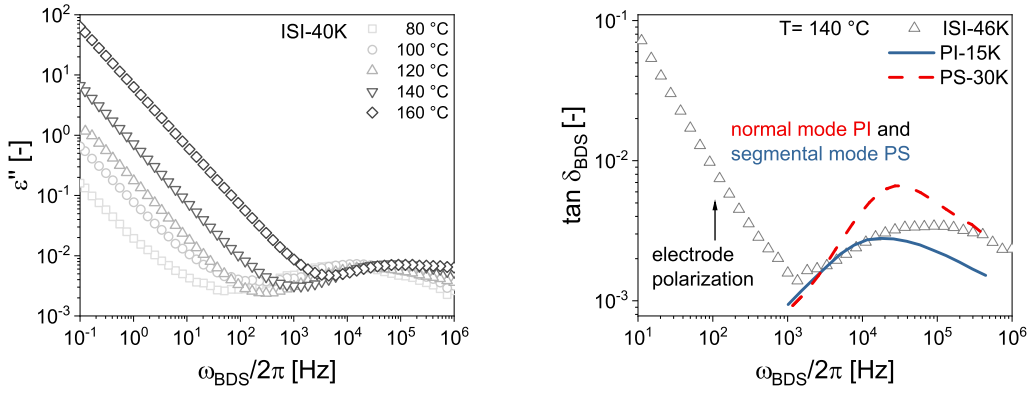

(a) (b)

Figure 5.6: **(a)** Frequency dependence of the dielectric loss ($\epsilon''(\omega_{\mathrm{BDS}})$) at different temperatures between 80 °C and 160 °C of ISI-40K and **(b)** $\tan\delta_{\mathrm{BDS}}(\omega_{\mathrm{BDS}})$ of ISI-40K at 140 °C including the corresponding homopolymers polyisoprene (PI, red) and polystyrene (PS, blue). The increase at low frequencies in both graphs is caused by the Li^{+}-ion conductivity (electrode polarization). Reprinted with permission from[159]. Copyright 2023 American Chemical Society.

The observed relaxation process in $\epsilon''(\omega_{\mathrm{BDS}})$ can be ascribed to the segmental mode of PS and the normal mode of PI, which are superposed in the observed temperature range as indicated by measurements of the corresponding homopolymers, see Figure 5.6b. Comparing the relaxation processes observed for the BCP to the homopolymers, a peak broadening and low frequency shift for the BCP is observed, which results from the tethered PI chains being constrained by the less mobile PS.[188,189] Additionally, as observed in Figure 5.6a, with increasing temperature, both relaxation processes shift to higher frequencies, indicating their thermal activation. An evaluation of the data via the classical Havriliak-Negami equation[55] for $\epsilon''(\omega_{\mathrm{BDS}})$ is not possible because of the overlapping relaxation processes of the phase separated system.

The rheological shear storage and loss moduli were obtained by SAOS measurements at different temperatures, all below T_{ODT} but above the glass transition temperature of PS. The data was shifted according to the TTS principle using $T_{\mathrm{ref}} = 140\,^{\circ}\mathrm{C}$. Figure 5.7a displays the master curve including the respective shift factors for ISI-40K.

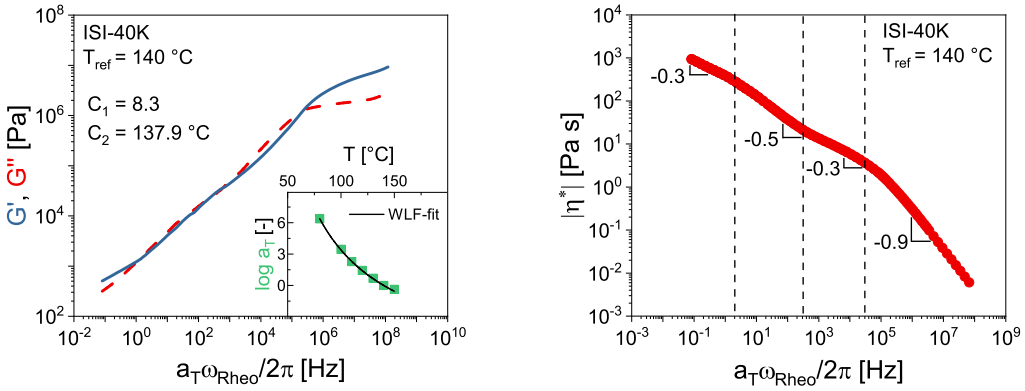

Figure 5.7: **(a)** Master curve of the shear storage ($G'(\omega_{\mathrm{Rheo}})$) and loss modulus ($G''(\omega_{\mathrm{Rheo}})$) including the WLF-shift factors in the inset and **(b)** master curve of the absolute value of the complex shear viscosity ($|\eta^*|$) of ISI-40K at $T_{\mathrm{ref}} = 140\,^{\circ}\mathrm{C}$. Reprinted with permission from[159]. Copyright 2023 American Chemical Society.

The TTS principle[40] has previously been shown to work for BCPs only in a limited temperature range (i.e., below T_{ODT}, above T_{g}).[162,176,190] At low frequencies, a terminal response as for linear homopolymers ($G' \propto \omega^2_{\mathrm{Rheo}}$, $G'' \propto \omega^1_{\mathrm{Rheo}}$) was not reached before T_{ODT} and $G' \propto \omega^{0.7}_{\mathrm{Rheo}}$ and $G'' \propto \omega^1_{\mathrm{Rheo}}$ was found. These values correspond to observations made for other triblock copolymers in literature ($G' > G''$ and G', $G'' \propto \omega^{0.7}_{\mathrm{Rheo}}$ at low ω_{Rheo}) and are characteristic of self-assembled BCP systems, because the flow at low ω_{Rheo} is constrained due to the significant difference in their molecular dynamics as reflected in the different T_{g}s ($\Delta T_{\mathrm{g}} \approx 100\,^{\circ}\mathrm{C}$) and interactions of the blocks, e.g., orientation processes at the polymer interfaces.[191]

The master curve of the absolute complex shear viscosity ($|\eta^*|$) in Figure 5.7b indicates four distinct frequency regimes identified by different slopes ranging from -0.3 at low rheological frequencies to -0.9 at higher rheological frequencies. In the literature, different alignment behaviors, e.g., parallel and perpendicular, were observed within the distinct regimes,

while the slope values were not determined.[15,161,164,190] However, the determination of these slopes on a log-log scale gave scaling exponents between −0.3 to −0.6 for diblock copolymers.[15,161]

5.2 Shear Alignment of ISI-40K

Large amplitude oscillatory shear was used for the alignment of ISI-40K. The LAOS measurements were conducted at $T = 140\,°C$ and a shear frequency of $\omega_{Rheo}/2\pi = 1\,Hz$. Before and after LAOS, small amplitude ($\gamma_0 = 0.1\,\%$) oscillatory shear frequency sweeps were conducted and are displayed in Figure 5.8a.

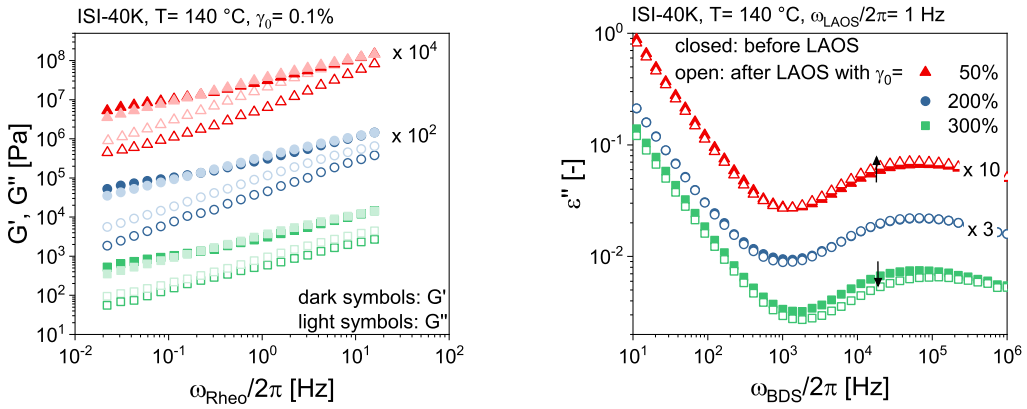

Figure 5.8: **(a)** Small amplitude oscillatory shear frequency sweeps ($\gamma_0 = 0.1\,\%$) before (closed symbols) and after (open symbols) the orientation of ISI-40K with $\gamma_0 = 50\,\%$ (red, perpendicular), 200 % (blue, biaxial) and 300 % (green, parallel) at 140 °C and $\omega_{Rheo} = 1\,Hz$. The dark symbols represent the storage modulus ($G'(\omega_{Rheo})$), whereas the light symbols represent the loss modulus ($G''(\omega_{Rheo})$). **(b)** Loss modulus ($\epsilon''(\omega_{BDS})$) of the dielectric permittivity before (closed symbols) and after (open symbols) orientation of ISI-40K with $\gamma_0 = 50\,\%$ (red, perpendicular), 200 % (blue, biaxial) and 300 % (green, parallel) at 140 °C and $\omega_{Rheo}/2\pi = 1\,Hz$. The curves were shifted vertically for clarity. The final orientation is evidenced by the change in $\epsilon''(t, \omega_{Rheo}/2\pi = 2 \times 10^4\,Hz)$ where an increase indicates a perpendicular and a decrease a parallel orientation, see Figure 5.1. No change is indicated for $\gamma_0 = 200\,\%$ because the effects of the induced parallel and perpendicular structure cancel each other. The behavior of $\tan\delta_{Rheo}$ and $\tan\delta_{BDS}$ is depicted in Figure A.2.10, p. 141. The total change in the dielectric data is rather small due to the parallel plate geometry used and the associated radially dependent shear rate, which results in a sample that is strongly oriented only at the edge. The dielectric data represent the behavior of the entire sample so the overall change is small. Reprinted with permission from[159]. Copyright 2023 American Chemical Society.

After shear alignment, $G'(\omega_{Rheo})$ and $G''(\omega_{Rheo})$ decreased and showed a higher slope, e.g., $G' \propto \omega_{Rheo}^{0.4}$ vs. $G' \propto \omega_{Rheo}^{0.7}$ for $\gamma_0 = 50\,\%$, which was almost independent of the strain amplitude during LAOS, compared to their initial behavior. The storage moduli decreased by a factor of 11 for $\gamma_0 = 50\,\%$, 16 for $\gamma_0 = 200\,\%$ and 8 for $\gamma_0 = 300\,\%$ at $\omega_{Rheo}/2\pi = 0.1\,Hz$ and $T = 140\,°C$, which presumably originates from the now ordered and layered structure. Furthermore, G'' is greater than G' over the whole frequency range. For the unoriented samples, a slope of $G' \propto \omega_{Rheo}^{0.4}$ and $G'' \propto \omega_{Rheo}^{0.6}$ was found. After LAOS, the slopes increased to $G' \propto \omega_{Rheo}^{0.7}$ and $G'' \propto \omega_{Rheo}^{0.8}$ ($\gamma_0 = 50\,\%$), G', $G'' \propto \omega_{Rheo}^{0.8}$ ($\gamma_0 = 200\,\%$)

and G', $G'' \propto \omega_{\mathrm{Rheo}}^{0.6}$ ($\gamma_0 = 300\,\%$) at low frequencies.
In addition to the change in SAOS, the change in $\epsilon''(\omega_{\mathrm{BDS}})$ was investigated, see Figure 5.8b. Figure A.2.10b, p. 141, additionally shows $\tan\delta_{\mathrm{BDS}}$ and clarifies that the changes in $\epsilon''(\omega_{\mathrm{BDS}})$ are due to changes in the polarity of the sample and do not result from changes in the gap because $\tan\delta_{\mathrm{BDS}}$ is independent of the gap. For Figure 5.8b and A.2.10b, it has to be noted that LAOS showed no effect on the Li^+-ion conductivity (electrode polarization) and the segmental relaxation of PS. Instead, clear differences in the normal mode of PI were observed depending on the applied strain amplitude. At $\omega_{\mathrm{BDS}}/2\pi = 2 \times 10^4\,\mathrm{Hz}$ a strain amplitude of $\gamma_0 = 50\,\%$ led to an increase in ϵ'', whereas with a strain amplitude of $\gamma_0 = 300\,\%$ a decrease was observed. Both changes were largest in the vicinity of the PI normal mode at $\omega_{\mathrm{BDS}}/2\pi = 2 \times 10^4\,\mathrm{Hz}$. However, an applied strain amplitude of $\gamma_0 = 200\,\%$ during LAOS did not impose any changes in $\epsilon''(\omega_{\mathrm{BDS}})$. Since the samples were not subjected to any shear at the time of the dielectric measurement, the changes must be due to macroscopic orientation previously induced by LAOS. The final orientation of the samples was determined by SAXS. In Figure 5.9, 2D-SAXS patterns along the normal, radial and tangential plane of the oriented ISI-40K are shown. All SAXS images are recorded at a specimen radius of 10 mm for a geometry with a diameter of 25 mm. The radial position has to be kept constant due to the radial depending shear rate when using parallel geometries.[21] Therefore, ordering or alignment effects are also dependent on the radial position.
The schematic explanation of the change in $\epsilon''(\omega_{\mathrm{BDS}})$ discussed in Scheme 5.1 is confirmed by the final orientations determined by SAXS: An increase in $\epsilon''(\omega_{\mathrm{BDS}})$ after LAOS indicated a perpendicular orientation, whereas a decrease indicated an orientation process towards a parallel orientation.
In addition to the results shown above, further LAOS measurements with different values of strain amplitude γ_0, temperature T and frequency ω_{Rheo} were performed to understand the correlation between the applied parameters and the final orientations. Figure 5.10 summarizes all conducted experiments and displays the resulting orientations in (a) with γ_0 as a function of ω_{Rheo} at a constant $T = 140\,^\circ\mathrm{C}$ and (b) with γ_0 as a function of T at a constant $\omega_{\mathrm{Rheo}}/2\pi = 1\,\mathrm{Hz}$.
With increasing γ_0, a transition from a perpendicular orientation to a parallel via a biaxial orientation was observed. The same transition from perpendicular to parallel orientation is observed with increasing ω_{Rheo} (T, $\gamma_0 = const.$) and decreasing T (ω_{Rheo}, $\gamma_0 = const.$). To observe how the LAOS parameters affect the different preferences in the developing orientations, the alignment process is studied *in-situ* using the unique rheo-dielectric setup (see Figure A.1.1, p. 132) and the orientation kinetics are evaluated.

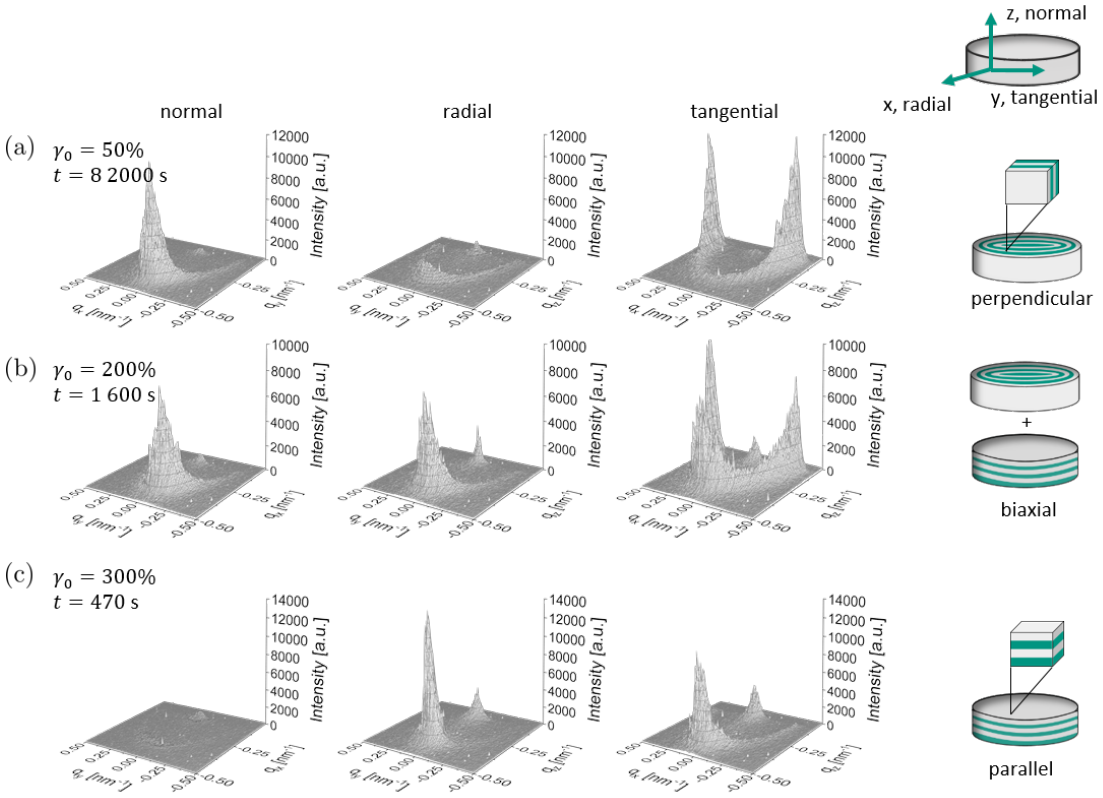

Figure 5.9: 2D-SAXS patterns of ISI-40K along the normal, radial and tangential plane, oriented for an orientation time t at 140 °C with $\omega_{\mathrm{Rheo}}/2\pi = 1$ Hz, a strain amplitude of **(a)** $\gamma_0 = 50\,\%$ ($t = 8200$ s), **(b)** 200 % ($t = 1600$ s) and **(c)** 300 % ($t = 470$ s). In **(a)** a perpendicular, in **(b)** a biaxial and in **(c)** a parallel orientation of the ordered lamellar microdomains is indicated. On the right side, the directions are defined and a schematic picture of the aligned disc and the cuboid taken from it is shown. Adapted with permission from[159]. Copyright 2023 American Chemical Society.

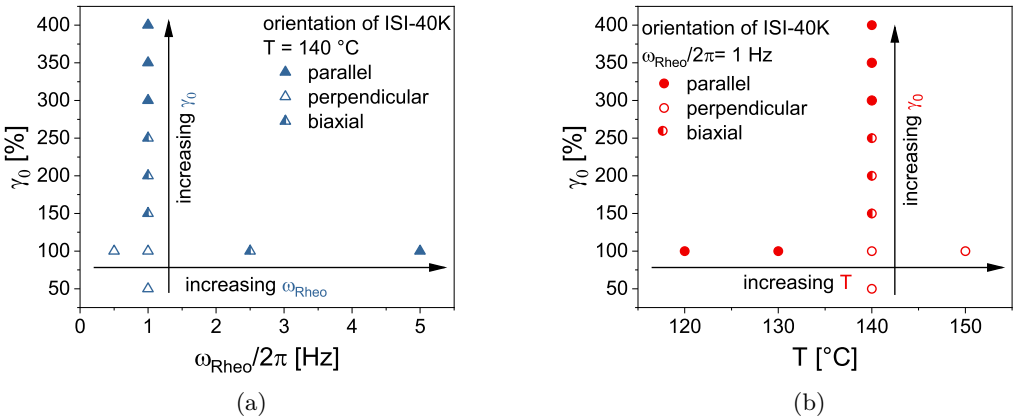

Figure 5.10: Summary of the obtained orientations for ISI-40K (closed: parallel, open: perpendicular, half: biaxial) with **(a)** strain amplitude (γ_0) as a function of the rheological frequency (ω_{Rheo}) and **(b)** strain amplitude (γ_0) as a function of temperature (T). Adapted with permission from[159]. Copyright 2023 American Chemical Society.

In-Situ Investigation of the Alignment of ISI-40K

For the in-situ investigation of the macroscopic alignment of ISI-40K by BDS, the dielectric normal mode of the tethered PI chains as observed in $\epsilon''(\omega_{\mathrm{BDS}})$ at a fixed dielectric frequency ω_{BDS} is monitored to probe the influence of shear-alignment on the dielectric response of the sample. The monitored dielectric frequency corresponded to the frequency with the maximum change after LAOS in Figure 5.8, $\omega_{\mathrm{BDS}}/2\pi = 2 \times 10^4\,\mathrm{Hz}$ at $T = 140\,^{\circ}\mathrm{C}$. It describes the fluctuations of the end-to-end vector during the alignment of the lamellar structure, because PI is a Stockmayer type A polymer (i.e., its electric dipole moment is parallel to the polymer chain).[58,180] Furthermore, the time-dependence of the nonlinear mechanical parameter $I_{3/1}(t)$, obtained as the relative intensity of the third harmonic by FT rheology during LAOS, was investigated.[51,192,193] Figure 5.11a shows the time-dependence of $\epsilon''(t)$ at $\omega_{\mathrm{BDS}}/2\pi = 2 \times 10^4\,\mathrm{Hz}$ and $I_{3/1}(t)$ while the sample is subjected to LAOS with $\gamma_0 = 50\,\%$ and $\omega_{\mathrm{Rheo}}/2\pi = 1\,\mathrm{Hz}$ at $T = 140\,^{\circ}\mathrm{C}$.

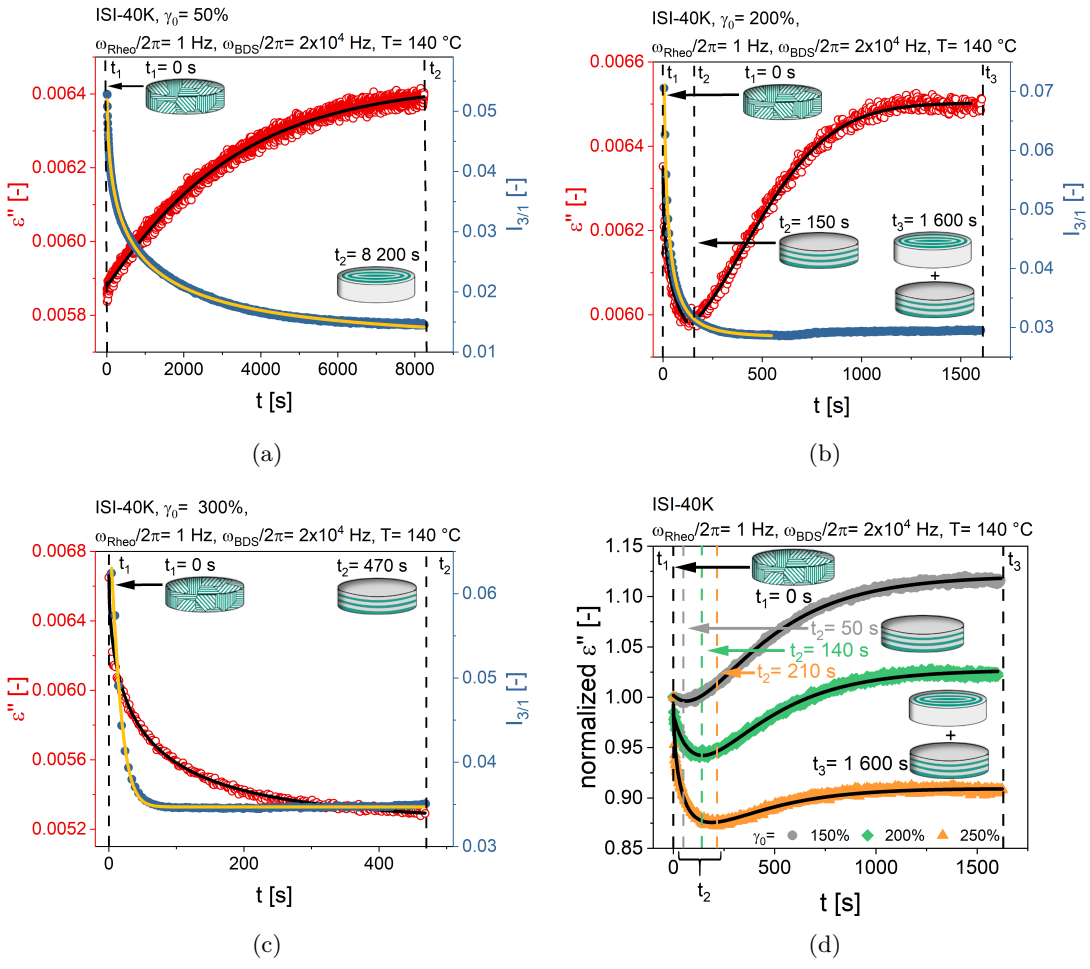

Figure 5.11: Time-dependent dielectric loss ($\epsilon''(t)$, red) and relative intensity of the third harmonic ($I_{3/1}(t)$, blue) including a stretched mono- or bi-exponential fit (solid lines), see Equation 5.2 and 5.5, obtained during the shear alignment of ISI-40K with an applied strain amplitude of **(a)** $\gamma_0 = 50\,\%$, **(b)** 200 %, **(c)** 300 % and **(d)** 150 %, 200 % and 250 % and $\omega_{\mathrm{Rheo}}/2\pi = 1\,\mathrm{Hz}$ at 140 °C. During all measurements $\epsilon''(t)$ was recorded at a fixed dielectric frequency, $\omega_{\mathrm{BDS}}/2\pi = 2 \times 10^4\,\mathrm{Hz}$. Data of additional strain amplitudes are shown in Figure A.2.11, p. 143. Adapted with permission from[159]. Copyright 2023 American Chemical Society.

The dielectric loss modulus $\epsilon''(t,\, \omega_{\mathrm{BDS}}/2\pi = 2 \times 10^4\,\mathrm{Hz})$ increases monotonically resulting in a plateau at $t = 8200\,\mathrm{s}$ and a perpendicular alignment. A decreasing behavior of $\epsilon''(t)$ has been previously described by a stretched exponential function[20,21,72]

$$y\,(t) = y_0 + A_1 e^{-(t/\tau_1)^{\beta_1}} \tag{5.2}$$

where y_0 corresponds to the plateau value at infinite times, A_1 is the decay amplitude, τ_1 is the time constant, and β_1 is the width of the distribution. If $A > 0$, Equation 5.2 describes a decreasing curve, while $A < 0$ results in an increasing one. For the biaxial alignment, a superposition of a decreasing and an increasing stretched exponential function was used, described by the following stretched bi-exponential function.

$$y\,(t) = y_0 + A_1 e^{(t/\tau_1)^{\beta_1}} + A_2 \left(1 - e^{(t/\tau_2)^{\beta_2}}\right) \tag{5.3}$$

$$= y_0 + A_2 + A_1 e^{(t/\tau_1)^{\beta_1}} - A_2 e^{(t/\tau_2)^{\beta_2}} \tag{5.4}$$

$$= z_0 + A_1 e^{(t/\tau_1)^{\beta_1}} - A_2 e^{(t/\tau_2)^{\beta_2}} \tag{5.5}$$

where $z_0 = y_0 + A_2$ and the indices 1 and 2 indicate the first and second process, respectively. The fit parameters for all strain amplitudes are listed in Table 5.2 and 5.3.

Table 5.2: Fit parameters of a stretched exponential function (see Equation 5.2) of $I_{3/1}(t)$ for ISI-40K oriented at different strain amplitudes γ_0, $\omega_{\mathrm{Rheo}}/2\pi = 1\,\mathrm{Hz}$ and $T = 140\,^{\circ}\mathrm{C}$. Reprinted with permission from[159]. Copyright 2023 American Chemical Society.

γ_0 [−]	y_0 [−]	A_1 [−]	τ_1 [s]	β_1 [−]
50	0.001	0.046	612	0.42
100	0.003	0.082	120	0.25
150	0.025	0.124	6	0.30
200	0.028	0.086	11	0.45
250	0.029	0.054	18	0.65
300	0.035	0.034	17	1.20
350	0.029	0.044	9	0.95
400	0.024	0.178	1	0.30

The time evolutions of the macroscopic orientation for $\gamma_0 = 200\,\%$ and $300\,\%$ at $\omega_{\mathrm{Rheo}}/2\pi = 1\,\mathrm{Hz}$ and $T = 140\,^{\circ}\mathrm{C}$ are displayed in Figure 5.11b and c, respectively. For a strain amplitude of $\gamma_0 = 300\,\%$ resulting in a final parallel orientation, a stretched exponential increase in $\epsilon''(t)$ is observed, while the development of the biaxial orientation with $\gamma_0 = 200\,\%$ shows a decrease until 140 s. Further shear leads to an increase of $\epsilon''(t)$ resulting in a plateau at approximately $\epsilon''_{\mathrm{plateau}} = \epsilon''_{t=0}$. In particular the development of $\epsilon''(t)$ for $\gamma_0 = 200\,\%$ emphasizes the importance of *in-situ* techniques to gain insights into the development of the final macroscopic orientation. Using the unique rheo-dielectric setup,[194] it was possible to observe *in-situ* the formation of a parallel orientation at the beginning, which was then superimposed by a perpendicular orientation to reach the biaxial state as seen in Figure 5.11b. These findings were corroborated by *ex-situ* SAXS measurements after quenching the orientation process at the minimum of $\epsilon''(t)$ ($t \approx 140\,\mathrm{s}$) showing an overall

Table 5.3: Fit parameters of a stretched mono- or bi-exponential function (see Equation 5.2 and 5.5) of $\epsilon''(t)$ for ISI-40K oriented at different strain amplitudes γ_0, $\omega_{\mathrm{Rheo}}/2\pi = 1\,\mathrm{Hz}$ and $T = 140\,^{\circ}\mathrm{C}$. Reprinted with permission from[159]. Copyright 2023 American Chemical Society.

γ_0 [%]	y_0 [$\mathrm{S\,cm^{-1}}$]	z_0 [$\mathrm{S\,cm^{-1}}$]	A_1 [$\mathrm{S\,cm^{-1}}$]	τ_1 [s]	β_1 [−]	A_2 [$\mathrm{S\,cm^{-1}}$]	τ_2 [s]	β_2 [−]
50	0.006	–	-5.4×10^{-4}	3232	1.07	–	–	–
100	0.006	–	-7.4×10^{-4}	1386	1	–	–	–
150	–	0.007	1.9×10^{-4}	152	1.14	9.1×10^{-4}	507	1.4
200	–	0.007	4.5×10^{-4}	49	0.67	6.2×10^{-4}	558	1.8
250	–	0.005	0.001	63	0.47	4.7×10^{-4}	49	1.6
300	0.005	–	0.001	51	0.50	–	–	–
350	0.004	–	0.002	79	0.45	–	–	–
400	0.004	–	0.002	100	0.34	–	–	–

parallel orientation, see Figure 5.12.

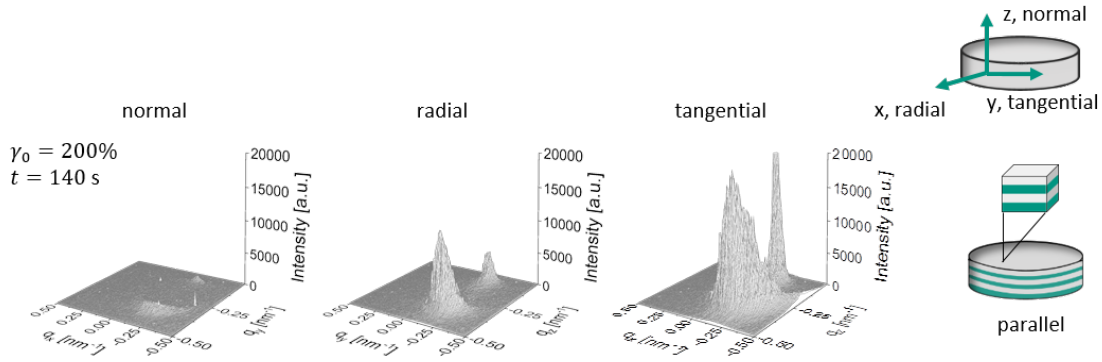

Figure 5.12: 2D-SAXS patterns of ISI-40K along the normal, radial and tangential plane, oriented at 200 %, $\omega_{\mathrm{Rheo}}/2\pi = 1\,\mathrm{Hz}$, $T = 140\,^{\circ}\mathrm{C}$ and an orientation time of $t = 140\,\mathrm{s}$, where a parallel macroscopic orientation is indicated. Adapted with permission from[159]. Copyright 2023 American Chemical Society.

This observation has been made for all samples showing a biaxial orientation (γ_0 = 150 %, 200 % and 250 %), see Figure 5.11d. However, the minimum shifted to longer times and lower ϵ'' with increasing strain amplitude indicating an overall more pronounced parallel orientation in the sample. These findings were confirmed by SAXS measurements in which the sample with $\gamma_0 = 250\,\%$ showed the highest share of parallel lamellae, see Figure A.2.12, p. 144. The development of $\epsilon''(t)$ and $I_{3/1}(t)$ for $\gamma_0 = 100\,\%$, $\gamma_0 = 150\,\%$, γ_0 = 250 %, $\gamma_0 = 350\,\%$ and 400 % is displayed in Figure A.2.11, p. 143.
In addition, the effect of the orientation process on the nonlinear oscillatory shear properties was followed by monitoring the relative intensity of the third harmonic $I_{3/1}(t)$. For all strain amplitudes displayed in Figure 5.11 and A.2.11, a stretched exponential decrease of $I_{3/1}(t)$ until a plateau value was observed while the plateau value was lowest ($I_{3/1\mathrm{final}} \approx$ 0.015) for the lowest strain amplitude of $\gamma_0 = 50\,\%$. In the literature, the evolution of $I_{3/1}(t)$ was shown to be related to the orientation process by *ex-situ* and *in-situ* SAXS measurements.[20,21,72,195] Comparing $\epsilon''(t)$ to $I_{3/1}(t)$, both functions seem to have a similar time-dependence for $\gamma_0 = 50\,\%$ while $I_{3/1}(t)$ reaches the plateau earlier. In contrast to

$\epsilon''(t)$, which already indicates the type of orientation during the alignment process, $I_{3/1}(t)$ does not allow any conclusions to be drawn on the resulting orientation.
Moreover, not only the type of orientation but also the degree of orientation might already be indicated by observing the evolution of $\epsilon''(t)$ and $I_{3/1}(t)$. For this, the degree of orientation is quantified using the azimuthally averaged SAXS data (Figure 3.11, p. 27) where a Gaussian fit,

$$y(x) = \frac{1}{\sigma_G\sqrt{2\pi}} e^{-\frac{1}{2}\left(\frac{x-\mu}{\sigma_G}\right)^2} \tag{5.6}$$

with σ_G as standard deviation and μ expectation value, determined the full width at half maximum (FWHM) as FWHM$= 2\sqrt{2\ln 2}\sigma_G \approx 2.3548\sigma_G$.[196]

The FWHM is then correlated with the change in $\epsilon''(t)$, e.g., $\Delta\epsilon'' = \epsilon''_{(t=0)} - \epsilon''_{\text{final}}$ or in case of two processes $\Delta\epsilon''$ for the second process is calculated as $\Delta\epsilon'' = \epsilon''_{\text{plateau}} - \epsilon''_{\text{final}}$ and the final value of $I_{3/1}(t)$ ($I_{3/1,\text{final}}$), see Figure 5.13. Compared to $\Delta\epsilon''$, $I_{3/1,\text{final}}$ is used instead of $\Delta I_{3/1}$ because $I_{3/1}$ is difficult to determine at $t = 0$. By measuring $I_{3/1}$, an orientation is already introduced so that different amplitudes result in different starting values.

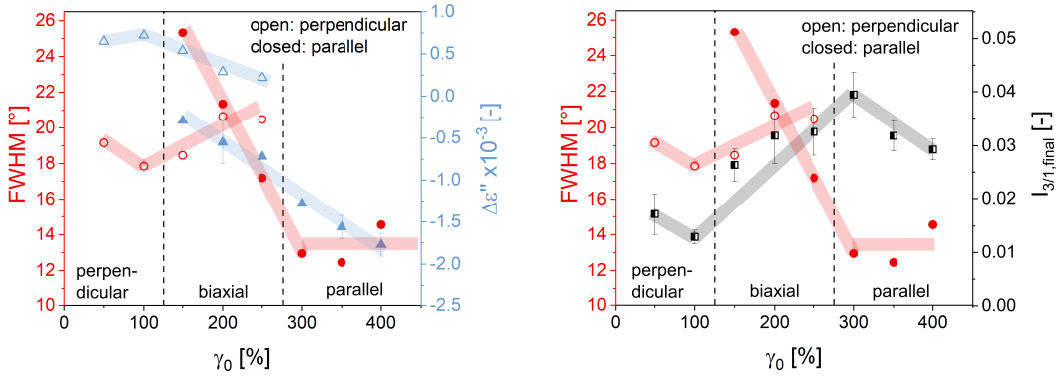

Figure 5.13: Overview of all oriented samples at 140 °C. The left y-axes display the full width at half maximum (FWHM, red circles) of the azimuthally averaged SAXS data as determined by a Gaussian fit (Equation 5.6) whereas the right y-axes display **(a)** the change in $\epsilon''(t)$ (blue triangles) and **(b)** the final value of $I_{3/1}(t)$ (black squares) as a function of the applied strain amplitude. The mean values and error bars for $\Delta\epsilon''$ and $I_{3/1,\text{final}}$ were obtained from three different measurements. The open symbols represent a macroscopic perpendicular orientation, the closed symbols indicate a macroscopic parallel orientation and the half closed symbols represent $I_{3/1,\text{final}}$ which does not allow a conclusion on the resulting orientation. The light colored bars indicate the trend of the different parameters which are discussed in more detail in the text to give a general picture of the orientation process. It should be noted that the orientation time is different for all of samples. Reprinted with permission from[159]. Copyright 2023 American Chemical Society.

Figure 5.13a shows the correlation between the degree of orientation and $\Delta\epsilon''(t)$ after intermediate orientation times. The degree of orientation increases with decreasing FWHM. Furthermore, an increase of $\Delta\epsilon''$ for the perpendicular orientation and a decrease for the parallel orientation would indicate a more ordered structure and a decrease in $I_{3/1,\text{final}}$ would

indicate increasing grain sizes. With increasing strain amplitude, the FWHM indicates an increasing order up to $\gamma_0 = 100\,\%$ for the perpendicular orientation, which is similar to the behavior in $\Delta\epsilon''$. With the onset of the biaxial orientation ($\gamma_0 = 150\,\%$), the FWHM for the parallel orientation starts to drop, indicating a more ordered structure, while the FWHM for the perpendicular orientation increases. Dielectric spectroscopy shows similar behavior: Increase in order in the parallel orientation ($\Delta\epsilon''$ is always negative but increases in magnitude) and a slight decrease in order for the perpendicular orientation ($\Delta\epsilon''$ is always positive but decreases in magnitude). This greatly reflects the process of orientation as a function of strain amplitude used for orientation: At first, the perpendicular structure dominates at small strain amplitudes and becomes more and more pronounced (up to $\gamma_0 = 100\,\%$). Then, the first parallel components appear, but they are still small and not well ordered. With increasing strain amplitude, the parallel components increase in size and order while the perpendicular parts are increasingly distorted ($\mathrm{FWHM}_\perp$ increases, $\mathrm{FWHM}_\parallel$ decreases). At even higher strain amplitudes, only parallel components are induced but with even higher order. The increase in FWHM at $\gamma_0 = 400\,\%$ may be related to edge fracture due to the high strain amplitudes. The picture of the orientation process is confirmed by the behavior of $I_{3/1,\mathrm{final}}$ which decreases until $\gamma_0 = 100\,\%$ and then increases again until the parallel regime is reached, see Figure 5.13b. The increase of the amount of grain boundaries is most likely due to the formation of the biaxial structure where grains break up. The decreasing $I_{3/1,\mathrm{final}}$ from $\gamma_0 = 300\,\%$ onwards shows that the grains subsequently regroup to form larger grains again.

Alignment Kinetics

The kinetic of the alignment process can be evaluated using the mean orientation time τ and the stretched exponential exponent β as obtained by a fit (see Equation 5.2 and 5.5) and already described for diblock copolymers.[20,72,197] The fit parameters for all strain amplitudes using a stretched mono- or bi-exponential function, depending on the number of orientations observed, are displayed in Table 5.2 and 5.3 while Figure 5.14 illustrates the mean orientation times as a function of strain amplitude γ_0. The mean orientation times and the related standard deviations are obtained from three different measurements; each of them performed using a new specimen.

In Figure 5.14 three distinct areas are identified corresponding to the following orientations: (1) perpendicular ($0\,\% \lesssim \gamma_{0,\mathrm{per.}} \lesssim 125\,\%$), (2) biaxial ($125\,\% \lesssim \gamma_{0,\mathrm{bia.}} \lesssim 175\,\%$) and (3) parallel ($275\,\% \lesssim \gamma_{0,\mathrm{para.}} \lesssim 450\,\%$). In regime (1), an increase in γ_0 results in a shorter orientation time, meaning that the plateau value is reached faster. In the perpendicular regime, $\tau_{\epsilon''}$ and $\tau_{I_{3/1}}$ decrease with increasing γ_0 and $\tau_{\epsilon''}$ was found to be 4.6x faster. As soon as the biaxial regime is reached, two different $\tau_{\epsilon''}$ are obtained from the increase and decrease of $\epsilon''(t)$ and therefore for the development of the perpendicular and parallel orientation, respectively. Furthermore, at first approximation, both τ appear to be independent of the strain amplitude. This behavior remains until the parallel regime, where only a slight decrease of $\tau_{I_{3/1}}$ is observed. Overall, $\tau_{I_{3/1}} < \tau_{\epsilon''}$ is observed for all strain amplitudes (e.g., $\tau_{I_{3/1}} = 580\,\mathrm{s}$ vs. $\tau_{I_{3/1}} = 2700\,\mathrm{s}$ for $\gamma_0 = 50\,\%$) most likely since both methods measure

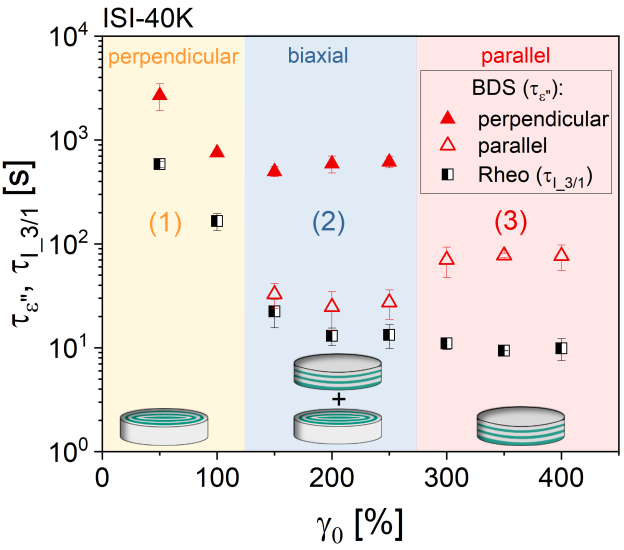

Figure 5.14: Mean orientation times obtained from a stretched mono- or bi-exponential fit, see Equation 5.2 and 5.5, of the *in-situ* measurement of the relative third harmonic ($I_{3/1}(t)$) and the dielectric loss modulus ($\epsilon''(t)$) with $\omega_{\mathrm{BDS}}/2\pi = 2 \times 10^4$ Hz, $\omega_{\mathrm{Rheo}}/2\pi = 1$ Hz at 140 °C as a function of the applied strain amplitude for ISI-40K. The mean values and error bars were calculated from three different measurements. Reprinted with permission from[159]. Copyright 2023 American Chemical Society.

different material properties attributed to different length scales. The stretching exponent β reflects a very broad distribution and decreases within the perpendicular and parallel regime, whereas it increases in the biaxial regime for $I_{3/1}$ ($\beta = 0.3$ for $\gamma_0 = 150\,\%$ to $\beta = 0.65$ for $\gamma_0 = 250\,\%$), see Table 5.2. In contrast to that, it decreases within each regime for $\epsilon''(t)$, see Table 5.3. In case of the biaxial regime, β is bigger than one for the second process (reorientation). A stretching exponent of $\beta < 1$ indicates a broadening which is often observed in disordered systems because of, e.g., a broad grain size distribution. The decrease of β with increasing strain amplitude for the perpendicular and parallel regime indicates a more heterogeneous grain size distribution with increasing strain amplitude.

Stability of the Observed Macroscopic Orientations Upon Prolonged Shear

The stability of the observed macroscopic orientations in ISI-40K upon prolonged shear was then investigated by subjecting the samples to further shear ($t > 10^4$ s) after the plateau observed in Figure 5.11 and A.2.11 was reached. For all samples with $\gamma_0 > 150\,\%$ the onset of a reorientation process that yielded a final biaxial ($\gamma_0 = 100\,\%$) or parallel ($\gamma_0 = 150\,\%$, 200 % or 250 %) macroscopic orientation after reaching the initial perpendicular (100 %) or biaxial state ($\gamma_0 = 150\,\%$, 200 % or 250 %) was found, see Figure 5.15 and A.2.13, p. 145. All samples except $\gamma_0 = 50\,\%$, display a substantial decrease of max. 74 % in $\epsilon''(t)$ over several hours (e.g., ca. 22 h for $\gamma_0 = 200\,\%$ and $\gamma_0 = 250\,\%$ (Figure A.2.13)) until a final biaxial ($\gamma_0 = 100\,\%$) or parallel state ($\gamma_0 = 150\,\%$ (Figure A.2.13), 200 % or 250 % (Figure A.2.13)) is reached. It should be noted, that this slow reorientation process, taking place over several hours, can be observed with both parameters. In all the experiments performed, this is the only reorientation process that is also clearly observed in $I_{3/1}(t)$. Hence, it might

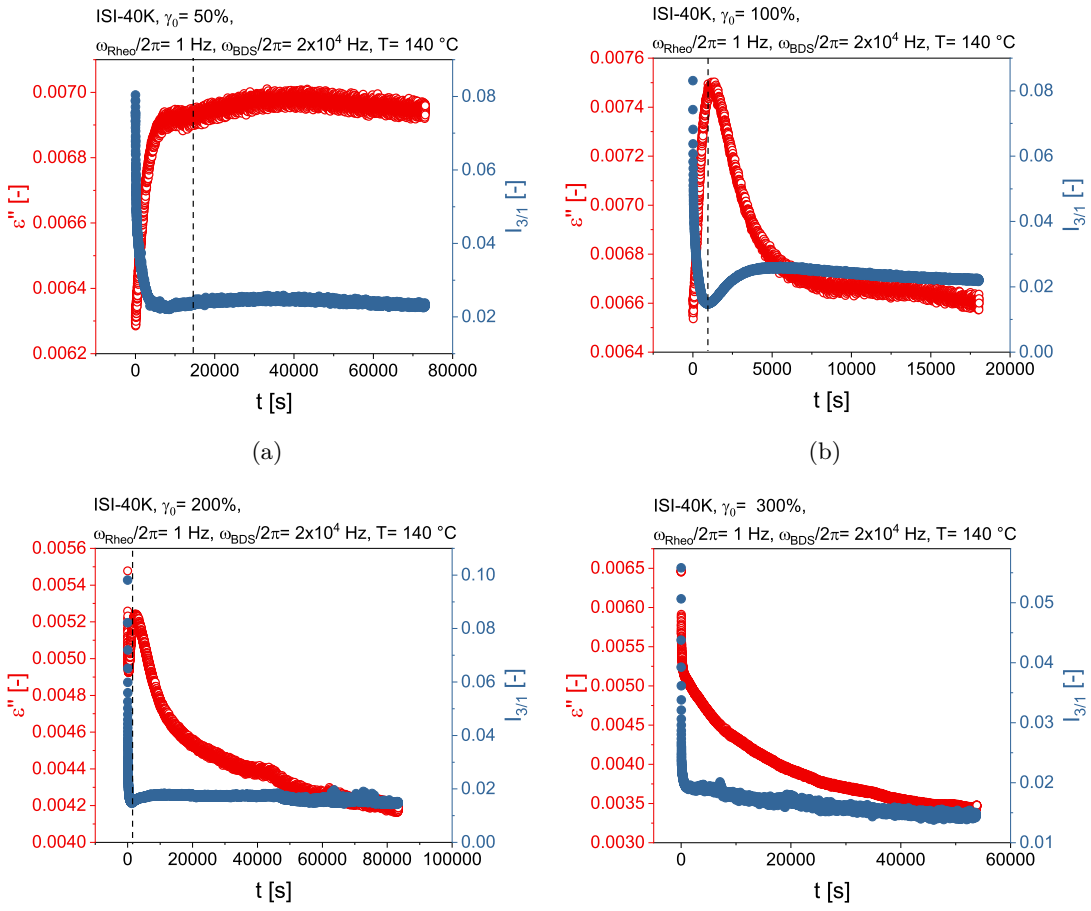

Figure 5.15: Long-term (up to 24 h) *in-situ* rheo-dielectric measurements of the time-dependent dielectric loss ($\epsilon''(t)$, red) and relative intensity of the third harmonic ($I_{3/1}(t)$, blue) with a strain amplitude of **(a)** $\gamma_0 = 50\,\%$, **(b)** $100\,\%$, **(c)** $200\,\%$ and **(d)** $300\,\%$. For all samples, except $\gamma_0 = 50\,\%$ and $300\,\%$, a reorientation process accompanied by a substantial decrease of $\epsilon''(t)$ is observed. During all measurements $\epsilon''(t)$ was recorded at a fixed dielectric frequency, $\omega_{\mathrm{BDS}}/2\pi = 2 \times 10^4\,\mathrm{Hz}$. Data of the additional strain amplitudes are shown in Figure A.2.13, p. 145. Adapted with permission from[159]. Copyright 2023 American Chemical Society.

be visible due to a bigger change in orientation (compare the more pronounced change in $\epsilon''(t)$). Again, the SAXS patterns confirm the macroscopic orientation predicted by $\epsilon''(t)$ and, while a biaxial state is found for $\gamma_0 = 100\,\%$, all other strain amplitudes yield a macroscopic parallel orientation, see Figure A.2.14 and A.2.15, p. 147.
As before, the slow reorientation process can be described by a stretched exponential function. However, the recorded data does not show a clean decay, but instead exhibits noise that increases with time and continues to increase with γ_0. This is assumed to result from experimental artifacts such as edge fracture or sample loss, especially at higher γ_0. In summary, only the macroscopic orientation of a sample under $\gamma_0 = 50\,\%$ has proven to be stable upon prolonged oscillatory shear while all other samples showed a slow reorientation process over several hours resulting in different macroscopic orientations (biaxial, parallel).

5.3 Shear Alignment of SIIS-40K

SIIS-40K was synthesized to investigate the influence of the sequence of the blocks, and thus the mobility, on the orientation and its mechanism. Unfortunately, it is not possible to detect any end-to-end vector fluctuations in SIS, since both ends are tethered to the more rigid PS phase, which impedes their movement. Using dipole-inverted SIIS circumvents this issue and allows for dielectric investigations.[181,182,198] The dielectric spectrum of SIIS-40K is displayed in Figure 5.16. The process at lower frequencies is attributed to interfacial processes (undulations, vibrations).[191] In ISI-40K this process is superimposed by electrode polarization effects and ions accumulating at the electrodes. Since SIIS-40K was fractionated several times, ionic impurities were reduced, thus allowing insights into interfacial processes.

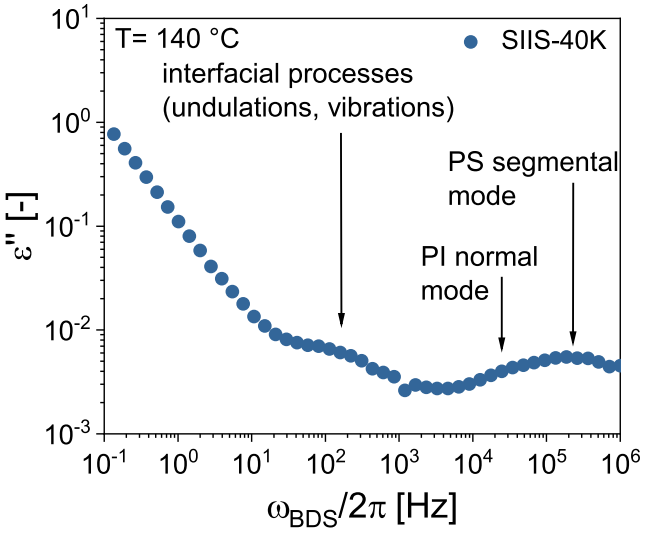

Figure 5.16: Dielectric loss ($\epsilon''(\omega_{BDS})$) of SIIS-40K at 140 °C. Due to the dipole inversion in SIIS-40K, the PI normal mode becomes accessible. Reprinted with permission from[159]. Copyright 2023 American Chemical Society.

The mobility of PI and therefore the fluctuations of its end-to-end vectors are crucial for the detection of local polymer dynamics via BDS during the orientation process. However, the behavior of $\epsilon''(t)$ could not be used as an indication for the final orientation of the sample in case of SIIS. Figure 5.17a and 5.18a display the change in polarization in the case of a perpendicular and parallel orientation for ISI 40K, respectively. Depending on the final orientation, $\epsilon''(t)$ is either increasing (perpendicular) or decreasing (parallel), see Figure 5.1, p. 70. The measurements of SIIS-40K show that the type of orientation is not clearly detectable by BDS for this sample. This can be qualitatively understood by the mobility of the PI chains as schematically depicted in Figure 5.17b and 5.17c for a perpendicular orientation and Figure 5.18b and 5.18c for a parallel orientation.

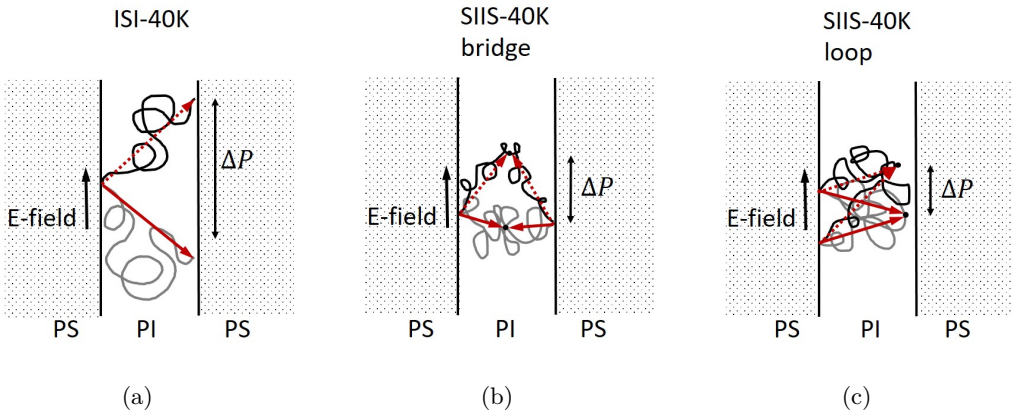

Figure 5.17: Comparison of the change in polarization of **(a)** ISI and **(b)** SIIS in a bridge and **(c)** loop conformation in a perpendicular alignment. The gray chains and red arrows depict the PI chains before the application of an E-field. The black polymer chains indicate the motion of the chains when an E-field is applied, while the dotted arrows indicate the corresponding dipole moments. The change in polarization is limited in the case of SIIS because it is associated to a stretching or compression of the chains, which are additionally tethered to the stiffer PS phase. Reprinted with permission from[159]. Copyright 2023 American Chemical Society.

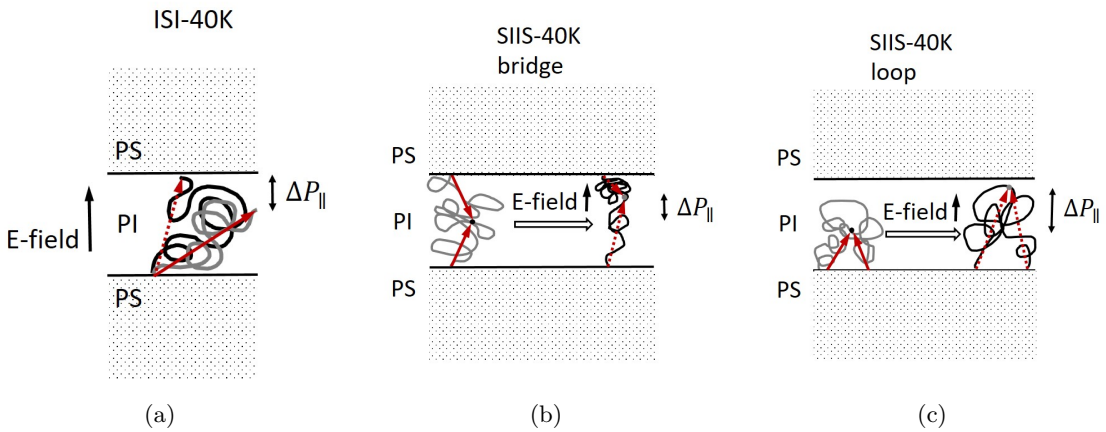

Figure 5.18: Comparison of the change in polarization of **(a)** ISI and **(b)** SIIS in a bridge and **(c)** loop conformation in a parallel alignment. The gray chains and red arrows depict the PI chains before the application of an E-field. The black polymer chains indicate the motion of the chains when an E-field is applied, while the dotted arrows indicate the corresponding dipole moments. Reprinted with permission from[159]. Copyright 2023 American Chemical Society.

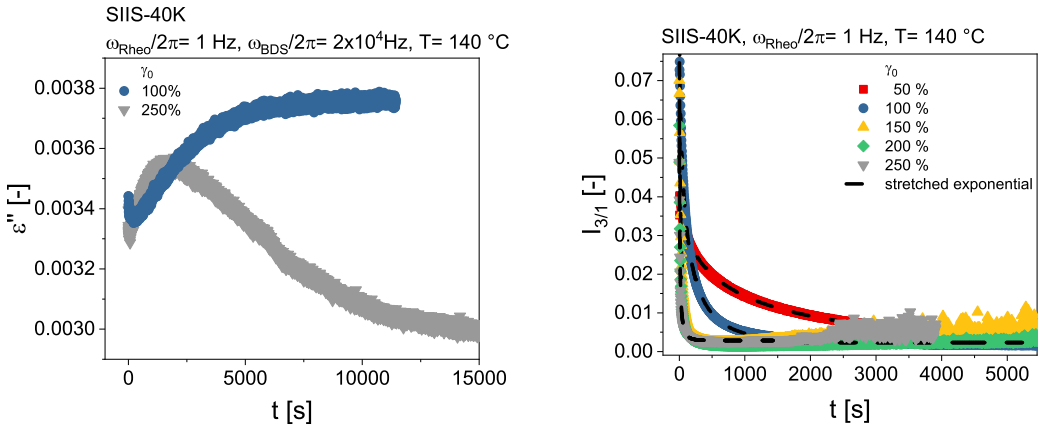

Figure 5.19: Time-dependence of **(a)** the dielectric loss modulus ($\epsilon''(t)$) at $\omega_{\mathrm{BDS}}/2\pi = 2 \times 10^4$ Hz with a strain amplitude of $\gamma_0 = 100\,\%$ and $250\,\%$ at $\omega_{\mathrm{Rheo}}/2\pi = 1$ Hz and $T = 140\,^{\circ}$C. In comparison to ISI-40K, the course of $\epsilon''(t)$ does not allow a conclusion on the final orientation and SAXS measurements reveal a perpendicular orientation for both courses. **(b)** Time-dependence of the relative intensity of the third harmonic ($I_{3/1}(t)$) of SIIS-40K with a strain amplitude of $\gamma_0 = 50-250\,\%$ at $\omega_{\mathrm{Rheo}}/2\pi = 1$ Hz and $T = 140\,^{\circ}$C including a stretched exponential fit. Reprinted with permission from[159]. Copyright 2023 American Chemical Society.

While a change in polarization is possible without a conformational change for ISI, a change in polarization is associated with chain stretching or compression in the case of SIIS, where the PI chains are additionally tethered to the stiffer PS phase at both ends. Due to these additional constraints, the change in polarization is smaller compared to ISI and the BDS measurements cannot predict the type of orientation. This is also shown in Figure 5.19a where the course of $\epsilon''(t)$ indicates two different alignments for $\gamma_0 = 100\,\%$ and $250\,\%$. However, SAXS measurements reveal that after both orientation experiments, a perpendicular orientation is obtained and thus $\epsilon''(t)$ does not predict the final orientation. To overcome this limitation in BDS, the orientation process was investigated using $I_{3/1}(t)$, see Figure 5.19b and A.2.16, p. 148, and the macroscopic orientations of the samples were obtained via SAXS measurements, see Figure A.2.17, p. 149, and A.2.18, p. 150.
In contrast to ISI-40K, all applied strain amplitudes γ_0 led to the same orientation, a perpendicular one, and also further shear (e.g., 5×10^4 s with $\gamma_0 = 100\,\%$) did not result in a further reorientation. As shown in Figure 5.5, the mechanical moduli of ISI-40K and SIIS-40K differ, with the latter having a higher shear storage modulus G' by more than a factor of ten at $\omega_{\mathrm{Rheo}}/2\pi = 1$ Hz, most probably due to its stiffer end blocks. The sequence of the BCPs not only influences the shear moduli in SAOS but also plays a crucial role in the development and kinetics of the macroscopic orientations. The maximum possible strain amplitude for SIIS-40K, before edge fracture and sample loss happened, was $\gamma_0 = 250\,\%$ and thus significantly lower than the one for ISI-40K. The orientation times and parameters of SIIS-40K and ISI-40K, obtained by fitting $I_{3/1}(t)$ with a stretched exponential function, are both similar, although, they develop different orientations, see Table 5.4. However, once the biaxial orientation develops in ISI-40K, the orientation times increase slightly.

Table 5.4: Comparison of the fit parameters of a stretched mono-exponential fit (see Equation 5.2, Table 5.11 (p. 79) and A.2.11 (p. 143) for ISI-40K and Figure 5.19 (p. 88) for SIIS-40K) for $I_{3/1}(t)$ and macroscopic orientation of ISI-40K and SIIS-40K for $\gamma_0 = 50\,\%$ to $250\,\%$. Reprinted with permission from[159]. Copyright 2023 American Chemical Society.

Sample	γ_0 [%]	y_0 [−]	A_1 [−]	τ_1 [s]	β_1 [−]	Orientation	Orientation Time [s]
ISI-40K	50	0.001	0.046	612	0.42	Perpendicular	8 200
	100	0.003	0.082	210	0.25	Perpendicular	3 100
	150	0.025	0.124	6	0.30	Biaxial	1 600
	200	0.028	0.086	11	0.45	Biaxial	1 600
	250	0.029	0.054	18	0.65	Biaxial	1 600
SIIS-40K	50	0.001	0.042	735	0.52	Perpendicular	16 000
	100	0.002	0.093	88	0.53	Perpendicular	6 000
	150	0.003	0.095	18	0.59	Perpendicular	6 000
	200	0.002	0.097	7	0.50	Perpendicular	6 000
	250	0.003	0.097	4	0.40	Perpendicular	1 300

5.4 Discussion

The results presented here suggest that the orientation process of ISI-40K can be followed by observing $\epsilon''(\omega_{\mathrm{BDS}}/2\pi = 2 \times 10^4\,\mathrm{Hz}, t)$ and $I_{3/1}(\omega_{\mathrm{Rheo}}/2\pi = 1\,\mathrm{Hz}, t)$ using the unique rheo-dielectric setup at $T_{\mathrm{g,PS}}$, $T_{\mathrm{g,PI}} < T < T_{\mathrm{ODT}}$. The time progression of $\epsilon''(t)$ already shows the type of the final orientation: a monotonically increasing $\epsilon''(\omega_{\mathrm{BDS}}/2\pi = const., t)$ led to an overall perpendicular alignment, whereas a monotonic decrease yielded a final parallel alignment as already schematically explained in Figure 5.1, p. 70, and, in addition, confirmed by SAXS measurements. The emergence of a biaxial orientation, where a parallel and perpendicular orientation coexist, was also observed by a decrease of $\epsilon''(t)$ at the beginning followed by a minimum and increase until a plateau value was reached. The difference in $\epsilon''(t)$ for the parallel and perpendicular alignment, i.e., $\Delta\epsilon''_{t=0} - \epsilon''_{\mathrm{final}}$, was found to correspond to the fractions of parallel and perpendicular orientation in the samples meaning an decreasing $\Delta\epsilon''$ for the parallel orientation resulted in greater shares of parallel-oriented lamellae. However, only one of the developed orientations of ISI-40K (perpendicular with $\gamma_0 = 50\,\%$) proved to be stable while it was exposed to prolonged shear. All other samples with a perpendicular or biaxial orientation showed a slow reorientation process to either a final biaxial ($\gamma_0 = 100\,\%$) or parallel orientation ($\gamma_0 = 150\,\%$, $200\,\%$ and $250\,\%$).

It was shown that the time evolution of $\epsilon''(t)$ results from anisotropic changes in the polarity of the sample depending on the developed orientation as the movement of the PI chains in direction of the applied E-field is restricted for parallel aligned samples because of the neighboring PS domains, see Figure 5.1, p. 70. As there is no restriction parallel to the applied E-field in the perpendicular aligned samples, a bigger change in the polarity is possible resulting in an increase in $\epsilon''(t)$.

Compared to $\epsilon''(t)$, the interpretation of $I_{3/1}(t)$ is more elusive. It is assumed that $I_{3/1}$ describes the deformation of the grain interface, because both neat polymers do not show

any detectable nonlinearities under the same conditions.[20,72,195,197] Furthermore, $I_{3/1}$ is assumed to be proportional to the number of defects (i.e., here total grain interfaces).[21,72] Meins *et al.* directly correlated $I_{3/1}(t)$ and $\epsilon''(t)$, where the latter was also sensitive to the actual orientation of the microdomains. The authors also observed a relative increase in $I_{3/1}(t)$ (ca. $17\,\% - 33\,\%$ increase, depending on the measurement conditions) caused by a reorientation process from a perpendicular to a biaxial orientation. Here, only a similar change in $I_{3/1}(t)$ upon the reorientation process to a biaxial orientation was observed (e.g., $1.9\,\%$ and $4.5\,\%$ change for $\gamma_0 = 200\,\%$ and $250\,\%$, respectively).

The detailed comparison of SAXS (FWHM), nonlinear rheology ($I_{3/1,\mathrm{final}}$) and dielectric spectroscopy ($\Delta\epsilon''$) allows a more detailed picture of the reorientation process with increasing γ_0: First, single grains are oriented (perpendicular orientation), then grains of parallel and perpendicular orientation are formed breaking up larger grains (biaxial orientation), and in the final step these grains regroup resulting in a parallel orientation. Long-term measurements ($t > 10^4$ s) reveal that a significant increase in $I_{3/1}(t)$ of $20\,\%$ after the minimum is connected to a reorientation process from the biaxial orientation resulting in a final parallel orientation for $\gamma_0 = 150\,\% - 250\,\%$. The further decrease in $I_{3/1}(t)$ might result from more and more grains grouping together, so that the average grain size increases, and this second slow process can be compared to the one observed for SI diblock copolymers.[20] For all strain amplitudes, except $\gamma_0 = 50\,\%$ and $100\,\%$, only the parallel orientation seemed to be stable while the mechanical excitation is continued. Furthermore, the samples already developing a parallel orientation at short time scales (e.g., $\gamma_0 = 300\,\%$) showed an even further decrease of $\epsilon''(t)$ and a clear change in the exponential decay. This shoulder could indicate the formation of a very small portion of a biaxial structure, which then reorients into a parallel structure. This reflects the results of all orientation processes performed at different conditions (Figure 5.13): At higher strain amplitudes γ_0, the parallel orientation is preferred, which is consistent with the observed behavior of the biaxial states, which were found to be metastable only. The results lead to the assumption that the development of the different orientations is strongly related to the block order and thus the dynamics of the individual blocks. Table 5.5 displays the development of the different orientations in ISI-40K during the orientation process and the corresponding strain amplitudes.

It is striking that the same transition from a perpendicular to a biaxial to a parallel macroscopic orientation is observed (on an intermediate time scale, i.e., before the slow reorientation process) with increasing frequency and decreasing temperature (see Figure 5.10, p. 78). If these parameters (γ_0, ω_{Rheo}, T) are changed as mentioned, the polymer chains will experience more local stress, either by increased mechanical stress due to increased ω_{Rheo} or γ_0 or by reduced mobility due to decreased T. Therefore, it is suggested that the change in orientation results from avoiding increased stress by allowing for better stress dissipation. The same transition from perpendicular to biaxial is found for diblock copolymers indicating the same stress accommodation mechanism.[20,197] Furthermore, longer mean orientation times, calculated by the stretched exponential fit, were obtained for the diblock copolymer SI-13K-13K compared to ISI-40K and SIIS-40K (e.g., $\tau = 612\,\mathrm{s}$

Table 5.5: Strain amplitude and different orientations developing during the orientation process with $\omega_{Rheo}/2\pi = 1\,Hz$ and at $T = 140\,°C$. The final macroscopic orientations which showed to be stable upon prolonged shear are shown in italics. Adapted with permission from[159]. Copyright 2023 American Chemical Society.

Strain Amplitude [%]	Orientations for ISI-40K	Orientations for SIIS-40K	Orientations for SI-13K-13K[b]
50	*Perpendicular*	*Perpendicular*	*Perpendicular* ($t = 10\,000\,s$)
100	Perpendicular → *Biaxial*	*Perpendicular*	*Perpendicular* ($t = 3500\,s$)
150, 200, 250	Perpendicular → Biaxial → *Parallel*	*Perpendicular*	Perpendicular → *Biaxial* ($\gamma_0 = 200\,\%$, $t = 7500\,s$)
300, 350, 400	*Parallel*	–[a]	Perpendicular → *Biaxial* ($\gamma_0 = 300\,\%$, $t = 7500\,s$)

[a]Cannot be measured due to sample failure. [b]Taken from Meins, the orientation experiments were conducted at $T = 150\,°C$.[20,197]

for ISI-40K and $\tau = 735\,s$ for SIIS-40K vs. $\tau = 2100\,s$ for SI 13K-13K with $\gamma_0 = 50\,\%$ and $\omega_{Rheo}/2\pi = 1\,Hz$ at $T = 140\,°C$ for the triblocks and $T = 150\,°C$ for the diblock, respectively).[197] In general, the chains in lamellae forming triblock copolymers either have a loop or bridge conformation. In a loop conformation both end blocks are in the same phase, while in a bridge conformation the end blocks are located in different phases, as shown in Figure 5.20.

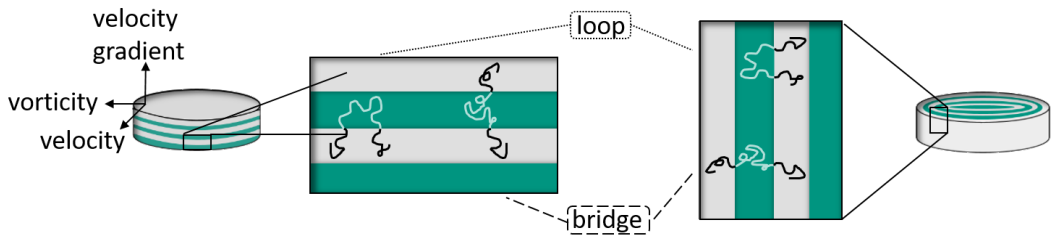

Figure 5.20: Illustration of the possible chain conformations (loop and bridge) in a triblock copolymer including their configuration in a macroscopic parallel or perpendicular orientation. Reprinted with permission from[159]. Copyright 2023 American Chemical Society.

Generally, a looping conformation is slightly favored over a bridged one with $\Phi_{loop} = 0.6$ and is also dependent on P_n.[181,199] It is assumed that the parallel orientation is favored at long t and high γ_0 (and low T and high ω_{Rheo}) because the parallel layers allow for sliding of the mobile PI layers at 140 °C (approx. 210 °C above the T_g of PI, 50 °C above the T_g of PS) and therefore for a better stress dissipation in the sample. Furthermore, during the orientation process, a bridge-to-loop transition can take place.[177,200] This would increase the share of loops even more, allowing for an improved layer sliding if loops are not entangled.[200] At low γ_0 (and high T and low ω_{Rheo}) lower stress arises. To dissipate this stress, the chains can stretch along the vorticity direction, resulting in a perpendicular orientation, see Figure 5.20.[201] Above a certain stress, the alignment along the vorticity direction becomes unfavorable. Then, a parallel structure is developed to account for

an improved stress accommodation by sliding of the layers. This may also explain the transition from a perpendicular to a parallel via a biaxial orientation, where with increasing strain amplitude a higher share of parallel lamellae is developed. At long orientation times, the bridge-to-loop transition may then cause the preference for the parallel orientation. This could explain the slow nature of the reorientation process because PI end blocks have to diffuse through the PS phase. The low molecular weight and the resulting intermediate segregation of the here investigated samples make this process more probable. At high strain amplitudes, a parallel orientation is directly favored. In summary, it is suggested that two processes, the alignment along the vorticity and the formation of sliding layers, can explain the behavior of ISI-40K, see Figure 5.20. Depending on the stress experienced and the ratio of loops and bridges in the sample, one of the two competing processes is favored and the final structure develops.
In contrast to the orientations observed for ISI-40K, different orientations were obtained for SIIS 40K under the same measurement conditions. For all applied strain amplitudes ($\gamma_0 = 50\,\%$ to $250\,\%$), a perpendicular orientation was observed and prolonged shear (e.g., for $\gamma_0 = 100\,\%$) showed it to be stable. Despite having the same molecular weight, the block sequence plays a crucial role in the rheological properties and orientation behavior of the investigated triblock copolymers and seems to change the way stress is dissipated in the sample. It is suspected that the perpendicular orientation is preferred for SIIS-40K compared to ISI-40K because of a restricted layer sliding in SIIS-40K. The PI is in the middle block in SIIS-40K and therefore tethered to PS on both sides. Consequently, its motion is significantly restricted, making layer sliding unfavorable. Wu *et al.* showed that a similar SIS ($43\,000\,\mathrm{g\,mol^{-1}}$, $f_{\mathrm{PS}} = 51\,\%$) showed a transition from a macroscopic perpendicular to parallel orientation at $\omega_{\mathrm{Rheo}}/2\pi = 6.28\,\mathrm{Hz}$, $\gamma_0 = 500\,\%$ and $180\,^{\circ}\mathrm{C}$.[163] Therefore, compared to the obtained results, it is assumed that the polymer interfaces or grain boundaries are not sufficiently mobile at $140\,^{\circ}\mathrm{C}$ to result in a parallel structure at the applied parameters.

5.5 Summary

In this Chapter, the impact of the block order in PS and PI triblock copolymers (ISI vs. SIIS) on the molecular conformation (bridges vs. loops) and the macroscopic orientation (perpendicular vs. parallel) under LAOS alignment was investigated *in-situ*. To engineer material properties, the controlled tuning of molecular confirmation and macroscopic orientation is of high importance. Therefore, coupled rheology and broadband dielectric spectroscopy combined with morphological *ex-situ* assessment via SAXS were used to cover the processes from the molecular length scale to the macroscopic level. While SAXS reveals the macroscopic orientation, changes in the mechanical nonlinearity relate to changes of the number of defects (i.e., grain interfaces) quantified via FT rheology with the $I_{3/1}(t)$ parameter and BDS detects the fluctuations of the end-to-end vector of 1,4-*cis*-PI, offering insights into polymer dynamics. Due to anisotropic polarization of the PI chains in the aligned samples, changes in $\epsilon''(t)$ predicted the final macroscopic orientation of ISI-40K, which was confirmed by *ex-situ* SAXS measurements.

For ISI-40K, a perpendicular, a biaxial or a parallel orientation can be tuned via the strain amplitude γ_0, oscillatory shear frequency ω_{Rheo} and temperature T. At low mechanical impact (low γ_0, low ω_{Rheo} and high T) the perpendicular orientation is favored due to chain stretching along the vorticity. At higher mechanical impact, i.e., $\gamma_0 > 100\,\%$, a transition from a perpendicular via a biaxial to a parallel orientation was obtained at prolonged shear over several hours, indicating bridge-to-loop transitions. The impact of the block sequence was investigated by the shear alignment of SIIS-40K, which resulted in perpendicular-oriented samples for strain amplitudes from $\gamma_0 > 50\,\%$ at $\omega_{\mathrm{Rheo}}/2\pi = 1\,\mathrm{Hz}$ and $T = 140\,^{\circ}\mathrm{C}$. This difference to ISI-40K is caused by the stiffer end blocks (ΔT_{g}(PI vs. PS) = 180 °C) and tethered PI-chains, so that the layer sliding mechanism might only take over at higher strain amplitudes or temperatures. These results demonstrate that the *in-situ* observation of the alignment mechanism of triblock copolymers leads to a better understanding of their dynamics and the molecular origin of macroscopic properties and highlights their differences compared to diblock copolymers. In addition, the findings for these model systems and the effect of block order serve as an approach for the orientation of ion-conductive BCPs that can be applied in energy storage systems.

6 Orientation of Ion-Conductive Block Copolymers

After studying the charge transport in ionic liquids and their polymers in Chapter 4 and the orientation of polystyrene and polyisoprene triblock copolymers in Chapter 5, the two topics are now combined in the following Chapter, which deals with the orientation of ion-conductive BCPs. Ions are introduced either by incorporating an IL into an uncharged block copolymer or by introducing charges into one of the polymer blocks. The samples are then oriented using LAOS and the macroscopic orientation of the samples is correlated with the change in their ionic conductivity.

The characteristics and properties of ILs and their polymers, as well as those of BCPs, have already been introduced in Chapters 4, p. 33, and 5, p. 67. The combination of these materials into ion-conductive BCPs combines their unique properties resulting in highly tunable, ion-conductive materials. One possible combination is the incorporation of an IL into one phase of a BCP, e.g., incorporation of imidazolium bis(trifluoromethane sulfonamide) into the poly(2-vinylpyridine) (P2VP) phase of poly(styrene-*b*-2-vinylpyridine)(PS-*b*-P2VP), resulting in an ion-conductive material whose mechanical stability is maintained by the rigid PS phase.[202] Another possibility is to make one of the blocks ion-conductive, for example, by post-functionalization of a BCP. In this way, anionic or controlled radical polymerization can be used before post-functionalization to obtain easily tunable, monodisperse and defined polymers, whereas the methods used in Chapter 4 (free radical and photopolymerization) lead to rather undefined samples with a higher Đ.
Especially in the field of LIBs, the great benefit of ion-conductive BCPs is already known, as the growth of lithium dendrites can be prevented by the rigid, non-conducting part of the BCP.[153] While the ionic conductivity can be tuned by the amount and nature of the (Poly)IL, the mechanical properties can be optimized separately and the structure is created by the self-assembly of the BCP.[203,204] To further improve ion diffusion in ion-conductive BCPs, the self-assembled structures can be macroscopically aligned, as previously shown in Chapter 5 for the mechanical alignment of PS-*b*-PI BCP model systems. The macroscopic alignment reduces defects and tortuosity in the sample and in case of a perpendicular alignment improves the transport pathways for ion conduction along the BCP domains, see Figure 6.1a. In contrast, the ionic conductivity should decrease in the case of parallel

alignment, since the parallel non-conductive layers act as insulators (see Figure 6.1b) and the ions can diffuse to the electrodes only through defects.

(a) (b)

Figure 6.1: Schematic representation of ion conduction in an **(a)** perpendicular and **(b)** parallel orientation on the example of Li^+. The ionic conductivity should increase with a perpendicular orientation and decrease with a parallel orientation because the direct path to the electrode is blocked by the non-conducting layers.

Other methods of inducing macroscopic alignment include electric or magnetic fields which also induce a long-range order in the sample.[11] Majewksi *et al.* oriented a lamellar diblock copolymer with Li^+-doped polyethylene oxide microdomains and found that an orientation perpendicular to the electrodes resulted in an increase in ionic conductivity of about 50 %.[12] The same observation has also been made for proton conduction in hydrated poly(styrenesulfonate-*b*-methylbutylene) copolymer films where a perpendicular orientation to the electrodes led to an increase in ionic conductivity of 30 %.[18] These examples show that the macroscopic alignment of ion-conductive BCPs is a method to improve the conductivity of SPEs while ensuring their mechanical stability for use in Li^+-ion batteries. To date, the literature has mainly focused on nanoscale structuring by self-assembly of BCPs, while mechanical alignment has been widely neglected.[11,153,203,205–207] Therefore, the following Chapter addresses the shear alignment of ion-conductive BCPs prepared by incorporation of an IL or post-functionalization of one block. The objective is to easily design an ion-conductive BCP that has high ionic conductivity and mechanical stability and to further increase the ionic conductivity by perpendicular alignment of the lamellae in the sample.

6.1 Ionic Liquid Incorporated Block Copolymers

The incorporation of an IL into one block of a BCP plasticizes this block and introduces ionic conductivity while the mechanical stability of the BCP can be maintained by the other block. This straightforward approach offers the possibility to use well characterized, anionically synthesized BCPs to obtain well defined SPEs. Virgili *et al.* investigated the phase behavior of PS-*b*-P2VP upon the incorporation of imidazolium bis(trifluoromethane sulfonamide).[202,208] They found that the IL behaves as a selective solvent for one of the blocks, which they believe to be P2VP, and observed different morphologies (e.g., lamellar, cylindrical) depending on the amount of IL.[208] Additionally, they observed an increased segregation of the different blocks upon the addition of IL. Another example is given by Masud *et al.* who recently prepared films of symmetric PS-*b*-PMMA and

1-ethyl-3-methylimidazolium bis(trifluoromethane sulfonyl)imide ([EMIM]TFSI).[77] For their system, they observed surface-induced parallel layering of the lamellae and formation of an anisotropic film.[77] Instead of an IL, salt can also be selectively added to one of the blocks. The salt-doping of PS-*b*-P2VP and PS-*b*-PEO BCPs with LiTFSI led to an increase of T_{ODT} and domain size.[209] Gunkel *et al.* suggested that the increase in T_{ODT} is due to increased incompatibility of the blocks and coordination between the polymer and the salt, resulting in chain stretching as evidenced by a change in domain spacing.[209] To the best of the author's knowledge, the macroscopic alignment of IL incorporated BCPs and its influence on the ionic conductivity have not been investigated yet. Therefore, in the following section the effect of the shear alignment on the ionic conductivity of a mixture of an anionically synthesized PS-*b*-P2VP and [BMIM]TFSI is addressed.

6.1.1 Synthesis and Characterization

The PS-*b*-P2VP block copolymer has been previously synthesized by anionic polymerization[210] and the molecular weight and composition were determined from SEC and ^{1}H-NMR spectroscopy with $M_{\mathrm{n,PS}} = 7000\,\mathrm{g\,mol^{-1}}$ and $M_{\mathrm{n,P2VP}} = 8000\,\mathrm{g\,mol^{-1}}$, resulting in a total molecular weight of $15\,000\,\mathrm{g\,mol^{-1}}$ and $f_{\mathrm{P2VP}} = 0.42\,\mathrm{vol\%}$ ($\rho_{\mathrm{PS}} = 1.05\,\mathrm{g\,cm^{-3}}$, $\rho_{\mathrm{P2VP}} = 1.14\,\mathrm{g\,cm^{-3}}$).[211] The corresponding amounts of PS-*b*-P2VP and [BMIM]TFSI as IL, see Figure 6.2, were dissolved in dioxane and, after stirring over night, freeze-dried for 12 h to receive PS-*b*-P2VP incorporated with 0.15 vol% of [BMIM]TFSI.

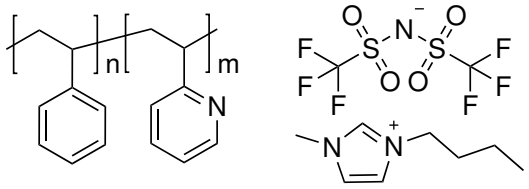

Figure 6.2: Structure of PS-*b*-P2VP (left) and the incorporated IL 1-butyl-3-methylimidazolium bis-(trifluoromethane sulfonyl)imide ([BMIM]TFSI) (right).

The DSC curve in Figure 6.3a shows two distinct T_{g}s at 21 °C and 86 °C in the second heating cycle, corresponding to the P2VP/[BMIM]TFSI and PS phase, respectively, while the T_{g} of the pure BCP is typically ca. 100 °C for both phases. The significantly lowered T_{g} of the P2VP phase indicates the increasing mobility with the addition of IL ($T_{\mathrm{g,IL}} = -93\,^{\circ}\mathrm{C}$) which acts as a plasticizer. A strong decrease of the T_{g} of the mixed phase was also observed for other PS-*b*-P2VP and PS-*b*-PMMA BCPs with incorporated IL.[202,212] The phase separation, which was already indicated by the different T_{g}s, was confirmed by the radially averaged SAXS diffractogram in Figure 6.3b. The pattern clearly shows a first scattering peak at $q_0 = 0.36\,\mathrm{nm^{-1}}$ ($d_0 = 17.45\,\mathrm{nm}$) and also a second and third higher order peak at $2q_0$ and $3q_0$, respectively, indicating a lamellar morphology.

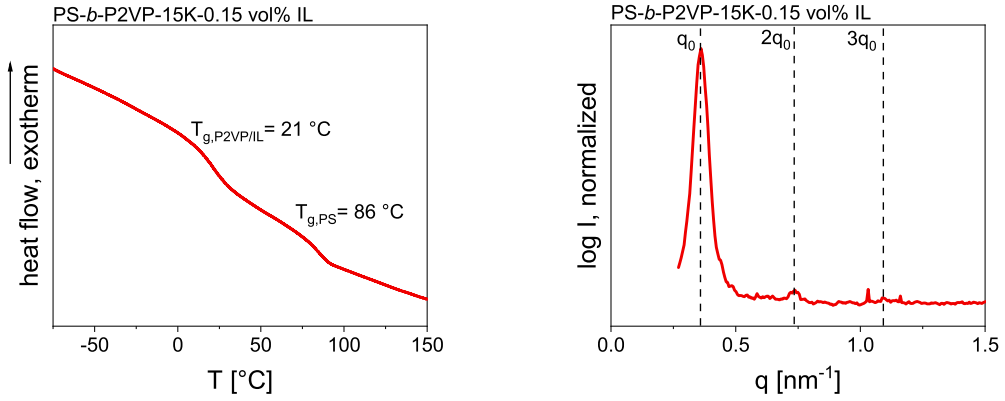

Figure 6.3: **(a)** DSC results revealing the phase separation of PS-*b*-P2VP-15K-0.15 vol% [BMIM]TFSI by displaying the T_g of the PS and P2VP/IL domains. **(b)** Radial averaged SAXS spectrum of the sample, indicating phase separation and a lamellar morphology with $q_0 = 0.36\,\mathrm{nm}^{-1}$ and higher maxima at $2q_0$ and $3q_0$.

The master curve in Figure 6.4a at $T_{\mathrm{ref}} = 150\,^{\circ}\mathrm{C}$ shows that the terminal regime has not yet been reached at low frequencies. The TTS principle works well for the investigated temperature range ($T_g < T < T_{\mathrm{ODT}}$), as indicated by the a_T shift factors and the WLF fit ($C_1 = 11.3$, $C_2 = 243.9\,^{\circ}\mathrm{C}$). Although the T_{ODT} of the pure BCP is T_{ODT}= 163 °C (see Figure A.2.19), no order-disorder transition is observed for PS-*b*-P2VP-0.15 vol% IL from 150 °C to 210 °C, see Figure 6.4b. The same observation is made in the literature for salt-doped BCPs and the increase in T_{ODT} with the addition of an IL or salt is expected to result from increased segregation strength of the blocks.[208,209]

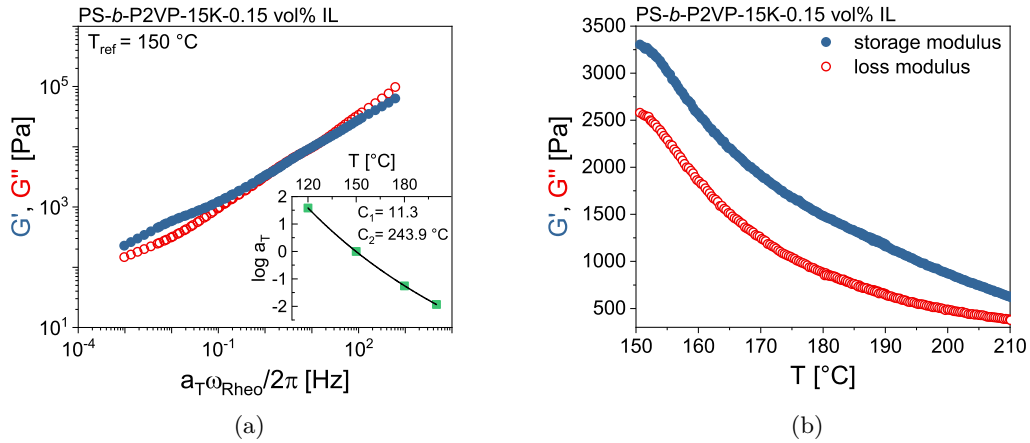

Figure 6.4: **(a)** Master curve of PS-*b*-P2VP-15K with 0.15 vol% [BMIM]TFSI including the a_T shift factors and the WLF fit in the inset. **(b)** Temperature sweep from 150 °C to 210 °C where no order-disorder transition was observed.

6.1.2 Orientation Experiments

The orientation experiments of PS-*b*-P2VP-0.15 vol% IL using LAOS were performed at 200 °C and $\omega_{\mathrm{Rheo}}/2\pi = 1$ Hz using different strain amplitudes. Figure 6.5a displays a rheological frequency sweep before and after shear alignment with $\gamma_0 = 50\,\%$. After shear alignment both shear moduli decreased and G'' is greater than G' which corresponds to the observations made for PS-*b*-PI BCPs in Chapter 5. In comparison to the previous Chapter, not $\epsilon''(\omega_{\mathrm{BDS}})$ but $\sigma'(\omega_{\mathrm{BDS}})$ is detected to investigate the impact of the macroscopic orientation on the ionic conductivity. For the shown example (Figure 6.5b), the plateau in $\sigma'(\omega_{\mathrm{BDS}})$, which is known to be the ionic conductivity, increases by 0.005 mS cm^{-1} (24 %) after orientation with $\gamma_0 = 50\,\%$ at $\omega_{\mathrm{Rheo}}/2\pi = 1$ Hz and $T = 200$ °C.

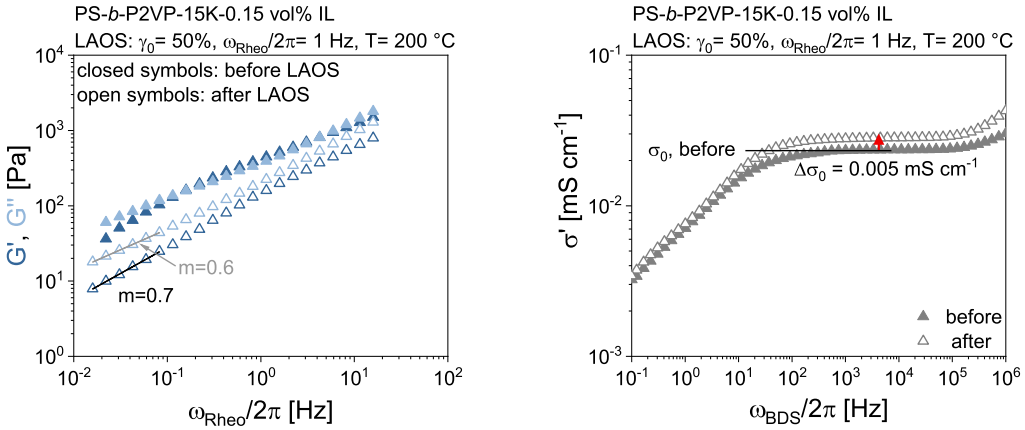

Figure 6.5: (a) Small amplitude oscillatory shear frequency sweeps ($\gamma_0 = 0.1\,\%$) before (closed symbols) and after (open symbols) the orientation of PS-*b*-P2VP-0.15 vol% IL with $\gamma_0 = 50\,\%$ at 200 °C and $\omega_{\mathrm{Rheo}}/2\pi = 1$ Hz. The dark symbols represent G', whereas the light symbols represent G''. **(b)** Real part of the conductivity (σ') before (closed symbols) and after (open symbols) the orientation of PS-*b*-P2VP-0.15 vol% IL with $\gamma_0 = 50\,\%$ at 200 °C and $\omega_{\mathrm{Rheo}}/2\pi = 1$ Hz.

To follow the alignment process, $I_{3/1}(t)$ and $\sigma_0(t)$ were monitored at a fixed rheological and dielectric frequency, respectively, see Figure 6.6. For both experiments, the same parameters (γ_0= 50 %, $\omega_{\mathrm{Rheo}}/2\pi = 1$ Hz and $\omega_{\mathrm{BDS}} = 1 \times 10^4$ Hz) were used at different temperatures (160 °C and 200 °C). At 160 °C, $I_{3/1}(t)$ showed a rapid and strong increase from approx. 0.042 to 0.075 (79 %) and a weak, slow decrease to 0.07 (7 %). Instead, a noisy decrease is observed at 200 °C from 0.11 to 0.095 (15 %). Both observations do not correspond to the behavior of $I_{3/1}(t)$ in Chapter 5, where $I_{3/1}(t)$ showed a clear stretched exponential decay. Furthermore, $I_{3/1}(t)$ cannot be correlated with the behavior of $\sigma_0(t)$, where σ_0 increases with time for 160 °C and decreases for 200 °C. However, both curves follow a stretched exponential function, see Equation 5.2, and the fit parameters are displayed in Table 6.1. The mean orientation time increases with increasing temperature (202 s at 160 °C vs. 376 s at 200 °C) meaning that the plateau is reached earlier under more viscous conditions. The stretching parameter β_1 was 0.5 and 0.8 at $T = 160$ °C and $T = 200$ °C, respectively, indicating a more homogeneous distribution at higher temperature.

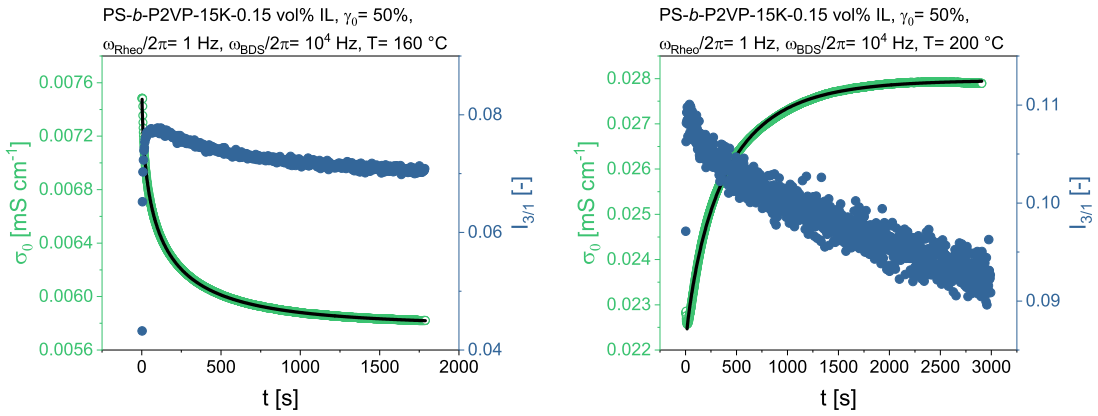

(a) (b)

Figure 6.6: Time-dependent ionic conductivity ($\sigma_0(t)$, green) and relative intensity of the third harmonic ($I_{3/1}(t)$, blue) including a stretched exponential fit (solid lines) obtained during the shear alignment of PS-*b*-P2VP-15K-0.15 vol% IL at a temperature of **(a)** 160 °C, and **(b)** 200 °C and $\omega_{\mathrm{Rheo}}/2\pi = 1\,\mathrm{Hz}$ and $\gamma_0 = 50\,\%$. During all measurements $\sigma'(t)$ was recorded at a fixed dielectric frequency, $\omega_{\mathrm{BDS}} = 1 \times 10^4\,\mathrm{Hz}$, which corresponds to its plateau value and thus $\sigma_0(t)$.

Table 6.1: Fit parameters of a stretched exponential function (see Equation 5.2, p. 80) for $\sigma_0(t)$ of PS-*b*-P2VP-15K-0.15 vol% IL.

T [°C]	y_0 [S cm^{-1}]	A_1 [S cm^{-1}]	τ_1 [s]	β_1 [−]
160	-5.8×10^{-6}	-2.0×10^{-6}	202	0.5
200	-2.8×10^{-5}	5.9×10^{-6}	376	0.8

According to the findings in Chapter 5 and the considerations made above (see Figure 6.1, p. 96), an increase of $\sigma_0(t)$ should indicate a perpendicular and a decrease a parallel orientation. However, the SAXS patterns in Figure 6.7 show that these assumptions do not hold, since a parallel orientation was obtained for both experiments. While the decrease in $\sigma_0(t)$ might be caused by the parallel orientation and a reduced tortuosity because of fewer defects, it remains unclear why in the case of 200 °C this should not apply. Since to the author's knowledge, this is the first time that IL incorporated PS-*b*-P2VP is oriented by LAOS, the observations made here cannot be compared to the literature. One reason could be the large difference from measurement temperature to T_g, as the samples contract on cooling and this flow possibly induces orientation. Rheo-SAXS could provide an answer to this question. Another problem may be that ILs tend to aggregate and aggregates in the lamellae may be polarized that a capacitor is formed so that less ions are available for ion conduction.[206] These effects would additionally influence the ionic conductivity of the sample and might also change during the orientation procedure, so that a prediction of the orientation by $\sigma_0(t)$ is no longer possible. To overcome this problem, in the following Section, ionic charges are introduced into a BCP by funtionalizing one block, resulting in a single ionic conductor.

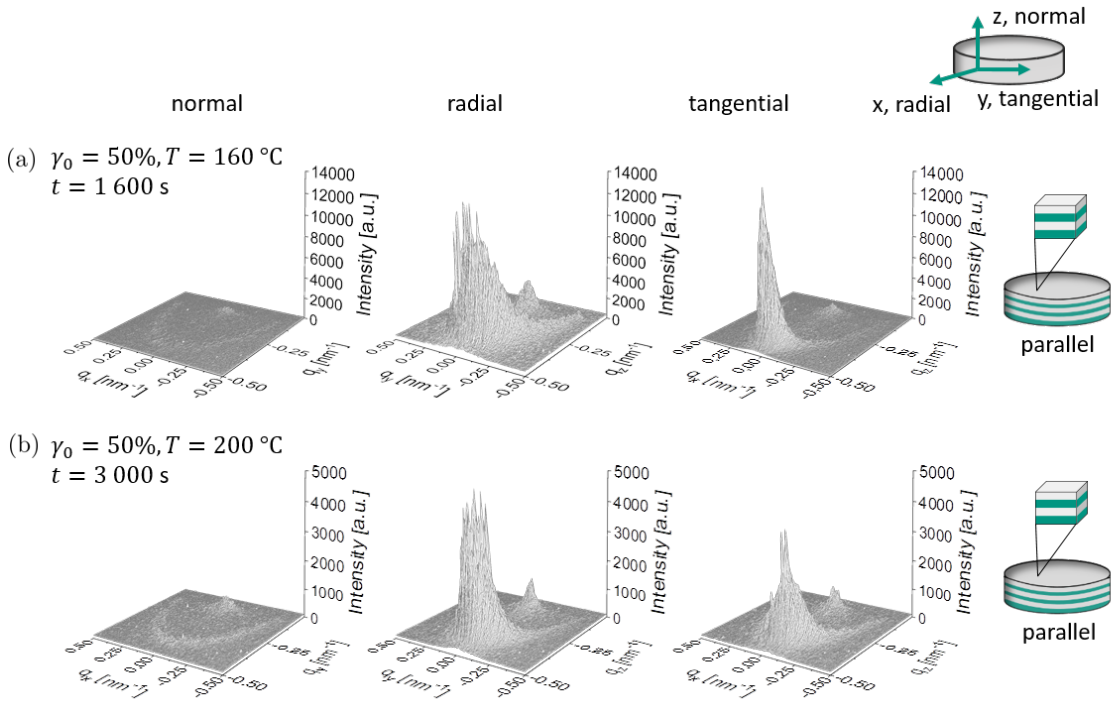

Figure 6.7: SAXS patterns of PS-*b*-P2VP-15K-0.15 vol% IL along the normal, radial and tangential plane, oriented with $\omega_{\mathrm{Rheo}}/2\pi = 1\,\mathrm{Hz}$, $\gamma_0 = 50\,\%$ and at **(a)** 160 °C, and **(b)** 200 °C. In both cases a parallel orientation of the ordered lamellar microdomains is indicated.

6.2 Charged Block Copolymers

Another possibility to design well-defined ion-conductive BCPs is post-functionalization, for example, after anionic or controlled radical polymerization. In particular in the field of controlled radical polymerization, various PS-*b*-PolyIL BCPs have been synthesized to investigate the influence of the chemical nature of the PolyIL on the morphology and ionic conductivity.[203,204,213] Carrasco *et al.* used RAFT polymerization and post-functionalization to synthesize different charged BCPs.[203] Furthermore, they exchanged the anions in the PolyIL while keeping the polymer to PolyIL ratio the same.[203] They studied the effects on the nanostructure of the BCP using atomic force microscopy and found different domain sizes by changing the type of anion.[203] Chen *et al.* used the same method to synthesize PS-*b*-PolyIL BCPs with different PolyILs.[204] The resulting PS-*b*-PolyIL BCPs were mixed with the corresponding Li-salts and the effects on the BCP properties such as morphology and ionic conductivity were evaluated and electrochemical experiments (e.g., lithium plating and stripping) were successfully performed.[204] Mäki-Ontto *et al.* went one step further and investigated the proton conductivity after the shear alignment of poly(styrene)-*b*-poly(4-vinyl pyridine) (PS-*b*-P4VP) with toluene sulfonic acid (TSA) and 3-*n*-pentadecylphenol (PDP) resulting in PS-*b*-P4VP(TSA)$_{10}$(PDP)$_{10}$.[13] After shear alignment, they found a tridirectional anisotropy in the proton conductivity, implying that the nanoscale anisotropy is reflected in the macroscopic conductivity.[13] Thus, it is shown that the shear alignment of the samples, which is associated with fewer domain boundaries and defects, can be directly related to proton transport. To the author's

knowledge, there has not been any detailed study of the mechanical alignment and its kinetics of charged BCPs. Hence, in the following section, the systems used in Chapters 4 and 5 are combined to form a charged BCP and its alignment is studied using coupled rheo-dielectric.

6.2.1 Synthesis and Characterization

The charged BCPs were synthesized by RAFT polymerization followed by functionalization of the BCP, see Figure 6.8.[204] First, the PS macromonomer was synthesized (1) and its molecular weight was determined by SEC. The second block was added (2) and then functionalized by substitution (3) and anion exchange (4). Details of the synthesis can be found in the Appendix A.1.2, p. 126. The molecular weight of the first block (PS, M_n= 12 000 g mol^{-1}, Đ = 1.16) was determined by SEC, while the molecular weight of the second block was calculated from ^{1}H-NMR (poly[VBBI]TFSI, M_n= 14 000 g mol^{-1}) resulting in $M_{n,total}$ = 26 000 g mol^{-1} for PS-*b*-Poly[VBBI]TFSI (PS-*b*-PolyIL-26K) and f_{PS} = 0.48 vol%. With this ratio, a lamellar structure is expected.[214]

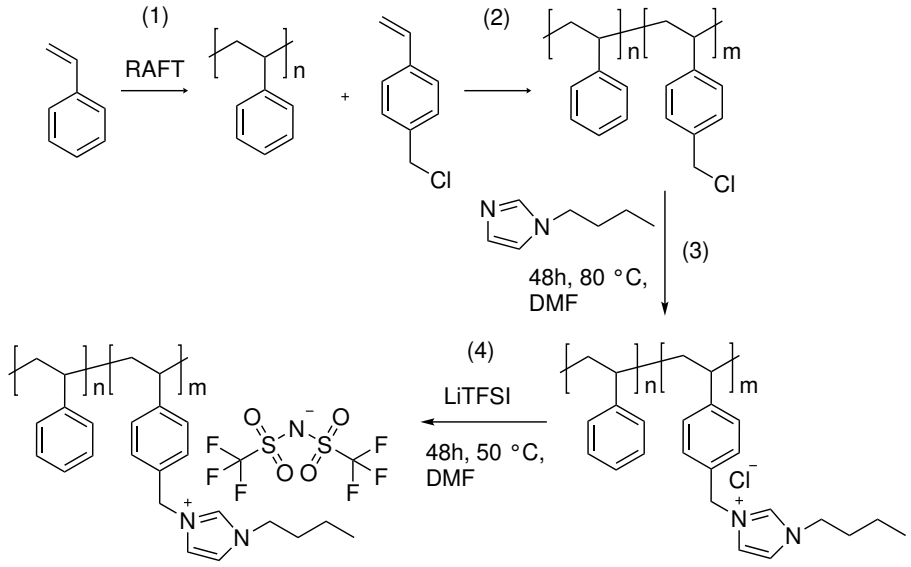

Figure 6.8: Synthesis of PS-*b*-Poly[VBBI]TFSI (PS-*b*-PolyIL) by RAFT polymerization and post-functionalization. The synthesis was adapted from Chen *et al.*[204]

The DSC curve of PS-*b*-PolyIL-26K in Figure 6.9a indicates phase separation with two distinct T_gs at 8 °C and 102 °C for the ionic and PS phase, respectively. The T_g of the ionic block corresponds to the value of the homopolymer in Chapter 4.1. The phase separation is confirmed by the SAXS pattern in Figure 6.9b where higher maxima confirm the assumed lamellar morphology. The first scattering peak at q_0 = 0.20 nm^{-1} indicates a lamella thickness of 31.4 nm.

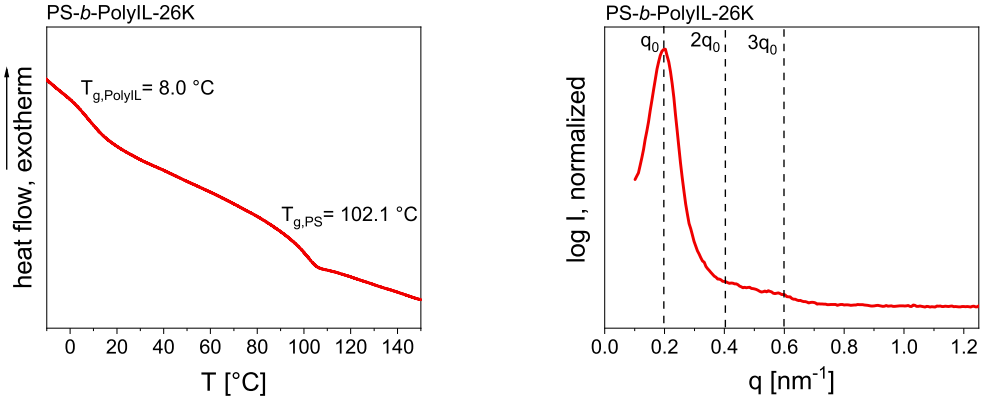

Figure 6.9: **(a)** DSC curve revealing the phase separation of PS-*b*-PolyIL-26K displaying the T_g of the PS and poly[VBBI]TFSI domains. **(b)** Radial averaged 2D-SAXS spectrum of an oriented sample, indicating phase separation and a lamellar morphology.

The master curve in Figure 6.10a including the a_T shift-factors in the inset shows that the TTS principle worked well for the investigated temperature range ($T_g < T < T_{ODT}$). Two rubber plateaus are indicated in the master curve, one corresponding to the PolyIL block and another one corresponding to the PS block. The terminal regime has not yet been reached at low frequencies. However, the crossover and hence longest relaxation time is observed at 1.2×10^{-4} Hz ($\tau_{relax} = 8333$ s). A temperature sweep from 160 °C to 210 °C did not show an order-disorder transition (see Figure 6.10b), indicating the strong phase separation because of the ionic block.

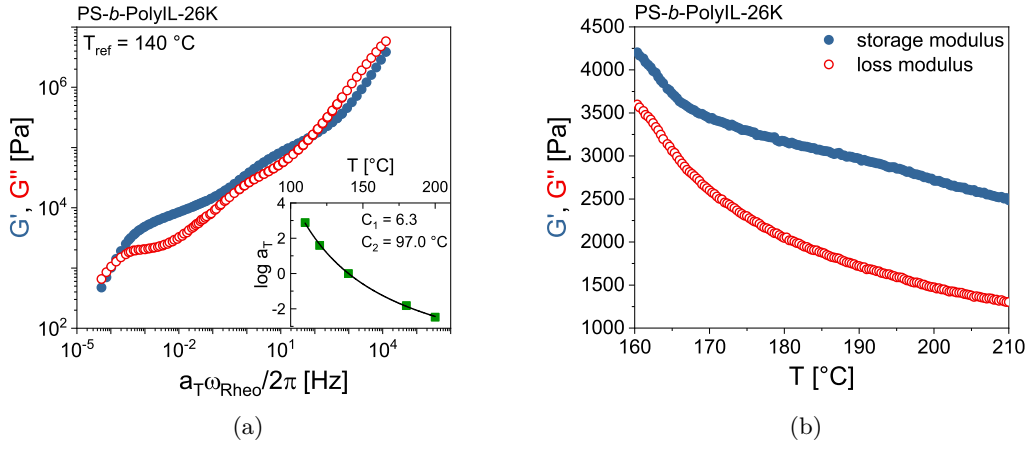

Figure 6.10: **(a)** Master curve of PS-*b*-PolyIL-26K at T_{ref}= 140 °C including the a_T shift factors and the WLF fit in the inset. **(b)** Temperature sweep from 160 °C to 210 °C where no order-disorder transition was observed.

6.2.2 Orientation Experiments

The change in the rheological and dielectric data upon orientation of PS-*b*-PolyIL-26K with $\gamma_0 = 50\,\%$, $\omega_{Rheo}/2\pi = 1$ Hz at 200 °C is displayed in Figure 6.11. As already

observed for the previous samples, the shear moduli are lower after the alignment process and also the crossover observed at 8 Hz shifts to lower frequencies (0.3 Hz). The ionic conductivity decreases about 0.1 mS cm^{-1} from 0.198 mS cm^{-1} to 0.096 mS cm^{-1} (52 %) after the orientation process.

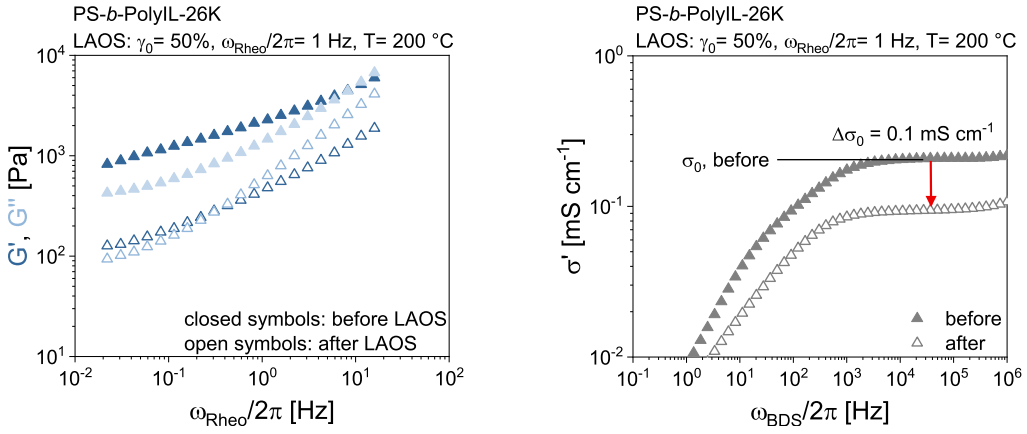

Figure 6.11: (a) Small amplitude oscillatory shear frequency sweeps ($\gamma_0 = 0.1\,\%$) before (closed symbols) and after (open symbols) the orientation of PS-*b*-PolyIL-26K with $\gamma_0 = 50\,\%$ at 200 °C and $\omega_{\mathrm{Rheo}}/2\pi = 1$ Hz. The dark symbols represent G', whereas the light symbols represent G''. **(b)** Real part of the conductivity (σ') before (closed symbols) and after (open symbols) the orientation of PS-*b*-PolyIL-26K with $\gamma_0 = 50\,\%$ at 200 °C and $\omega_{\mathrm{Rheo}}/2\pi = 1$ Hz.

The alignment process was again followed by the change of $I_{3/1}(t)$ and $\sigma_0(t)$ at a fixed $\omega_{\mathrm{Rheo}}/2\pi$ and $\omega_{\mathrm{BDS}}/2\pi$, respectively, see Figure 6.12. In comparison to the model systems, different courses were found for $I_{3/1}(t)$ and only one set of parameters (γ_0= 250 %, $\omega_{\mathrm{Rheo}}/2\pi = 1$ Hz, $T = 200$ °C) resulted in a stretched exponential decay with a mean orientation time of 245 s and $\beta_1 = 0.7$. A strain amplitude of $\gamma_0 = 50\,\%$ led to a strong increase of $I_{3/1}(t)$ until 110 s followed by a compressed exponential with a mean orientation time of 1218 s and $\beta_1 = 1.2$. Another course of $I_{3/1}(t)$ is found for γ_0= 50 %, $\omega_{\mathrm{Rheo}}/2\pi = 1$ Hz at 220 °C where it is increasing within 1138 s from 0.05 to result in a plateau at $I_{3/1} = 0.09$. For all three experiments, $\sigma_0(t)$ decreases exponentially and a faster decrease is observed with increasing γ_0 at the same T or increasing T using the same γ_0. This trend is also reflected in the stretched exponential fit parameters displayed in Table 6.2, where the mean orientation time decreased from 9631 s to 157 s with increasing γ_0 from 50 % to 250 % at 200 °C. A weaker decrease in orientation time was observed with increasing temperature from 200 °C (9631 s) to 220 °C (2413 s). The stretching parameter is found between 0.5 and 0.9 and a more homogeneous distribution is observed with increasing T and decreasing γ_0. The ionic conductivities at the start of the measurements are not equal at the same temperature but in the range of error due to sample loading and the fact that T_{ODT} could not be reached before the measurement. If T_{ODT} could be reached it is expected that the error by sample loading is decreased. Based on the previous considerations, a decrease in $\sigma_0(t)$ should indicate a parallel orientation of the lamellae, since the ions have fewer direct paths from one electrode to the other, see Figure 6.1b. This assumptions is confirmed by the SAXS patterns in Figure 6.13 where a final

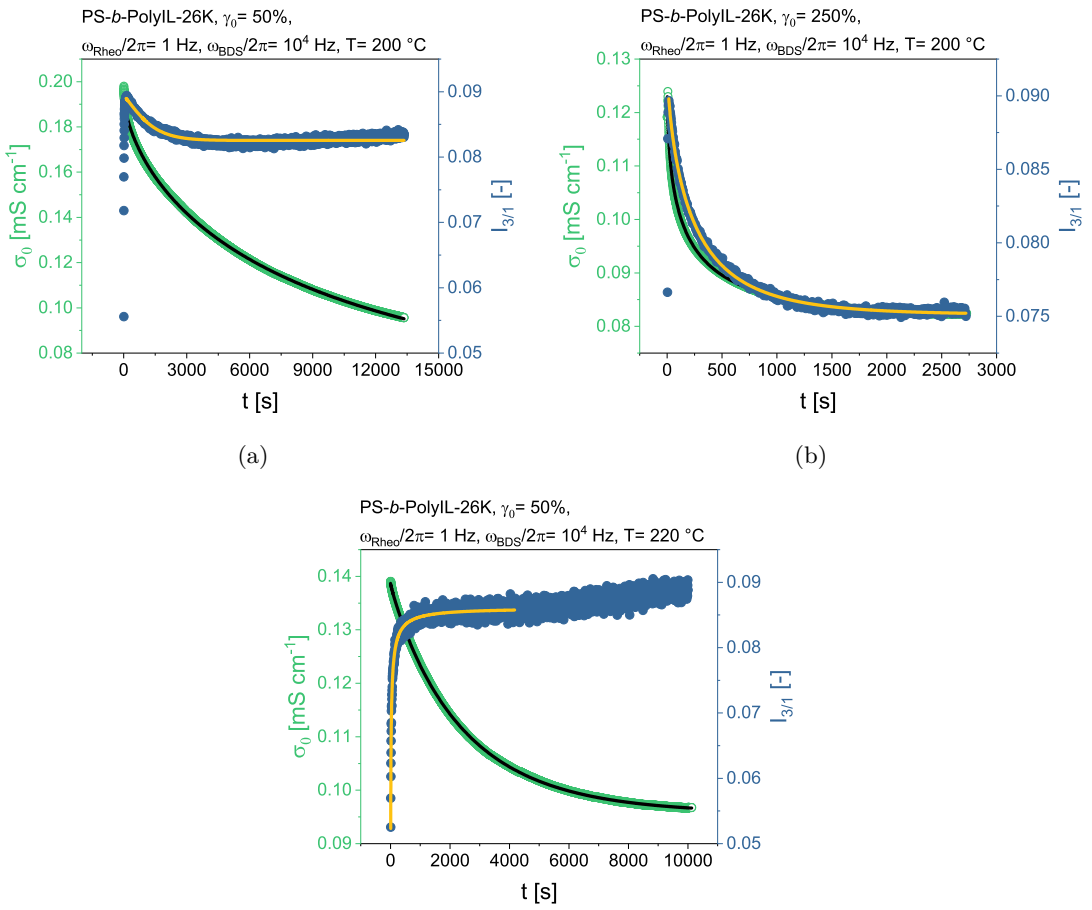

Figure 6.12: Time-dependent ionic conductivity ($\sigma_0(t)$, green) and relative intensity of the third harmonic ($I_{3/1}(t)$, blue) including a stretched exponential fit (solid lines) obtained during the shear alignment of PS-*b*-PolyIL-26K with an applied strain amplitude of **(a)** 50 % at 200 °C, **(b)** 250 % at 200 °C, and **(c)** with $\gamma_0 = 50\,\%$ at 220 °C and $\omega_{\mathrm{Rheo}}/2\pi = 1\,\mathrm{Hz}$. During all measurements $\sigma'(t)$ was recorded at a fixed dielectric frequency, $\omega_{\mathrm{BDS}}/2\pi = 1 \times 10^4\,\mathrm{Hz}$, which corresponds to its plateau value and thus $\sigma_0(t)$.

parallel orientation is found for all experiments. The course of $I_{3/1}(t)$ however, remains elusive as a decrease of $I_{3/1}(t)$ would be expected upon alignment because of fewer grain boundaries. The increase in Figure 6.12c and initial increase in 6.12c would thus indicate an increasing amount of grain boundaries due to break up of grains. Ding *et al.* also observed a stretched exponential increase of $I_{3/1}(t)$ during the mechanical orientation of a poly(styrene-*b*-lauryl acrylate-*b*-styrene) triblock copolymer with a close-packed sphere morphology and suspected that a reorientation process takes place which increases the number of grain boundaries.[54] Unfortunately, with the sample and analytics used here, no concrete statement can be made about the reason for the behavior of $I_{3/1}(t)$. One possibility to investigate the behavior in more detail would be rheo-SAXS, in which the formation of the orientation during shear can be detected online via SAXS.

Table 6.2: Fit parameters of a stretched exponential function (see Equation 5.2) for $\sigma_0(t)$ of PS-*b*-PolyIL-26K.

T [°C]	γ_0 [%]	y_0 [S cm^{-1}]	A_1 [S cm^{-1}]	τ_1 [s]	β_1 [−]
200	50	-5.5×10^{-5}	-1.4×10^{-4}	9631	0.7
200	250	-8.1×10^{-5}	-4.7×10^{-5}	157	0.5
220	50	-9.6×10^{-5}	-4.2×10^{-5}	2413	0.9

Table 6.3: Fit parameters of a stretched exponential function (see Equation 5.2) for $I_{3/1}(t)$ of PS-*b*-PolyIL-26K.

T [°C]	γ_0 [%]	y_0 [−]	A_1 [−]	τ_1 [s]	β_1 [−]
200	50	-7.9×10^{-2}	-6.7×10^{-3}	1218	1.2
200	250	-7.5×10^{-2}	-1.7×10^{-2}	245	0.7
220	50	−0.1	0.9	0.1	0.2

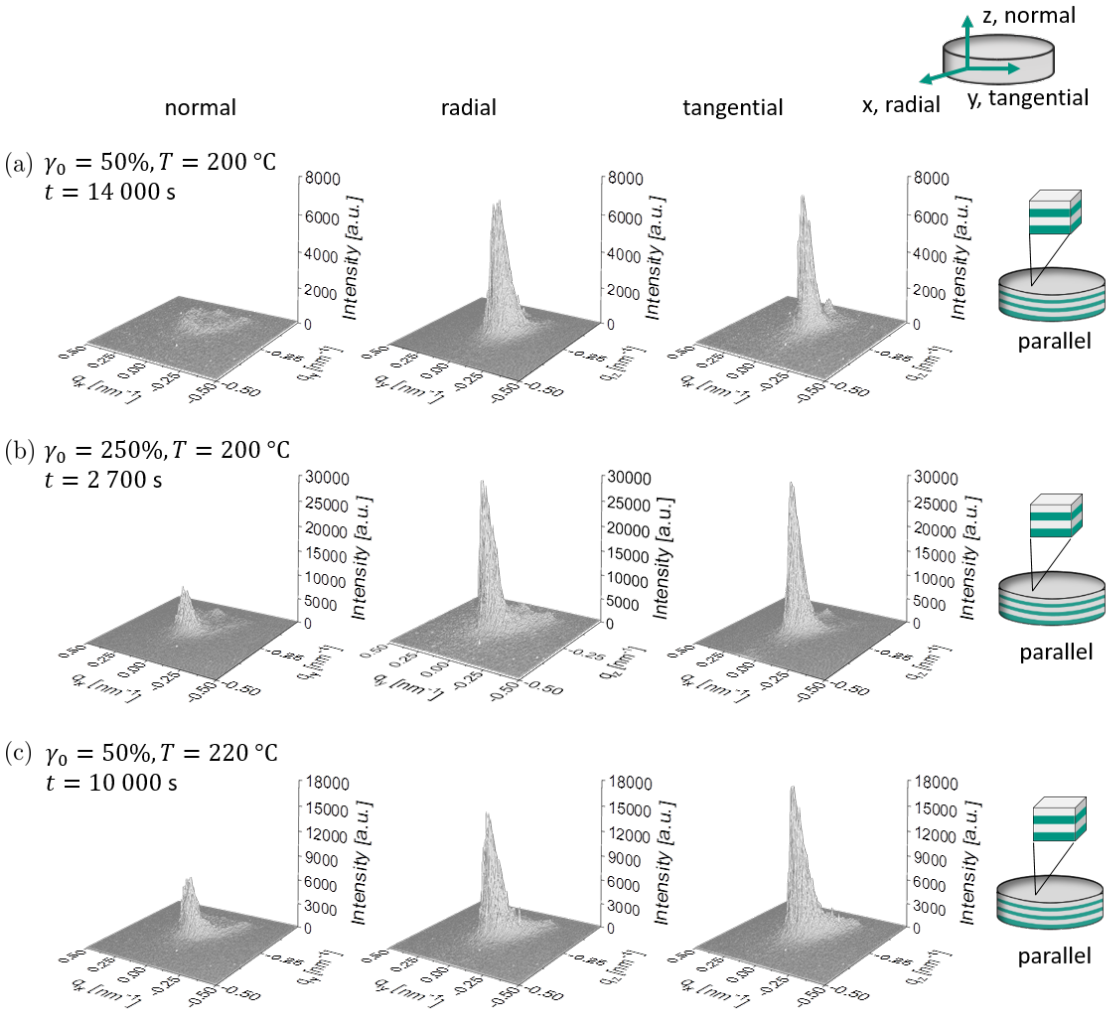

Figure 6.13: 2D-SAXS patterns of PS-*b*-PolyIL-26K along the normal, radial and tangential plane, oriented with an applied strain amplitude of **(a)** 50 % and **(b)** 250 % at 200 °C and **(c)** with $\gamma_0 = 50\,\%$ at $T = 220\,°C$ and $\omega_{Rheo}/2\pi = 1\,Hz$. In all cases a parallel orientation of the ordered lamellar microdomains is indicated.

The degree of order is determined by fitting a Gaussian function to the azimuthal average (see Equation 5.6 and Figure 3.15) and the FWHM is then correlated with the change in the ionic conductivity, see Table 6.4. A high degree of order, i.e., low FWHM, should indicate fewer defects and less tortuosity in the sample and thus a greater change in the ionic conductivity. While the FWHMs of the tangential direction are similar, the lowest FWHM of 8° is found for $T = 200\,°C, \gamma_0 = 50\,\%$ and increases with increasing strain amplitude (FWHM = 10° with $\gamma_0 = 250\,\%$) and temperature (FWHM = 16° at $T = 220\,°C$) in radial direction. The absolute change in the ionic conductivity does not reveal a clear trend when correlated to the FWHM. However, using the percentage change, it can be seen that the largest change in ionic conductivity is associated with the highest order in the sample as depicted in Figure 6.14, confirming the previous suggestion.

Table 6.4: Full width at half maximum (FWHM) of the azimuthally averaged SAXS pattern in radial and tangential direction and the change in ionic conductivity upon macroscopic orientation of the samples.

T [°C]	γ_0 [%]	$\mathrm{FWHM}_{\mathrm{radial}}$ [°]	$\mathrm{FWHM}_{\mathrm{tangential}}$ [°]	$\Delta\sigma_0$ [mS cm^{-1}]	$\Delta\sigma_0$ [%]
200	50	8	17	0.10	52
200	250	10	18	0.04	34
220	50	16	15	0.04	30

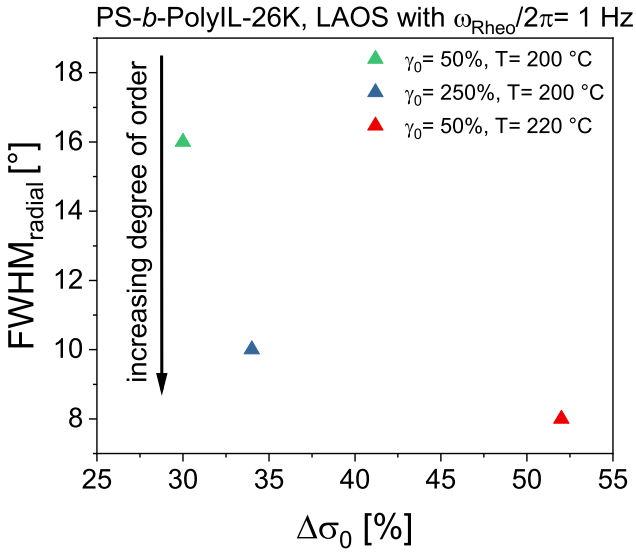

Figure 6.14: Correlation of $\mathrm{FWHM}_{\mathrm{radial}}$ with the percent change in ionic conductivity ($\Delta\sigma_0$) after orientation. A higher degree of order is associated with a stronger decrease in $\sigma_0(t)$.

Unfortunately, it was not possible to achieve a perpendicular orientation with the sample used, but by changing the molecular parameters, such as molecular weight and volume fraction, a perpendicular orientation should be accessible. Nevertheless, these results serve as a proof of concept that macroscopic orientation can be used to tune the ionic conductivity of phase separated samples.

6.3 Summary

This Chapter has provided insight into the orientation of ion-conductive BCPs. Two different ion-conductive BCPs were prepared and characterized. The SAXS images show increased segregation compared to their non-conductive analogs and confirm the lamellar morphology. An order-disorder transition temperature was not found in the investigated temperature range, most likely due to the increased segregation. Unfortunately, the orientation process of IL-doped PS-*b*-P2VP could not be followed by the change in ionic conductivity. It is suggested that ionic interactions lead to aggregates and additional change in ionic conductivity during the orientation process. Nevertheless, the sample could be oriented macroscopically and a parallel orientation was obtained for all experiments. Moreover, for the first time, the orientation process in charged block copolymers was observed *in-situ* using rheo-dielectrics. The obtained parallel orientation of the samples led to a decrease of the ionic conductivity as previously suggested. Furthermore, the highest decrease of 52 % was observed for the sample with the lowest FWHM (8°) and thus the highest degree of order. Unfortunately, a perpendicular orientation could not be obtained with the available sample. However, it is assumed that this can be achieved with a lower molecular weight or by synthesizing a PS-*b*-PolyIL-PS triblock copolymer (see influence of block order on orientation in Chapter 5). It should also be noted that the ionic conductivity of the prepared samples may not be sufficient for use in LIBs. However, this Chapter serves only as a proof of concept and the samples can be further modified by adding a higher amount of IL or adjusting the ionic to non-ionic block ratio to achieve a sufficient ionic conductivity of about $1\,\mathrm{mS\,cm^{-1}}$.

7 Conclusion and Outlook

Conclusion

This work aims to contribute to research in the field of polymer electrolytes for the development of materials for battery storage systems for, e.g., the storage of renewble energy. For this purpose, different polymer electrolytes based on polymerized ionic liquids were investigated, especially with respect to their use in Li^+-ion batteries. In addition, a macroscopic orientation was mechanically introduced into a triblock copolymer model system, allowing conclusions to be drawn about the influence of block dynamics and sequence on the final orientation. Finally, ion-conductive diblock copolymers were prepared and mechanically oriented to investigate the influence of macroscopic orientation on ionic conductivity.

The first part of this thesis investigated the properties and ion diffusion in different mixtures of an imidazolium-based ionic liquid (IL) and the corresponding polymer (poly(1-butyl-3-(4-vinylbenzyl)imidazolium bis(trifluoromethane sulfonyl)imide), poly[VBBI]TFSI). The mixtures with different blending ratios were characterized by DSC, combined rheo-dielectric and PFG-NMR. Their glass transition temperatures followed the Gordon-Taylor equation (Equation 4.9, $k = 0.144$) and were between the values of the pure materials. The rheological measurements revealed an increasing G' with increasing amount of PolyIL at a fixed frequency and a maximum increase from the highest (90 wt%) to lowest (10 wt%) amount of IL by a factor 10^3 at room temperature. In contrast, the ionic conductivity showed the opposite behavior, decreasing by a factor of 10^4 from the polymer to the corresponding monomer at room temperature and the temperature behavior of all samples followed a Vogel-Fulcher-Tammann (VFT) trend. However, for 90 wt% and the pure PolyIL, this behavior changed to an Arrhenius behavior at the corresponding T_g, indicating the decoupling of charge transport and segmental motion in these samples. The static dielectric constant was observed to be around $\epsilon_s = 12.5$ from 70 wt% to 30 wt% IL and also a constant Haven ratio ($H_R = D_{mean}/D_\sigma$) of 1.45 was observed for these samples, while $H_R = 1.4$ for the IL and $H_R > 5$[103] for the PolyIL. These values show that the increase in ionic conductivity upon blending the PolyIL with the corresponding IL results not only from the additional mobility and ions, but may also result from reduced ion-ion correlation in the mixtures. However, high ionic conductivities were reached to the detriment of mechanical stability and the resulting materials could not be applied in Li^+-ion batteries. Therefore, an IL crosslinker (IL-CL) was synthesized based on the previously used IL in order to prepare crosslinked PolyILs by photopolymerization to improve mechanical stability. These so-called ionogels consisted of the IL crosslinker, an IL monomer, an IL and LiTFSI as a

lithium salt, see Figure 4.13, p. 51. For comparison, ionogels of the same composition were prepared using a commercial non-ionic crosslinker. The crosslinking resulted in high shear moduli ($G' \approx 10^5$ Pa), while at the same time a high ionic conductivity of, for example, ca. 0.3 mS cm^{-1} was achieved. In general, the IL-CL based samples exhibited slightly higher shear moduli ($G' = 4 \times 10^5$ Pa vs. 1×10^5 Pa) compared to the non-ionic counterpart. The ionic conductivity, and thus the ion transport, seemed to be independent of the polymer matrix (non-ionic or ionic) and the same value (ca. 0.3 mS cm^{-1}) is found for comparable samples at 25 °C. The addition of LiTFSI led to a decrease of the ionic conductivity, where a stronger decrease (maximum decrease of one decade) was observed for the IL-CL most likely due to the formation of aggregates that reduce ion motion and diffusion. However, much more important for the application in Li^+-ion batteries is the Li^+-ion transference number (t_{Li^+}), since only Li^+-ions are responsible for the performance of the polymer electrolyte. Here, a factor of $4-7$ higher t_{Li^+} was found for the IL-CL based samples ($0.02-0.043$ vs. 0.006), which also featured higher current densities, lower overvoltage and more stable lithium deposition in lithium plating/stripping experiments. Eventually, successful long term plating/stripping experiments ($t = 106$ h) provided an outlook for the application in actual Li^+-ion batteries.

The second part of this thesis investigated the influence of the block order in polystyrene (PS) and polyisoprene (PI) triblock copolymers (ISI vs. SIIS) on the alignment kinetics and macroscopic orientation by large amplitude oscillatory shear (LAOS). Rheo-dielectric and small angle X-ray scattering (SAXS) were used to cover the processes from the molecular length scale to the macroscopic level. The macroscopic orientation is revealed by SAXS measurements, while the use of FT rheology, where the nonlinear parameter $I_{3/1}$ quantifies the nonlinear behavior, is hypothesized to provide information about the number of grain interfaces. Eventually, BDS detects the fluctuations of the end-to-end vector of 1,4-*cis*-PI thus offering insight into its dynamics. The orientation of the triblock copolymers led to an anisotropic polarization of the PI chains and thus BDS already predicted the final microscopic orientation of ISI-40K. A perpendicular, biaxial, and parallel macroscopic orientation was found for ISI-40K with increasing γ_0. The perpendicular orientation was favored at low mechanical impact (low γ_0, low ω_{Rheo} and high T) because of chain stretching along the direction of the vorticity while with increasing mechanical impact a parallel orientation was preferred due to enhanced stress accommodation by layer sliding. The shear alignment of SIIS-40K, on the other hand, resulted in a perpendicular orientation only highlighting the influence of the block order on the macroscopic orientation and the limitation of layer sliding due to the tethered PI-chains. The investigation of orientation kinetics and intermediate states *in-situ* by rheo-dielectric provided the opportunity to better understand the dynamics in triblock copolymers and the molecular origin of macroscopic properties.

In the third part of this thesis, two different ion-conductive block copolymers were prepared by (I) mixing an IL with PS-*b*-P2VP and (II) post-functionalizing a polystyrene derivative in a block copolymer of polystyrene and a polystyrene derivative to introduce charges and were then oriented using LAOS. The aim was to correlate the change in ionic

conductivity with the macroscopic orientation. Unfortunately, no correlation could be found for the orientation of IL doped PS-*b*-P2VP. All orientation experiments resulted in macroscopic parallel orientations, while different trends were observed for the ionic conductivity. It is suggested that ion aggregates in the sample prevent a correlation between the macroscopic orientation and the ionic conductivity. However, in comparison, the charged block copolymer behaved differently and the observed parallel orientation was accompanied by a decrease in ionic conductivity in several experiments at different temperatures and strain amplitudes most likely due to the parallel lamellae hindering ion transport. Unfortunately, it was not possible to induce a perpendicular orientation in the prepared sample. However, from the results obtained for the PS-*b*-PI model systems, it is assumed, that a lower molecular weight or the synthesis of a triblock copolymer with PS as endblock (PS-*b*-PolyIL-PS) could lead to a perpendicular macroscopic orientation. In addition, after adjusting the ratio of non-ionic and ionic block, an IL could be incorporated to (I) further enhance the ionic conductivity by addition of ions and plasticization and (II) gain insights into the behavior of IL doped block copolymers.

Outlook

For future investigations, the synthesized ionogels could be tested in Li^+-ion batteries to evaluate their performance compared to currently used polymer electrolytes. Furthermore, lithium plating/stripping experiments could be performed by applying a sinusoidal voltage profile. After Fourier transform, the higher harmonics obtained could provide further insight into the performance and aging of the polymer electrolytes.

In addition, model systems with a higher number of blocks or different molecular weights could be investigated to obtain an even more ordered perpendicular structure. The findings for these model systems, especially the influence of block order, serve as a starting point for the orientation of ion-conducting block copolymers.

Ion-conductive BCPs with a lower molecular weight or triblock copolymer system with PS endblocks could be synthesized to achieve a perpendicular macrocopic orientation using LAOS. It is also suggested that more IL could be incorporated into PS-*b*-PolyIL-*b*-PS compared to a PS-*b*-PolyIL with similar molecular weight due to the two stiff endblocks and hence higher mechanical stability in the case of the diblock copolymer. The next step would cope with the addition of LiTFSI. The oriented and unoriented samples could be studied in symmetric lithium cells and then in Li^+-ion batteries thus providing insights into the effect of macroscopic orientation on their performance in cells.

Additionally, new insights into the orientation process of different BCPs could be obtained by using combined rheo-SAXS, which allows online SAXS measurements during orientation process. The thus obtained spectra provide information on the developement of the different induced orientations and of their degree of order during the alignment process.

Overall, this thesis presents a fundamental contribution to the investigation of solid polymer electrolytes by coupled rheo-dielectric as well as to the orientation of (ion-conductive) block copolymers. This supports the research in the field of polymer electrolytes as materials for battery storage systems and thus contributes to mitigate global warming.

Bibliography

[1] P. C. D. Milly, R. T. Wetherald, K. A. Dunne, T. L. Delworth, *Nature* **2002**, *415*, 514–517.

[2] P. M. Della-Marta, M. R. Haylock, J. Luterbacher, H. Wanner, *Journal of Geophysical Research* **2007**, *112*.

[3] T. Kim, W. Song, D.-Y. Son, L. K. Ono, Y. Qi, *Journal of Materials Chemistry A* **2019**, *7*, 2942–2964.

[4] A. Manthiram, X. Yu, S. Wang, *Nature Reviews Materials* **2017**, *2*, 294.

[5] E. Quartarone, P. Mustarelli, *Chemical Society Reviews* **2011**, *40*, 2525–2540.

[6] G. G. Eshetu, D. Mecerreyes, M. Forsyth, H. Zhang, M. Armand, *Molecular Systems Design & Engineering* **2019**, *4*, 294–309.

[7] K. Põhako-Esko, M. Timusk, K. Saal, R. Lõhmus, I. Kink, U. Mäeorg, *Journal of Materials Research* **2013**, *28*, 3086–3093.

[8] R. Marcilla, F. Alcaide, H. Sardon, J. A. Pomposo, C. Pozo-Gonzalo, D. Mecerreyes, *Electrochemistry Communications* **2006**, *8*, 482–488.

[9] S. Mogurampelly, J. R. Keith, V. Ganesan, *Journal of the American Chemical Society* **2017**, *139*, 9511–9514.

[10] S. Mogurampelly, V. Ganesan, *Macromolecules* **2018**, *51*, 9471–9483.

[11] Y. Kambe, C. G. Arges, S. Patel, M. P. Stoykovish, P. F. Nealey, *The Electrochemical Society Interface* **2017**, *26*, 61–67.

[12] P. W. Majewski, M. Gopinadhan, C. O. Osuji, *Polymers* **2019**, *11*, 887.

[13] R. Mäki-Ontto, K. de Moel, E. Polushkin, G. van Alberda Ekenstein, G. ten Brinke, O. Ikkala, *Advanced Materials* **2002**, *14*, 357–361.

[14] S. H. Kim, M. J. Misner, T. Xu, M. Kimura, T. P. Russell, *Advanced Materials* **2004**, *16*, 226–231.

[15] U. Wiesner, *Macromolecular Chemistry and Physics* **1997**, *198*, 3319–3352.

[16] Z.-R. Chen, A. M. Issaian, J. A. Kornfield, S. D. Smith, J. T. Grothaus, M. M. Satkowski, *Macromolecules* **1997**, *30*, 7096–7114.

[17] H. Leist, D. Maring, T. Thurn-Albrecht, U. Wiesner, *The Journal of Chemical Physics* **1999**, *110*, 8225–8228.

[18] M. J. Park, N. P. Balsara, *Macromolecules* **2010**, *43*, 292–298.

[19] B. L. Riise, G. H. Fredrickson, R. G. Larson, D. S. Pearson, *Macromolecules* **1995**, *28*, 7653–7659.

[20] T. Meins, N. Dingenouts, J. Kübel, M. Wilhelm, *Macromolecules* **2012**, *45*, 7206–7219.

[21] T. Meins, K. Hyun, N. Dingenouts, M. Fotouhi Ardakani, B. Struth, M. Wilhelm, *Macromolecules* **2012**, *45*, 455–472.

[22] M. Szwarc, M. Levy, R. Milkovich, *Journal of the American Chemical Society* **1956**, *78*, 2656–2657.

[23] *Anionic Polymerization: Principles, Practice, Strength, Consequences and Applications*, 1st ed. 2015, (Eds.: N. Hadjichristidis, A. Hirao), Springer, Tokyo, **2015**.

[24] K. Matyjaszewski, *Controlled and Living Polymerizations: From Mechanisms to Applications*, 1st ed., John Wiley & Sons Incorporated, Weinheim, **2009**.

[25] M.-C. Röpert, M. G. Schußmann, M. K. Esfahani, M. Wilhelm, V. Hirschberg, *Macromolecules* **2022**, *55*, 5485–5496.

[26] H. Frey, T. Ishizone, *Macromolecular Chemistry and Physics* **2017**, *218*, 1700217.

[27] PlascticsEurope, *https://plasticseurope.org/wp-content/uploads/2021/10/2018-Plastics-the-facts.pdf* **08.03.2023**.

[28] G. Odian, *Principles of Polymerization*, Wiley-VCH, Weinheim, **2004**.

[29] M. D. Lechner, K. Gehrke, E. H. Nordmeier, *Makromolekulare Chemie*, Springer Berlin Heidelberg, Berlin, Heidelberg, **2014**.

[30] H. R. Kricheldorf, O. Nuyken, G. Swift, *Handbook of Polymer Synthesis*, CRC Press, **2004**.

[31] D. J. Worsfold, S. Bywater, *Macromolecules* **1978**, *11*, 582–586.

[32] B. Tieke, *Makromolekulare Chemie: Eine Einführung*, 3. Auflage, Wiley-VCH, Weinheim, **2014**.

[33] S. Koltzenburg, M. Maskos, O. Nuyken, R. Mülhaupt, K. Matyjaszewski, *Polymer Chemistry*, Springer, Berlin and Heidelberg, **2017**.

[34] J. Chiefari, Y. K. Chong, F. Ercole, J. Krstina, J. Jeffery, T. P. T. Le, R. T. A. Mayadunne, G. F. Meijs, C. L. Moad, G. Moad, E. Rizzardo, S. H. Thang, *Macromolecules* **1998**, *31*, 5559–5562.

[35] M. K. Georges, R. P. N. Veregin, P. M. Kazmaier, G. K. Hamer, *Macromolecules* **1993**, *26*, 2987–2988.

[36] M. Kato, M. Kamigaito, M. Sawamoto, T. Higashimura, *Macromolecules* **1995**, *28*, 1721–1723.

[37] J.-S. Wang, K. Matyjaszewski, *Journal of the American Chemical Society* **1995**, *117*, 5614–5615.

[38] J. Nicolas, Y. Guillaneuf, C. Lefay, D. Bertin, D. Gigmes, B. Charleux, *Progress in Polymer Science* **2013**, *38*, 63–235.

[39] G. Moad, E. Rizzardo, S. H. Thang, *Polymer* **2008**, *49*, 1079–1131.

[40] J. M. Dealy, *Structure and Rheology of Molten Polymers: From Structure to Flow Behavior and Back Again*, Hanser Verlag, München, **2006**.

[41] H. A. Barnes, *A Handbook of Elementary Rheology*, University of Wales Institute of Non-Newtonian Fluid Mechanics, Aberystwyth, **2000**.

[42] A. J. Malkin, *Rheology Fundamentals*, ChemTec Publ, Toronto, Ontario, **1994**.

[43] R. G. Larson, K. I. Winey, S. S. Patel, H. Watanabe, R. Bruinsma, *Rheologica Acta* **1993**, *32*, 245–253.

[44] C. W. Macosko, *Rheology: Principles, Measurements, and Applications*, Wiley-VCH, Weinheim, **1994**.

[45] M. L. Williams, R. F. Landel, J. D. Ferry, *Journal of the American Chemical Society* **1955**, *77*, 3701–3707.

[46] C. Storm, J. J. Pastore, F. C. MacKintosh, T. C. Lubensky, P. A. Janmey, *Nature* **2005**, *435*, 191–194.

[47] T. G. Mason, D. A. Weitz, *Physical Review Letters* **1995**, *75*, 2770–2773.

[48] F. Bossard, M. Moan, T. Aubry, *Journal of Rheology* **2007**, *51*, 1253–1270.

[49] M. Wilhelm, D. Maring, H.-W. Spiess, *Rheologica Acta* **1998**, *37*, 399–405.

[50] M. Wilhelm, P. Reinheimer, M. Ortseifer, *Rheologica Acta* **1999**, *38*, 349–356.

[51] M. Wilhelm, *Macromolecular Materials and Engineering* **2002**, *287*, 83–105.

[52] R. N. Bracewell, *The Fourier Transform and its Applications*, 3. ed., internat. ed., McGraw Hill, Boston, Mass., **2000**.

[53] T. Butz, *Fouriertransformation für Fußgänger*, 7., aktualisierte Auflage, Vieweg+Teubner Verlag, Wiesbaden, **2012**.

[54] W. Ding, J. Hanson, W. R. Burghardt, C. R. López-Barrón, M. L. Robertson, *Macromolecules* **2022**, *55*, 9465–9477.

[55] *Broadband Dielectric Spectroscopy*, (Eds.: F. Kremer, A. Schönhals), Springer, Berlin, **2003**.

[56] N. G. McCrum, B. E. Read, G. Williams, *Anelastic and Dielectric Effects in Polymeric Solids*, Dover ed., Dover, New York, **1991**.

[57] S. Havriliak, S. Negami, *Polymer* **1967**, *8*, 161–210.

[58] W. H. Stockmayer, *Pure and Applied Chemistry* **1967**, *15*, 539–554.

[59] I. W. Hamley, V. Castelletto, *Progress in Polymer Science* **2004**, *29*, 909–948.

[60] A. Guinier, *X-Ray Diffraction: In Crystals, Imperfect Crystals, and Amorphous Bodies*, Wiley-VCH, Weinheim, **2013**.

[61] *Polymer Science: A Comprehensive Reference*, (Eds.: K. Matyjaszewski, M. Möller), Elseiver, Amsterdam, **2012**.

[62] W.H. Bragg, W. L. Bragg, *Proceedings of the Royal Society of London. Series A Containing Papers of a Mathematical and Physical Character* **1913**, *88*, 428–438.

[63] C. M. Bates, F. S. Bates, *Macromolecules* **2017**, *50*, 3–22.

[64] I. W. Hamley, *The Physics of Block Copolymers*, Oxford Univ. Press, Oxford, **2003**.

[65] R. C. Thunell, S. M. Locke, D. F. Williams, *Nature* **0334**, *1988*, 598–601.

[66] J. L. Adams, W. W. Graessley, R. A. Register, *Macromolecules* **1994**, *27*, 6026–6032.

[67] M. D. Gehlsen, K. Almdal, F. S. Bates, *Macromolecules* **1992**, *25*, 939–943.

[68] S. Seiffert, *Physical Chemistry of Polymers: A Conceptual Introduction*, De Gruyter, Berlin and Boston, **2020**.

[69] P. J. Flory, *Principles of Polymer Chemistry*, 19. print, Cornell Univ. Press, Ithaca, NY, **2006**.

[70] R.-J. Roe, M. Fishkis, J. C. Chang, *Macromolecules* **1981**, *14*, 1091–1103.

[71] J. K. Kim, H. H. Lee, Q.-J. Gu, T. Chang, Y. H. Jeong, *Macromolecules* **1998**, *31*, 4045–4048.

[72] C. Oelschlaeger, J. S. Gutmann, M. Wolkenhauer, H.-W. Spiess, K. Knoll, M. Wilhelm, *Macromolecular Chemistry and Physics* **2007**, *208*, 1719–1729.

[73] A. M. Mayes, M. La Olvera de Cruz, *The Journal of Chemical Physics* **1989**, *91*, 7228–7235.

[74] M. W. Matsen, F. S. Bates, *Macromolecules* **1996**, *29*, 1091–1098.

[75] M. W. Matsen, F. S. Bates, *Macromolecules* **1996**, *29*, 7641–7644.

[76] I. W. Hamley, *Journal of Physics: Condensed Matter* **2001**, *13*, 643–671.

[77] A. Masud, M. Longanecker, S. Bhadauriya, M. Singh, W. Wu, K. Sharma, T. Terlier, A. M. Al-Enizi, S. Satija, J. F. Douglas, A. Karim, *Macromolecules* **2021**, *54*, 4531–4545.

[78] Z.-R. Chen, J. A. Kornfield, S. D. Smith, J. T. Grothaus, M. M. Satkowski, *Science* **1997**, *277*, 1248–1253.

[79] M. E. Vigild, C. Chu, M. Sugiyama, K. A. Chaffin, F. S. Bates, *Macromolecules* **2001**, *34*, 951–964.

[80] M. Hoffmann, C. Iacob, G. Kaysan, M. Simmler, H. Nirschl, G. Guthausen, M. Wilhelm, *Polymers* **2022**, *14*, 2423.

[81] M. Hoffmann, A. J. Butzelaar, C. Iacob, P. Theato, M. Wilhelm, *ACS Applied Polymer Materials* **2022**, *4*, 2794–2805.

[82] I. Osada, H. de Vries, B. Scrosati, S. Passerini, *Angewandte Chemie International Edition* **2016**, *55*, 500–513.

[83] F. Xu, S. Deng, Q. Guo, D. Zhou, X. Yao, *Advanced Science* **2021**, *5*, 2100262.

[84] M. Forsyth, L. Porcarelli, X. Wang, N. Goujon, D. Mecerreyes, *Accounts of Chemical Research* **2019**, *52*, 686–694.

[85] L. Miao, Z. Song, D. Zhu, L. Li, L. Gan, M. Liu, *Energy & Fuels* **2021**, *35*, 8443–8455.

[86] K. Karuppasamy, J. Theerthagiri, D. Vikraman, C.-J. Yim, S. Hussain, R. Sharma, T. Maiyalagan, J. Qin, H.-S. Kim, *Polymers* **2020**, *12*, 918.

[87] Y.-S. Ye, J. Rick, B.-J. Hwang, *Journal of Materials Chemistry A* **2012**, *1*, 2719–2743.

[88] T. Stettner, A. Balducci, *Energy Storage Materials* **2021**, *40*, 402–414.

[89] M. A. Ratner, D. F. Shriver, *Chemical Reviews* **1988**, *88*, 109–124.

[90] H. Sasabe, S. Saito, *Polymer Journal* **1972**, *1972*, 624–630.

[91] C. T. Imrie, M. D. Ingram, *Electrochimica Acta* **2001**, *46*, 1413–1417.

[92] A. L. Agapov, A. P. Sokolov, *Macromolecules* **2011**, *44*, 4410–4414.

[93] Z. Wojnarowska, H. Feng, Y. Fu, S. Cheng, B. Carroll, R. Kumar, V. N. Novikov, A. M. Kisliuk, T. Saito, N.-G. Kang, J. W. Mays, A. P. Sokolov, V. Bocharova, *Macromolecules* **2017**, *50*, 6710–6721.

[94] X. Wei, D. F. Shriver, *Chemistry of Materials* **1998**, *10*, 2307–2308.

[95] Y. Wang, A. L. Agapov, F. Fan, K. Hong, X. Yu, J. Mays, A. P. Sokolov, *Physical review letters* **2012**, *108*, 088303.

[96] F. Fan, Y. Wang, T. Hong, M. F. Heres, T. Saito, A. P. Sokolov, *Macromolecules* **2015**, *48*, 4461–4470.

[97] S. Schuhmann, G. Guthausen, *Chemie in unserer Zeit* **2021**, *55*, 236–250.

[98] X. Guo, K. S. Wetzel, S. C. Solleder, S. Spann, M. A. R. Meier, M. Wilhelm, B. Luy, G. Guthausen, *Macromolecular Chemistry and Physics* **2019**, *220*, 1900155.

[99] X. Guo, E. Laryea, M. Wilhelm, B. Luy, H. Nirschl, G. Guthausen, *Macromolecular Chemistry and Physics* **2017**, *218*, 1600440.

[100] X. Guo, S. Theissen, J. Claussen, V. Hildebrand, J. Kamphus, M. Wilhelm, B. Luy, G. Guthausen, *Macromolecular Chemistry and Physics* **2019**, *220*, 1800350.

[101] J. E. Bostwick, C. J. Zanelotti, C. Iacob, A. G. Korovich, L. A. Madsen, R. H. Colby, *Macromolecules* **2020**, *53*, 1405–1414.

[102] E. W. Stacy, C. P. Gainaru, M. Gobet, Z. Wojnarowska, V. Bocharova, S. G. Greenbaum, A. P. Sokolov, *Macromolecules* **2018**, *51*, 8637–8645.

[103] C. Gainaru, E. W. Stacy, V. Bocharova, M. Gobet, A. P. Holt, T. Saito, S. Greenbaum, A. P. Sokolov, *The Journal of Physical Chemistry B* **2016**, *120*, 11074–11083.

[104] H. Tokuda, K. Hayamizu, K. Ishii, M. A. B. H. Susan, M. Watanabe, *The Journal of Physical Chemistry B* **2004**, *108*, 16593–16600.

[105] U. H. Choi, M. Lee, S. Wang, W. Liu, K. I. Winey, H. W. Gibson, R. H. Colby, *Macromolecules* **2012**, *45*, 3974–3985.

[106] U. H. Choi, Y. Ye, D. La Salas de Cruz, W. Liu, K. I. Winey, Y. A. Elabd, J. Runt, R. H. Colby, *Macromolecules* **2014**, *47*, 777–790.

[107] J. R. Sangoro, A. Serghei, S. Naumov, P. Galvosas, J. Kärger, C. Wespe, F. Bordusa, F. Kremer, *Physical Review E* **2008**, *77*, 051202.

[108] S. Emmert, M. Wolf, R. Gulich, S. Krohns, S. Kastner, P. Lunkenheimer, A. Loidl, *The European Physical Journal B* **2011**, *83*, 157–165.

[109] C. Krause, J. R. Sangoro, C. Iacob, F. Kremer, *The Journal of Physical Chemistry B* **2010**, *114*, 382–386.

[110] K. M. Diederichsen, H. G. Buss, B. D. McCloskey, *Macromolecules* **2017**, *50*, 3831–3840.

[111] S. Arrhenius, *Zeitschrift für Physikalische Chemie* **1889**, 226–248.

[112] C. Iacob, J. R. Sangoro, A. Serghei, S. Naumov, Y. Korth, J. Kärger, C. Friedrich, F. Kremer, *The Journal of Chemical Physics* **2008**, *129*, 234511.

[113] P. Kuray, T. Noda, A. Matsumoto, C. Iacob, T. Inoue, M. A. Hickner, J. Runt, *Macromolecules* **2019**, *52*, 6438–6448.

[114] K. Nakamura, K. Fukao, T. Inoue, *Macromolecules* **2012**, *45*, 3850–3858.

[115] C. Iacob, A. Matsumoto, M. Brennan, H. Liu, S. J. Paddison, O. Urakawa, T. Inoue, J. Sangoro, J. Runt, *ACS Macro Letters* **2017**, *6*, 941–946.

[116] J. R. Sangoro, C. Iacob, S. Naumov, R. Valiullin, H. Rexhausen, J. Hunger, R. Buchner, V. Strehmel, J. Kärger, F. Kremer, *Soft Matter* **2011**, *7*, 1678.

[117] J. C. Dyre, *Physics Letters* **1985**, *1985*, 457–461.

[118] J. R. Sangoro, C. Iacob, A. L. Agapov, Y. Wang, S. Berdzinski, H. Rexhausen, V. Strehmel, C. Friedrich, A. P. Sokolov, F. Kremer, *Soft Matter* **2014**, *10*, 3536–3540.

[119] M. Gordon, J. S. Taylor, *Journal of Applied Chemistry* **1952**, *2*, 493–500.

[120] R. G. Fox, *Bulletin of the American Physical Society* **1956**, 123.

[121] A. J. Peltekoff, V. E. Hiller, G. P. Lopinski, O. A. Melville, B. H. Lessard, *ACS Applied Polymer Materials* **2019**, *1*, 3210–3221.

[122] Y. Ye, J.-H. Choi, K. I. Winey, Y. A. Elabd, *Macromolecules* **2012**, *45*, 7027–7035.

[123] B. K. Wheatle, J. R. Keith, S. Mogurampelly, N. A. Lynd, V. Ganesan, *ACS Macro Letters* **2017**, *6*, 1362–1367.

[124] J. Imbrogno, K. Maruyama, F. Rivers, J. R. Baltzegar, Z. Zhang, P. W. Meyer, V. Ganesan, S. Aoshima, N. A. Lynd, *ACS Macro Letters* **2021**, *10*, 1002–1007.

[125] M.-M. Huang, Y. Jiang, P. Sasisanker, G. W. Driver, H. Weingärtner, *Journal of Chemical & Engineering Data* **2011**, *56*, 1494–1499.

[126] B. K. Wheatle, E. F. Fuentes, N. A. Lynd, V. Ganesan, *Macromolecules* **2020**, *53*, 9449–9459.

[127] O. Green, S. Grubjesic, S. Lee, M. A. Firestone, *Polymer Reviews* **2009**, *49*, 339–360.

[128] A. F. Visentin, S. Alimena, M. J. Panzer, *ChemElectroChem* **2014**, *1*, 718–721.

[129] A. J. D'Angelo, M. J. Panzer, *The Journal of Physical Chemistry B* **2017**, *121*, 890–895.

[130] J. Yuan, M. Antonietti, *Polymer* **2011**, *52*, 1469–1482.

[131] M. Brinkkötter, E. I. Lozinskaya, D. O. Ponkratov, P. S. Vlasov, M. P. Rosenwinkel, I. A. Malyshkina, Y. Vygodskii, A. S. Shaplov, M. Schönhoff, *Electrochimica Acta* **2017**, *237*, 237–247.

[132] M. Brinkkötter, E. I. Lozinskaya, D. O. Ponkratov, Y. Vygodskii, D. F. Schmidt, A. S. Shaplov, M. Schönhoff, *The Journal of Physical Chemistry C* **2019**, *123*, 13225–13235.

[133] S. Sen, S. E. Goodwin, P. V. Barbará, G. A. Rance, D. Wales, J. M. Cameron, V. Sans, M. Mamlouk, K. Scott, D. A. Walsh, *ACS Applied Polymer Materials* **2021**, *3*, 200–208.

[134] F. Zhang, Y. Sun, Z. Wang, D. Fu, J. Li, J. Hu, J. Xu, X. Wu, *ACS Applied Materials & Interfaces* **2020**, *12*, 23774–23780.

[135] Y. Lu, C.-Z. Zhao, H. Yuan, X.-B. Cheng, J.-Q. Huang, Q. Zhang, *Advanced Functional Materials* **2021**, *31*, 2009925.

[136] M. Watanabe, S. Nagano, K. Sanui, N. Ogata, *Solid State Ionics* **1988**, *28-30*, 911–917.

[137] J. Evans, C. A. Vincent, P. G. Bruce, *Polymer* **1987**, *28*, 2324–2328.

[138] X. Guo, C. Pfeifer, M. Wilhelm, B. Luy, G. Guthausen, *Macromolecular Chemistry and Physics* **2019**, *220*, 1800525.

[139] B. G. Ndefru, B. S. Ringstrand, S. I.-Y. Diouf, S. Seifert, J. H. Leal, T. A. Semelsberger, T. A. Dreier, M. A. Firestone, *Molecular Systems Design & Engineering* **2019**, *4*, 580–585.

[140] P. Barai, K. Higa, V. Srinivasan, *Physical Chemistry Chemical Physics* **2017**, *19*, 20493–20505.

[141] C. Monroe, J. Newman, *Journal of The Electrochemical Society* **2005**, *152*, A396.

[142] O. Oparaji, S. Narayanan, A. Sandy, S. Ramakrishnan, D. Hallinan, *Macromolecules* **2018**, *51*, 2591–2603.

[143] D. Bresser, S. Lyonnard, C. Iojoiu, L. Picard, S. Passerini, *Molecular Systems Design & Engineering* **2019**, *4*, 779–792.

[144] M. J. Monteiro, F. F. C. Bazito, L. J. A. Siqueira, M. C. C. Ribeiro, R. M. Torresi, *The Journal of Physical Chemistry B* **2008**, *112*, 2102–2109.

[145] M. S. Ding, T. Richard Jow, *Journal of The Electrochemical Society* **2004**, *151*, 2007–2015.

[146] J. Skolnick, M. Fixman, *Macromolecules* **1977**, *10*, 944–948.

[147] A. Fdz De Anastro, L. Porcarelli, M. Hilder, C. Berlanga, M. Galceran, P. Howlett, M. Forsyth, D. Mecerreyes, *ACS Applied Energy Materials* **2019**, *2*, 6960–6966.

[148] L. Porcarelli, A. S. Shaplov, F. Bella, J. R. Nair, D. Mecerreyes, C. Gerbaldi, *ACS Energy Letters* **2016**, *1*, 678–682.

[149] J. Gao, C. Wang, D.-W. Han, D.-M. Shin, *Chemical Science* **2021**, *12*, 13248–13272.

[150] C. H. Krause, A. J. Butzelaar, D. Diddens, D. Dong, P. Théato, D. Bedrov, B.-J. Hwang, M. Winter, G. Brunklaus, *Journal of Power Sources* **2021**, *484*, 229267.

[151] Y. Zhao, L. Wang, Y. Zhou, Z. Liang, N. Tavajohi, B. Li, T. Li, *Advanced Science* **2021**, *8*, 2003675.

[152] C.-H. Tsao, H.-M. Su, H.-T. Huang, P.-L. Kuo, H. Teng, *Journal of Membrane Science* **2019**, *572*, 382–389.

[153] A. J. Butzelaar, P. Röring, T. P. Mach, M. Hoffmann, F. Jeschull, M. Wilhelm, M. Winter, G. Brunklaus, P. Théato, *ACS Applied Materials & Interfaces* **2021**, *13*, 39257–39270.

[154] A. J. Butzelaar, K. L. Liu, P. Röring, G. Brunklaus, M. Winter, P. Theato, *ACS Applied Polymer Materials* **2021**, *3*, 1573–1582.

[155] G. Mao, M.-L. Saboungi, D. L. Price, M. B. Armand, W. S. Howells, *Physical Review Letters* **2000**, *84*, 5536–5539.

[156] Z. Xue, D. He, X. Xie, *Journal of Materials Chemistry A* **2015**, *3*, 19218–19253.

[157] B. Xu, X. Li, C. Yang, Y. Li, N. S. Grundish, P.-H. Chien, K. Dong, I. Manke, R. Fang, N. Wu, H. Xu, A. Dolocan, J. B. Goodenough, *Journal of the American Chemical Society* **2021**, *143*, 6542–6550.

[158] J. Atik, D. Diddens, J. H. Thienenkamp, G. Brunklaus, M. Winter, E. Paillard, *Angewandte Chemie International Edition* **2021**, *60*, 11919–11927.

[159] M. Hoffmann, H. Hirschberg, N. Dingenouts, M. Wilhelm, *Macromolecules* **2023**, *24*, 10236–10253.

[160] B. J. Rancatore, C. E. Mauldin, S.-H. Tung, C. Wang, A. Hexemer, J. Strzalka, J. M. J. Fréchet, T. Xu, *ACS Nano* **2010**, *4*, 2721–2729.

[161] Z.-R. Chen, J. A. Kornfield, *Polymer* **1998**, *39*, 4679–4699.

[162] S. S. Patel, R. G. Larson, K. I. Winey, H. Watanabe, *Macromolecules* **1995**, *28*, 4313–4318.

[163] L. Wu, T. P. Lodge, F. S. Bates, *Journal of Rheology* **2005**, *49*, 1231–1252.

[164] V. K. Gupta, R. Krishnamoorti, J. A. Kornfield, S. D. Smith, *Macromolecules* **1995**, *28*, 4464–4474.

[165] V. K. Gupta, R. Krishnamoorti, Z.-R. Chen, J. A. Kornfield, S. D. Smith, M. M. Satkowski, J. T. Grothaus, *Macromolecules* **1996**, *29*, 875–884.

[166] B. Struth, K. Hyun, E. Kats, T. Meins, M. Walther, M. Wilhelm, G. Grübel, *Langmuir* **2011**, *27*, 2880–2887.

[167] E. Polushkin, S. Bondzic, J. de Wit, G. van Alberda Ekenstein, I. Dolbnya, W. Bras, O. Ikkala, G. ten Brinke, *Macromolecules* **2005**, *38*, 1804–1813.

[168] S. Okamoto, K. Saijo, T. Hashimoto, *Macromolecules* **1994**, *27*, 5547–5555.

[169] R. Kádár, M. Abbasi, R. Figuli, M. Rigdahl, M. Wilhelm, *Nanomaterials* **2017**, *7*, 23.

[170] S. Capaccioli, D. Prevosto, A. Best, A. Hanewald, T. Pakula, *Journal of Non-Crystalline Solids* **2007**, *353*, 4267–4272.

[171] K. Negita, H. Kaneko, *Physical Review E* **2009**, *80*, 011705.

[172] H. Watanabe, Y. Matsumiya, T. Inoue, *Journal of Physics: Condensed Matter* **2003**, *15*, 909–921.

[173] K. Hyun, S. Höfl, S. Kahle, M. Wilhelm, *Journal of Non-Newtonian Fluid Mechanics* **2009**, *160*, 93–103.

[174] K. Reinheimer, M. Grosso, M. Wilhelm, *Journal of Colloid and Interface Science* **2011**, *360*, 818–825.

[175] K. Reinheimer, M. Grosso, F. Hetzel, J. Kübel, M. Wilhelm, *Journal of Colloid and Interface Science* **2012**, *380*, 201–212.

[176] F. A. Morrison, H. H. Winter, *Macromolecules* **1989**, *22*, 3533–3540.

[177] L. Wu, T. P. Lodge, F. S. Bates, *Macromolecules* **2004**, *37*, 8184–8187.

[178] V. Hirschberg, L. Faust, D. Rodrigue, M. Wilhelm, *Macromolecules* **2020**, *53*, 5572–5587.

[179] L. Wu, E. W. Cochran, T. P. Lodge, F. S. Bates, *Macromolecules* **2004**, *37*, 3360–3368.

[180] H. Watanabe, *Progress in Polymer Science* **1999**, *24*, 1253–1403.

[181] H. Watanabe, *Macromolecules* **1995**, *28*, 5006–5011.

[182] H. Watanabe, O. Urakawa, T. Kotaka, *Macromolecules* **1993**, *26*, 5073–5083.

[183] N. Hadjichristidis, H. Iatrou, S. Pispas, M. Pitsikalis, *Journal of Polymer Science Part A: Polymer Chemistry* **2000**, *38*, 3211–3234.

[184] N. Politakos, I. Moutsios, G.-M. Manesi, K. Artopoiadis, K. Tsitoni, D. Moschovas, A. A. Piryazev, D. S. Kotlyarskiy, G. Kortaberria, D. A. Ivanov, A. Avgeropoulos, *Polymers* **2021**, *13*.

[185] H. Frielinghaus, N. Hermsdorf, K. Almdal, K. Mortensen, L. Messé, L. Corvazier, J. P. A. Fairclough, A. J. Ryan, P. D. Olmsted, I. W. Hamley, *Europhysics Letters* **2001**, *53*, 680.

[186] A. Arora, N. Pillai, F. S. Bates, K. D. Dorfman, *Polymer* **2018**, *154*, 305–314.

[187] B. Abu-Sharkh, A. AlSunaidi, *Macromolecular Theory and Simulations* **2006**, *15*, 507–515.

[188] P. Georgopanos, U. A. Handge, C. Abetz, V. Abetz, *Polymer* **2016**, *104*, 279–295.

[189] K. Adachi, T. Kotaka, *Pure and Applied Chemistry* **1997**, *69*, 125–130.

[190] Y. Zhang, U. Wiesner, *Macromolecular Chemistry and Physics* **1998**, *199*, 1771–1784.

[191] I. Alig, G. Floudas, A. Avgeropoulos, N. Hadjichristidis, *Macromolecules* **1997**, *30*, 5004–5011.

[192] K. Hyun, M. Wilhelm, *Macromolecules* **2009**, *42*, 411–422.

[193] M. A. Cziep, M. Abbasi, M. Heck, L. Arens, M. Wilhelm, *Macromolecules* **2016**, *49*, 3566–3579.

[194] C. Iacob, M. Heck, M. Wilhelm, *Macromolecules* **2023**, *56*, 188–197.

[195] M. Langela, U. Wiesner, H. W. Spiess, M. Wilhelm, *Macromolecules* **2002**, *35*, 3198–3204.

[196] W. R. Leo, *Techniques for Nuclear and Particle Physics Experiments: A How-to Approach*, 1st ed., Springer, Berlin/Heidelberg, **1994**.

[197] T. Meins, *In-situ Investigation of the Shear-Induced Alignment of Diblock Copolymer Melts using Rheo-SAXS, Rheo-Dielectric and FT-Rheology*, Karlsruhe, **2011**.

[198] Y. Matsumiya, Q. Chen, A. Uno, H. Watanabe, A. Takano, K. Matsuoka, Y. Matsushita, *Macromolecules* **2012**, *45*, 7050–7060.

[199] M. W. Matsen, R. B. Thompson, *The Journal of Chemical Physics* **1999**, *111*, 7139–7146.

[200] V. Ganesan, G. H. Fredrickson, *Journal of Rheology* **2001**, *45*, 161–185.

[201] T. J. Hermel, L. Wu, S. F. Hahn, T. P. Lodge, F. S. Bates, *Macromolecules* **2002**, *35*, 4685–4689.

[202] J. M. Virgili, A. Hexemer, J. A. Pople, N. P. Balsara, R. A. Segalman, *Macromolecules* **2009**, *42*, 4604–4613.

[203] P. M. Carrasco, A. Ruiz de Luzuriaga, M. Constantinou, P. Georgopanos, S. Rangou, A. Avgeropoulos, N. E. Zafeiropoulos, H.-J. Grande, G. Cabañero, D. Mecerreyes, I. Garcia, *Macromolecules* **2011**, *44*, 4936–4941.

[204] T.-L. Chen, P. M. Lathrop, R. Sun, Y. A. Elabd, *Macromolecules* **2021**, *54*, 8780–8797.

[205] A. J. Butzelaar, P. Röring, M. Hoffmann, J. Atik, E. Paillard, M. Wilhelm, M. Winter, G. Brunklaus, P. Theato, *Macromolecules* **2021**, *54*, 11101–11112.

[206] M. L. Hoarfrost, M. S. Tyagi, R. A. Segalman, J. A. Reimer, *Macromolecules* **2012**, *45*, 3112–3120.

[207] C. G. Arges, Y. Kambe, H. S. Suh, L. E. Ocola, P. F. Nealey, *Chemistry of Materials* **2016**, *28*, 1377–1389.

[208] J. M. Virgili, M. L. Hoarfrost, R. A. Segalman, *Macromolecules* **2010**, *43*, 5417–5423.

[209] I. Gunkel, T. Thurn-Albrecht, *Macromolecules* **2012**, *45*, 283–291.

[210] M. Heck, L. Schneider, M. Müller, M. Wilhelm, *Macromolecular Chemistry and Physics* **2018**, *219*, 1700559.

[211] W. Zha, C. D. Han, D. H. Lee, S. H. Han, J. K. Kim, J. H. Kang, C. Park, *Macromolecules* **2007**, *40*, 2109–2119.

[212] S. Sharick, J. Koski, R. A. Riggleman, K. I. Winey, *Macromolecules* **2016**, *49*, 2245–2256.

[213] J.-H. Choi, W. Xie, Y. Gu, C. D. Frisbie, T. P. Lodge, *ACS Applied Materials & Interfaces* **2015**, *7*, 7294–7302.

[214] A. W. May, Z. Shi, D. B. Wijayasekara, D. L. Gin, T. S. Bailey, *Polymer Chemistry* **2019**, *10*, 751–765.

[215] J. Tang, H. Tang, W. Sun, H. Plancher, M. Radosz, Y. Shen, *Chemical Communications* **2005**, 3325–3327.

[216] S. Biria, S. Pathreeker, F. S. Genier, I. D. Hosein, *ACS Applied Polymer Materials* **2020**, *2*, 2111–2118.

[217] T. C. Huang, H. Toraya, T. N. Blanton, Y. Wu, *Journal of Applied Crystallography* **1993**, *26*, 180–184.

[218] P. W. Kuchel, G. Pagès, K. Nagashima, S. Velan, V. Vijayaragavan, V. Nagarajan, K. H. Chuang, *Concepts in Magnetic Resonance Part A* **2012**, *40*, 205–214.

[219] E. O. Stejskal, J. E. Tanner, *The Journal of Chemical Physics* **1965**, *42*, 288–292.

[220] C. Ammann, P. Meier, A. E. Merbach, *Journal of Magnetic Resonance* **1982**, *46*, 319–321.

[221] A. Abou Elfadl, R. Kahlau, A. Herrmann, V. N. Novikov, E. A. Rössler, *Macromolecules* **2010**, *43*, 3340–3351.

Appendix

A.1 Materials and Methods

A.1.1 Materials and Purification

Purification of solvents and monomers for the anionic polymerization as well as the anionic polymerization itself were carried out under argon protection using standard Schlenk techniques.[23]

A.1.1.1 Purification of Monomers

Orientation of Block Copolymers

Prior to purification, all monomers were degassed by three freeze-pump-thaw cycles.
Styrene (99 %, Acros) for anionic polymerization was purified by stirring over calcium hydride (CaH_2, 93 %, Acros) over night, distilled at reduced pressure and then distilled from di-*n*-butylmagnesium (di-*n*-BuMg; Sigma-Aldrich, 1 M in heptane) into Schlenk-type ampoules.
Isoprene (>98 %, stabilized with 100 to 250 ppm 4-tert-butylcatechol, Acros) was purified using *n*-butyllithium (*n*-BuLi) while cooling with an ice bath and distillation at reduced pressure was started as soon as the solution turned yellow.
The purified monomers were stored under argon protection in the refrigerator at −18 °C until needed.

Orientation of Ion-Conductive Block Copolymers

Styrene (99 %, Acros) and 4-vinylbenzylchloride (90 %, stabilized with 500 ppm *tert*-butylcatechol, Sigma Aldrich) for RAFT polymerization were purified by running through a basic alumina oxide column prior to use. The purified monomers were stored at −18 °C.

A.1.1.2 Purification of Solvents

Orientation of Block Copolymers

Cyclohexane (>99 %, Fisher Scientific) was dried using *n*-BuLi with living PS as an indicator. It was distilled under reduced pressure prior to use.
Tetrahydrofuran (THF, 99 %, Acros) was stirred over CaH_2 overnight. After distillation it was stored over sodium/benzophenone and refluxed until a purple color was observed. The required amount of solvent was distilled as needed.

Methanol (MeOH, >99 %, Acros) was degassed by three successive freeze-pump-thaw cycles.

A.1.1.3 Further Chemicals

Blends of PolyILs and ILs

4-Vinylbenzylchloride (90 %, stabilized with 500 ppm *tert*-butylcatechol, Sigma-Aldrich), 1-butylimidazole (>90 %, Alfa Aesar), acetonitrile (>99.7 %, VWR), 2,6-di-*tert*-butyl-4-methylphenol (BHT, for synthesis, Merck), diethyl ether (99.5 %, stabilized with BHT, Acros), lithium bis(trifluoromethanesulfonyl)methylpropionitrile (LiTFSI, >99 %, Acros), acetone (>99.5 %, Acros), *n*-pentane (>99 %, VWR), 2,2'-azobis(2-methylpropionitrile) (AIBN, 98 %, Merck), dimethylformamide (DMF, 99.8 %, Acros), methanol (MeOH, >99 %, Acros) and tetrahydrofuran (THF, >99 %, Acros Organics) were used as received.

Ionogels

4-Vinylbenzylchloride (90 %, stabilized with 500 ppm *tert*-butylcatechol, Sigma-Aldrich), 1-butylimidazole (>90 %, Alfa Aesar), 1-vinylimidazole (>99 %, Sigma-Aldrich), acetonitrile (>99.7 %, VWR), 2,6-di-*tert*-butyl-4-methylphenol (BHT, for synthesis, Merck), diethyl ether (99.5 %, stabilized with BHT, Acros), lithium bis(trifluoromethane sulfonyl)imide (LiTFSI, >99 %, Acros), acetone (>99.5 %, Acros), *n*-pentane (>99 %, VWR), methanol (MeOH, >99 %), ethyl acetate (>99.5 %, VWR), poly(ethylene glycol)diacrylate (PEGDA, >99 %, Sigma-Aldrich, $M_n = 575\,\mathrm{g\,mol^{-1}}$, 10 repetition units on average, 600 ppm MEHQ as inhibitor), 2-hydroxy-2-methylpropiophenone (DAROCUR, 98 %, Fisher Scientific), 1-butyl-3-methylimidazolium bis(trifluoromethane sulfonyl)imide ([BMIM]TFSI, >99 %, ioLiTec), and tetrahydrofuran (99 %, Acros) were used as received.

Orientation of Block Copolymers

S-butyllithium (*s*-BuLi, 1.3 M in cyclohexane, Fisher Scientific), *n*-butyllithium (*n*-BuLi, 1.4 M in cyclohexane, Fisher Scientific), butylated hydroxytoluene (BHT, for synthesis, Merck), α,α'-dibrom-p-xylol (97 %, Fisher Scientific) and isopropanol (>99.5 %, Fisher Scientific) were used as received.

Orientation of Ion-Conductive Block Copolymers

2-Cyano-2-propyldodecyltrithiocarbonat (CPDT, 97 %, Sigma-Aldrich), 4-vinylbenzylchloride (90 %, stabilized with 500 ppm *tert*-butylcatechol, Sigma-Aldrich), 1-butylimidazole (>90 %, Alfa Aesar), dimethylformamide (99.8 %, Acros), 1,4-Dioxane (>99.8 %, Fisher Scientific), lithium bis(trifluoromethane sulfonyl)imide (LiTFSI, >99 %, Acros), acetone (>99.5 %, Acros) and cyclohexane (>99 %, Fisher Scientific) were used as received.

A.1.2 Synthesis

Blends of PolyILs and ILs

The synthesis of poly[VBBI]TFSI was adapted from Tang *et al.*[215] The IL was synthesized

by nucleophilic substitution followed by anion exchange. It was then polymerized by radical polymerization to give the corresponding PolyIL.

[VBBI]Cl. 13.1 mL 4-vinylbenzylchloride, 15.5 mL 1-butylimidazole, 30 mL acetonitrile and 0.1 g BHT were mixed and stirred under argon at 45 °C for 24 h. The resulting light yellow solution was poured into 400 mL of diethylether and stirred for 30 min. The phases were separated and the viscous phase was washed twice with diethylether. The viscous liquid was dried under reduced pressure and a transparent, very viscous material was obtained. Purity was confirmed by ^{1}H-NMR.

[VBBI]TFSI. 23.1 g [VBBI]Cl and 0.1 g BHT were dissolved in 50 mL acetone and a solution of 24 g LiTFSI in 50 mL acetone was slowly added. The mixture was stirred overnight at room temperature, filtered and the solvent was removed under reduced pressure (<50 mbar). The yellow oil was washed with an excess of water, dissolved in acetone and precipitated in pentane. The phases were separated and the viscous oil was dried under reduced pressure at 50 °C. Purity was confirmed by ^{1}H-NMR and the spectrum is displayed in Figure A.2.1, p. 134.

Poly[VBBI]TFSI. 2 g [VBBI]TFSI, 2 mg 2,2'-azobis(2-methylpropionitrile) (AIBN), and 2 mL dimethylformamide (DMF) were mixed and stirred for 7 h at 75 °C. The polymer was precipitated in deionized water, dissolved in acetone and precipitated in deionized water. It was dissolved in methanol and dialyzed against methanol for two days using Spectra/Por® 7 dialysis tubes (Roth, MWCO 1000). The polymer was dried under reduced pressure at 50 °C and the purity was confirmed by ^{1}H-NMR and the spectrum is displayed in Figure A.2.2, p. 134.

Ionogels

The IL-M was prepared as described in the previous section, see [VBBI]TFSI. The synthesis of the IL-CL followed the same procedure but used 1-vinylimidazole instead of 1-butylimidazole. The IGs were prepared by UV-induced photopolymerization (UV lamp from Analytik Jena, 100 W, 365 nm). Before the polymerization procedure, the corresponding amounts of PEGDA or [VBVI]TFSI as IL-CL, [VBBI]TFSI as IL-M, [BMIM]TFSI and LiTFSI as IL-E and DAROCUR as the radical photoinitiator were mixed for 3 h.[134,216] Then, the samples were transferred into a custom-built Teflon mold (15 mm diameter); see Figure 4.12, p. 51. After UV polymerization for 10 min, self-standing, transparent, yellow films with a diameter of 15 mm and a thickness of 0.5 mm were obtained.

Orientation of Block Copolymers

All samples were synthesized via sequential anionic polymerization using high vacuum technique at room temperature using cyclohexane as solvent and *s*-BuLi as initiator, see Figure 5.2, p. 71, and 5.3, p. 71. The polymerization of SIIS was adapted from Watanabe *et al.*[181] and is depicted in Scheme 5.3, p. 71. First, SI^- was synthesized which was then coupled using α,α'-dibrom-p-xylol dissolved in dry THF. Subsequently, the uncoupled diblock was removed by several fractionation cycles in cyclohexane and isopropanol to obtain monodisperse SIIS, see Figure A.2.8. A detailed description of the synthetic procedures

can be found in the literature.[181,183] After the synthesis, the samples were precipitated in methanol, redissolved in cyclohexane and 0.1 wt% BHT was added as a stabilizer before freeze-drying.

Orientation of Ion-Conductive Block Copolymers

PS-*b*-P2VP doped with IL

PS-*b*-P2VP has been synthesized by anionic polymerization prior to this thesis ($M_{n,total}$ = 15 000 g mol^{-1}).[210] For this thesis, the respective amounts of PS-*b*-P2VP and [BMIM]TFSI were dissolved in dioxane and stirred over night. Then, the samples were freeze dried.

PS-*b*-Poly[VBBI]TFSI

The synthesis was adapted from Chen *et al.*[204] and is shown in Figure 6.8, p. 102.

PS-Macro-CTA. First, the PS macro-chain transfer agent (CTA) was synthesized. For this, 0.199 g 2-cyano-2-propyldodecyltrithiocarbonat and 0.022 g AIBN were dissolved in 3.5 mL dioxane. Then, 16.5 mL styrene were added, the flask was sealed with a rubber septum and purged with nitrogen for 20 min. The solution was stirred for 23 h at 80 °C and the polymerization was stopped by placing the flask in the freezer. The solution was diluted with 3 mL THF. Then, the polymer was precipitated in MeOH and dried at 40 °C under reduced pressure. The molecular weight of the PS Macro-CTA was determined by SEC ($M_{n,PS}$ =12 000 g mol^{-1}).

PS-*b*-Poly(vinylbenzylchloride) (PS-*b*-PolyVBC). For the synthesis of the second block, 4 g of PS-Macro-CTA and 0.028 g AIBN were dissolved 25 mL dioxane. Then, 2.8 mL 4-vinylbenzylchloride were added, the flask was sealed with a rubber septum and purged with nitrogen for 20 min. The polymerization was carried out for 23 h at 80 °C and was stopped by placing the flask in the freezer. The solution was diluted with 3 mL of THF. Then, the polymer was precipitated in MeOH and dried at 40 °C under reduced pressure. The molecular weight of the second block was determined by ^{1}H-NMR ($M_{n,PolyVBC}$ =14 000 g mol^{-1}).

PS-*b*-Poly(vinylbenzylbutylimidazolium chloride)(PS-*b*-Poly[VBBI]Cl). 2 g PS-*b*-PolyVBC and 2 g 1-butylimidazole were added to 8 mL DMF. The flask was sealed with a rubber septum and the solution was stirred at 80 °C for 48 h. The polymer was precipitated in cyclohexane, washed with cyclohexane, washed with acetone and dried at 40 °C under reduced pressure.

PS-*b*-Poly(vinylbenzylbutylimidazolium bis(trifluoromethyl sulfonyl)imide) (PS-*b*-Poly[VBBI]TFSI). 2 g PS-*b*-P[VBBI]Cl and 2 g LiTFSI were dissolved in 15 mL DMF. The flask was sealed with a rubber septum and the solution was stirred for 48 h at 50 °C. The polymer was precipitated in methanol and distilled water (50/50 v/v), washed with distilled water and dried at 40 °C under reduced pressure.

A.1.3 Characterization Techniques

A.1.3.1 Dynamic Scanning Calorimetry

All DSC measurements were performed on a DSC G200 (TA Instruments). All measurements were performed at a heating rate of 10 K min^{-1} under nitrogen atmosphere. The

T_gs were determined from the inflection point of the second heating cycle.

A.1.3.2 SEC-MALLS

Polymerized Ionic Liquid

The number and weight average molecular weights (M_n and M_w) of the PolyIL were determined by size exclusion chromatography (SEC). The Agilent system was equipped with an iso-pump (1100 series), an UV detector (1200 series), a differential refractive index detector (1200 series), a PSS SLD 7000 MALLS detector and two PSS SDV Lux 8x300 mm columns. The column materials possessed a mean effective pore size diameter of 1×10^3 Å and 1×10^5 Å, respectively. For the analysis, the polymer was dissolved in a solution of 10 mM 1-butylimidazole and 10 mM LiTFSI in THF, which was also used as eluent, and was analyzed at room temperature with a flow rate of $1\,\mathrm{mL\,min^{-1}}$.[12] The absolute molecular weight was obtained using the multi angle laser light scattering (MALLS) detector and therefore, the refractive index increment (dn/dc) was determined with a refractometer dn/dc 2010 from PSS (Mainz, Germany) using ten different solutions from $1\,\mathrm{g\,L^{-1}}$ to $10\,\mathrm{g\,L^{-1}}$ PolyIL in a solution of 10 mM 1-butylimidazole and 10 mM LiTFSI in THF ($\mathrm{dn/dc} = 0.1027\,\mathrm{mL\,g^{-1}}$). Prior to the measurements, the different solutions were filtered two times through a 0.2 µm PVDF membrane. The molecular weight of the PolyIL was $M_n = 57\,000\,\mathrm{g\,mol^{-1}}$, $M_w = 129\,000\,\mathrm{g\,mol^{-1}}$ and $Đ = 2.25$.

Orientation of Block Copolymers

For the characterization of the first block, an Agilent system, equipped with an iso-pump (1100 series), a UV detector (1200 series), a differential refractive index (DRI) detector (1200 series), a PSS SLD 7000 MALLS detector and two PSS SDV Lux 8x300 mm columns (pore size of 1×10^3 Å and 1×10^5 Å), was used. For the analysis, the polymer was dissolved in THF, which was also used as an eluent and was analyzed at room temperature with a flow rate of $1\,\mathrm{mL\,min^{-1}}$. The calibration was performed using PS or PI standards (Polymer Standard Service, Mainz, Germany) for the first block of SIIS or ISI, respectively.

A.1.3.3 ^{1}H-NMR

Ionic Liquid Based (Charged) Compounds

^{1}H-NMR spectra at 400 MHz were recorded on a Bruker Ascend 400 NMR spectrometer at 25 °C in deuterated chloroform dimethyl sulfoxide (DMSO).

Non-Charged Compounds

^{1}H-NMR spectra at 400 MHz were recorded on a Bruker Ascend 400 NMR spectrometer at 25 °C in deuterated $CHCl_3$.

A.1.3.4 Fourier-Transform Infrared Spectroscopy

Fourier-transform infrared (FTIR) measurements were performed on a VERTEX 70

(Bruker) spectrometer using a diamond ATR crystal from 600 cm^{-1} to 4000 cm^{-1} at 25 °C. As a detector, a liquid nitrogen cooled MCT detector was used.

A.1.3.5 Thermal Gravimetric Analysis

Thermal gravimetric analysis (TGA) measurements were performed on a TGA 5500 (TA Instruments) from 30 °C to 800 °C with a heating rate of 10 °C under air.

A.1.3.6 Lithium-Transference Number (t_{Li^+})

The Li^+-ion transference number (t_{Li^+}) was determined using a VMP-300 potentiostat (BioLogic Science Instruments) at 40 °C. Symmetrical Li|SPE|Li cells were assembled and conditioned for 1 h. Impedance measuremnts were conducted every 4 h for a total of 20 h to 40 h to follow interface formation and guaranteeing a stable SEI between the SPE and lithium metal (from Honjo metal, thickness of 300 µm). Impedance measurements were performed starting at 1 MHz measuring down to 100 mHz with an amplitude of 10 mV. Then, a direct current potential with a polarization voltage of $\Delta V = 10$ mV was applied and the impedance was measured directly before and after the polarization. The calculation of t_{Li^+} is explained in the appendix in Section A.2.2.

A.1.3.7 Lithium Plating and Stripping

Lithium plating and stripping tests were performed on a VMP-300 potentiostat (BioLogic Science Instruments) at 60 °C using symmetric Li|SPE|Li cells. The cells were conditioned for 2 h before lithium plating and stripping experiments were performed with alternating CDs. The CDs were increased stepwise for each cycle starting with a CD of 0.05 mA cm^{-2} to 0.1 mA cm^{-2}, 0.2 mA cm^{-2}, 0.3 mA cm^{-2} and so forth, until a short circuit was observed or the safety limits (±5 V) were reached. Before long-term plating and stripping, the cells were conditioned for five cycles with a CD of 0.05 mA cm^{-2}. Then, lithium was plated and stripped for 1 h with a CD of 0.1 mA cm^{-2} over 53 cycles (106 h) at 30 °C and 60 °C.

A.1.3.8 Small Angle X-Ray Scattering

Orientation of (Ion-Conductive) Block Copolymers

The morphology of the samples was investigated by 2D-SAXS measurements using a Hecus S3-micro X-ray system with a point microfocus source, 2D X-ray mirrors and a two-dimensional CCD detector from Photonic science (q-range from 0.06 nm^{-1} to 4.7 nm^{-1}). By using a block collimation system, a low background scattering was ensured but only half of the 2D-SAXS pattern could be recorded. However, SAXS patterns obey point symmetry so that no relevant information is lost. After the orientation by LAOS, the sample was cooled down to room temperature in the rheometer and the axial force was kept constant to prevent any structural changes until the orientation of the sample was frozen by reaching T_g of the PS block. Then, the sample was carefully removed from the geometries. Before the SAXS measurements, small squares of ca. 2 x 2 mm were cut out at a radius of 10 mm.[20,210] The macroscopic orientation of these pieces was determined

by SAXS measurements along the three major directions (normal to the surface, radial and tangential in the disc plane). 2D spectra were radially and azimuthally averaged using self-developed plugins for ImageJ including correction for absorption and primary beam intensity. Normalization of the q-range was done using crystalline silver behenate as a standard.[217]

A.1.3.9 Wide Angle X-Ray Scattering

Wide angle X-ray scattering (WAXS) measurements were performed on a Xeuss 2.0 (Xenocs, Grenoble, France) system with a point collimated X-ray beam ($0.8 \times 0.8\,\mathrm{mm}^2$), monochromatized on Cu-K-alpha ($\lambda = 0.154\,\mathrm{nm}$) and focused on the detection plane at a sample detector distance of 80 mm. The samples were transferred into a gel capsule (diameter: 4 mm, thickness: 1 mm) with polyimide foils (Kapton) as windows. The scattering intensity $I(q)$ was measured for 1800 s and detected by a 2D-detector (PILATUS 100K-S, Dectris, Baden, Switzerland, q-range from $0.001\,\mathrm{nm}^{-1}$ to $4.0\,\mathrm{nm}^{-1}$). The Kapton background was subtracted from the data after normalization to the primary beam.

A.1.3.10 Pulsed-Field Gradient Nuclear Magnetic Resonance Spectroscopy

A 400 MHz spectrometer (Bruker Avance Neo 400 WB) equipped with a DiffBB probe was used for the PFG-NMR measurements. Dry [VBBI]TFSI was directly placed in a conventional 5 mm NMR glass tube whereas the other samples were dissolved in 0.5 mL of acetonitrile overnight and placed into the NMR tubes. The tubes were dried at 60 °C under reduced pressure for at least 72 h. All tubes were filled approximately 1 cm in height to avoid fluidic convection. Diffusion coefficients for the cation and anion were obtained by ^{1}H-NMR (cation) and ^{19}F-NMR (anion) using a pulsed-field gradient stimulated echo (PFG-STE) sequence at different temperatures. Diffusion coefficients were calculated using the Stejskal–Tanner equation[97,218,219] by measuring the ratio S/S_0 as follows:

$$S = S_0 \exp\left(-D_{\mathrm{diff}}\gamma_{\mathrm{gm}}^2 g^2 \delta_{\mathrm{diff}}^2 \left(\Delta_{\mathrm{diff}} - \frac{\delta_{\mathrm{diff}}}{3}\right)\right) \tag{A.1}$$

where S_0 is the signal at $g_{\max} = 0$, D_{diff} the translation diffusion coefficient, γ_{gm} the gyromagnetic ratio, g the pulsed gradient amplitude, δ_{diff} the duration of the gradient pulses, and Δ_{diff} the diffusion time. The duration of the gradient pulses was set to $\delta = 1.6\,\mathrm{ms}$, the diffusion time to $\Delta = 40\,\mathrm{ms}$ with an acquisition time of 4 ms, and $g_{\max} \in [3,\ 15]\ \mathrm{T\,m}^{-1}$ depending on the temperature. The number of scans was set to 2 for all samples and the temperature was allowed to equilibrate for at least 30 min. As a reference substance, 200 µL of ethylene glycol was filled into the NMR tube and the sample temperature was deduced from the shift of the peaks according to Ammann *et al.*[220]

A.1.3.11 Coupled Rheology and Broadband Dielectric Spectroscopy (Rheo-Dielectric)

Rheological and dielectric measurements were performed on a unique rheo-dielectric setup consisting of a strain-controlled ARES G2 rheometer (TA Instruments, Milford, CT, USA)

and an ALPHA-Analyzer (Novocontrol, Montabaur, Germany).[173] The setup is displayed in Figure A.1.1 and additional information on the setup and the custom-made geometries can be found elsewhere.[81,173]

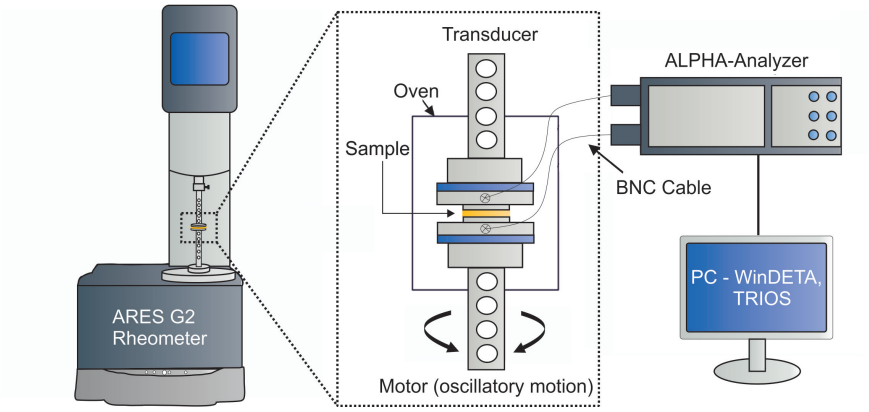

Figure A.1.1: Schematic representation of the experimental setup. An ARES G2 rheometer is coupled to an ALPHA-Analyzer.[173] Reprinted with permission from[81]. Copyright 2022 American Chemical Society.

Blends of Polymerized Ionic Liquids and Ionic Liquids

For BDS and rheological measurements, typically 100 mg of sample was prepared. The respective amounts of IL and PolyIL were dissolved in 0.3 mL of acetonitrile and stirred overnight to prepare homogeneous solutions. The sample was injected into a plastic mold and placed in a fume hood for 2 h. Then, the sample was dried under reduced pressure (approx. 1×10^{-3} mbar) at 50 °C for 48 h. Comparison of NMR measurements of the samples with the pure solvent revealed a remaining water content of approximately 1 %. Oscillatory shear measurements were performed using a homemade 8 mm parallel plate-plate geometry with ceramic insulation between the parallel plates and the fixture and it was connected to the ALPHA-Analyzer by a highly temperature resistant wire. SAOS measurements were performed in an angular frequency range from 0.1 rad s^{-1} to 100 rad s^{-1} at different temperatures and the master curves were obtained using the TTS principle reduced to $T_{\mathrm{ref}} = 0$ °C. Dielectric measurements were performed between 0.1 Hz and 1 MHz by applying a voltage of 0.1 V (E-field strength ca. 100 V m^{-1}) at a distance between the plates of about 1 mm in order to avoid any electrochemical process at the interface between electrolyte and electrode. Before the measurements, the samples were annealed at 100 °C for 15 min and allowed to equilibrate at each temperature for 10 min.

Ionogels

Rheo-dielectric measurements were performed using a homemade 8 mm parallel plate geometry. Small amplitude oscillatory shear (SAOS) measurements were conducted in a frequency range from 0.1 rad s^{-1} to 100 rad s^{-1} at different temperatures under nitrogen atmosphere. Dielectric measurements were performed from 0.1 Hz to 1 MHz with an applied voltage of 0.1 V (E-field strength ca. 100 V m^{-1}). Before the measurements, samples were punched out to 8 mm in diameter and ca. 1 mm height and were annealed at 100 °C for

15 min under nitrogen atmosphere.

Orientation of (Ion-Conductive) Block Copolymers

The measurements were performed on the above introduced rheo-dielectric setup using custom-made 25 mm parallel plate geometries. Before the measurements, the samples were compression molded into discs with a diameter of 25 mm and a thickness of ca. 0.5 mm at 150 °C under vacuum. For the orientation experiment, the sample discs were heated to 10 °C above T_{ODT} for 20 min under nitrogen atmosphere (99.98 % purity). If T_{ODT} could not be reached, the samples were heated to 200 °C for 20 min under nitrogen atmosphere. The samples were cooled down to the measurement temperature while constantly adjusting the gap so that an axial force maximum of 0.05 N (101 Pa) was maintained to prevent squeeze flow-induced orientation. When the measurement temperature was reached, the samples were allowed to equilibrate for 15 min before the start of the LAOS measurement to ensure a uniform temperature. During the LAOS measurement, the nonlinear mechanical response of the material under oscillatory shear excitation was monitored using $I_{3/1}$ via FT rheology. To do so, the normalized third higher harmonic of the time dependent stress response $I_{3/1}$ was used to quantify the nonlinear behavior of the sample during the orientation procedure.[20] Additionally, the dielectric normal mode of 1,4-*cis*-PI was followed at one specific frequency, determined from the maximum of the peak in $\epsilon''(\omega_{BDS})$, compare Figure 5.6.[20,221] Before and after each LAOS experiment, SAOS measurements (from $\omega_{Rheo} = 0.01\,rad\,s^{-1}$ to $100\,rad\,s^{-1}$) and dielectric frequency sweeps (starting from $\omega_{BDS}/2\pi = 10^6$ Hz to 0.1 Hz) were conducted to detect changes in the linear behavior of the sample.

A.2 Supporting Information

A.2.1 Blends of PolyILs and ILs

^{1}H-NMR measurements were conducted in deuterated DMSO using a spectrometer at 400 MHz Larmor frequency. The spectra of the IL monomer and PolyIL are displayed and assigned in Figure A.2.1 and A.2.2.

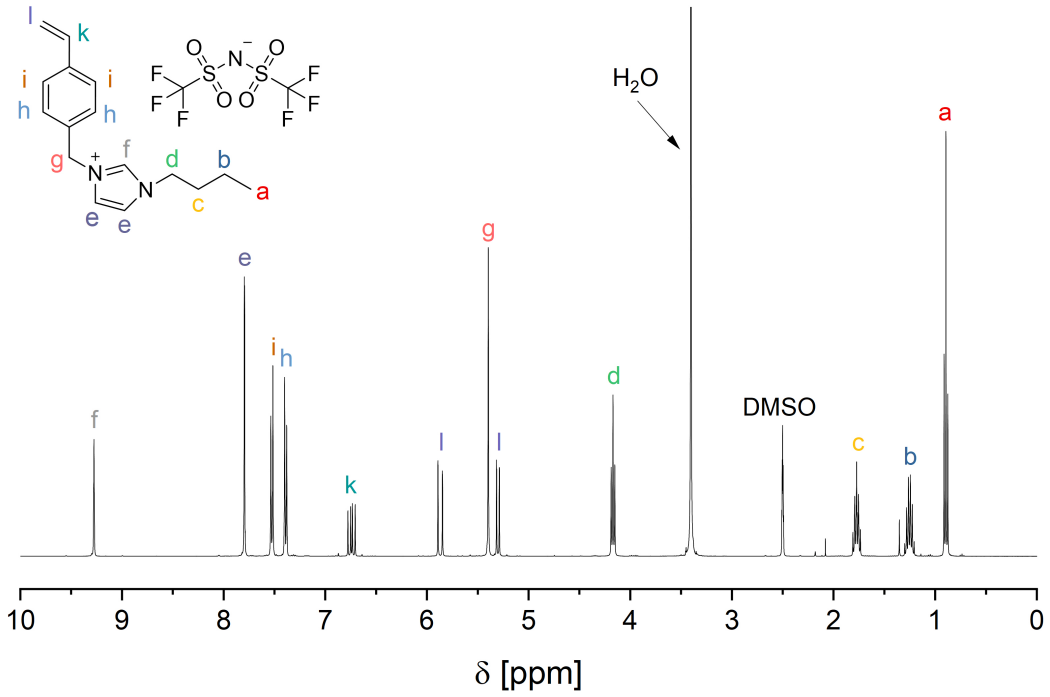

Figure A.2.1: ^{1}H-NMR spectrum (400 MHz) of the ionic liquid monomer in deuterated DMSO.

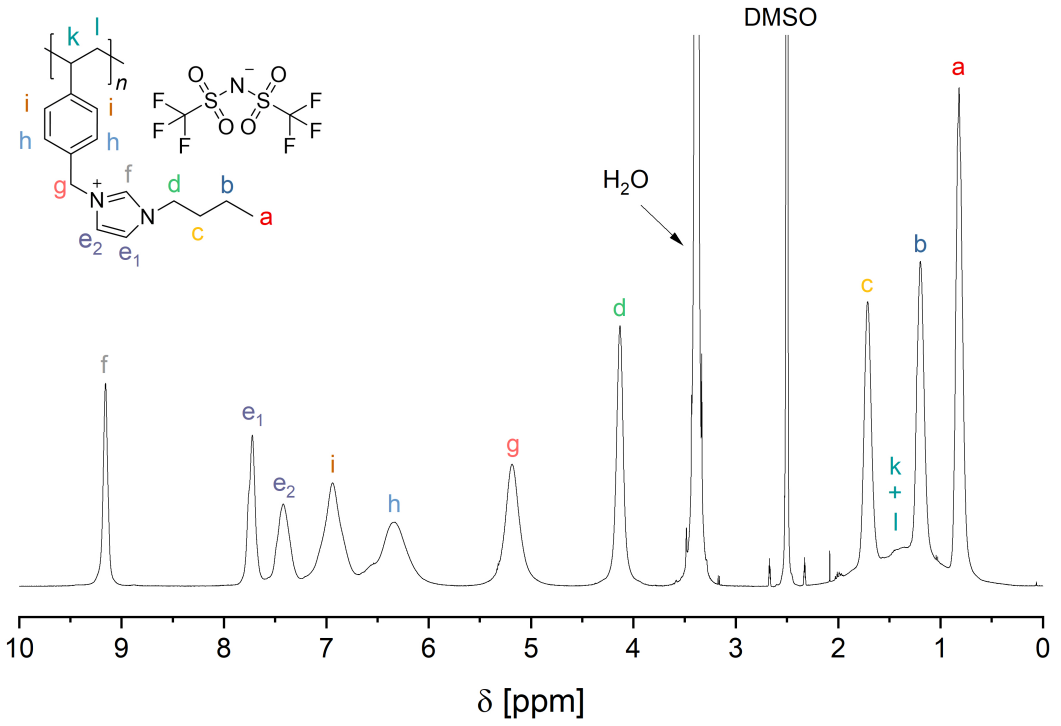

Figure A.2.2: ^{1}H-NMR spectrum (400 MHz) of the polymerized ionic liquid in deuterated DMSO.

In Figure A.2.3, σ_0 and G' at $\omega_{\mathrm{Rheo}}/2\pi = 15.9\,\mathrm{Hz}$ as a function of c_{IL} are displayed at 25 °C. The values behave inversely such as increasing the IL concentration results in increased σ_0 and decreased G'.

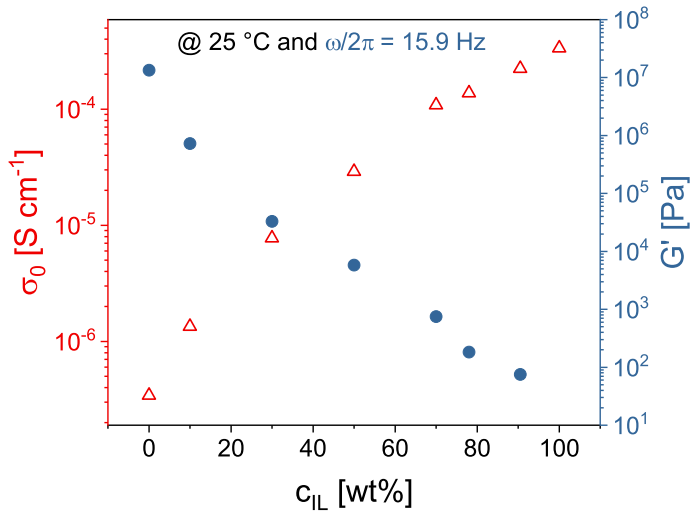

Figure A.2.3: Ionic conductivity (σ_0) and storage modulus (G') as function of ionic liquid concentration (c_{IL}).

In Figure A.2.4 the rheological master curves of the remaining samples are shown. The samples with 10 wt% and 20 wt% PolyIL show almost the same rheological behavior, whereas for the sample with 50 wt% PolyIL an increase in the moduli is observed.

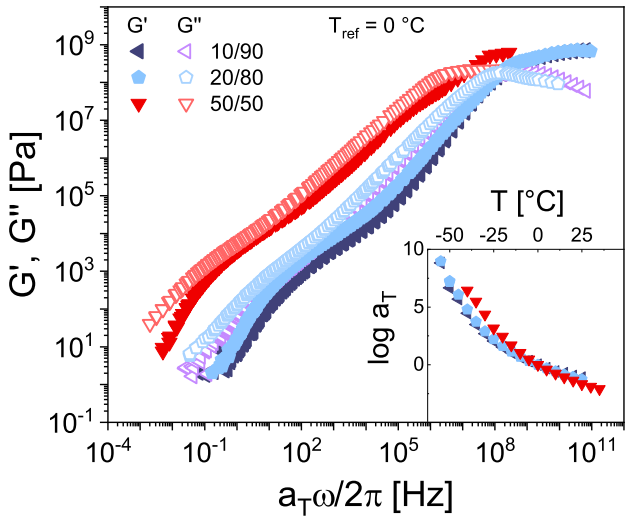

Figure A.2.4: Rheological master curves of three different samples with 10 wt% PolyIL, 20 wt% PolyIL and 50 wt% PolyIL constructed using TTS at $T_{\mathrm{ref}} = 0\,°\mathrm{C}$.

A.2.2 Ionogels

Figure A.2.5 displays the ^{1}H-NMR-spectrum of the IL-CL. The water peak results from residual water in the deuterated solvent.

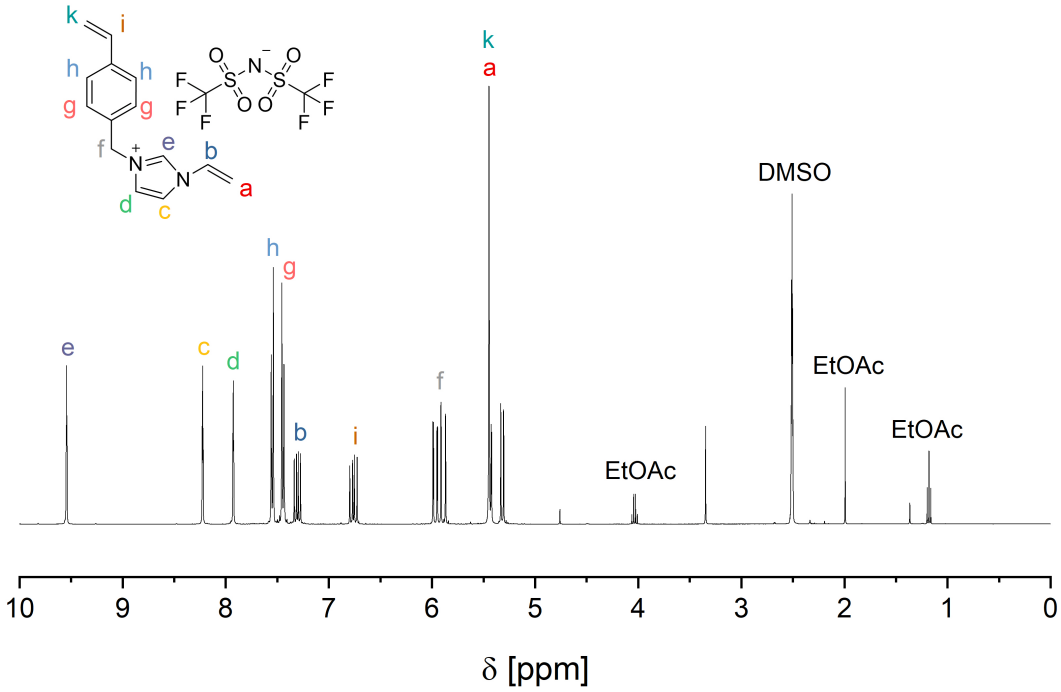

Figure A.2.5: ^{1}H-NMR spectrum (400 MHz) of the ionic liquid crosslinker [VBVI]TFSI in deuterated DMSO. Reprinted with permission from[81]. Copyright 2022 American Chemical Society.

The second heating cycle of the DSC measurements of the IL-M and IL-CL using a heating rate of 10 °C min^{-1} is displayed in Figure A.2.6. The T_gs were determined at the inflection point and were found to be −56 °C and −51 °C, respectively.

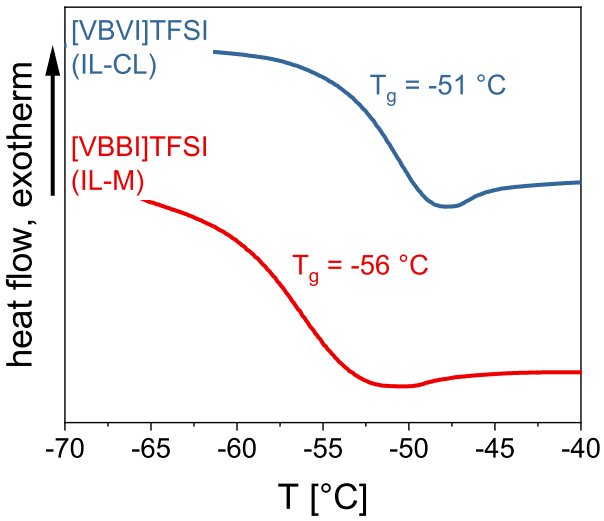

Figure A.2.6: Second heating cycle of the DSC curves of the IL-CL and IL-M at a heating rate of 10 °C min^{-1}. The T_gs were determined at the inflection point. Reprinted with permission from[81]. Copyright 2022 American Chemical Society.

The Li^+-transference numbers (t_{Li^+}) were calculated as suggested by Evans *et al.*[137] (Equation 4.11, p. 59) and Watanabe *et al.*[136] (Equation 4.12, p. 59). Additionally, $I_{0,calc}$ was calculated according to Equation 4.13 which is based on Ohm's law. Subsequently, t_{Li^+} was calculated based on either Watanabe's calculation or Evans' calculation, while for the latter the experimentally obtained initial current ($I_{0,exp}$) as well as $I_{0,calc}$ was used. As shown in Table A1, the results based on Watanabe's formula and Evans' formula were identical, when $I_{0,calc}$ for the latter was used. However, when $I_{0,exp}$ was used for the calculation, quite different results were obtained as a consequence of the small difference between $I_{0,exp}$ and $I_{0,calc}$ (only $\approx 2-3\,\%$). Normally, these small deviations are negligible regarding the calculated t_{Li^+}, but it seems that in the range of such low t_{Li^+} values it plays an important role. Consequently, since $I_{0,calc}$ is based on Ohm's law and $I_{0,exp}$ is limited by the accuracy of the device, in the author's opinion $I_{0,calc}$ should be taken for the calculations. However, to avoid misunderstandings the calculation of Watanabe was used, which does not rely on a perfect determination of I_0.

Figure A.2.7 displays the long-term plating and stripping of Li|30/70-V70-20|Li cells with 0.2 mA cm^{-2} over 60 full cycles (120 h) and only a marginal increase in the overvoltage is found which shows a good compatibility of the samples with the lithium metal.

Table A1: Calculated t_{Li+} using Watanabe's formula as well as Evans' formula (utilizing either $I_{0,\mathrm{exp}}$ or $I_{0,\mathrm{calc}}$).

Ionogel	t_{Li+} Watanabe	t_{Li+} Evans $I_{0,\mathrm{exp}}$	t_{Li+} Evans $I_{0,\mathrm{calc}}$
30/70-P100-40	0.006	0.005	0.006
30/70-P100-20	0.006	0.017	0.006
30/70-V100-40	0.043	0.044	0.043
30/70-V100-20	0.028	0.012	0.028
30/70-V70-20	0.022	−0.011	0.022
30/70-V50-20	0.023	−0.005	0.023

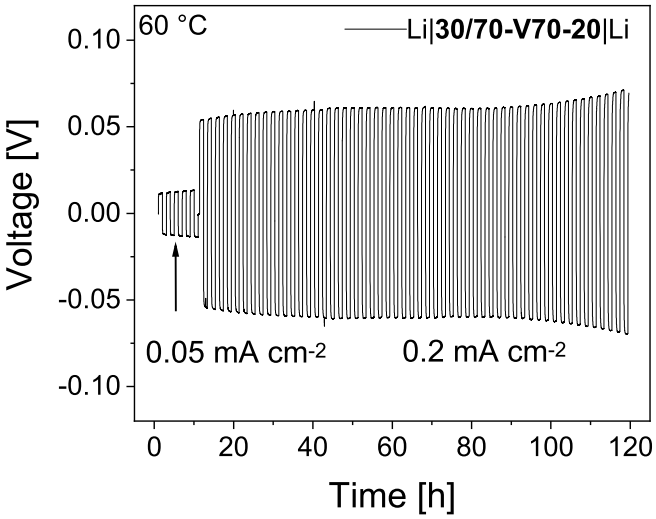

Figure A.2.7: Long-term plating and stripping of Li|30/70-V70-20|Li cells with 0.2 mA cm^{-2} over 60 full cycles (120 h) at 60 °C. Reprinted with permission from[81]. Copyright 2022 American Chemical Society.

A.2.3 Orientation of Block Copolymers

Figure A.2.8 displays the elugrams of raw and fractionated SIIS-40K. In the raw material, a small fraction of uncoupled chains is indicated by the low molecular weight shoulder, which is absent in the fractionated SIIS-40K, indicating successful fractionation.
Figure A.2.9 displays the SAXS patterns of macroscopically oriented ISI-40K ($\gamma_0 = 200\,\%$, $\omega_{\mathrm{Rheo}}/2\pi = 1\,\mathrm{Hz}$, $T = 140\,°\mathrm{C}$) and SIIS-40K ($\gamma_0 = 150\,\%$, $\omega_{\mathrm{Rheo}}/2\pi = 1\,\mathrm{Hz}$, $T = 140\,°\mathrm{C}$) along the radial and normal direction, respectively. The maximum of the primary scattering peak was found at $q_0 = 0.35\,\mathrm{nm}^{-1}$ and higher maxima at $2q_0 = 0.71\,\mathrm{nm}^{-1}$ and $3q_0 = 1.07\,\mathrm{nm}^{-1}$ for ISI-40K and $q_0 = 0.36\,\mathrm{nm}^{-1}$, $2q_0 = 0.74\,\mathrm{nm}^{-1}$ and $3q_0 = 1.11\,\mathrm{nm}^{-1}$ for SIIS-40K indicating a lamellar structure as expected for a triblock copolymer with a block ratio of around 45/55 PS/PI.[64,187] For both polymers, slightly higher q_0-values ($\Delta q_0 = 0.01\,\mathrm{nm}^{-1}$) were found for the oriented samples independent of the macroscopic orientation, see Table A2.

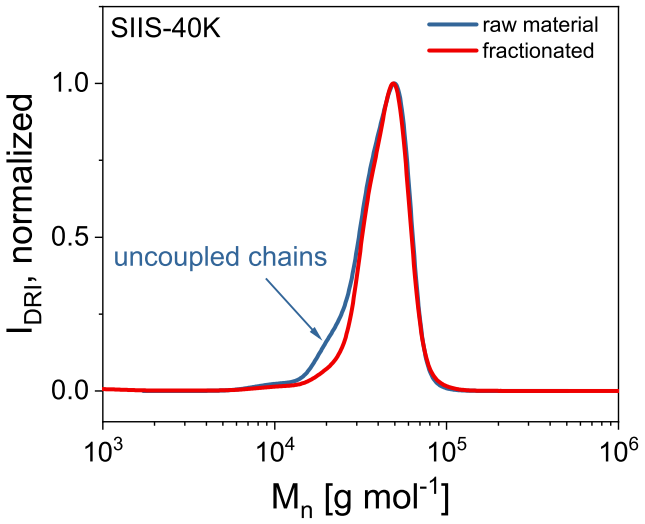

Figure A.2.8: Elugrams of raw and fractionated SIIS-40K. The disappearance of the shoulder at 20 kg mol^{-1} weight indicates successful fractionation. Reprinted with permission from[159]. Copyright 2023 American Chemical Society.

In Figure A.2.10 $\tan\delta_{\mathrm{Rheo}}(\omega_{\mathrm{Rheo}})$ and $\tan\delta_{\mathrm{BDS}}(\omega_{\mathrm{BDS}})$ before and after the orientation process are shown. For $\tan\delta_{\mathrm{BDS}}(\omega_{\mathrm{BDS}})$ the same changes in data as for ϵ'' are observed clarifies that the changes in $\epsilon''(\omega_{\mathrm{BDS}})$ are due to changes in the polarity of the sample and do not result from changes in the gap because $\tan\delta_{\mathrm{BDS}}$ is independent of the gap.

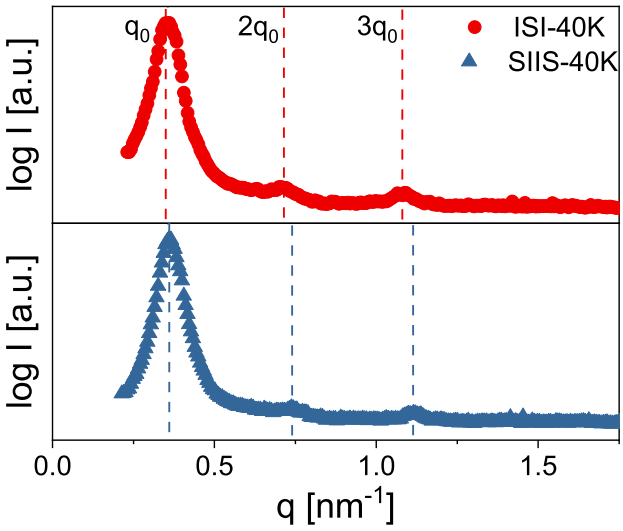

Figure A.2.9: SAXS spectra of ISI-40K and SIIS-40K, indicating microphase separation and a lamellar structure. Reprinted with permission from[159]. Copyright 2023 American Chemical Society.

Table A2: The q_0-values for unoriented and oriented ISI-40K and SIIS-40K. The q_0-values reduced by $0.1\,\mathrm{nm}^{-1}$ upon orientation. Reprinted with permission from[159]. Copyright 2023 American Chemical Society.

	ISI-40K			SIIS-40K		
γ_0 [%]	q_0 [nm^{-1}]	d_0 [nm]	Orientation	q_0 [nm^{-1}]	d_0 [nm]	Orientation
0	0.34	18.5	–	0.35	18.0	–
50	0.35	18.0	Perpendicular	0.37	17.0	Perpendicular
100	0.35	18.0	Perpendicular	0.37	17.0	Perpendicular
150	0.35	18.0	Biaxial	0.36	17.5	Perpendicular
200	0.36	17.5	Biaxial	0.36	17.5	Perpendicular
250	0.35	18.0	Biaxial	0.36	17.5	Perpendicular
300	0.33	19.0	Parallel	0.37	17.0	Perpendicular
350	0.36	17.5	Parallel	0.36	17.5	Perpendicular
400	0.35	18.0	Parallel	–[a]	–[a]	–[a]

[a]No values were obtained for SIIS-40K at $\gamma_0 = 400\,\%$ because of sample failure.

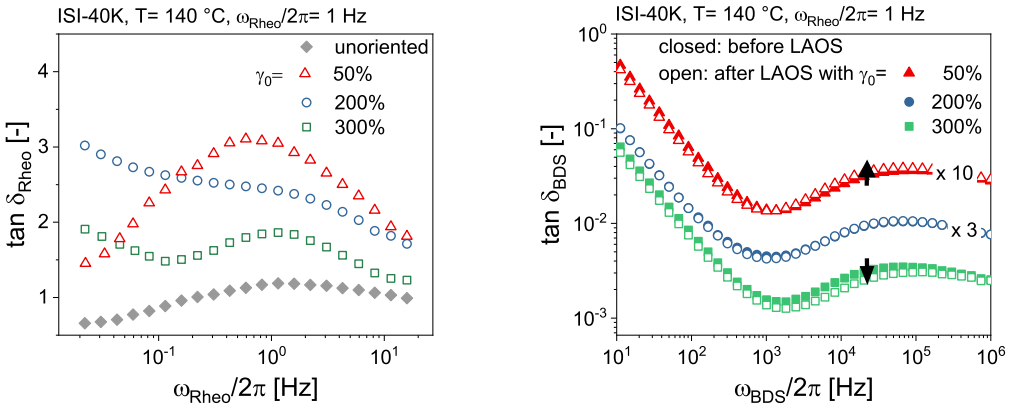

Figure A.2.10: **(a)** Tangent δ_{Rheo} ($\tan\delta_{\mathrm{Rheo}} = G''/G'$) from rheology and **(b)** tangent δ_{BDS} ($\tan\delta_{\mathrm{BDS}} = \epsilon''/\epsilon'$) from dielectric spectroscopy before (closed symbols) and after (open symbols) orientation of ISI-40K with γ_0= 50 % (red), 200 % (blue) and 300 % (green) at 140 °C and $\omega_{\mathrm{Rheo}}/2\pi$ = 1 Hz. The curves in **(b)** were shifted vertically for clarity. The final orientation can be predicted by the change in $\tan\delta_{\mathrm{BDS}}(\omega_{\mathrm{BDS}})$ where an increase indicates a perpendicular and a decrease a parallel orientation. Reprinted with permission from[159]. Copyright 2023 American Chemical Society.

Orientation of ISI-40K

In Figure A.2.11 the development of $\epsilon''(t)$ and $I_{3/1}$(t) during an orientation process at 140 °C and with $\omega_{\mathrm{Rheo}}/2\pi = 1\,\mathrm{Hz}$ and $\gamma_0 = 100\,\%$, 150 %, 250 %, 350 % and 400 % are shown. The lines represent a stretched mono- or bi-exponential fit and the corresponding fit parameters are displayed in Table 5.2 and Table 5.3.

The 2D-SAXS patterns obtained after the orientation process observed in Figure A.2.11 are displayed in Figure A.2.12. In A.2.12a a perpendicular, in A.2.12b and A.2.12c a biaxial orientation, and in A.2.12d and A.2.12e a parallel macroscopic orientation is indicated.

The stability of the observed orientations was assessed by long-term measurements and the development of $\epsilon''(t)$ and $I_{3/1}(t)$ for $\gamma_0 = 150\,\%$, 250 % and 350 % is displayed in Figure A.2.13. The higher the strain amplitude, the more noise is observed in $I_{3/1}$ due to its sensitivity and the high strain amplitude leading to edge fracture and sample failure.

The 2D-SAXS patterns received after the long-term orientation process are displayed in Figure A.2.14 and Figure A.2.15.

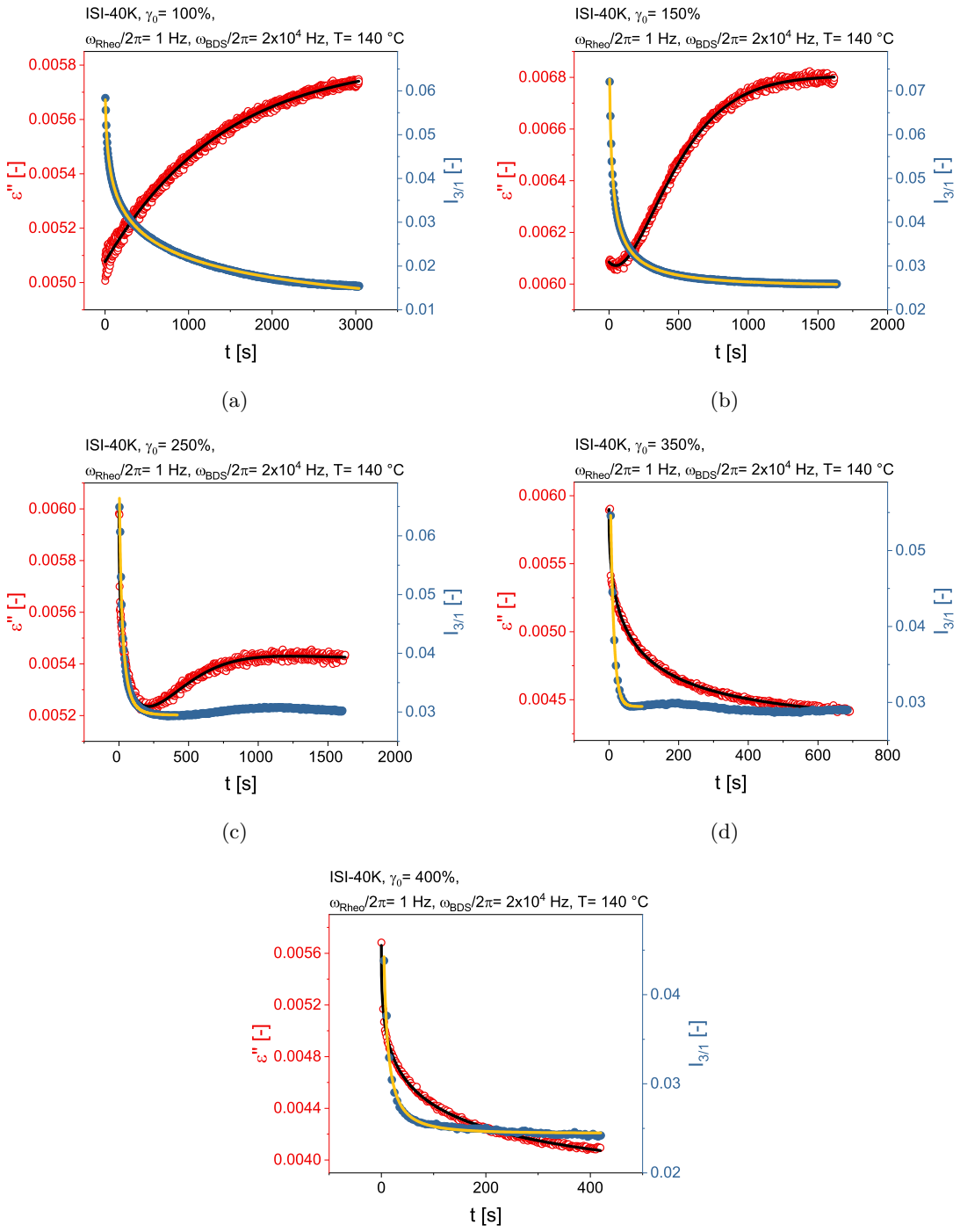

Figure A.2.11: Time-dependent dielectric loss ($\epsilon''(t)$, red) and relative intensity of the third harmonic ($I_{3/1}(t)$, blue) including a stretched mono- or bi-exponential fit (solid lines, see Equation 5.2 and 5.5) obtained by in-situ rheo-dielectric during the shear alignment of ISI-40K with an applied strain amplitude of **(a)** 100 %, **(b)** 150 %, **(c)** 250 %, **(d)** 350 % and **(d)** 400 % at $\omega_{\mathrm{Rheo}}/2\pi = 1\,\mathrm{Hz}$ and $T = 140\,^{\circ}\mathrm{C}$. For all measurements, $\epsilon''(t)$ was recorded at a fixed dielectric frequency, $\omega_{\mathrm{BDS}}/2\pi = 2 \times 10^4\,\mathrm{Hz}$. Reprinted with permission from[159]. Copyright 2023 American Chemical Society.

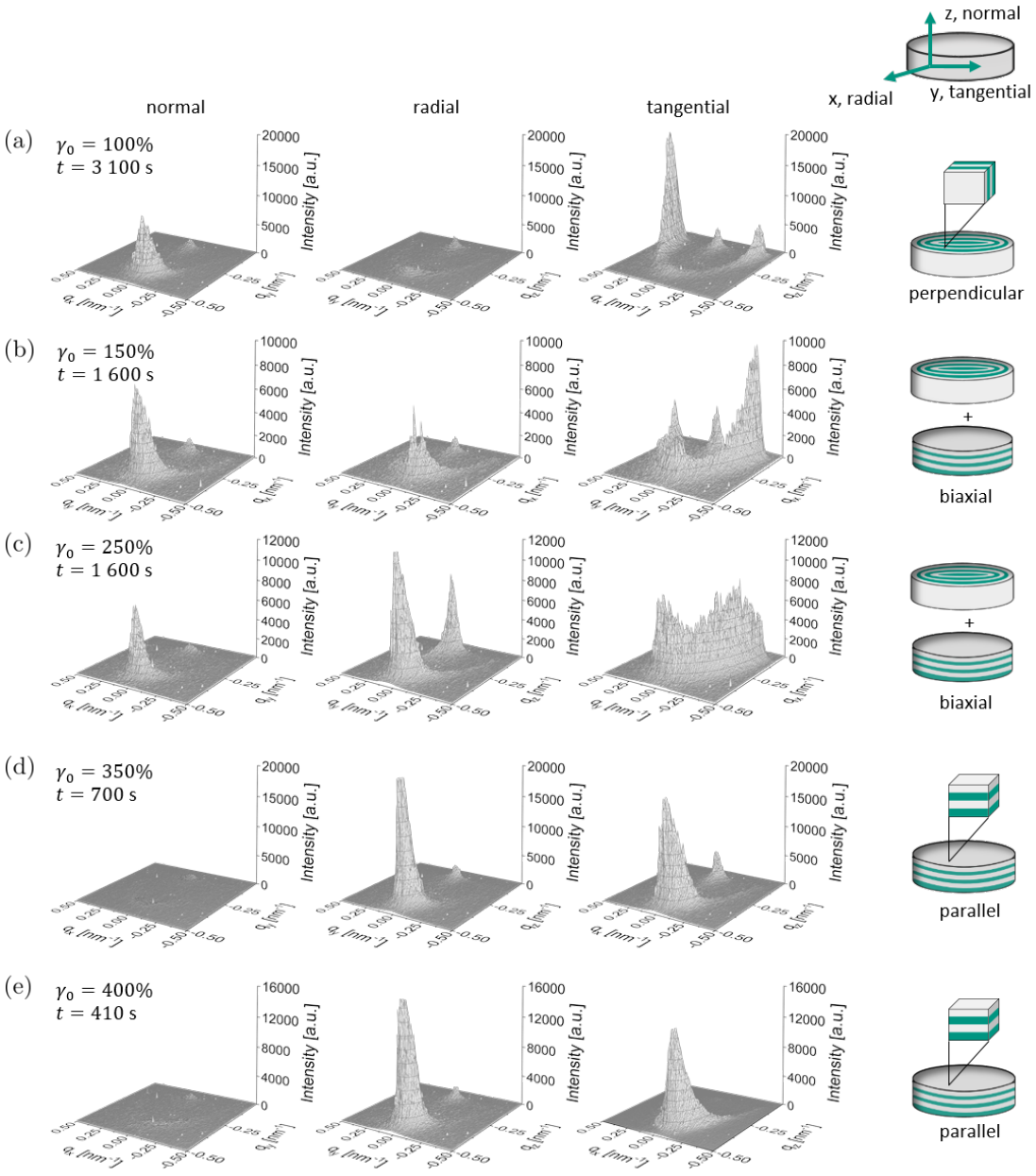

Figure A.2.12: 2D-SAXS patterns of PS-*b*-PolyIL-26K along the normal, radial and tangential plane, oriented for an orientation time t with an applied strain amplitude of **(a)** $\gamma_0 = 100\,\%$ ($t = 3100\,\mathrm{s}$), **(b)** $150\,\%$ ($t = 1600\,\mathrm{s}$), **(c)** $250\,\%$ ($t = 1600\,\mathrm{s}$), **(d)** $350\,\%$ ($t = 700\,\mathrm{s}$) and **(e)** $400\,\%$ ($t = 410\,\mathrm{s}$) at $140\,^{\circ}\mathrm{C}$ and $\omega_{\mathrm{Rheo}}/2\pi = 1\,\mathrm{Hz}$. In **(a)** a perpendicular, in **(b)** and **(c)** a biaxial orientation, and in **(d)** and **(e)** a parallel macroscopic orientation is indicated. Adapted with permission from[159]. Copyright 2023 American Chemical Society.

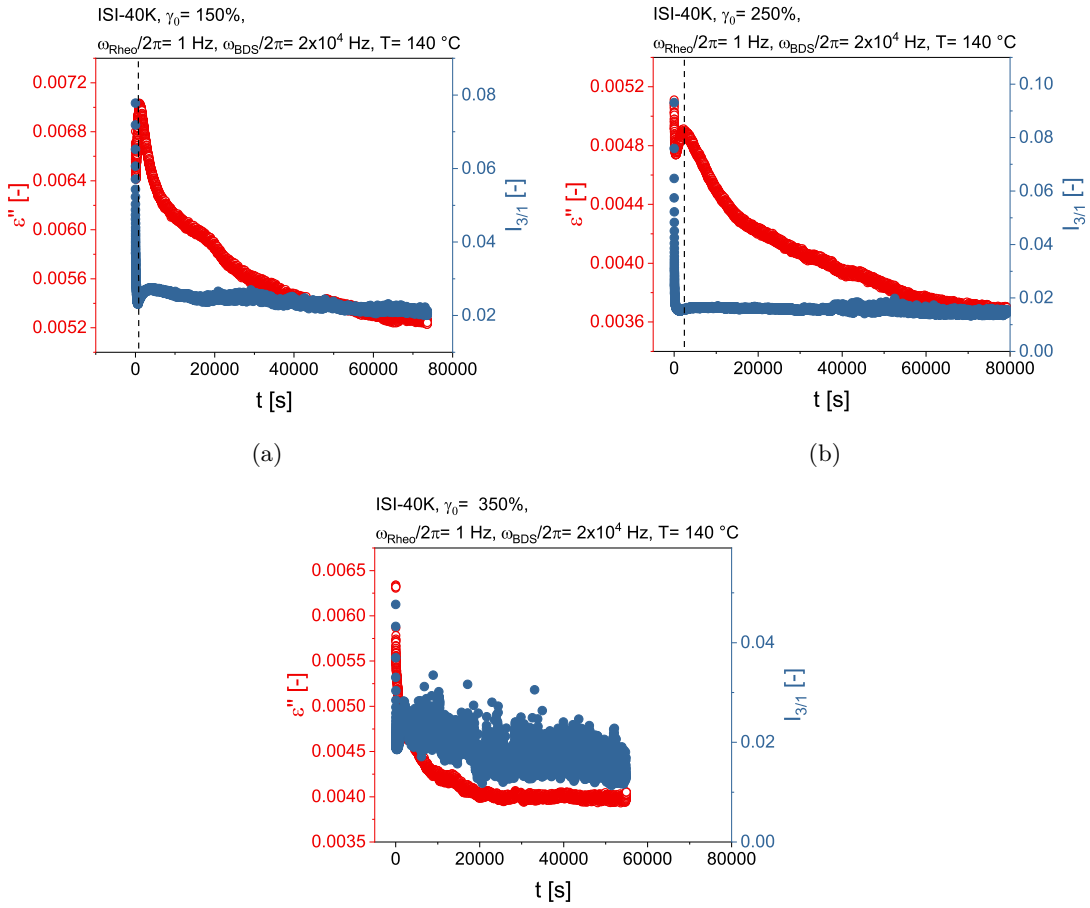

Figure A.2.13: Long-term rheo-dielectric measurements of the time-dependent dielectric loss ($\epsilon''(t)$, red) and relative intensity of the third harmonic ($I_{3/1}(t)$, blue) with an applied strain amplitude of **(a)** $\gamma_0 = 150\,\%$, **(b)** $250\,\%$ and **(c)** $350\,\%$ at $\omega_{\mathrm{Rheo}}/2\pi = 1\,\mathrm{Hz}$ and $T = 140\,^{\circ}\mathrm{C}$. For all samples, except $\gamma_0 = 350\,\%$, a reorientation process accompanied by a substantial decrease of $\epsilon''(t)$ is observed. During all measurements, $\epsilon''(t)$ was recorded at a fixed dielectric frequency, $\omega_{\mathrm{BDS}}/2\pi = 2 \times 10^4\,\mathrm{Hz}$. Reprinted with permission from[159]. Copyright 2023 American Chemical Society.

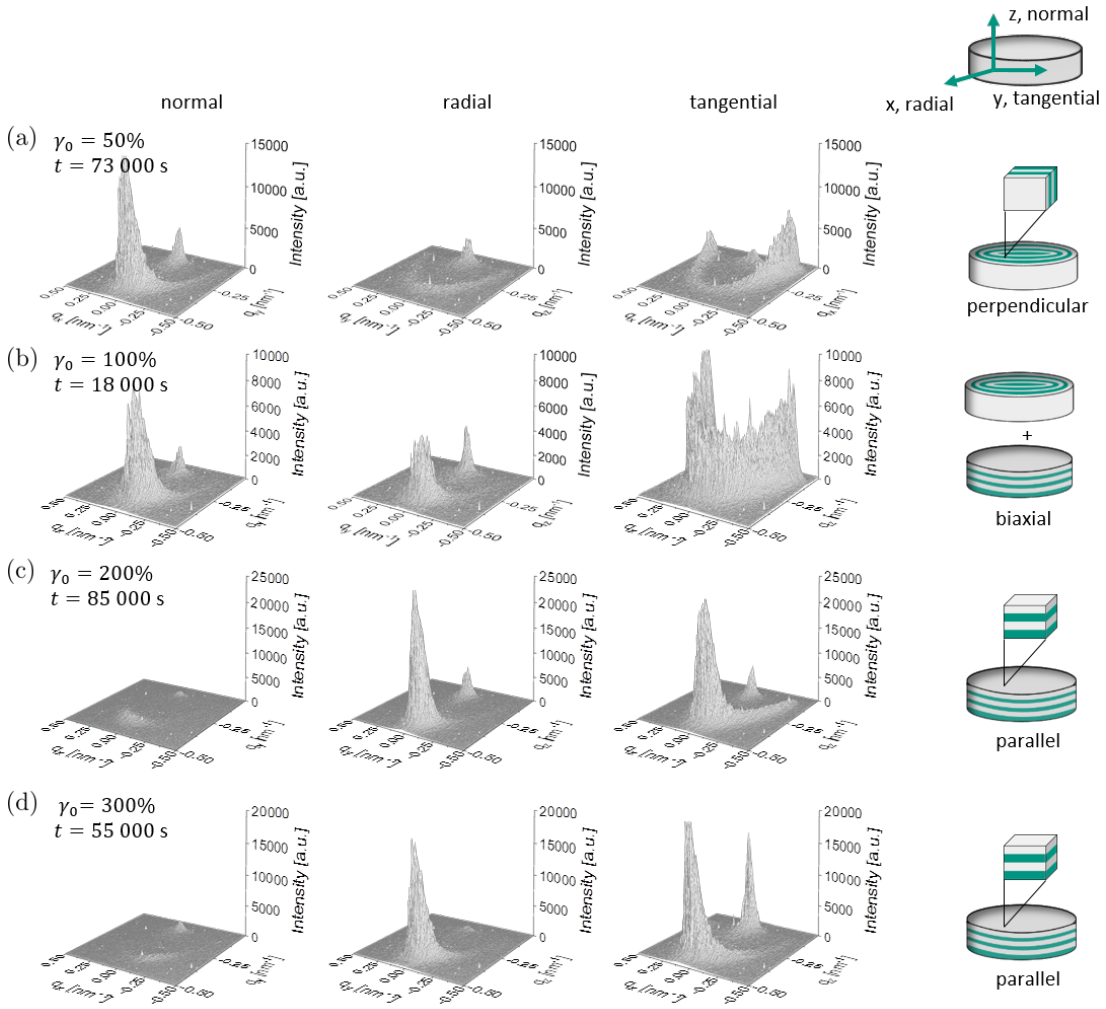

Figure A.2.14: 2D-SAXS patterns of ISI-40K along the normal, radial and tangential plane, after long-term orientation for an orientation time t with an applied strain amplitude of **(a)** $\gamma_0 = 50\,\%$ ($t = 73\,000\,\mathrm{s}$), **(b)** $100\,\%$ ($t = 18\,000\,\mathrm{s}$), **(c)** $200\,\%$ ($t = 85\,000\,\mathrm{s}$) and **(d)** $300\,\%$ ($t = 55\,000\,\mathrm{s}$) at $140\,^{\circ}\mathrm{C}$ and $\omega_{\mathrm{Rheo}}/2\pi = 1\,\mathrm{Hz}$. In **(a)** a perpendicular, in **(b)** a biaxial orientation, and in **(c)** and **(d)** a parallel orientation of the lamellar microdomains is indicated. Adapted with permission from[159]. Copyright 2023 American Chemical Society.

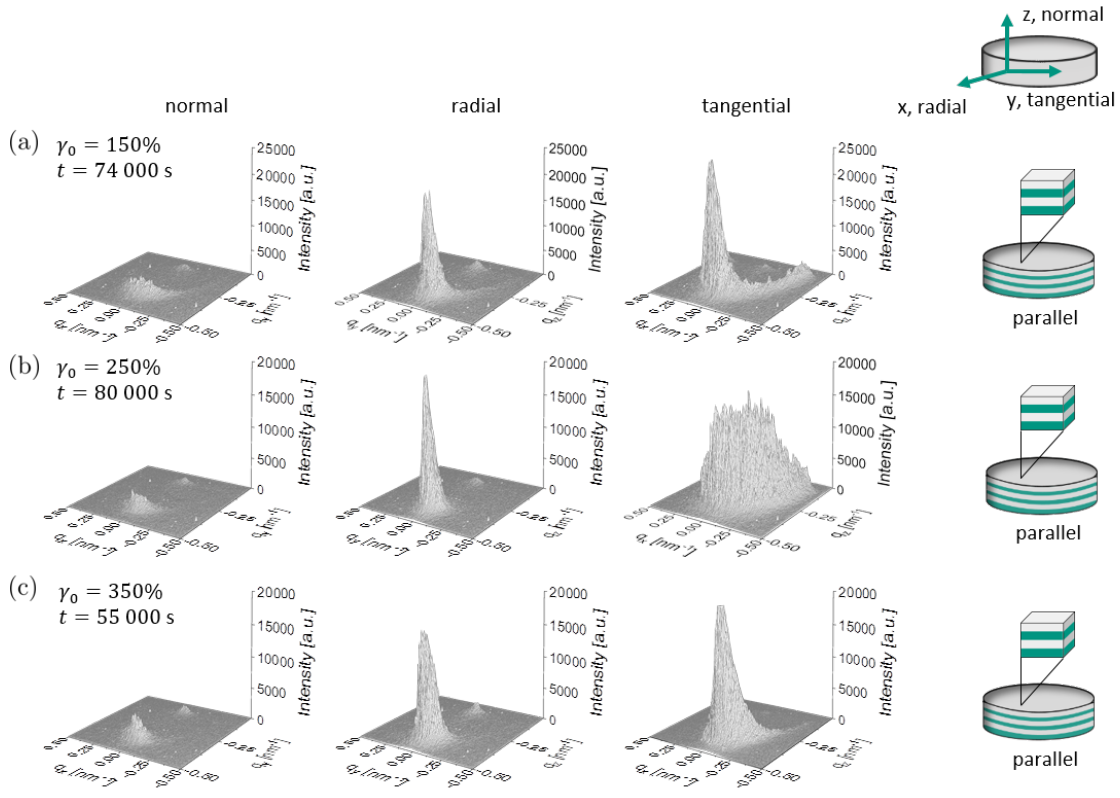

Figure A.2.15: 2D-SAXS patterns of ISI-40K along the normal, radial and tangential plane, after long-term orientation for an orientation time t with an applied strain amplitude of **(a)** $\gamma_0 = 150\,\%$ ($t = 74\,000\,\mathrm{s}$), **(b)** $250\,\%$ ($t = 80\,000\,\mathrm{s}$) and **(c)** $350\,\%$ ($t = 55\,000\,\mathrm{s}$) at $140\,^{\circ}\mathrm{C}$ and $\omega_{\mathrm{Rheo}}/2\pi = 1\,\mathrm{Hz}$. In all cases a parallel orientation of the ordered lamellar microdomains is indicated. Adapted with permission from[159]. Copyright 2023 American Chemical Society.

Orientation of SIIS-40K

Figure A.2.16 shows the development of $I_{3/1}(t)$ during the orientation process for SIIS-40K using a strain amplitude of 300, 350, and 400 %. At such high strain amplitudes, $I_{3/1}(t)$ does not show a purely exponential decay anymore. The signal becomes very noisy at higher times because $I_{3/1}$ is very sensitive to sample failure. Despite that, the SAXS patterns of the samples showed a macroscopic perpendicular alignment, see Figure A.2.18.

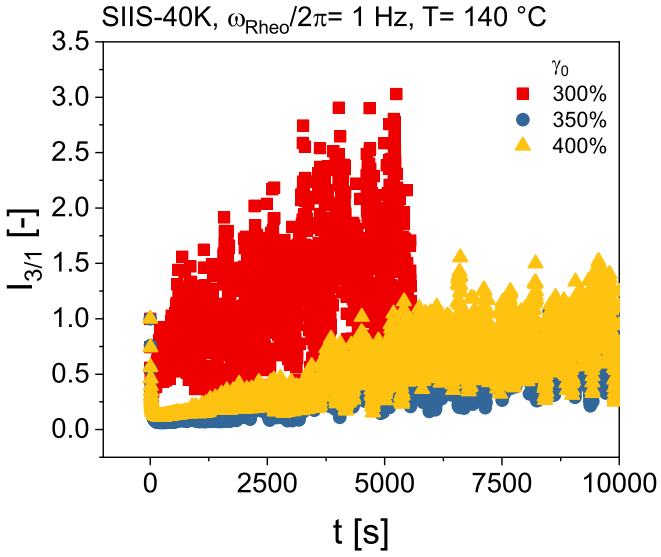

Figure A.2.16: Time-dependence of the relative intensity of the third harmonic ($I_{3/1}(t)$) of SIIS-40K with a strain amplitude of $\gamma_0 = 300\,\%$, $350\,\%$ and $400\,\%$ at $\omega_{\mathrm{Rheo}}/2\pi = 1\,\mathrm{Hz}$ and $T = 140\,^{\circ}\mathrm{C}$. Reprinted with permission from[159]. Copyright 2023 American Chemical Society.

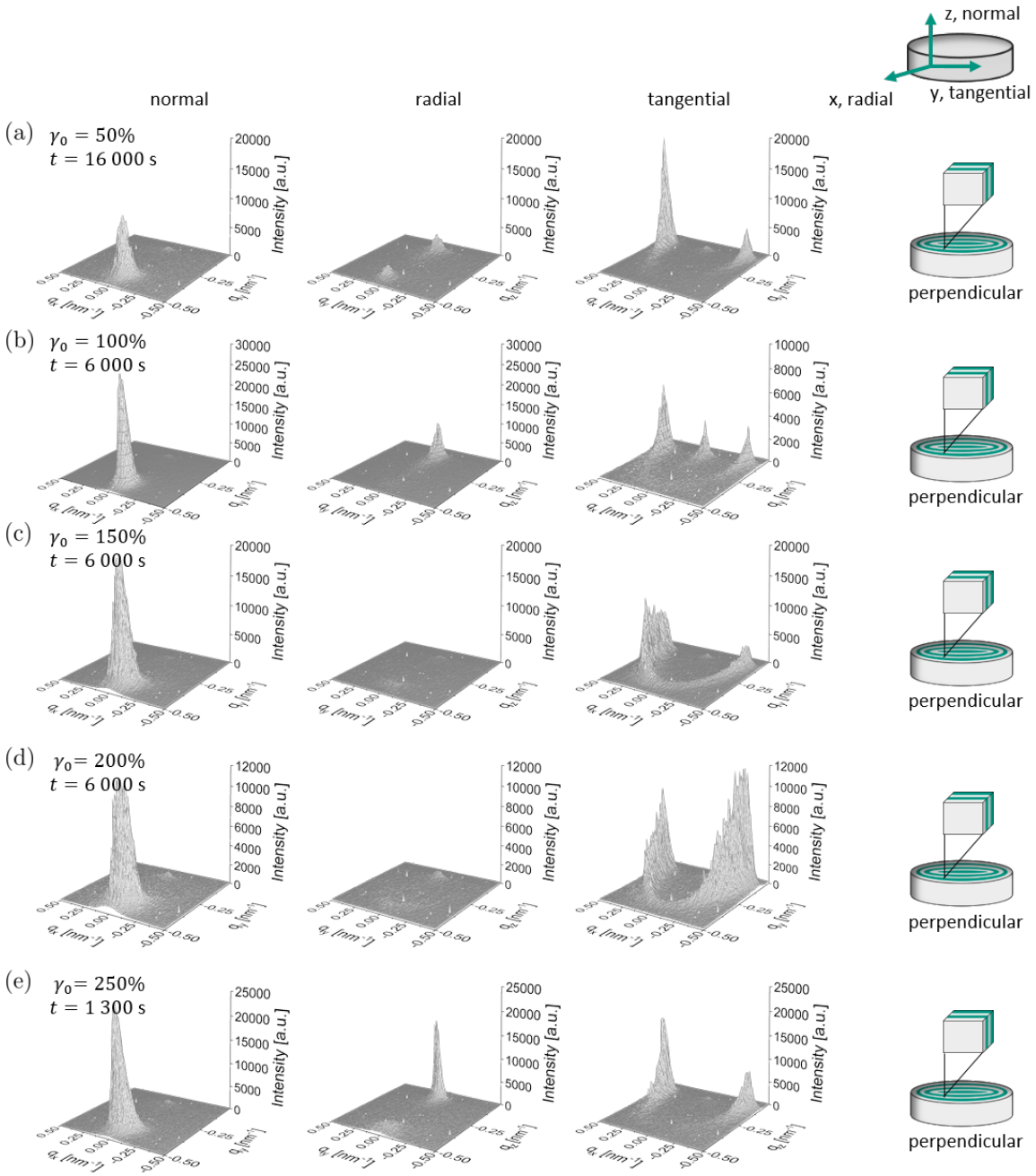

Figure A.2.17: 2D-SAXS patterns of SIIS-40K along the normal, radial and tangential plane, oriented for an orientation time t with an applied strain amplitude of **(a)** $\gamma_0 = 50\,\%$ ($t = 16\,000\,\mathrm{s}$), **(b)** $100\,\%$ ($t = 6000\,\mathrm{s}$), **(c)** $150\,\%$ ($t = 6000\,\mathrm{s}$), **(d)** $200\,\%$ ($t = 6000\,\mathrm{s}$) and **(e)** $250\,\%$ ($t = 1300\,\mathrm{s}$) at $140\,^{\circ}\mathrm{C}$ and $\omega_{\mathrm{Rheo}}/2\pi = 1\,\mathrm{Hz}$. In all cases a perpendicular orientation of the ordered lamellar microdomains is indicated. Adapted with permission from[159]. Copyright 2023 American Chemical Society.

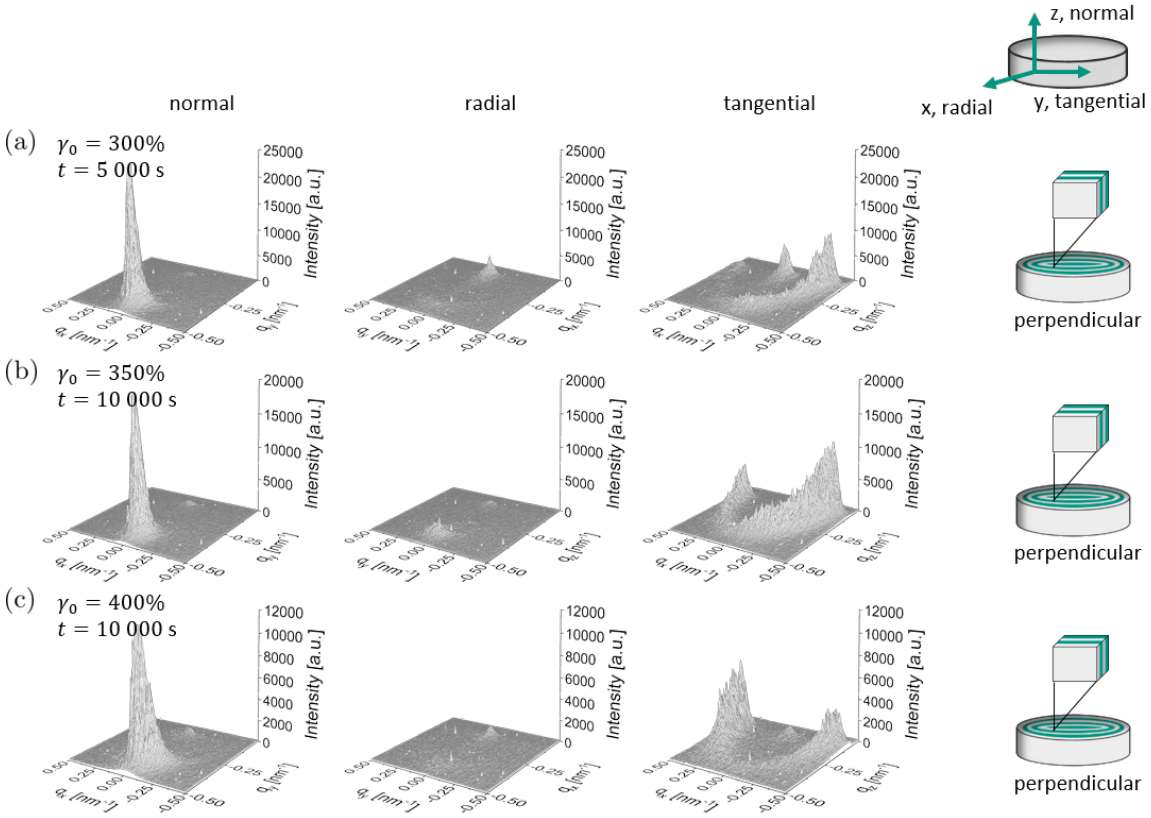

Figure A.2.18: 2D-SAXS patterns of SIIS-40K along the normal, radial and tangential plane, oriented for an orientation time t with an applied strain amplitude of **(a)** $\gamma_0 = 300\,\%$ ($t = 5000\,\mathrm{s}$), **(b)** $350\,\%$ ($t = 10\,000\,\mathrm{s}$) and **(c)** $400\,\%$ ($t = 10\,000\,\mathrm{s}$) at $140\,^\circ\mathrm{C}$ and $\omega_{\mathrm{Rheo}}/2\pi = 1\,\mathrm{Hz}$. In all cases a perpendicular orientation of the ordered lamellar microdomains is indicated. Adapted with permission from[159]. Copyright 2023 American Chemical Society.

A.2.4 Orientation of Ion-Conductive Block Copolymers

The order-disorder transition temperature of the pure PS-*b*-P2VP was determined at the inflection point of $G'(T)$ during a temperature sweep with $\omega_{\mathrm{BDS}} = 1\,\mathrm{rad\,s^{-1}}$ and $\gamma_0 = 3\,\%$, see Figure A.2.19.

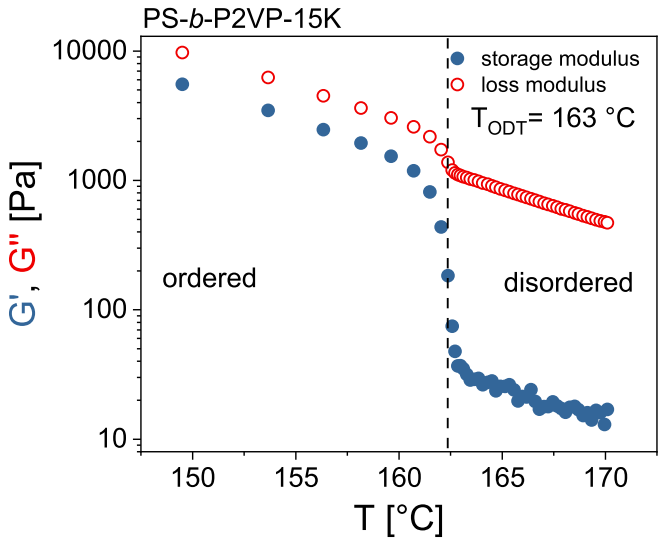

Figure A.2.19: Temperature sweep of the pure PS-*b*-P2VP-15K with $T_{\mathrm{ODT}} = 163\,^{\circ}\mathrm{C}$.

The structure of the copolymer after addition of the second block is confirmed by ^{1}H-NMR spectroscopy, see Figure A.2.20.

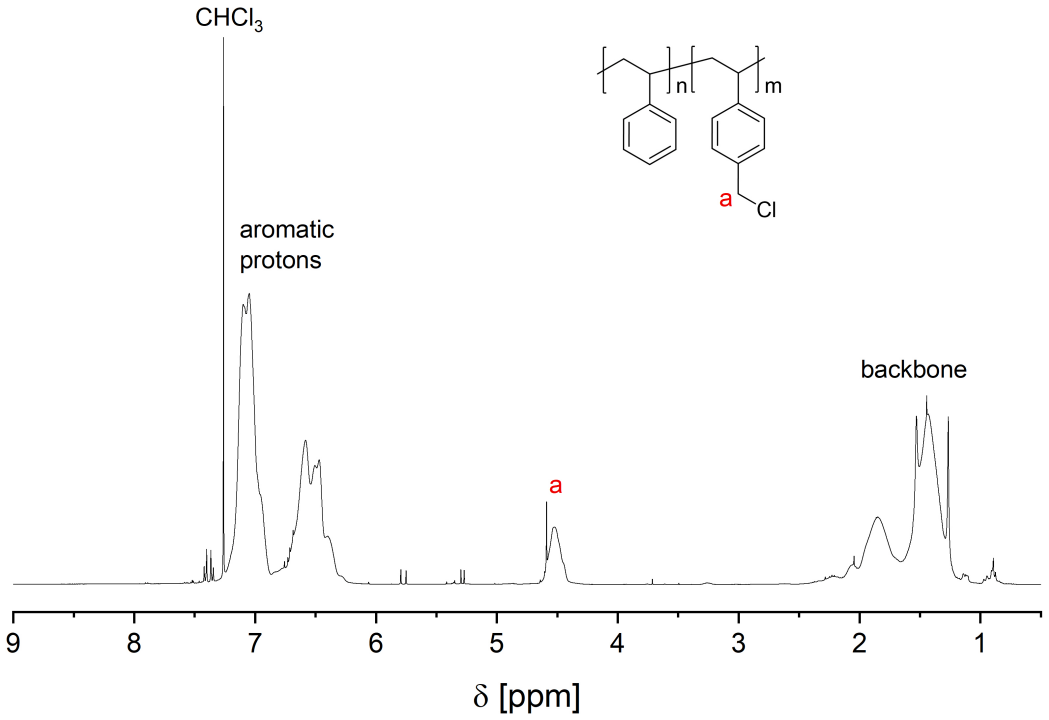

Figure A.2.20: ^{1}H-NMR spectrum (400 MHz) of PS-*b*-PolyVBC monomer in deuterated chloroform.

The ^{1}H-NMR spectra of the block copolymer after addition of 1-butylimidazole and anion exchange are displayed in Figure A.2.21 and A.2.22, respectively.

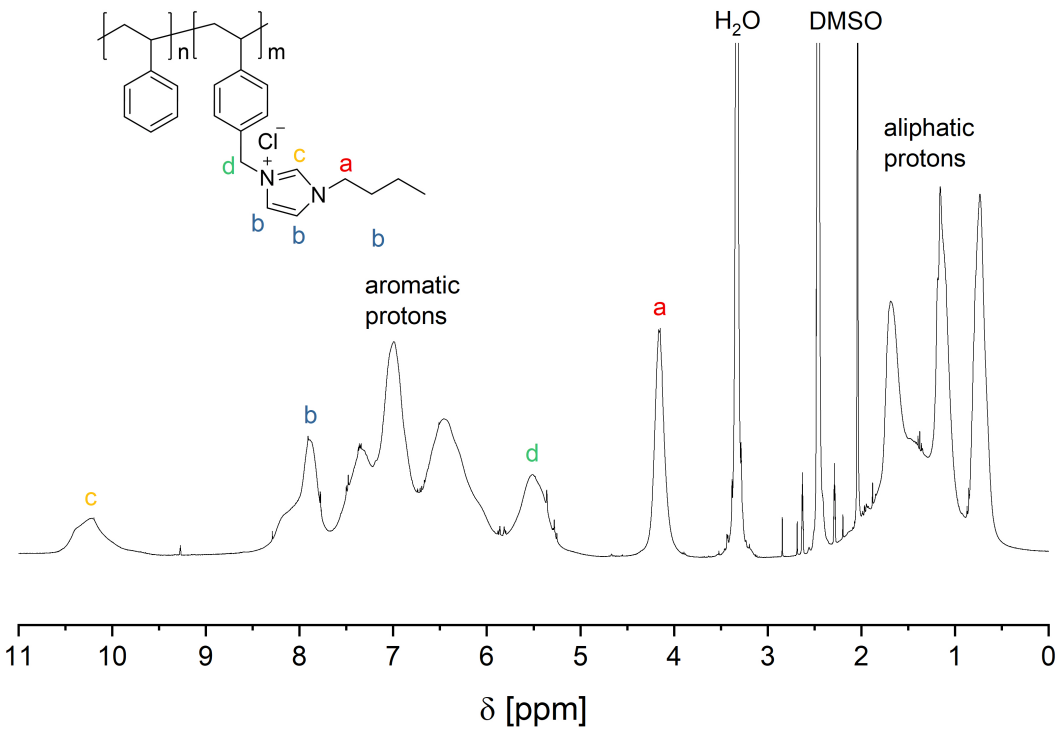

Figure A.2.21: ^{1}H-NMR spectrum (400 MHz) of PS-*b*-Poly[VBBI]Cl in deuterated DMSO.

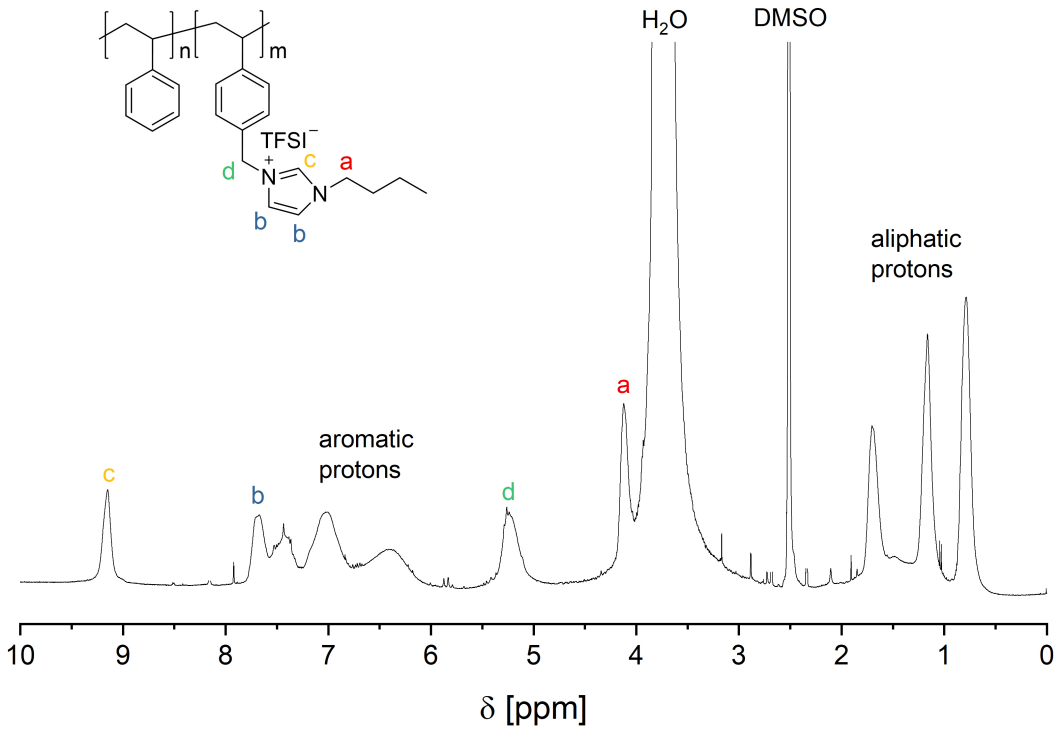

Figure A.2.22: ^{1}H-NMR Spectrum (400 MHz) of PS-*b*-Poly[VBBI]TFSI in deuterated DMSO.

List of Figures

List of Tables

Nomenclature

Abbreviations

AIBN	2,2'-azobis(2-methylpropionitrile)
ATRP	atom transfer radical polymerization
BCE	block copolymer electrolyte
BCP	block copolymer
BDS	broadband dielectric spectroscopy
[BMIM]TFSI	1-butyl-3-methylimidazolium bis-(trifluoromethane sulfonyl)imide
CC-model	Cole/Cole model
CD-model	Cole/Davidson model
CD	current density
DCA^-	dicyanamide
DMF	dimethylformamide
DMSO	dimethyl sulfoxide
DSC	dynamic scanning calorimetry
[EMIM]FAP	1 ethyl-3-methylimidazolium tris(pentafluoroethyl)trifluorophosphate
[EMIM]TCB	1-ethyl-3-methylimidazolium tetra-cyanoborate
[EMIM]TFSI	1-ethyl-3-methylimidazolium bis(trifluoromethane sulfonyl)imide
FSI^-	bis(fluoro sulfonyl)imide
FTIR	Fourier-transform infrared
FT	Fourier-transform
FWHM	full width at half maximum
HN	Havriliak/Negami
IC	ionic conductivity
IG	ionogel
IL	ionic liquid
IL-CL	ionic liquid crosslinker
IL-E	ionic liquid electrolyte
IL-M	ionic liquid monomer
IR	infrared
LAOS	large amplitude oscillatory shear
LIB	lithium ion battery
LiTFSI	lithium bis(trifluoromethane sulfonyl)imide
MALLS	multi angle laser light scattering
n-BuLi	*n*-butyllithium
NMP	nitroxide-mediated radical polymerization
NMR	nuclear magnetic resonance

PEGDA	poly(ethylene glycol)diacrylate
[PDADMA]TFSI	poly(diallyldimethylammonium) bis(trifluoromethane sulfonyl)imide
PFG-NMR	pulsed-field gradient nuclear magnetic resonance spectroscopy
PI	polyisoprene
PolyIL	polymerized ionic liquid
poly[VBBI]TFSI	poly(1-butyl-3-(4-vinylbenzyl)imidazolium bis(trifluoromethane sulfonyl)imide)
PS	polystyrene
RAFT	reversible-addition-fragmentation chain-transfer polymerization
SAOS	small amplitude oscillatory shear
SAXS	small angle X-ray scattering
s-BuLi	*s*-butyllithium
SE	solid electrolyte
SEC	size exclusion chromatography
SEI	solid electrolyte interface
SPE	solid polymer electrolyte
TfO^-	trifluoromethane sulfonate
TFSAM	2,2,2-trifluoromethane sulfonyl-N-cyanoamide
$TFSI^-$	bis(trifluromethane sulfonyl)imide
TGA	thermal gravimetric analysis
THF	tetrahdrofuran
TTS	time-temperature superposition
[VBBI]TFSI	1-butyl-3-(4-vinylbenzyl)imidazolium bis(trifluoromethane sulfonyl)imide
[VBVI]TFSI	1-(p-vinylbenzyl)-3-vinyl imidazolium bis(trifluoromethane sulfonyl)imide
VFT	Vogel-Fulcher-Tammann
WAXS	wide angle X-ray scattering
WLF	Williams-Landell-Ferry

Physical Quantities

a_T	horizontal shift factor
A	are of the plates (two plate model)
A_1	decay amplitude (stretched exponential function)
$ASR_\mathrm{CT+SEI}$	area-specific resistance
B	fit parameter (VFT)
a_T	horizontal shift factor
β	width of the distribution (stretched exponential function)
C_1	empirical parameter from the WLF equation
C_2	empirical parameter from the WLF equation
c_IL	concentration of ionic liquid
Đ	dispersity
$\overrightarrow{D}$	dielectric displacement
d	spatial periodicity
D_anion	diffusion coefficient of the anions
D_cation	diffusion coefficient of the cations
D_diff	translational diffusion coefficient
D_mean	mean diffusion coefficient
D_σ	diffusion coefficient determined via BDS
$\overrightarrow{E}$	electric field
E_a	activation energy
$\overrightarrow{E_0}$	amplitude of the electric field
f	volume fraction
g	pulsed gradient amplitude
G^*	complex shear modulus
G'	storage modulus
G''	loss modulus
G_m	Gibbs free energy
h	distance between the plates (shear experiment)
H_R	Haven ratio
I_0	initial current
$[I_0]$	initiator concentration at time 0
$I_{3/1}$	nonlinear mechanical parameter
I_s	scattering intensity
I_ss	steady-state current
$\overrightarrow{k}$	wave vector
$\overrightarrow{k'}$	scattered wave vector
k_GT	Gordon-Taylor constant
k_B	Boltzmann constant
m	magnitude
m_f	fragility
M^*	electric modulus
M'	electric storage modulus
M''	electric loss modulus
$[M_0]$	monomer concentration at time 0
M_n	number average molecular weight

$[M_\mathrm{t}]$	monomer concentration at time t
M_w	weight average molecular weight
n_0	number density of the ions
$\overrightarrow{p}$	dipole moment
$\overrightarrow{P}$	polarization
P_n	degree of polymerization
$\overrightarrow{P}$	polarization
$P(\overrightarrow{q})$	form factor
q	elementary charge
$\overrightarrow{q}$	scattering vector
q_0	primary scattering peak
$R_\mathrm{CT+SEI}$	interfacial resistance
s	displacement (shear experiment)
$S(\overrightarrow{q})$	structure factor
t	time
t_{Li^+}	Li^+-ion transference number
T	temperature
T_0	Vogel temperature
T_2	transverse relaxation time
$T_{50\%}$	temperature at a weight loss of 50%
T_ODT	order-disorder transition temperature
T_g	glass transition temperature
T_ref	reference temperature
v	velocity
V	volume
y_0	plateau value at infinite times (stretched exponential function)
α_FH	experimentally determined fit parameter (Flory-Huggins)
β_CC	exponent symmetric broadening Cole/Cole
β_FH	experimentally determined fit parameter (Flory-Huggins)
β_HN	exponent symmetric broadening Havriliak-Negami
γ	strain
γ_0	strain amplitude
$\dot{\gamma}$	shear rate
γ_CD	exponent asymmetric broadening Cole/Davidson
γ_HN	exponent asymmetric broadening Havriliak-Negami
γ_gm	gyromagnetic ratio
$\tan\delta_\mathrm{BDS}$	loss tangent from BDS
$\tan\delta_\mathrm{rheo}$	loss tangent from rheology
δ_BDS	phase angle from BDS
δ_diff	duration of the gradient pulse
δ_Rheo	phase angle from rheology
Δ_diff	diffusion time
$\Delta\epsilon$	dielectric relaxation strength
ϵ_0	vacuum permittivity
ϵ^*	complex permittivity

ϵ'	real part of the permittivity
ϵ''	imaginary part of the permittivity
ϵ_s	static dielectric constant
η	viscosity
η^*	complex viscosity
Θ	scattering angle
λ	wave length
μ	expectation value (Gauss)
σ_0	ionic conductivity
σ_∞	conductivity at an infinitely high temperature
σ_∞^A	conductivity at an infinitely high temperature (Arrhenius model)
σ	stress
σ_G	standard deviation (Gauss)
σ^*	complex conductivity
σ'	real part of the conductivity
σ''	imaginary part of the conductivity
T_ODT	order-disorder temperature
τ_α	relaxation time of the segmental relaxation
τ_c	relaxation time of the charge transport
τ_CC	relaxation time Cole/Cole
τ_CD	relaxation time Cole/Davidson
τ_D	relaxation time Debye
τ_HN	relaxation time Havriliak-Negami
τ_relax	longest relaxation time
Φ	phase
χ^*	dielectric susceptibility
χ_FH	Flory-Huggins parameter
χ_SAXS	azimuthal angle
ω	angular frequency
ω_BDS	dielectric frequency
ω_c	rate of charge transport
ω_Rheo	rheological frequency

Publications and Conference Contributions

Publications

Butzelaar, A. J.; Röring, P.; Mach, T. P.; Hoffmann, M.; Jeschull, F.; Wilhelm, M.; Winter, M.; Brunklaus, G.; Theato, P. Styrene-Based Poly(ethylene oxide) Side-Chain Block Copolymers as Solid Polymer Electrolytes for High-Voltage Lithium-Metal Batteries. *ACS Appl. Mater. Interfaces* **2021**, *13*, 39257–39270.

Butzelaar, A. J.; Röring, P.; Hoffmann, M.; Atik, J.; Paillard, E.; Wilhelm, M.; Winter, M.; Brunklaus, G.; Theato, P. Advanced Block Copolymer Design for Polymer Electrolytes: Prospects of Microphase Separation. *Macromolecules* **2021**, *54*, 11101–11112.

Wang, Z.; Cui, H.; Liu, M.; Grage, S. L.; Hoffmann, M.; Sedghamiz, E.; Wenzel, W.; Levkin, P. A. Tough, Transparent, 3D-Printable, and Self-Healing Poly(ethylene glycol)-Gel (PEGgel). *Advanced materials* **2022**, *34* , e2107791.

Scheiger, J. M.; Hoffmann, M.; Falkenstein, P.; Wang, Z.; Rutschmann, M.; Scheiger, V. W.; Grimm, A.; Urbschat, K.; Sengpiel, T.; Matysik, J.; Wilhelm, M.; Levkin, P. A.; Theato, P. Inverse Vulcanization of Norbornenylsilanes: Soluble Polymers with Controllable Molecular Properties via Siloxane Bonds. *Angewandte Chemie (International ed. in English)* **2022**, *61*, e202114896.

Khudyshkina, A. D.; Morozova, P. A.; Butzelaar, A. J.; Hoffmann, M.; Wilhelm, M.; Theato, P.; Fedotov, S. S.; Jeschull, F. Poly(ethylene oxide)-Based Electrolytes for Solid-State Potassium Metal Batteries with a Prussian Blue Positive Electrode. *ACS Appl. Polym. Mater.* **2022**, *4*, 2734–2746.

Hoffmann, M.; Butzelaar, A. J.; Iacob, C.; Theato, P.; Wilhelm, M. Ionogels as Polymer Electrolytes for Lithium–Metal Batteries: Comparison of Poly(ethylene glycol) Diacrylate and an Imidazolium-Based Ionic Liquid Crosslinker. *ACS Appl. Polym. Mater.* **2022**, *4*, 2794–2805.

Hoffmann, M.; Iacob, C.; Kaysan, G.; Simmler, M.; Nirschl, H.; Guthausen, G.; Wilhelm, M. Charge Transport and Glassy Dynamics in Blends Based on 1-Butyl-3-vinylbenzylimidazolium

Bis(trifluoromethanesulfonyl)imide Ionic Liquid and the Corresponding Polymer. *Polymers* **2022**, *14*, 2423.

Khudyshkina, A. D.; Butzelaar, A. J.; Guo, Y.; Hoffmann, M.; Bergfeldt, T.; Schaller, M.; Indris, S.; Wilhelm, M.; Theato, P.; Jeschull, F. From Lithium to Potassium: Comparison of Cations in Poly(ethylene oxide)-Based Block Copolymer Electrolytes for Solid-State Alkali Metal Batteries. *Electrochim. Acta.* **2023**, *454*, 142421.

Li, S.; Scheiger, J. M.; Wang, Z.; Huber, B.; Hoffmann, M.; Wilhelm, M.; Levkin, P. A. Diapers to Thickeners and Pressure-Sensitive Adhesives: Recycling of Superabsorbers via UV Degradation. *ACS Appl. Mater. Interfaces* **2023**, *37*, 44186-44193.

Hoffmann, M.; Hirschberg, V.; Dingenouts, N.; Wilhelm, M. Macroscopic Orientation and Local Mobility of PI during Shear Alignment of ISI and SIIS Triblock Copolymers Investigated by SAXS and Rheo-Dielectric Spectroscopy. *Macromolecules* **2023**, *24*, 10236-10253.

Khudyshkina, A. D.; Rauska, U.-C.; Butzelaar, A. J.; Hoffmann, M.; Wilhelm, M.; Theato, P.; Jeschull, F. Impact of Nano-sized Inorganic Fillers on PEO-based Electrolytes for Potassium Batteries. *Batteries & Supercaps* **2023**, *7*, e202300404.

Bhusari, S.; Hoffmann, M.; Herbeck-Engel, P.; Snkaran, S.; Wilhelm, M.; del Campo, A. Rheological Behavior of Pluronic/Pluronic Diacrylate Hydrogels Used for Bacteria Encapsulation in Engineered Living Materials. *Soft Matter* **2024**, *20*, 1320-1332.

Conference Contributions

ICR 2020 M. Hoffmann, C. Iacob, M. Wilhelm, *Investigation of Charge Transport and Glassy Dynamics in Polymerized Ionic Liquids by Combined Rheo-Dielectric*, 18th International Congress on Rheology (2020), online. – **Oral**

AERC 2021 C. Iacob, M. Hoffmann, M. Heck, A. Matsumoto, M. Wilhelm, *Charge Transport and Glassy Dynamics in Polymerized Ionic Liquids*, Annual European Rheology Conference (2021), online. – **Oral**

MAKRO 2021 C. Iacob, M. Hoffmann, M. Wilhelm, *Charge Transport and Glassy Dynamics in Polymerized Ionic Liquids*, Makromolekulares Kolloquium (2021), online. – **Poster**

ISP 2021 M. Hoffmann, C. Iacob, M. Wilhelm, *Investigation of Charge Transport and Glassy Dynamics in Polymerized Ionic Liquids by Combined Rheo-Dielectric*, 13th International Symposium on Polyelectrolytes (2021), online. – **Oral**

AERC 2022 M. Hoffmann, M. Wilhelm, *Coupled Rheo-Dielectric: In-situ Investigation of the Alignment of Lamellar Block Copolymers*, Annual European Rheology Conference (2022), Seville, Spain. – **Oral**

Acknowledgements

This thesis could not have been completed without the support of the people around me. Therefore, I would like to take this opportunity to thank everyone who has supported me all the way here:

First and foremost I would like to thank my supervisor *Prof. Dr. Manfred Wilhelm* for giving me the opportunity to pursue my PhD in his group and for his support. Thank you for your trust, the freedom to develop my own ideas and giving me the feeling for numbers! A special thank you also goes to *Prof. Dr. Michael Meier* for co-examining this work.
I am grateful for the opportunity to spend some months at Cornell University in Ithaca, NY with *Prof. Dr. Ulrich Wiesner*. Thank you for your openness and honesty! I enjoyed working with *William Tait* whose helpfulness and patience immersed me in a new subject and taught me many useful new skills.
Furthermore, I would like to thank and acknowledge *Dr. Ciprian Iacob* for teaching me all he knows about rheo-dielectric and introducing me to polymerized ionic liquids.
Thank you, *Dr. Nico Dingenouts*, for the enthusiastic introduction to SAXS and the data processing, as well as the many scientific discussions and organizational support.
To *Dr. Valerian Hirschberg*, for your advice and countless proofreading. Thank you for always being willing to help. All the best on your way!
Thanks to *Dr. Matthias Heck* for the detailed answers to my questions about the orientation of block copolymers and for providing the PS-*b*-P2VP sample.
I would also like to thank all my collaboration partners: *Prof. Dr. Gisela Guthausen* for giving me the opportunity to measure PFG-NMR all by myself as well as *Gina Kaysan* for introducing me to the instrument. Thanks to *Dr. Andreas Butzelaar*, *Dr. Johannes Scheiger*, *Anna Khudyshkina* and *Mira Simmler* for their scientific help and support.
I gratefully acknowledge the support of the *Foundation of German Business* (Stiftung der deutschen Wirtschaft, sdw) for the financial and non-material support of my studies and my PhD, as well as the regional group in Karlsruhe for many insights beyond the horizon and new friendships.
My deepest gratitude goes to the whole *AKW* for the pleasant and inspiring working atmosphere and your helpfulness. Thanks to all the hardworking proofreaders! Many thanks also to *Klara Urbschat* and *Eileen Schwarz*, who supported me in the lab. A big thanks goes to *Sabine Weiland*, *Ingrid Zeller* and *Daniel Zimmermann* for their organizational support in all matters and for keeping AKW going. Special thanks to *Lea Fischer* for her

solution-oriented thinking and to my dearest office colleague *Marie Röpert* - we made it!
Thanks to my Ultimate Frisbee team *Colorado* for being my healthy distraction, for many weekends full of Ultimate Frisbee, for the possibility to play a world championship with you and for wonderful friendships!
I am very grateful for the support of my family and friends, especially my *parents and grandparents*. I appreciate your interest in my work and your support, even though I took a completely different path than you. Thank you for your unconditional love and trust in me!
Thank you, *Armin*, for everything and much more. Thank you for being by my side!